On the Transition Boundary Between Regular and Mach Reflections From a Wedge in Inviscid and Polytropic Gases

by

Maciej K. Hryniewicki

A thesis submitted in conformity with the requirements
for the degree of Doctor of Philosophy
Graduate Department of Aerospace Science and Engineering
Institute for Aerospace Studies
University of Toronto

Abstract

On the Transition Boundary Between Regular and Mach Reflections From a Wedge in Inviscid and Polytropic Gases

Maciej K. Hryniewicki
Doctor of Philosophy
Graduate Department of Aerospace Science and Engineering
Institute for Aerospace Studies
University of Toronto
2016

The transition boundary separating the region of regular reflection from the regions of single-, transitional- and double-Mach reflections for the collision of a planar shock wave moving in argon and atmospheric air and interacting with an inclined reflecting plane is studied by both analytical methods and high-resolution computational-fluid-dynamic flow-field simulations. The analytical solution for regular reflection and the corresponding solutions for the extreme-angle (or detachment) and mechanical-equilibrium criteria of John von Neumann in 1945 are first revisited and revised. The boundary between regular and Mach reflections is then determined numerically by using a parallel anisotropic block-based adaptive mesh refinement finite-volume scheme for the study of compressible flows associated with unsteady, oblique shock-reflection processes in two spatial dimensions. This numerical transition boundary is computed by post-processing closely stationed flow-field simulations, to determine the transition point when the Mach stem of the Mach-reflection pattern just disappears and this pattern transcends into that of regular reflection. The new transition boundary agrees well with von Neumann's sonic and extreme-angle boundaries for weak incident shock Mach numbers from 1.0 to 1.6, but then trends unexpectedly upward and above von Neumann's sonic and extreme-angle boundaries by a few degrees at stronger incident shock Mach numbers from 1.6 to 4.0. This upward trend for the new numerical transition boundary at stronger incident shock Mach numbers is noticeable, significant, occurs in a uniform and systematic manner and is shown to be well outside any influences of numerical error. Furthermore, the numerically determined boundary is shown to agree well with the very few available experimental data from past experiments designed to reflect symmetrical oblique shock waves along a plane without a combined viscous and thermal boundary layer.

To my beloved parents, Izabela and Waldemar,
who sacrificed all of their accomplishments in one country,
to ensure that their two young children had limitless opportunity in another.

Acknowledgements

First and foremost, my endeavour into the undertakings of this research would not have bore good fruit without the guidance and oversight of my thesis supervisors, Professor James J. Gottlieb and Professor Clinton P. T. Groth. I thank them for their motivation, inspiration, enthusiasm, patience, care, insight and expertise throughout the duration of this thesis. Towards these two I express my gratitude and appreciation as well as my admiration and respect, firstly for providing me with the opportunity to embark upon my doctoral studies at the University of Toronto Institute for Aerospace Studies (UTIAS) and, secondly, for selflessly imparting upon me their wealth of knowledge while I studied under their proficient and charismatic leads.

A warmhearted thank you extends to the chair of my doctoral examination committee, Professor David W. Zingg, for stimulating numerous, thought-provoking discussions as well as for contributing his apt and comprehensive counsel to my research topic. I would also like to thank the respective external and internal examiners of my thesis, Professor Evgeny V. Timofeev and Professor Craig A. Steeves, for their assessments of this dissertation.

I would like to recognize the research stipend granted to me by UTIAS throughout my doctoral studies. In addition, I would like to acknowledge the computational resources that have been used to perform all of the calculations reported herein, as provided by the SciNet High Performance Computing Consortium at the University of Toronto and Compute/Calcul Canada, through funding from the Canada Foundation for Innovation (CFI) and the Province of Ontario, Canada.

I am thankful to the entire faculty and staff at UTIAS for nurturing me with a world-class level of education that because of them ranks highly amongst the top aerospace departments in the world. Moreover, I am thankful to all of my academic colleagues and companions for their generous assistances in my research and for their long-lasting, unforgettable friendships.

Finally, an affectionate thank you belongs to my dear parents, Izabela and Waldemar, as well as my benevolent sister, Magdalena, for their endless love and unwavering encouragement. They have instilled in me the importance of education, in conjunction with the traits of hard work and perseverance, and I am forever grateful to them for supporting my desire to further my education in the field of aerospace science and engineering.

Maciej K. Hryniewicki
University of Toronto Institute for Aerospace Studies
July 2016

Contents

List of Tables

List of Figures

Chapter 1

Introduction

1.1 Regular and Mach Reflection

The interaction of a moving, constant-velocity, planar shock wave with a rigid, inclined wedge in a shock tube filled with a gas produces four basic shock-reflection configurations or patterns. These four patterns named regular reflection (RR), single Mach reflection (SMR), transitional Mach reflection (TMR) and double-Mach reflection (DMR) are illustrated in Fig. 1.1 by computational-fluid-dynamic images for shock-wave interactions with inclined wedges in air. The type of reflection pattern depends on the strength or Mach number $M_{\rm i}$ of the incident shock wave, the inclination angle $\theta_{\rm w}$ of the wedge relative to the direction of an oncoming flow field, and the properties of the gas (e.g. with or without high-temperature effects such as dissociation, ionization and chemical reactions). The dependence of the type of reflection pattern on the incident shock strength $M_{\rm i}$ and the wedge angle $\theta_{\rm w}$ is illustrated in Fig. 1.2 for air (with the specific heat ratio $\gamma = 7/5$ for a polytropic gas), by showing the boundaries between the regions of RR, SMR, TMR and DMR, including the dual region of regular reflection and Mach reflection (mainly TMR and DMR).

Regular reflection (RR) is composed of the planar incident shock along with the straight and curved reflected shock which are joined at the wedge surface. As the shocks propagate this two-shock confluence point moves along the wedge surface. This RR pattern occurs at large wedge angles for strong shocks and also at small wedge angles for weak shocks. In single Mach reflection (SMR) the confluence of the incident planar shock and curved reflected shock occurs above the wedge, and a third shock called the Mach stem extends from the confluence point to the wedge surface. Also, from the triple-shock confluence point a curved shear layer called the slip stream trails the moving triple point and shocks. This SMR pattern occurs typically at small wedge angles. Double Mach reflection (DMR) features two triple shock confluence points,

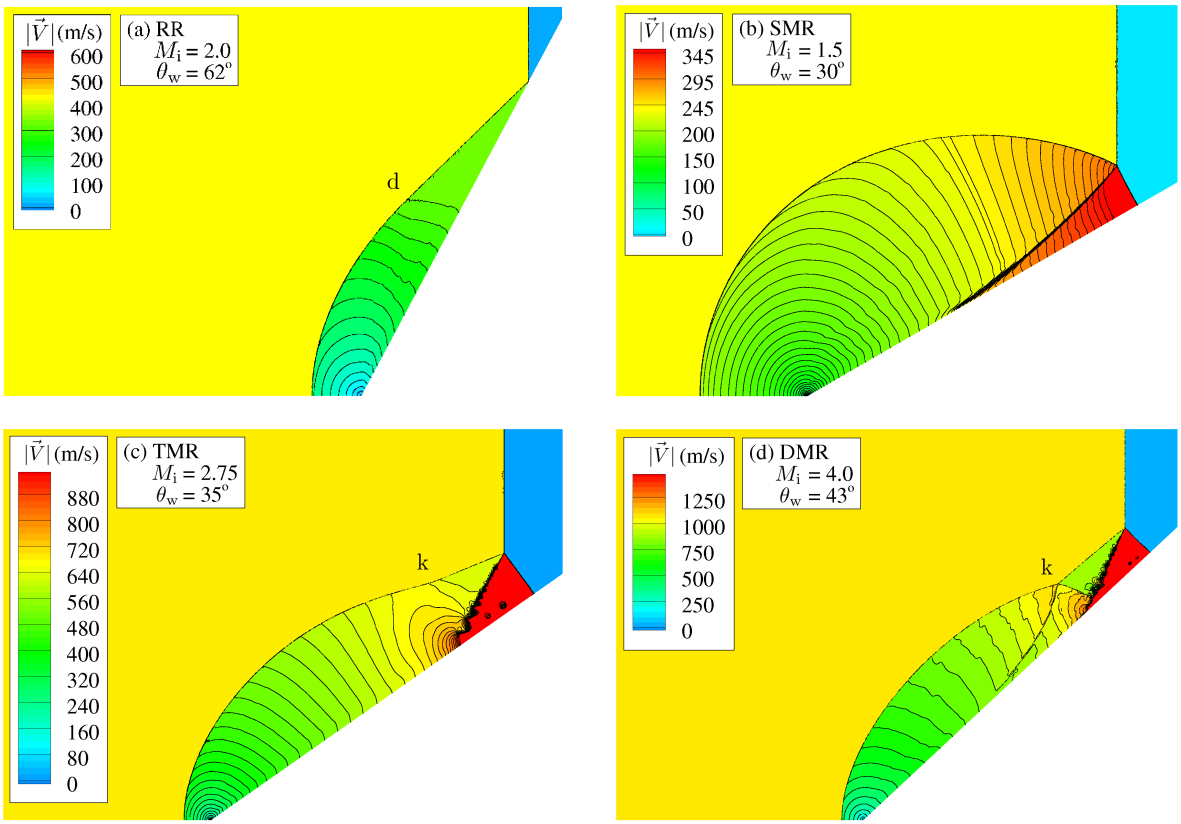

Figure 1.1: Regular- and Mach-reflection flow-field patterns from the interaction of a moving planar shock wave with a wedge in air. These four examples were produced by using the computational-fluid-dynamics algorithm described in Chapter 5.

each with a slip stream, and the latter has a distinct kink ('k' in Fig. 1.1). In transitional Mach reflection (TMR) the second triple point is barely visible and occurs as a slight kink in the reflected shock, and a second slip stream is not observable. The slight kink in the TMR patterns is more noticeable near the TMR-DMR boundary and disappears near the SMR-TMR boundary (see Fig. 1.2). The DMR and TMR patterns occur at intermediate wedge angles. Note that the labels 'd' and 'k' in Fig. 1.1 both indicate the locations on the reflected shock of the front of the disturbance or signal that emanates from the wedge corner and surface.

The basic Mach-reflection (MR) pattern was discovered in double-spark separated discharges made in 1878 by Ernst Mach [1], from experimental observations of smeared carbon soot patterns on coated glass plates exposed to the flow field. The four patterns of regular, single-Mach, transitional-Mach and double-Mach reflections were discovered in shock-tube experiments in the 1940s and 1950s by Smith [2] and White [3]. Two-shock regular-reflection and three-shock Mach-reflection configurations were studied theoretically in the 1940s by von Neumann [4–6], Courant and Friedrichs [7] and Bleakney and Taub [8], and in the 1950s by Cabannes [9] and Kawamura and Saito [10].

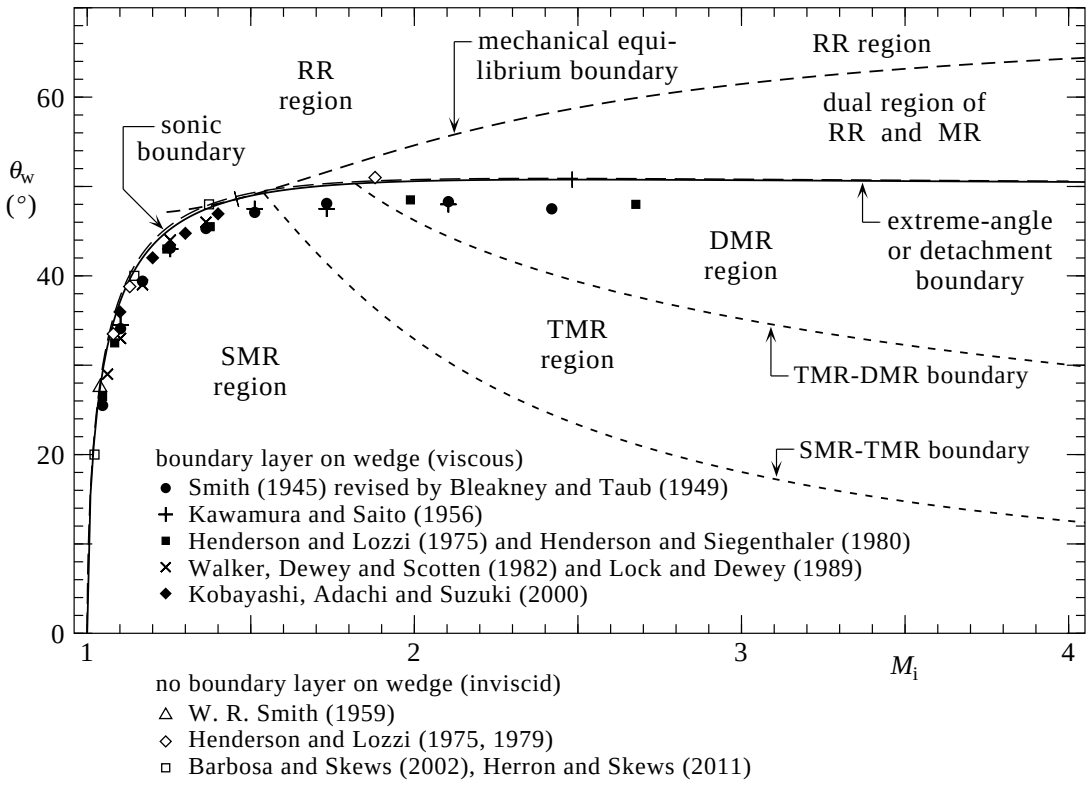

Figure 1.2: Regions of regular and Mach reflection separated by analytical and experimental transition boundaries in air.

The basic regions and boundaries between regular- and Mach-reflection patterns in air are illustrated in Fig. 1.2, in a graph of the wedge angle θ_w versus the incident shock Mach number M_i. As mentioned earlier, regular reflections occur typically at larger wedge angles and single-Mach reflections occur typically at smaller wedge angles. The influence of the incident shock strength is also important, as depicted in the figure. Double- and transitional-Mach reflections occur in the mid to lower range of wedge angles and at large incident shock Mach numbers. The two upper transition boundaries are based on the two criteria of mechanical equilibrium and detachment, and they originate from von Neumann [5]. Von Neumann's additional transition boundary based on the sonic criterion is very close to the extreme-angle boundary (within half of a degree). Note that the analytical solutions for the extreme-angle, mechanical-equilibrium and sonic boundaries will be fully discussed in Chapter 3 of this thesis. These transition boundaries establish three regions: one upper region for regular reflection only, one adjacent dual region for either regular reflection or Mach reflection (TMR and DMR), and one lower region for only Mach reflection (SMR, TMR and DMR). The two other boundaries that subdivide the region of Mach reflection (MR) into the regions of SMR, TMR and DMR are the results of research by Ben-Dor and Glass [11,12]. For additional information on shock waves and Mach reflection, see the books by Glass and Sislian [13] and Ben-Dor [14]. Ben-Dor includes another weak Mach-reflection configuration called von Neumann reflection (vNR), which resembles a SMR

pattern with a band of compression waves near the triple point, a curved Mach stem, and a barely noticeable slip stream. The region of vNR occurs at the left side of the SMR region, but no boundary between vNR and SMR is available to illustrate the vNR region in Fig. 1.2. The paper by Semenov, Berezkina and Krassovskaya [15] provides a more recent and extensive classification of Mach-reflection configurations and their properties.

All of the transition boundaries shown in Fig. 1.2 between the various shock-reflection patterns are the result of analytical methods using the theory of shock waves moving in a polytropic gas ($\gamma = 7/5$), where the presence of a combined viscous and thermal boundary layer on the wedge surface has been ignored. For shock-tube experiments using air as the working gas and wedges with smoothly machined surfaces, a combined viscous and thermal boundary layer is produced behind the incident and reflected shocks on the wedge surface.

The experimental data for air presented in Fig. 1.2 come from detailed investigations aimed specifically at finding the transition boundary between regular and Mach reflections. Shadowgraph and schlieren photographs were taken of moving shocks interacting with wedges in a shock tube for various wedge angles and incident shock Mach numbers near the boundary between regular and Mach reflections, in order to locate the point at which the Mach-stem length or triple-point angle with the wedge just diminishes to zero. Various incident and reflected shock angles, including that of the triple-shock confluence point, were measured from these photographs and plotted as a means to determine the experimental transition boundary.

The dark experimental markers for air in Fig. 1.2 that lie below the extreme-angle boundary, which were obtained with a combined viscous and thermal boundary layer on the wedge surface, clearly show that the experimental transition boundary between regular and Mach reflection lies a few degrees below the closely spaced sonic and extreme-angle boundaries. This persistence of regular reflection into the region of Mach reflection occurs for all experimental cases of incident shock Mach numbers ranging from 1.05 to 2.68. See the papers of relevance by Smith [2], Bleakney and Taub [8], Kawamura and Saito [10], Henderson and Lozzi [16], Henderson and Siegenthaler [17], Walker, Dewey and Scotten [18], Lock and Dewey [19] and Kobayashi, Adachi and Suzuki [20] for details of their experimental methods and data-processing techniques.

The scarce, white-filled experimental markers for air in Fig. 1.2 that lie on the sonic and/or extreme-angle boundaries were obtained without the influence of a combined viscous and thermal boundary layer on the wedge surface. The experiments used either bifurcated shock tubes or angled reflecting duct ends to ensure that no boundary or shear layer was produced along the reflecting surface behind the moving shock waves. These data illustrate that the sonic and extreme-angle boundaries are a good transition boundary for incident shock Mach numbers M_i from 1.0 to 1.4. See the papers of Smith [21], Henderson and Lozzi [16, 22], Barbosa and Skews [23] and Herron and Skews [24] for details of their experimental methods and data-processing techniques. Note that the experimental data is also summarized in Chapter 8.

All sets of data in Fig. 1.2 for the case of air illustrate the importance of the combined viscous and thermal boundary layer on shifting the transition boundary between regular and Mach reflection. This shift occurs from above (inviscid, no boundary layer) to below (viscous, boundary layer) the closely spaced sonic and extreme-angle boundaries. The resulting persistence of regular reflection for strong shock waves across von Neumann's sonic and extreme-angle boundaries and downward into the Mach-reflection region by a few degrees is normally attributed to the presence of the boundary layer and on the wedge surface in the experiments and the lack thereof in analytical predictions of the transition boundaries. Although this explanation is fairly well accepted, additional supporting evidence is desirable to validate the theoretical transition criteria for shock-wave reflections that are generally agreed upon, but not yet fully understood or entirely proved. See the reviews and papers on shock-wave reflections by Bleakney and Taub [8], Pack [25], Griffith [26], Bazhenova, Gvozdeva and Nettleton [27], Hornung [28], Ben-Dor [29], Henderson, Takayama, Crutchfield and Itabashi [30] and Adachi, Sakurai and Kobayashi [31] for more information.

1.2 Motivation and Objective

The goal of this doctoral research is to provide more detailed information and understanding related to the transition boundary separating regular- and Mach-reflection patterns for unsteady shock-wave interactions with rigid, inclined wedges in inviscid and polytropic gases. In this study, the transition boundary is sought numerically by using an advanced computational-fluid-dynamics code in conjunction with sophisticated post-processing techniques to accurately determine local RR to MR transition points from a collection of closely stationed computational flow fields at various shock strengths and wedge angles. The simulations greatly facilitate the controlled exclusion of transport properties that are otherwise intrinsic to the flow field, yielding a highly reproducible setting in which the numerical results are obtained. The transition boundary is systematically examined and extended herein by means of shock waves striking wedges without a combined viscous and thermal boundary layer on the wedge surface, in argon and atmospheric air, over incident shock Mach numbers ranging from 1.0 to 4.0. The findings presented in this thesis address the requirement for precise verification of the theoretical transition criteria that are generally accepted in oblique shock-wave reflection studies.

1.3 Thesis Organization

The remaining portions of this thesis are organized as follows. In Chapter 2, the governing continuum-fluid-dynamic equations for the conservation of mass, momentum and energy in gaseous fluid flows are reviewed and the molecular transport properties for argon, nitrogen and atmospheric air are provided. In Chapter 3, analytical solutions for regular reflection and

the transition criteria for the extreme-angle and mechanical-equilibrium conditions of von Neumann [5] are revisited and revised. In Chapter 4, internal structures of shock-front transitions in argon, nitrogen and atmospheric air are examined based on solutions of the Navier-Stokes equations of motion. This is followed in Chapter 5 by a description of the computational-fluid-dynamics (CFD) solution method utilized extensively within this research. Numerical verification and validation of this computational framework is reported in Chapter 6. Chapter 7 describes the methodology of post-processing the CFD flow-field data to determine the numerical transition between regular and Mach reflections. In Chapter 8, past experimental data for the case of no combined viscous or thermal boundary on the wedge surface are collected to verify the numerical transition boundary between regular and Mach reflections. Computed solutions of oblique shock-wave reflections as well as novel results for the new numerical transition boundary separating regular and Mach reflections in argon and atmospheric air are presented in Chapter 9. Chapter 10 provides a summary of the observed findings and original contributions established in this thesis, closing with a discussion regarding recommendations for future research.

Chapter 2

Navier-Stokes Equations

The gas-dynamic equations governing two-dimensional, laminar, compressible, unsteady, gaseous fluid flows are used herein to describe the unsteady shock-wave reflection processes of interest. The generic, multi-dimensional, conservation form of these coupled, non-linear, partial differential equations (PDEs), with neglected external body forces and source terms, can be conveniently expressed using vector notation as

$$\frac{\partial \rho}{\partial t} + \vec{\nabla} \cdot (\rho \vec{u}) = 0, \tag{2.1}$$

$$\frac{\partial}{\partial t}(\rho \vec{u}) + \vec{\nabla} \cdot \left(\rho \vec{u} \otimes \vec{u} + p \vec{\vec{I}}\right) = \vec{\nabla} \cdot \vec{\vec{\tau}}, \tag{2.2}$$

$$\frac{\partial}{\partial t}(\rho e) + \vec{\nabla} \cdot \left[\rho \vec{u} \left(e + \frac{p}{\rho}\right)\right] = \vec{\nabla} \cdot (\vec{u} \cdot \vec{\vec{\tau}}) - \vec{\nabla} \cdot \vec{q}, \tag{2.3}$$

as found in Hirsch [32]. These Navier-Stokes equations govern the conservation of mass and momentum in a viscous, heat-conducting fluid flow, with the addition of a transport equation for the conservation of energy. The inviscid terms are situated on the left-hand sides of these equations, whereas the viscous terms are located on the right-hand sides. For inviscid flow fields, the latter are omitted to yield the classical Euler equations. As the influence of the unsteady transition to turbulence and turbulent flow on the shock reflection process, which should occur far from the vicinity of the confluent shocks and slipstreams, is expected to be minimal at most, the assumption of laminar flow is sufficient for the present research.

The inviscid terms on the left-hand sides of Eqs. (2.1) to (2.3) govern the gas-particle transport of fluid-dynamic properties by means of the bulk motion of the flow field. These terms consist of the following physical variables: t is the time, ρ is the fluid density, $\vec{u}$ is the flow velocity vector, p is the fluid pressure and $e = \varepsilon + \vec{u}^2/2$ is the specific total energy, where ε is the specific internal energy and $\vec{u}^2/2$ is the specific kinetic energy. The symbol $\otimes$ in Eq. (2.2) denotes the operator for the vector outer product whose result is a dyadic quantity. Moreover, $\vec{\nabla}$

is the vector differential operator and $\vec{\vec{I}}$ is the identity tensor. The gas is assumed to behave in a polytropic manner, satisfying the ideal-gas equation of state $p = \rho RT$, where R is the specific gas constant and T is the fluid temperature. The specific internal energy and specific internal enthalpy in this case take the forms $\varepsilon = c_v T$ and $h = c_p T$, respectively, where $c_v = R/(\gamma - 1)$ and $c_p = \gamma R/(\gamma - 1)$ are the corresponding specific heats at constant volume and at constant pressure, and $\gamma = c_p/c_v$ is their ratio.

The molecular transport of macroscopic flow quantities due to fluid stresses and heat conduction is governed by the viscous terms on the right-hand sides of Eqs. (2.2) and (2.3). For a Newtonian fluid, the viscous stress tensor, $\vec{\vec{\tau}}$, appearing in the conservation equations for momentum and energy, is defined as

$$\vec{\vec{\tau}} = 2\eta \vec{\vec{S}} + \lambda_v \vec{\nabla} \cdot \vec{u} \vec{\vec{I}}, \tag{2.4}$$

in which η is the dynamic viscosity, $\vec{\vec{S}} = \frac{1}{2}[\vec{\nabla}\vec{u} + (\vec{\nabla}\vec{u})^\top]$ is the strain rate tensor, where the superscript $\top$ denotes the matrix transpose, and $\lambda_v = \eta_v - \frac{2}{3}\eta$ is the second coefficient of viscosity, where η_v is the volume viscosity. Within the equation for the conservation of energy, the heat flux vector, $\vec{q}$, is defined as

$$\vec{q} = -\kappa \vec{\nabla} T, \tag{2.5}$$

according to Fourier's law of heat conduction, where κ is the thermal conductivity. In this research, additional sources of heat transfer with the surrounding environment are ignored.

2.1 Species Properties of Atmospheric Air

Atmospheric air at the Earth's surface is a mixture of gaseous species whose concentrations are changing slowly with time. The concentrations and thermodynamic properties of atmospheric air have been updated to the year 2016 in this research, based on earlier work for the U.S. standard atmosphere in 1976 [33], by the study of Park, Kim, Lee, Esler, Davis and Wielgosz in 2004 [34] and by the work of Picard, Davis, Gläser and Fujii in 2007 [35]. The mixture species of air, their molecular weights and related gas physical properties are listed in table 2.1. The values of c_p were calculated at a room temperature of 295 K by using the Chemical Equilibrium with Applications (CEA) computer program developed at the National Aeronautics and Space Administration (NASA) by McBride, Zehe and Gordon [36]. The values of γ then follow from $\gamma = c_p/(c_p - R)$. The updated values of the air species concentrations for 2016 are included in the table as well. The main changes in these concentrations are the result of increased amounts of carbon dioxide (CO_2) released into the atmosphere in recent years and some concentration changes for trace species like carbon monoxide (CO), ammonia (NH_3) and sulfur dioxide (SO_2).

The molecular weight of dry air is determined by using the mixture rule $M_{\text{mix}} = \sum_{i=1}^{16} \mathrm{X}_i M_i$ to obtain $M_{\text{air}} = 28.9655$ kg/mol, in which X_i is the mole fraction of species i. The specific gas

constant for air follows as $R_{\text{air}} = \mathcal{R}/M_{\text{air}} = 287.048$ J/kg·K, in which the universal gas constant $\mathcal{R} = 8,314.472$ J/mol·K. The mixture specific heat is given by $c_{p_{\text{mix}}} = \sum_{i=1}^{16} \text{X}_i c_{p_i}$, yielding $c_{p_{\text{air}}} = 1004.59$ J/kg at 295 K. The specific heat ratio of air follows as $\gamma_{\text{air}} = c_{p_{\text{air}}} / \left(c_{p_{\text{air}}} - R_{\text{air}}\right) = 1.4004$, which is frequently rounded to the value 1.40. These properties of dry air are used in this research, with the value of γ reduced slightly to 7/5 to conform to the specific case of a diatomic gas.

The variations with temperature of the specific heat at constant pressure and the specific heat ratio of dry air are illustrated in Fig. 2.1. The assumption of a polytropic gas in this research with c_p and γ both held constant is reasonable only for temperatures ranging from 80 K to about 500–700 K, or for incident shock Mach numbers less than about 2.5.

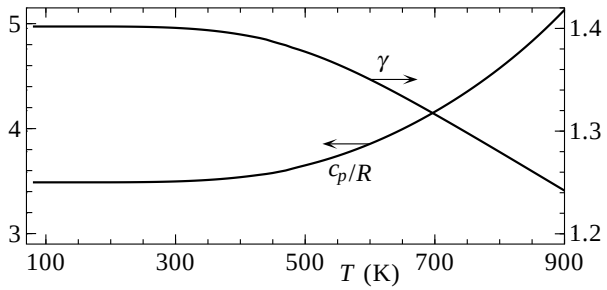

Figure 2.1: Specific heat at constant pressure and specific heat ratio versus temperature for dry air.

2.2 Molecular Transport Properties of Atmospheric Air

The macroscopic transport of bulk fluid-dynamic quantities within the flow field involves the interaction and collision of molecules and is represented herein using empirical transport coefficients. Within a viscous, heat-conducting gas, the molecular transport properties that correlate the viscous stresses to the divergence of the velocity field and also the heat flux to the spatial temperature gradient are the viscosity and the thermal conductivity, respectively. The viscous stresses can be further decomposed into two components and their respective transport coefficients: for shear stresses and shear strain rates, the shear or dynamic viscosity, and for normal (e.g. tensile or compressive) stresses and volumetric strain rates, the bulk, dilatational or volume viscosity. Descriptions outlining the techniques used in the evaluation of each of these three transport coefficients are given in the following subsections and the calculated results for the molecular transport properties of dry atmospheric air and its constituent components are also provided.

Table 2.1: Composition of dry atmospheric air at sea level updated to the year 2016.

i	gas species	chemical formula	M (g/mol)	concentration (ppm)	c_p/R	γ	ϵ/k_B (K)	σ_o (Å)	μ (debye)	Z_rot (at 295 K)
1	nitrogen	N_2	28.0134	780850.463	3.50182	1.39971	91.5	3.681		5.85
2	oxygen	O_2	31.9988	209386.53	3.53455	1.39455	113.0	3.433		4.32
3	argon	Ar	39.948	9332.0	2.5	1.66667	124.0	3.418		
4	carbon dioxide	CO_2	44.0095	403.47	4.33638	1.29973	190.0	3.996		29899.80
5	neon	Ne	20.1797	18.179	2.5	1.66667	35.7	2.789		
6	helium	He	4.002602	5.235	2.5	1.66667	10.22	2.576		
7	methane	CH_4	16.04246	1.863	4.33475	1.29987	137.0	3.882		9.57
8	krypton	Kr	83.798	1.139	2.5	1.66667	190.0	3.610		
9	hydrogen	H_2	2.01588	0.532	3.57588	1.38822	33.3	2.968		209.69
10	nitrous oxide	N_2O	44.0128	0.329	4.52555	1.28364	220.0	3.879	0.167	4409.07
11	carbon monoxide	CO	28.0101	0.119	3.50351	1.39944	110.0	3.590	0.1172	4.23
12	xenon	Xe	131.293	0.087	2.5	1.66667	229.0	4.055		
13	ozone	O_3	47.9982	0.042	4.69976	1.27029	249.0†	3.753†	0.53	4.91
14	nitrogen dioxide	NO_2	46.0055	0.009	4.42849	1.29167	377.7‡	3.919‡	0.316	4.93
15	ammonia	NH_3	17.03052	0.002	4.27317	1.30551	146.8	3.441	1.437	14.06
16	sulfur dioxide	SO_2	64.0638	0.001	4.76720	1.26545	252.0	4.290	1.611	5.13

† These parameters have been tuned to ensure agreement of computed dynamic viscosities with past experimental measurements.

‡ This is the mean value of the three similar triatomic molecules of CO_2, SO_2 and NOCl, as per the work of de Gouw and Lovejoy [37].

2.2.1 Dynamic Viscosity and Thermal Conductivity

The dynamic viscosity η and thermal conductivity κ for the constituents of dry atmospheric air are calculated according to the formulation adopted in the NASA CEA computer program developed by McBride and Gordon [38, 39]. For individual pure species, least squares curve fits to empirical data for these two transport properties are of the form

$$\left.\begin{matrix}\ln(\eta)\\ \ln(\kappa)\end{matrix}\right\} = A\ln(T) + \frac{B}{T} + \frac{C}{T^2} + D, \tag{2.6}$$

where A, B, C and D are least-squares coefficients pertaining to a specific gas species. These coefficients in Eq. (2.6) yield dynamic viscosity in units of micropoise (μP) and thermal conductivity in units of microwatts per centimeter-kelvin (μW/cm·K), as per the NASA CEA formulation. Detailed tabulations of these coefficients versus temperature are found in the technical memorandum by Svehla [40] for a wide variety of gases, including most of the constituents of atmospheric air (including nitrogen and argon) that are listed in table 2.1.

For ozone (O_3) in atmospheric air, the curve-fit coefficients A, B, C and D for use in Eq. (2.6) are not available in the NASA CEA tabulations. Hence, the dynamic viscosity for ozone is obtained by using the expression of Monchick and Mason [41] for polar gases, given by

$$\eta = \frac{5}{16}\left(\frac{m k_\mathrm{B} T}{\pi}\right)^{\frac{1}{2}} \frac{f_\eta}{\sigma_\mathrm{o}^2 \left\langle \Omega^{(2,2)*} \right\rangle}, \tag{2.7}$$

whereas the thermal conductivity is obtained from the Prandtl number using a modified expression of Svehla [42], yielding

$$\kappa = \eta R \left[\frac{15}{4} + 1.32\left(\frac{c_p}{R} - c\,\frac{5}{2}\right)\right]. \tag{2.8}$$

in which η and c_p/R in Eq. (2.8) are all temperature dependant and the correction factor $c = 0.72348$. In Eq. (2.7), the molecular mass $m = M/N_\mathrm{A}$ is equal to the species molar mass, M, divided by Avogadro's number, $N_\mathrm{A} = 6.0221413 \times 10^{23}$ mol^{-1}, and the Boltzmann constant is $k_\mathrm{B} = 1.3806488 \times 10^{-23}$ J/K. The expression $f_\eta = 1 + \frac{3}{196}\left[8\langle E^* \rangle - 7\right]^2$ is a correction term that accounts for higher kinetic-theory approximations. The term σ_o is the force constant known as the collision diameter and denotes the location of balanced repulsive and attractive interactions between two molecules. The values of the collision diameter σ_o stem from the book by Hirschfelder, Curtiss and Bird [43] and they are tabulated for each constituent species of dry atmospheric air in table 2.1. Lastly, the terms $\langle E^* \rangle$ and $\left\langle \Omega^{(2,2)*} \right\rangle$ represent various temperature-dependent collision integrals. See the paper by Monchick and Mason [41] for details.

The coefficients A, B, C and D that are obtained when the least squares curve fit given by Eq. (2.6) is applied to the resulting calculations of Eqs. (2.7) and (2.8) for ozone are provided in table 2.2. These coefficients have been calculated according to the temperature ranges that are

provided in the NASA CEA thermochemical tables [40]. For $T = 273$ K, the computed transport properties for ozone using this method yield $\eta = 139.23$ μP and $\kappa = 178.888$ μW/cm$\cdot$K, which are in agreement with the experimental values reported by the Air Liquide Group [44].

The accuracy of these curve fits is tied closely to the standard deviation of the respective dynamic viscosity or thermal conductivity data from the fitted curves. An estimate for the root-mean-square error of the least squares curve fits from the fitted data is given as

$$\sigma_{\text{error}} = \left[\frac{1}{n} \sum_{i=1}^{n} \left\{ \omega(T_i) - \omega_i \right\}^2 \right]^{1/2}, \tag{2.9}$$

for which n is the number of (ω_i, T_i) data pairs, where ω is an arbitrary solution variable that represents either η or κ. When ω is replaced by η in Eq. (2.9), σ_{error} is given in units of micropoise (μP), whereas when ω is replaced by κ, the units of σ_{error} are in microwatts per centimeter-kelvin (μW/cm$\cdot$K). The standard deviation measures are also listed in table 2.2.

Table 2.2: Curve-fit properties for the dynamic viscosity and thermal conductivity of ozone.

	dynamic viscosity, η		thermal conductivity, κ	
	200 K$\leq T \leq$1000 K	1000 K$\leq T \leq$5000 K	200 K$\leq T \leq$1000 K	1000 K$\leq T \leq$5000 K
A	0.56733495×10^{0}	0.63541323×10^{0}	0.43066226×10^{0}	$-0.11765607 \times 10^{1}$
B	$-0.19278957 \times 10^{3}$	$-0.38873636 \times 10^{2}$	$-0.50818979 \times 10^{3}$	$-0.90982917 \times 10^{4}$
C	0.10579958×10^{5}	$-0.29476814 \times 10^{5}$	0.37944868×10^{5}	0.40646348×10^{7}
D	0.23179731×10^{1}	0.17336996×10^{1}	0.41233469×10^{1}	0.19801670×10^{2}
σ_{error}	$2.39720268 \times 10^{-1}$	$2.84130368 \times 10^{-1}$	$3.86459933 \times 10^{-1}$	8.21715693×10^{1}

For multi-component gaseous systems, the calculation of mixture transport properties arises from the kinetic theory of pure species and their binary molecular interactions. These approximate mixture methods stem from the early work of Sutherland [45] for mixture dynamic viscosity, η_{mix}, and Wassiljewa [46] for mixture thermal conductivity, κ_{mix}. Their forms of the mixture equations are

$$\eta_{\text{mix}} = \sum_{i=1}^{n} \frac{\text{X}_i \eta_i}{\text{X}_i + \sum\limits_{\substack{j=1 \\ j \neq i}}^{n} \text{X}_j \phi_{ij}} \tag{2.10}$$

and

$$\kappa_{\text{mix}} = \sum_{i=1}^{n} \frac{\text{X}_i \kappa_i}{\text{X}_i + \sum\limits_{\substack{j=1 \\ j \neq i}}^{n} \text{X}_j \psi_{ij}}, \tag{2.11}$$

corresponding to a mixture that is comprised of n individual pure species. In Eqs. (2.10) and (2.11), the coefficients ϕ_{ij} and ψ_{ij} are the respective viscous and thermal interaction parameters

between species pairs i and j in the gaseous mixture. These terms are given by

$$\phi_{ij} = \frac{1}{4}\left[1 + \left(\frac{\eta_i}{\eta_j}\right)^{\frac{1}{2}}\left(\frac{M_j}{M_i}\right)^{\frac{1}{4}}\right]^2 \left(\frac{2M_j}{M_i + M_j}\right)^{\frac{1}{2}} \tag{2.12}$$

from Wilke [47] and

$$\psi_{\mathrm{ij}} = \phi_{ij}\left[1 + \frac{2.41\,(M_i - M_j)\,(M_i - 0.142M_j)}{(M_i + M_j)^2}\right] \tag{2.13}$$

from Brokaw [48]. Note that the binary molecular interaction parameters are non-commutative, i.e. $\phi_{ij} \neq \phi_{ji}$ and $\psi_{ij} \neq \psi_{ji}$.

The coefficients A, B, C and D that are obtained when the least squares curve fit given by Eq. (2.6) is applied to the resulting calculations of Eqs. (2.10) and (2.11) for atmospheric air are provided in table 2.3. The standard deviations σ_{error} of the respective dynamic viscosity or

Table 2.3: Curve-fit properties for the dynamic viscosity and thermal conductivity of atmospheric air.

	dynamic viscosity, η		thermal conductivity, κ	
	200 K$\leq T \leq$1000 K	1000 K$\leq T \leq$5000 K	200 K$\leq T \leq$1000 K	1000 K$\leq T \leq$5000 K
A	0.62157508×10^{0}	0.83881847×10^{0}	0.83610067×10^{0}	0.88927507×10^{0}
B	$-0.36699986 \times 10^{2}$	0.47164294×10^{3}	0.84093416×10^{2}	0.16819080×10^{3}
C	$-0.13890933 \times 10^{4}$	$-0.14691171 \times 10^{6}$	$-0.10888893 \times 10^{5}$	$-0.26265034 \times 10^{5}$
D	0.18154734×10^{1}	$-0.48010372 \times 10^{-1}$	0.63750546×10^{0}	0.20146860×10^{0}
σ_{error}	$3.48664926 \times 10^{-5}$	$2.13536850 \times 10^{-3}$	$2.53044864 \times 10^{-3}$	$4.95296810 \times 10^{-3}$

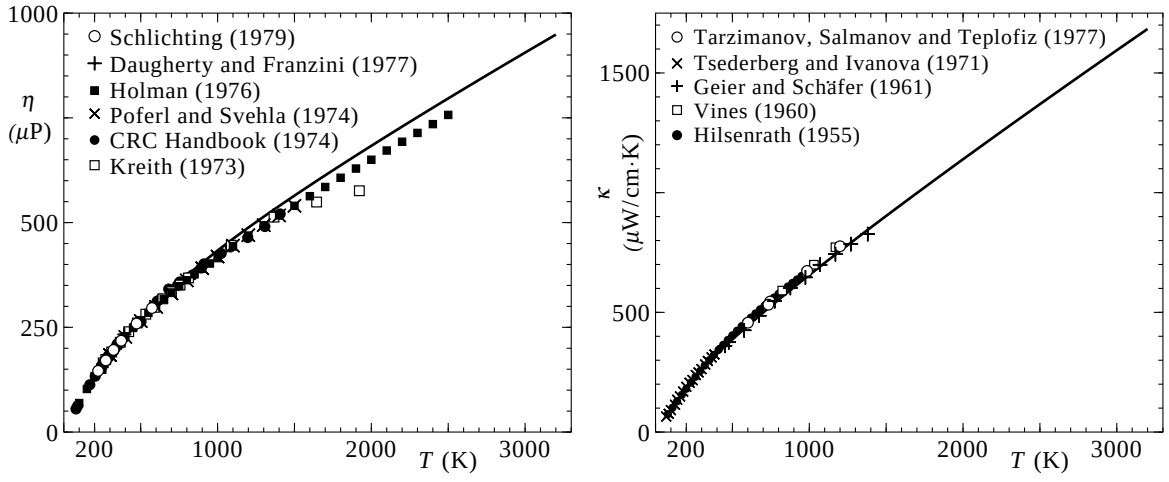

(a) Dynamic viscosity, η.

(b) Thermal conductivity, κ.

Figure 2.2: Comparisons of least squares curve fits (solid lines) with experimental markers for molecular transport properties versus temperature in dry air.

thermal conductivity data from the fitted curves are also listed in the table. Comparisons of the least squares curve fits for atmospheric air with experimental data [49–58] are illustrated in Fig. 2.2. The agreement with low-temperature data is good, but the agreement with the experimental data for temperatures greater than 1200 K is relatively poor. This behaviour is similar to that of several other thermal transport correlations from NASA, which tend to disagree with experimental measurements at elevated temperatures.

2.2.2 Volume Viscosity via Rotational Relaxation

The volume viscosity η_v is an indicative measure of the rotational motion of molecules in fluids and gases, just as the shear viscosity is a representative measure of a collection of fluid particles' stochastic translational motion. For fluids consisting purely of molecules with no inherent rotational modes, such as all stable and inert monatomic gases, the volume viscosity does not exist. Alternatively, for fluids comprised of polyatomic molecules with innate rotational modes, the volume viscosity can generally be determined and often has a significant influence upon the overall physical characteristics of the fluid, such as those associated with the attenuation and absorption of sound waves propagating through an arbitrary medium. In particular, this molecular transport property is important for compressible flow applications when density gradients are relatively large, as in the study of shock waves and their internal structures occurring in high-speed aerothermodynamic and high-temperature gas-dynamic flows. For further reading into both its practical applications as well as the theoretical and experimental measurement techniques used in the evaluation of volume viscosity, see the work of Karim and Rosenhead [59], Prangsma, Alberga and Beenakker [60] and Graves and Argrow [61].

The underlying physical mechanisms governing volume viscosity can be described by considering the sudden isovolumetric compression of a polyatomic gas—as, for example, by a shock wave—which consequently results in the departure of this gas from a state of local thermodynamic equilibrium. In order to satisfy the equipartition of energy, the newly perturbed internal modes of translation, rotation and vibration of this gas must be re-equilibrated through an adequate number of molecular collisions. Assuming that the fluid temperatures are sufficiently low, such that the characteristic temperatures for vibrational modes to become excited are not reached, the transfer of energy between the remaining translational and rotational modes will be governed by the rotational relaxation times of the gas molecules [62]. This is due to the fact that the time scales corresponding to the relaxation of rotational modes are typically on the same order of, but are slightly larger than, those required for the adjustment of translational modes [63,64]. Due to this reasoning, the dissipation of rotational energy is incorporated directly into the dissipative terms in the continuum-fluid-dynamic equations through a multiplication of the volume viscosity with the divergence of the velocity field, in a manner analogous to the dissipation of translational energy of an arbitrary fluid by means of its shear viscosity.

In this research, explicit expressions for the volume viscosity of multi-component gaseous mixtures and their constituent individual species have been adopted from the kinetic theory of dilute polyatomic gases. This specific formulation has been selected as it is well-suited for relatively low-cost implementation into numerical algorithms, in comparison to traditional computational methods that require the solution of linear systems to evaluate this particular molecular transport property at a given temperature (see the book by Ern and Giovangigli [65]).

The procedure utilized herein to compute the volume viscosity η_v for polyatomic gases and their mixtures stems primarily from the research efforts of Ern and Giovangigli [66] for the explicit description and incorporates the work of Brau and Jonkman [67], Cramer [68] and Widom [69] for the evaluation of the rotational relaxation collision numbers of the individual species. Related gas properties and physical data are also included from several references [43, 70–72] and are tabulated in table 2.1.

For the volume viscosity of an individual i^{th} pure species, Ern and Giovangigli [66] state that the analytical form of the species volume viscosity, $\eta_{v,i}$, is given explicitly by

$$\eta_{v,i} = \frac{k_{\text{B}}\pi}{4} \frac{c_i^{\text{rot}} Z_{\text{rot},i}}{\left(c_{v,i}\right)^2} \eta_i \qquad \text{for} \qquad i \in \mathcal{P}. \tag{2.14}$$

Here, the parameter $\mathcal{P}$ designates the set of species within a gaseous mixture that have at least two different internal energy levels or modes (e.g. non-monatomic gases). For a gaseous mixture that is composed of n individual pure species components, the mixture volume viscosity, $\eta_{v,\text{mix}}$, also stems from the work of Ern and Giovangigli [66] and is evaluated explicitly as

$$\eta_{v,\text{mix}} = \frac{k_{\text{B}}\pi}{4c_v^2} \sum_{i\in\mathcal{P}} \frac{\text{X}_i c_i^{\text{rot}} Z_{\text{rot},i}}{\sum\limits_{j\in\mathcal{S}} \text{X}_j/\eta_{ij}}, \tag{2.15}$$

where the parameter $\mathcal{S} = \{1, 2, \ldots, n\}$ denotes the set of species indices.

In Eqs. (2.14) and (2.15), X is the species mole fraction. The constant volume specific heat capacity, c_v, is given according to

$$c_v = c_v^{\text{tr}} + c^{\text{rot}}, \tag{2.16}$$

in which $c_v^{\text{tr}} = \frac{3}{2}k_{\text{B}}$ is the translational constant volume specific heat capacity and

$$c^{\text{rot}} = \sum_{i\in\mathcal{S}} \text{X}_i c_i^{\text{rot}} \tag{2.17}$$

is the rotational heat capacity, where $c_i^{\text{rot}} = 0$ for monatomic species, $c_i^{\text{rot}} = k_{\text{B}}$ for species whose molecules have a linear geometric orientation and $c_i^{\text{rot}} = \frac{3}{2}k_{\text{B}}$ otherwise.

The viscous interaction parameter, η_{ij}, in Eq. (2.15) is given by the expression

$$\eta_{ij} = \frac{5}{8} \frac{k_{\text{B}}T}{\Omega_{ij}^{(2,2)}}, \tag{2.18}$$

where $\eta_{ii} = \eta_i$ simplifies to become the dynamic viscosity of the i^{th} species, η_i, when the indices i and j are equal. The collision integral, $\Omega_{ij}^{(2,2)}$, in Eq. (2.18) is described in the book by Chapman and Cowling [73] and involves the law of force between pairs of molecules. For polar gases, the temperature-dependent values of $\Omega_{ij}^{(2,2)}$ are available in the paper by Monchick and Mason [41]. For non-polar gases, $\Omega_{ij}^{(2,2)}$ is related to the temperature-dependent function $\mathcal{W}^{(2,2)}$ through the expression

$$\Omega_{ij}^{(2,2)} = \sigma_{\text{o}}^2 \left(\frac{2\pi k_{\text{B}} T}{\tilde{m}_{ij}} \right)^{\frac{1}{2}} \mathcal{W}^{(2,2)}, \tag{2.19}$$

where the reduced mass, $\tilde{m}_{ij}$, is given by

$$\tilde{m}_{ij} = \frac{m_i m_j}{m_i + m_j}. \tag{2.20}$$

The temperature-dependent values for $\mathcal{W}^{(2,2)}$ in Eq. (2.19) are available in the paper by Hirschfelder, Bird and Spotz [74] for non-polar gases.

The deviation of the behaviour of the polar gas molecules from that of a non-polar substance is based upon the strength of the reduced dipole energy, represented using the parameter δ. This measure is given by

$$\delta = \frac{\mu^2}{2\epsilon_{\text{o}}\sigma_{\text{o}}^3}, \tag{2.21}$$

where μ is the dipole moment and ϵ_{o} is the force constant known as the characteristic energy that denotes the depth of the potential well when the intermolecular potential is a minimum. In this research, the strengths of the reduced dipoles for polar molecules are computed as the maximum allowable values, i.e. $\delta = \delta_{\max}$. See the paper by Monchick and Mason [41] for details. The values of the dipole moment μ and the characteristic energy ϵ_{o} used herein stem from Hirschfelder, Curtiss and Bird [43] and Williams, Schwingel and Winning [70]. These are tabulated for each polar constituent of dry atmospheric air in table 2.1.

Intrinsic to the evaluation of Eq. (2.15) to compute the volume viscosity of a gaseous mixture is the calculation of the rotational relaxation collision number Z_{rot} for each of the comprising individual, polyatomic pure species. This parameter represents the number of intermolecular collisions which are required to establish rotational equilibrium for a given gaseous species. Within the context of this research for the concentrations of dry atmospheric air, the determination of Z_{rot} for each constituent polyatomic species listed in table 2.1 is performed using several different strategies, depending on the species under investigation, which are described as follows.

For the linear diatomic molecules of nitrogen (N_2) and oxygen (O_2), Z_{rot} is modelled directly as a function of the fluid temperature via

$$Z_{\text{rot}} = Z_{\infty} \left[1 + \frac{\pi^{\frac{3}{2}}}{2} \sqrt{\frac{T_v}{T}} + \left(2 + \frac{\pi^2}{4} \right) \frac{T_v}{T} + \pi^{\frac{3}{2}} \left(\frac{T_v}{T} \right)^{\frac{3}{2}} \right]^{-1}, \tag{2.22}$$

which stems from the work of Brau and Jonkman [67]. In Eq. (2.22) the parameter Z_∞ is the reference rotational relaxation collision number and T_v is the characteristic temperature of the volume viscosity. In this research, $T_v = 91.5$ K for nitrogen and $T_v = 113.0$ K for oxygen (see the book by Hirschfelder, Curtiss and Bird [43]). Using the data of Lordi and Mates [72], the values for Z_∞ and Z_{rot}, with $T = 295$ K, are 28.65 and 5.85 for nitrogen and 24.86 and 4.32 for oxygen, respectively. These values for Z_{rot} at $T = 295$ K are included in table 2.1.

For molecules of carbon dioxide (CO_2), methane (CH_4), hydrogen (H_2), nitrous oxide (N_2O) and carbon monoxide (CO), Z_{rot} is explicitly inferred from the rearrangement of Eq. (2.14), which reduces appreciably to yield

$$Z_{\text{rot}} = \frac{n_z}{\pi}\frac{\eta_v}{\eta}, \tag{2.23}$$

where the coefficient $n_z = 25$ for species with a geometrically linear molecular structure and $n_z = 24$ otherwise. In Eq. (2.23), η_v is computed according to the temperature-dependent empirical expressions for volume viscosity that are found in the work of Cramer [68] for each of these five gases. Based on Cramer's equations for η_v and this methodology, the values of Z_{rot} calculated via Eq. (2.23) for carbon dioxide, methane, hydrogen, nitrous oxide and carbon monoxide, with $T = 295$ K, are 29899.80, 9.57, 209.69, 4409.07 and 4.23, respectively. These values for Z_{rot} at $T = 295$ K are included in table 2.1. The large Z_{rot} values that have been computed for carbon dioxide, hydrogen and nitrous oxide are the result of these gases having large volume viscosities relative to their shear viscosities within this low to moderate temperature range. See the paper by Cramer [68] for details.

For the polar molecules of ozone (O_3), nitrogen dioxide (NO_2), ammonia (NH_3) and sulfur dioxide (SO_2), Z_{rot} is calculated according to the work of Widom [69] for the rotational relaxation of rough spheres. In this form, Z_{rot} for each species is calculated according to

$$Z_{\text{rot}} = \frac{3(1+b)^2}{8b}, \tag{2.24}$$

which is independent of temperature, where the parameter b is given by

$$b = \frac{I}{\tilde{m}d_{\text{o}}^2}. \tag{2.25}$$

In Eq. (2.25), the reduced mass is $\tilde{m} = \frac{1}{2}m$, d_{o} is the force constant that represents the intermolecular distance at zero net potential energy and I is the molecular moment of inertia, given by

$$I = \sum_{i=1}^{n_a} \left(m_a d_a^2\right)_i, \tag{2.26}$$

where m_a and d_a represent the atomic mass and atomic diameter of each one of the n_a number of atoms comprising the polyatomic molecule of interest. Data corresponding to molecular geometries and related properties used in Eq. (2.26) have been sourced from the book by Herzberg [71]. Based on Herzberg's data and this methodology, the values of Z_{rot} calculated

via Eq. (2.24) for ozone, nitrogen dioxide, ammonia and sulfur dioxide are 4.91, 4.93, 14.06 and 5.13, respectively. These values for Z_{rot} at $T = 295$ K are included in table 2.1.

When the least squares curve fit resembling Eq. (2.6), of the form

$$\ln(\eta_v) = A\ln(T) + \frac{B}{T} + \frac{C}{T^2} + D, \tag{2.27}$$

is applied to the resulting calculations of Eq. (2.15) for the volume viscosity of atmospheric air, the coefficients A, B, C and D that result are provided in table 2.4. Equation (2.27) yields volume viscosity in units of micropoise (μP). The standard deviation σ_{error} of the volume viscosity data from the fitted curve, computed using Eq. (2.9) with ω replaced by η_v, is also listed in table 2.4 and is in units of micropoise (μP). The results of the least squares curve fit for the volume viscosity of atmospheric air is illustrated in Fig. 2.3. The ratio of volume to dynamic viscosities η_v/η is also shown in the figure. The large rise in η_v/η at low temperatures occurs because the dynamic viscosity decreases rapidly within this temperature range.

Table 2.4: Curve-fit properties for the volume viscosity of atmospheric air.

	volume viscosity, η_v	
	200 K$\leq T\leq$1000 K	1000 K$\leq T\leq$ 5000 K
A	0.14768577×10^{1}	0.88038374×10^{0}
B	0.40000756×10^{3}	-0.27805256×10^{3}
C	0.14840753×10^{5}	0.10238810×10^{6}
D	-0.41488499×10^{1}	0.56084032×10^{0}
σ_{error}	3.02270240×10^{0}	3.00004581×10^{-1}

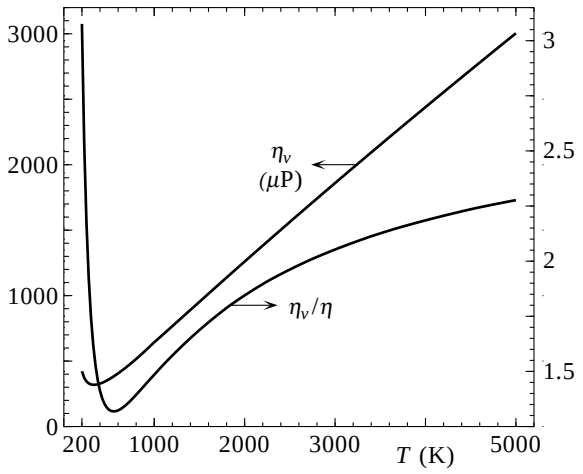

Figure 2.3: Least squares curve fit for volume viscosity versus temperature in dry air.

Chapter 3

Analytical Solutions

Von Neumann [5, 6] was the first to derive the complete solution for regular reflection and propose several possible transition boundaries separating basic regular- and Mach-reflection patterns. These transition boundaries include the extreme-angle or detachment boundary, the mechanical-equilibrium boundary and the sonic boundary, each of which are shown in Fig. 3.1 for the case of air. The work of von Neumann was later studied by Henderson [75], who provided long and cumbersome analytical expressions for these transition boundaries and their characteristics (e.g. minima, maxima and cross-over locations). In this chapter, the analytical

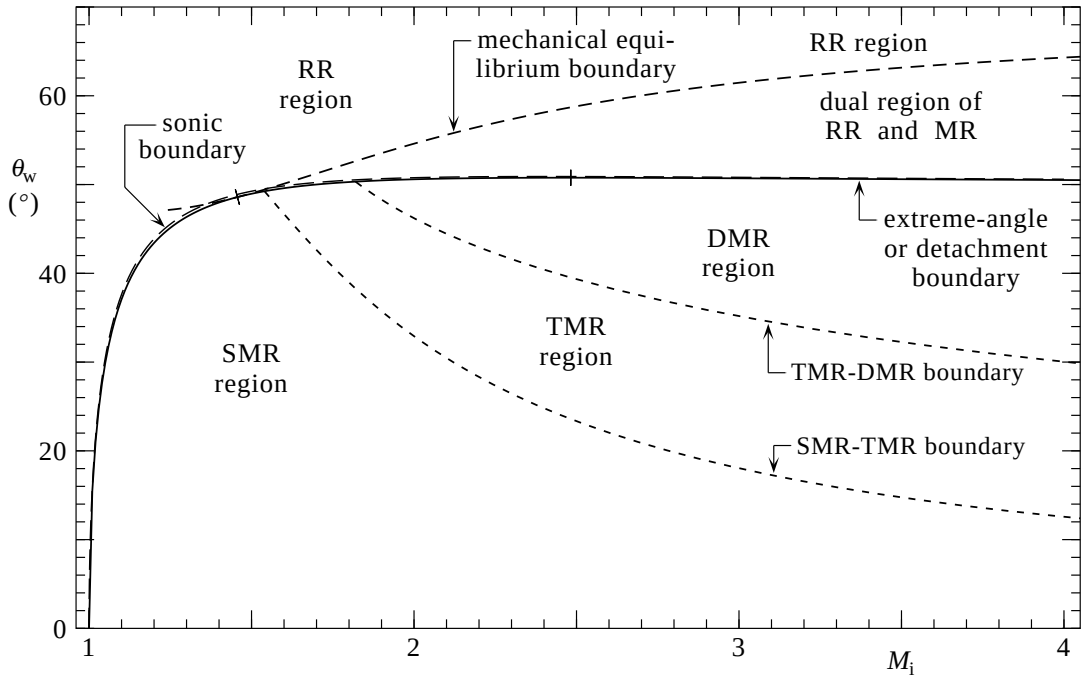

Figure 3.1: Regions of regular and Mach reflection separated by analytical transition boundaries in air.

solution for regular reflection and corresponding solutions for the transition boundaries of von Neumann [5] are revisited and revised into shorter and simpler forms for convenient usage.

3.1 Solution for Regular Reflection

Consider a moving planar shock wave interacting with an inclined wedge with a known angle θ_w, as illustrated in Fig. 3.2. The incident shock (S_i) moves into a quiescent fluid (gas or liquid) in region (1) with known pre-shock flow properties (e.g. pressure p_1, density ρ_1, sound speed a_1, temperature T_1, and flow velocity $u_1 = 0$ m/s). Let the strength of this incident shock be specified by its speed V_i or Mach number $M_i = V_i/a_1$. Based on the given value of M_i, and knowledge of the fluid properties and its equation of state, all of the flow properties in region (2) can be determined (i.e. p_2, ρ_2, a_2, T_2, $u_2 = u_1 + \Delta u_i$, in which Δu_i is the flow speed induced by the incident shock). If the reflected shock Mach number M_r and its angle θ_r with the wedge surface were also known, then the knowledge of the fluid properties and its equation of state could be used to subsequently determine all of the flow properties in region (3) (i.e. p_3, ρ_3, a_3, T_3, u_3).

For regular reflection to occur, the reflected shock (S_r) must remain attached to the incident shock (S_i) at the wedge surface. Hence, the speed $V_i/\sin(\theta_i) = V_i/\cos(\theta_w)$ of the incident shock along the wedge surface must be matched to the speed V_r of the reflected shock up the wedge. This requirement yields

$$V_r = V_i \frac{\sin(\theta_r)}{\sin(\theta_i)} + \Delta u_i \cos(\theta_i + \theta_r), \tag{3.1}$$

in which the second term on the right side of the equation results from the interaction of the reflected shock with the flow field in region (2). The component of the induced flow ($u_2 = u_1 + \Delta u_i = \Delta u_i$) by the incident shock in region (2) that is directed normal to but toward the

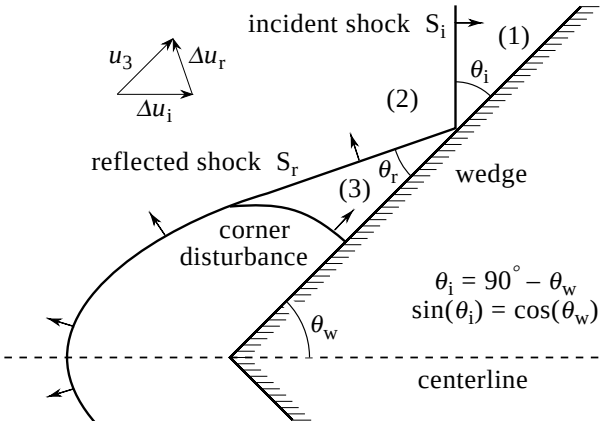

Figure 3.2: Regular-reflection pattern showing moving shocks, flow-field regions and various shock and wedge angles.

wedge surface is given by $\Delta u_\mathrm{i} \cos(\theta_\mathrm{i})$. This component must be countered by the component of the induced flow from the reflected shock that is normal to but away from the wedge surface, so that no flow enters the nonporous wedge surface. This requirement yields

$$\Delta u_\mathrm{i} \cos(\theta_\mathrm{i}) = \Delta u_\mathrm{r} \cos(\theta_\mathrm{r}). \tag{3.2}$$

The flow along the wedge surface in region (3) can be determined from

$$u_3 = \Delta u_\mathrm{i} \sin(\theta_\mathrm{i}) + \Delta u_\mathrm{r} \sin(\theta_\mathrm{r}), \tag{3.3}$$

by considering the components of both shock-induced flows behind the reflected shock in the direction parallel to the wedge surface.

Equations (3.1) to (3.3) apply to arbitrary gases or fluids, and the physical properties of a specific fluid enter the problem only through the shock-jump conditions. In the case of a polytropic gas, the conventional Rankine-Hugoniot equations (see the book by Thompson [76]) for the incident shock are summarized as

$$\frac{p_2}{p_1} = 1 + \frac{2\gamma}{\gamma+1}\left(M_\mathrm{i}^2 - 1\right), \tag{3.4}$$

$$\frac{\rho_2}{\rho_1} = \frac{(\gamma+1)\,M_\mathrm{i}^2}{2+(\gamma-1)M_\mathrm{i}^2}, \tag{3.5}$$

$$\frac{a_2^2}{a_1^2} = \frac{T_2}{T_1} = \frac{p_2/p_1}{\rho_2/\rho_1}, \tag{3.6}$$

$$\frac{\Delta u_\mathrm{i}}{a_1} = \frac{2}{\gamma+1}\frac{M_\mathrm{i}^2 - 1}{M_\mathrm{i}}, \tag{3.7}$$

in which γ is the specific heat ratio. Similar equations apply to the reflected shock, with appropriate subscript changes (i.e. $2 \to 3$, $1 \to 2$, $\mathrm{i} \to \mathrm{r}$).

Several solutions for regular reflection for the three cases of polytropic air, liquid water, and equilibrium air are illustrated by the three graphs collected in Fig. 3.3. For the first case of polytropic air, the reflected shock angle θ_r is varied from 0° to $180^\circ - \theta_\mathrm{i}$, and the reflected shock speed V_r is then calculated by means of Eq. (3.1) for the specified incident shock Mach number $M_\mathrm{i} = 2$, which also yields the value of Δu_i from using Eq. (3.7). The calculations are done three times for wedge angles $\theta_\mathrm{w} = 70$, 50.59, and 40°, or shock angles $\theta_\mathrm{i} = 90^\circ - \theta_\mathrm{w} = 20$, 39.41, and 50°, giving the three curves shown in the top graph of Fig. 3.3. The value of V_r releases the value of Δu_r by means of Eq. (3.7) with appropriate subscripts. An error is constructed from Eq. (3.2) as

$$E(\theta_\mathrm{r}) = 1 - \frac{\Delta u_\mathrm{r} \cos(\theta_\mathrm{r})}{\Delta u_\mathrm{i} \cos(\theta_\mathrm{i})}. \tag{3.8}$$

When this error equals zero, a solution for regular reflection occurs. For the case of polytropic air with the incident shock angle $\theta_\mathrm{i} = 20^\circ$, the weak reflected shock solution (well known from oblique shock-reflection theory) with the values of V_r and θ_r corresponds to location (a) in the

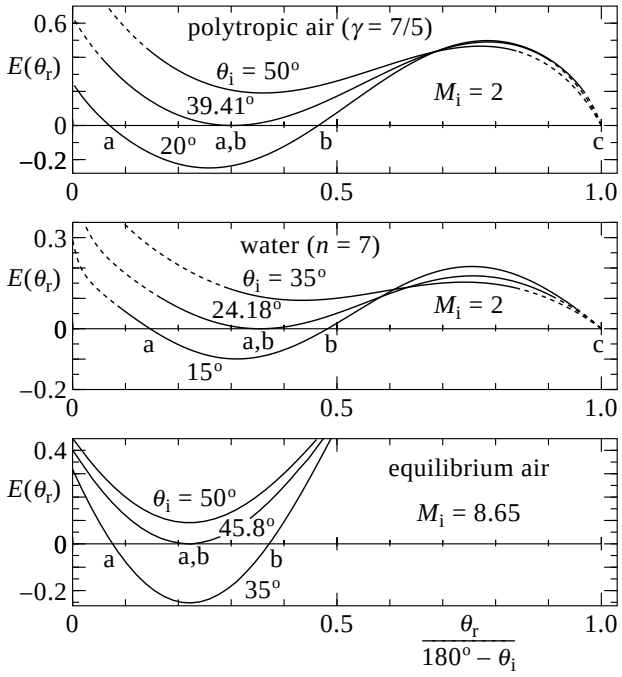

Figure 3.3: Solutions for shock-wave reflections from a wedge in polytropic air, liquid water and equilibrium air.

figure, the strong reflected shock solution corresponds to location (b), and an aphysical solution occurs at location (c). For the shock angle $\theta_i = 39.41°$, the solutions (a) and (b) merge and yield the same values for V_r and θ_r, which corresponds to von Neumann's extreme angle at which regular reflection switches to Mach reflection. For the incident shock angle $\theta_i = 50°$, the weak and strong shock solutions are imaginary and aphysical, and regular reflection cannot occur, replaced instead by Mach reflection.

The three regular-reflection solutions for liquid water shown in the middle graph of Fig. 3.3 feature curves of similar shape to those for polytropic air, but the numerical values differ substantially. These solutions were obtained by using a simplified version for the shock Hugoniot and isentrope from Murnaghan [77], also discussed in the book by Poirier [78], taking the revised form of

$$p_2 = p_1 + \frac{\rho_1 a_1^2}{n}\left[\left(\frac{\rho_2}{\rho_1}\right)^n - 1\right]. \tag{3.9}$$

The other shock-jump relationships

$$a_2 = \frac{\partial p_2}{\partial \rho_2} = a_1 \left(\frac{\rho_2}{\rho_1}\right)^{(n-1)/2}, \tag{3.10}$$

$$M_i^2 = \frac{1}{a_2^2}\frac{\rho_2}{\rho_1}\frac{p_2 - p_1}{\rho_2 - \rho_1} = \frac{1}{n}\frac{\rho_2/\rho_1}{\rho_2/\rho_1 - 1}\left[\left(\frac{\rho_2}{\rho_1}\right)^n - 1\right], \tag{3.11}$$

$$\Delta u_i^2 = \left[\frac{\rho_2 - \rho_1}{\rho_2} V_i\right]^2 = \frac{a_1^2}{n}\frac{\rho_2/\rho_1 - 1}{\rho_2/\rho_1}\left[\left(\frac{\rho_2}{\rho_1}\right)^n - 1\right], \tag{3.12}$$

follow for the sound speed, incident shock Mach number and induced flow by the shock. The normal properties of liquid water at room pressure and temperature are also used. Equations (3.9) to (3.12) also apply to the reflected shock wave, with appropriate subscript changes.

The three regular-reflection solutions for equilibrium air shown in the bottom graph of Fig. 3.3 were computed by using the NASA-CEA software from Gordon and McBride [38,39] to provide the shock-jump conditions for Eqs. (3.1) and (3.2). This software was used to include the effects of vibration, dissociation, electrical excitation and ionization of molecules and atoms in air.

A simple analytical solution for regular reflection can be derived for the case of the polytropic gas. The reflected shock angle θ_r is eliminated first from Eqs. (3.1) and (3.2). For this solution, the reflected shock Mach number takes the form of a cubic polynomial (e.g. in V_r^2). However, the aphysical solution given by $V_\mathrm{r} - V_\mathrm{i} + \Delta u_\mathrm{i} = 0$ or $p_3 - p_1 = 0$ can be factored out so that the solution for the reflected shock speed V_r reduces to a quadratic polynomial in terms of V_r^2. The derivation is complicated and tedious. The quadratic polynomial, its coefficients, and the solution for the square of the reflected shock Mach number $M_\mathrm{r}^2 = V_\mathrm{r}^2/a_2^2$, are given succinctly as

$$M_\mathrm{r}^4 - 2\,b\,M_\mathrm{r}^2 + c^2 = 0\,, \tag{3.13}$$

where

$$b = 1 + \frac{1 + \gamma d^2 \cos^2(\theta_\mathrm{w})}{2 - (3-\gamma)\,d - (\gamma - 1)\,d^2} \tan^2(\theta_\mathrm{w})\ , \tag{3.14}$$

$$c = \frac{1 - d\cos^2(\theta_\mathrm{w})}{(1-d)\cos\left(\theta_\mathrm{w}\right)}\,, \tag{3.15}$$

$$d = 1 - \frac{\rho_1}{\rho_2} = \frac{2}{\gamma+1}\frac{M_\mathrm{i}^2 - 1}{M_\mathrm{i}^2} = \frac{\Delta u_\mathrm{i}}{V_\mathrm{i}}\,, \tag{3.16}$$

and

$$M_\mathrm{r}^2 = b \mp \sqrt{b^2 - c^2}\,, \tag{3.17}$$

$$p_3 = p_2\left[1 + \frac{2\gamma}{\gamma+1}\left(M_\mathrm{r}^2 - 1\right)\right]\,, \tag{3.18}$$

in terms of the input specification of incident shock Mach number M_i and wedge angle θ_w. The weak and strong shock solutions correspond to the negative and positive signs in Eq. (3.17), respectively. The solution for the reflected shock angle follows from Eq. (3.2), and the pressure p_3 behind the reflected shock is given by Eq. (3.18). The regular-reflection solution was derived first by von Neumann [5] and reproduced later by others like Polachek and Seeger [79] and Henderson [75]. They adopt the transformed plane of steady flow with a supersonic flow imposed down the wedge into the incident shock to make the self-similar shock-reflection pattern stationary. These conventional equations are well illustrated by previous researchers [5, 8, 10, 14, 16, 22, 80]. However, the derivation using Eqs. (3.1) to (3.3) for moving shocks is simpler and less cumbersome than using the conventional equations in the form employed by previous researchers.

3.2 Solution for the Extreme-Angle Boundary

The solution for the extreme angle by von Neumann [5] can be obtained from Eq. (3.17) by setting the discriminant $b^2 - c^2$ to zero, for the case when the two roots merge for the weak and strong reflected shocks in Fig. 3.3. After substantial manipulation, the cubic polynomial in $\cos(\theta_w)$, its coefficients, and the physically realistic solution for the shock and wedge angles θ_i and θ_w, are summarized as

$$\frac{1}{\cos^3(\theta_w)} - \frac{3a}{\cos^2(\theta_w)} - \frac{b}{\cos(\theta_w)} + c = 0, \tag{3.19}$$

where

$$a = \frac{1 + (\gamma - 1)\, d}{3}, \tag{3.20}$$

$$b = 2d - d^2, \tag{3.21}$$

$$c = \gamma d^2, \tag{3.22}$$

$$d = 1 - \frac{\rho_1}{\rho_2} = \frac{2}{\gamma + 1}\frac{M_i^2 - 1}{M_i^2} = \frac{\Delta u_i}{V_i}, \tag{3.23}$$

$$e = \sqrt{a^2 + b/3}, \tag{3.24}$$

$$f = \cos^{-1}\left(\frac{ab + 2a^3 - c}{2e^3}\right), \tag{3.25}$$

to yield the solution

$$\cos(\theta_w) = \sin(\theta_i) = \frac{1}{a + 2e\cos(f/3)}, \tag{3.26}$$

in terms of the input specification of the incident shock Mach number M_i or inverse shock density ratio in term d. This revision of the extreme-angle boundary derived originally by von Neumann [5] is given herein as a cubic polynomial in terms of the wedge angle $\cos(\theta_w)$ and incident shock angle $\sin(\theta_i)$. In the previous work of von Neumann [5], and others like Polachek and Seeger [79] and Henderson [75], the solutions were given as a cubic polynomial in terms of the incident shock angle squared, that is $\sin^2(\theta_i)$, with much longer expressions for the coefficients a, b and c in Eq. (3.19). The extreme-angle boundary shown in Fig. 3.1 was calculated by means of Eq. (3.26).

The derivative $\mathrm{d}\sin(\theta_w)/\mathrm{d}M_i$ is required later in this research. This derivative is obtained from Eq. (3.19) as

$$\frac{\mathrm{d}z}{\mathrm{d}M_i} = \frac{-4}{\gamma + 1}\frac{z}{M_i^3}\frac{a}{b}, \tag{3.27}$$

where

$$z = \cos(\theta_w) = \sin(\theta_i), \tag{3.28}$$

$$a = \gamma - 1 + 2(1 - d)\, z - 2\gamma d\, z^2, \tag{3.29}$$

$$b = 1 + (\gamma - 1)\, d + 2d(2 - d)\, z - 3d^2 z^2, \tag{3.30}$$

$$d = 1 - \frac{\rho_1}{\rho_2} = \frac{2}{\gamma + 1}\frac{M_i^2 - 1}{M_i^2} = \frac{\Delta u_i}{V_i}, \tag{3.31}$$

which can be manipulated to yield

$$\frac{\mathrm{d}\sin(\theta_\mathrm{w})}{\mathrm{d}M_\mathrm{i}} = \frac{-z}{\sqrt{1-z^2}}\frac{\mathrm{d}z}{\mathrm{d}M_\mathrm{i}}. \tag{3.32}$$

The cubic polynomial given by Eq. (3.19) in terms of $\cos(\theta_\mathrm{w})$ can be rearranged into a quadratic polynomial for the density ratio ρ_2/ρ_1 as a function of the wedge angle θ_w or $\cos(\theta_\mathrm{w})$. This quadratic polynomial, its coefficients, and the solutions for the density ratio and incident shock Mach number are summarized as

$$a\left(\cos(\theta_\mathrm{w})\frac{\rho_1}{\rho_2}\right)^2 - b\left(\cos(\theta_\mathrm{w})\frac{\rho_1}{\rho_2}\right) + c = 0, \tag{3.33}$$

where

$$a = 1 + \gamma\cos(\theta_\mathrm{w}), \tag{3.34}$$

$$b = 1 - \gamma + 2\gamma\cos^2(\theta_\mathrm{w}), \tag{3.35}$$

$$c = [1 - \gamma\cos(\theta_\mathrm{w})]\sin^2(\theta_\mathrm{w}), \tag{3.36}$$

and

$$\frac{\rho_2}{\rho_1} = \frac{2a\cos(\theta_\mathrm{w})}{b \pm \sqrt{b^2 - 4ac}}, \tag{3.37}$$

$$M_\mathrm{i}^2 = \frac{2(\rho_2/\rho_1)}{\gamma + 1 - (\gamma-1)(\rho_2/\rho_1)}. \tag{3.38}$$

The input values of the wedge angle lie in the restricted range $0 \le \cos(\theta_\mathrm{w}) \le \sqrt{(3-\gamma)/4}$, and the physically realistic solutions for the density ratio lie in the range $1 \le \rho_2/\rho_1 \le (\gamma+1)/(\gamma-1)$, corresponding to the shock Mach number range $1 \le M_\mathrm{i} \le \infty$.

The upper value of the wedge-angle range corresponds to a maximum in the wedge angle versus the shock Mach number M_i. Although barely visible, it is marked with the short line crossing the extreme-angle boundary near $M_\mathrm{i} \approx 2.48$ in Fig. 3.1 for $\gamma = 7/5$. For $\gamma = 5/3$, no local maximum exists in the extreme-angle boundary as it trends continually upward as $M_\mathrm{i} \to \infty$. This maximum wedge angle is obtained by setting the discriminant $b^2 - 4ac$ in Eq. (3.37) equal to zero. The maximum wedge angle and the corresponding density ratio and shock Mach number are

$$\theta_\mathrm{w} = \cos^{-1}\left[\sqrt{\frac{3-\gamma}{4}}\right], \tag{3.39}$$

$$\frac{\rho_2}{\rho_1} = \frac{2\sqrt{3-\gamma} + \gamma(3-\gamma)}{(\gamma+1)(2-\gamma)}, \tag{3.40}$$

$$M_\mathrm{i}^2 = \frac{2\sqrt{3-\gamma} + \gamma(3-\gamma)}{1 + 3\gamma - 2\gamma^2 - (\gamma-1)\sqrt{3-\gamma}}, \tag{3.41}$$

which are all functions of the specific heat ratio only. When $\gamma = 7/5$, the three previous equations yield values for θ_w, ρ_2/ρ_1 and M_i of 50.7685°, 3.31238 and 2.48239, respectively.

3.3 Solution for the Sonic Boundary

The criterion for the sonic boundary is that the formation of a Mach stem should occur once the disturbance or signal $(u_3 + a_3)$ that is generated by the interaction of the incident shock with the wedge corner and surface catches up to the speed $V_\mathrm{i}/\sin(\theta_\mathrm{i})$ of the reflection point along the wedge surface. The analytical solution for the boundary based on the sonic criterion of von Neumann [5] is taken directly from Henderson [75]. This boundary is given by a fifth-order polynomial in terms of $\sin^2(\theta_\mathrm{i})$ versus the inverse incident shock strength p_1/p_2, and it is not reproduced or revised here because the coefficients are long and cumbersome. The sonic boundary lies very close to the extreme-angle boundary, differing by less than a half of a degree for each given value of the shock strength. When plotted in Fig. 3.1 it is barely distinguishable from the extreme-angle boundary. The sonic criterion was supported by the additional research of Hornung, Oertel and Sandeman [81] as well as Lock and Dewey [19].

3.4 Solution for the Mechanical-Equilibrium Boundary

The solution for the mechanical-equilibrium boundary of von Neumann [5] starts with the three-shock pattern of Mach reflection, as shown in Fig. 3.4. This upper boundary for the dual region of regular and Mach reflection (see Fig. 3.1) occurs when the triple-point trajectory angle χ diminishes to zero, the Mach stem diminishes to an infinitesimal height, and the slip stream collapses onto the wedge surface.

The Mach stem of infinitesimal length moves along the wedge with a speed $V_\mathrm{m} = V_\mathrm{i}/\sin(\theta_\mathrm{i})$, produces a post-shock pressure $p_4 = p_3 = p_1 + p_1 \frac{2\gamma}{\gamma+1}\left(M_\mathrm{m}^2 - 1\right)$, which is set equal to the pressure p_3 on the other side of the slip stream and behind the reflected shock. This results in a reflected

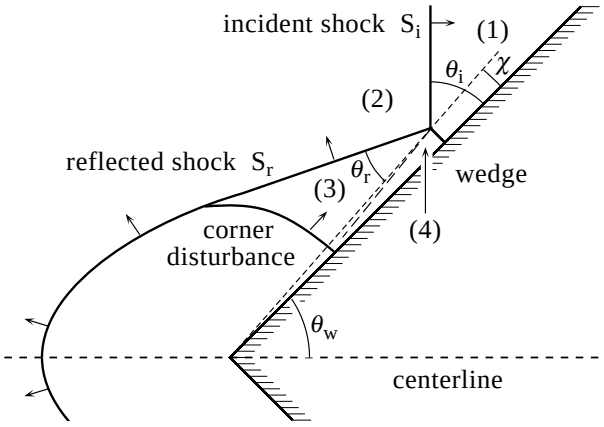

Figure 3.4: Mach-reflection pattern showing moving shocks, slip stream, triple-point trajectory angle χ, and flow-field regions.

shock Mach number given by

$$M_{\mathrm{r}}^2 = 1 + \frac{\rho_2/\rho_1}{1 + \frac{\gamma+1}{2}\left(\rho_2/\rho_1 - 1\right)} \frac{1}{\tan^2(\theta_{\mathrm{i}})}. \tag{3.42}$$

This equation is substituted into Eq. (3.13) to eliminate M_{r}, so that the remaining equation can be solved for an expression for the mechanical-equilibrium boundary in terms of the incident shock angle θ_{i} versus the incident shock Mach number M_{i}. After considerable manipulation, the resulting quadratic polynomial in terms of $\cos^2(\theta_{\mathrm{w}})$, its coefficients, and the physically realistic solutions for the angles θ_{w} and θ_{i} are summarized as

$$a\cos^4(\theta_{\mathrm{w}}) - 2b\cos^2(\theta_{\mathrm{w}}) + c = 0, \tag{3.43}$$

where

$$a = 4d + 2(\gamma-1)(\gamma+2)d^2 - \left(\gamma^2-1\right)d^3, \tag{3.44}$$

$$b = \gamma + 3 - \frac{1}{2}(5-\gamma)(\gamma+1)d + 2\gamma d^2, \tag{3.45}$$

$$c = 4 - 4d, \tag{3.46}$$

$$d = 1 - \frac{\rho_1}{\rho_2} = \frac{2}{\gamma+1}\frac{M_{\mathrm{i}}^2 - 1}{M_{\mathrm{i}}^2} = \frac{\Delta u_{\mathrm{i}}}{V_{\mathrm{i}}}, \tag{3.47}$$

to yield the solution

$$\cos^2(\theta_{\mathrm{w}}) = \sin^2(\theta_{\mathrm{i}}) = \frac{c}{b + \sqrt{b^2 - ac}}. \tag{3.48}$$

This revised solution of von Neumann [5] was used to plot the mechanical-equilibrium boundary in Fig. 3.1.

The mechanical-equilibrium boundary touches the extreme-angle boundary and shares the same slope at one location in the plane of θ_{w} versus M_{i}, as can be seen in Fig. 3.1. This point of contact has physical significance as it represents the boundary between weak and strong incident shock strengths for oblique shock-wave reflections (see the paper by Kawamura and Saito [10] for more information). It can be obtained by combining Eqs. (3.19) and (3.43) to eliminate $\cos(\theta_{\mathrm{w}})$. The solution for the incident shock strength ρ_2/ρ_1 in terms of the variable $z = \frac{\gamma+1}{2}\left(\rho_2/\rho_1 - 1\right)$ is then given by the quartic polynomial

$$4z^4 + 4z^3 - \left(\gamma^2+3\right)z^2 - 2(\gamma+1)z + \gamma + 1 = 0, \tag{3.49}$$

followed by the solutions for the density ratio and incident shock Mach number (once z is determined), as follows

$$\frac{\rho_2}{\rho_1} = 1 + \frac{2}{\gamma+1}z, \tag{3.50}$$

$$M_{\mathrm{i}}^2 = \frac{\gamma + 1 + 2z}{\gamma + 1 - (\gamma-1)z}. \tag{3.51}$$

The corresponding wedge angle θ_{w} is then calculated from either Eq. (3.26) or (3.48). For a polytropic gas with $\gamma = 7/5$, the solutions are given by $z = 0.944980$, $\rho_2/\rho_1 = 1.78748$, $M_{\mathrm{i}} = 1.45658$ and $\theta_{\mathrm{w}} = 48.5876°$, respectively, whereas for a polytropic gas with $\gamma = 5/3$, the respective solutions are $z = 1.036324$, $\rho_2/\rho_1 = 1.77724$, $M_{\mathrm{i}} = 1.54877$ and $\theta_{\mathrm{w}} = 51.1666°$.

Chapter 4

Shock-Front Transition Solutions

The transition and thickness of the rapidly changing flow properties through planar shock fronts in monatomic, diatomic and polyatomic gases are examined in this chapter, using solutions of the Navier-Stokes equations of motion. The study of the internal structure of shock waves provided a starting point for the research presented in this thesis and the shock-front transition solutions provided a benchmark for the verification and validation of the numerical solution method for evaluating shock-reflection flow fields (see Chapter 6). The governing ordinary differential equations (ODEs) describing steady, one-dimensional, compressible fluid flows with viscous and thermal heat conduction effects, including volume viscosity, are solved to obtain the variation of temperature, pressure, density, flow velocity and entropy through shock waves of varying strength. The effects of volume viscosity on the transition and thickness of shock fronts are examined for gases including argon (Ar), molecular nitrogen (N_2) and atmospheric air. The predicted shock transition and thickness for solutions including volume viscosity are compared to past experimental measurements for shock Mach numbers up to 7.0, well into the range where Navier-Stokes solutions are considered inadequate [82] and kinetic-theory solutions are deemed necessary [83].

4.1 Governing Equations

For the special case of one-dimensional, compressible, unsteady, gaseous fluid flows that are aligned parallel to the x-coordinate direction in a laboratory frame of reference and include the internal effects of viscosity and heat conduction, the Navier-Stokes equations for unsteady gas

flows given by Eqs. (2.1) through (2.3) can be reduced considerably to yield

$$\frac{\partial \rho}{\partial t} + \frac{\partial}{\partial x}\left(\rho u\right) = 0, \tag{4.1}$$

$$\rho\frac{\partial u}{\partial t} + \rho u\frac{\partial u}{\partial x} + \frac{\partial p}{\partial x} = \frac{\partial}{\partial x}\left(\frac{4}{3}\eta + \eta_v\right)\frac{\partial u}{\partial x}, \tag{4.2}$$

$$\rho\frac{\partial e}{\partial t} + \rho u\frac{\partial e}{\partial x} + p\frac{\partial u}{\partial x} = \left(\frac{4}{3}\eta + \eta_v\right)\left(\frac{\partial u}{\partial x}\right)^2 + \frac{\partial}{\partial x}\left(\kappa\frac{\partial T}{\partial x}\right). \tag{4.3}$$

This system of coupled, non-linear, partial differential equations (PDEs), governing the transport of mass, momentum and energy, can be further simplified by using the frame of reference connected to the shock front. In the shock-wave reference frame, a one-dimensional coordinate system is attached to the planar, constant-velocity shock front, wherein the direction normal to the shock wave is aligned parallel with the x-coordinate direction. Consequently, the temporal partial derivative terms in Eqs. (4.1) through (4.3) for unsteady flows are eliminated to obtain a system of ODEs in which the solution variables depend only on their spatial derivatives with respect to the distance x normal to the shock-wave motion. One integration of these ODEs with respect to x yields

$$\rho u = \rho_1 u_1, \tag{4.4}$$

$$p + \rho u^2 - \left(\frac{4}{3}\eta + \eta_v\right)\frac{\mathrm{d}u}{\mathrm{d}x} = p_1 + \rho_1 u_1^2, \tag{4.5}$$

$$\rho u\left(c_p T + \frac{u^2}{2}\right) - \left(\frac{4}{3}\eta + \eta_v\right)u\frac{\mathrm{d}u}{\mathrm{d}x} - \kappa\frac{\mathrm{d}T}{\mathrm{d}x} = \rho_1 u_1\left(c_p T_1 + \frac{u_1^2}{2}\right), \tag{4.6}$$

in which the specific internal enthalpy $h = \varepsilon + p/\rho = c_p T$. The values on the right-hand sides of Eqs. (4.4) through (4.6) are specified as the initial flow condition far upstream or ahead of the shock wave in region (1), when $x \to +\infty$. The flow condition far downstream or behind the shock-front transition in region (2), when $x \to -\infty$, is governed by the strength of the shock wave. The viscous and thermal conduction terms disappear from Eqs. (4.5) and (4.6) when $x \to \pm\infty$, as the spatial gradients $\mathrm{d}u/\mathrm{d}x$ and $\mathrm{d}T/\mathrm{d}x$ tend to zero, giving rise to the conventional Rankine-Hugoniot equations of Eqs. (3.4) through (3.7).

For the study of stationary, planar shock waves, it is convenient to express the Navier-Stokes equations written in the form of Eqs. (4.4) through (4.6) in an alternative, non-dimensional form. The various non-dimensional variables and constants, as well as some other useful and related relationships, used in the subsequent numerical integration of the governing ODEs are defined in the shock-wave frame of reference according to:

$$D = \frac{\rho - \rho_1}{\rho_2 - \rho_1}, \qquad U = \frac{u - u_1}{u_2 - u_1}, \qquad P = \frac{p - p_1}{p_2 - p_1}, \qquad \mathcal{T} = \frac{T - T_1}{T_2 - T_1},$$

$$S = \frac{s - s_1}{s_2 - s_1} = \frac{\ln\left[\left(\frac{T}{T_1}\right)^{\left(\frac{\gamma}{\gamma-1}\right)}\left(\frac{p_1}{p}\right)\right]}{\ln\left[\left(\frac{T_2}{T_1}\right)^{\left(\frac{\gamma}{\gamma-1}\right)}\left(\frac{p_2}{p_1}\right)^{-1}\right]}, \qquad X = \frac{\rho_1 u_1 x}{\eta_1}, \qquad \mathrm{Pr}_1 = \frac{\eta_1 c_p}{\kappa_1},$$

$$\Omega_v = \frac{\eta_v}{\eta}, \qquad M_\mathrm{i} = \frac{u_1}{a_1}, \qquad a_1 = \sqrt{\frac{\gamma p_1}{\rho_1}} = \sqrt{\gamma R T_1}. \tag{4.7}$$

In Eq. (4.7), the variables D, U, P, $\mathcal{T}$, S and X are non-dimensional forms of the density, velocity, pressure, temperature, entropy and distance normal to the shock wave, respectively. The upstream Prandtl number is Pr_1 and the temperature-dependent ratio of volume to dynamic viscosities at a given point in the flow field is Ω_v. The variable M_i is the shock Mach number or shock-wave strength and a_1 is the reference sound speed of the fluid. The respective pressure, density and temperature ratios p_2/p_1, ρ_2/ρ_1 and T_2/T_1 are calculated using the conventional Rankine-Hugoniot equations given earlier in Eqs. (3.4) through (3.7).

The resulting conservation equations which govern the transport of mass, momentum, and energy through a stationary, one-dimensional shock wave can then be written in terms of the preceding non-dimensional variables and constants of Eq. (4.7) as follows:

$$D = \frac{U}{1 + \left(\frac{\rho_2}{\rho_1} - 1\right)(1 - U)}, \tag{4.8}$$

$$U - P = \left(\frac{4}{3} + \Omega_v\right) \frac{\eta}{\eta_1} \frac{\mathrm{d}U}{\mathrm{d}X}, \tag{4.9}$$

$$\mathcal{T} - U = \frac{\left(\frac{\rho_2}{\rho_1} - 1\right)}{\left(\frac{\rho_2}{\rho_1} + 1\right)}(1 - U)U + \frac{\kappa}{\eta_1 c_p} \frac{\mathrm{d}\mathcal{T}}{\mathrm{d}X} - \left(\frac{4}{3} + \Omega_v\right) \frac{\eta}{\eta_1} \frac{2}{\left(\frac{\rho_2}{\rho_1} + 1\right)} \frac{U}{D} \frac{\mathrm{d}U}{\mathrm{d}X}. \tag{4.10}$$

The ideal-gas equation of state $p = \rho R T$ is written in non-dimensional form as

$$P = \frac{U + \frac{\gamma - 1}{2\gamma}\left(\frac{\rho_2}{\rho_1} + 1\right)(\mathcal{T} - U)}{1 + \left(\frac{\rho_2}{\rho_1} - 1\right)(1 - U)} \tag{4.11}$$

after some algebraic re-organization of replacing D by U.

4.2 ODE Solution Method

The numerical solution of the variables $U = U(X)$ and $\mathcal{T} = \mathcal{T}(X)$ through the shock front in the physical plane requires the simultaneous integration of the two coupled non-linear ODEs:

$$\frac{\mathrm{d}U}{\mathrm{d}X} = \frac{3}{4 + 3\Omega_v} \frac{\eta_1}{\eta} \left[\frac{\left(\frac{\rho_2}{\rho_1} - 1\right)(1 - U)U - \frac{\gamma - 1}{2\gamma}\left(\frac{\rho_2}{\rho_1} + 1\right)(\mathcal{T} - U)}{1 + \left(\frac{\rho_2}{\rho_1} - 1\right)(1 - U)} \right], \tag{4.12}$$

$$\frac{\mathrm{d}\mathcal{T}}{\mathrm{d}X} = \frac{\kappa_1}{\kappa} \frac{\mathrm{Pr}_1}{\left(\frac{\rho_2}{\rho_1} + 1\right)} \left[\left(\frac{\rho_2}{\rho_1} - 1\right)(1 - U)U + \frac{1}{\gamma}\left(\frac{\rho_2}{\rho_1} + 1\right)(\mathcal{T} - U) \right]. \tag{4.13}$$

These equations arise from further algebraic manipulation of Eqs. (4.8) through (4.11): Eq. (4.12) for $\mathrm{d}U/\mathrm{d}X$ is obtained by substituting Eq. (4.11) into Eq. (4.9) and simplifying, whereas

Eq. (4.13) for $\mathrm{d}\mathcal{T}/\mathrm{d}X$ is obtained by substituting Eqs. (4.8) and (4.11) into Eq. (4.10) and simplifying. Alternatively, Eq. (4.12) can be divided by Eq. (4.13) to yield the expression

$$\frac{\mathrm{d}U}{\mathrm{d}\mathcal{T}} = \frac{3}{4+3\Omega_v}\,\frac{\eta_1}{\eta}\,\frac{\kappa}{\kappa_1}\,\frac{\left(\frac{\rho_2}{\rho_1}+1\right)}{\mathrm{Pr}_1}\,\frac{D}{U}\left[\frac{\left(\frac{\rho_2}{\rho_1}-1\right)(1-U)U - \frac{\gamma-1}{2\gamma}\left(\frac{\rho_2}{\rho_1}+1\right)(\mathcal{T}-U)}{\left(\frac{\rho_2}{\rho_1}-1\right)(1-U)U + \frac{1}{\gamma}\left(\frac{\rho_2}{\rho_1}+1\right)(\mathcal{T}-U)}\right], \tag{4.14}$$

which may be integrated to obtain the solution for $U = U(\mathcal{T})$ in the state plane, with D specified using Eq. (4.8). Note that the variable $\Omega_v = \eta_v/\eta$ in Eqs. (4.12) and (4.14) is the temperature-dependent ratio of volume to dynamic viscosities.

A standard, fourth-order Runge-Kutta (RK4) integration method is used to solve the coupled system of ODEs given by $\mathrm{d}U/\mathrm{d}X = f(X,U,\mathcal{T})$ and $\mathrm{d}\mathcal{T}/\mathrm{d}X = g(X,U,\mathcal{T})$ in Eqs. (4.12) and (4.13) with the boundary conditions $U = 0$ and $\mathcal{T} = 0$ for $X \to +\infty$ and $U = 1$ and $\mathcal{T} = 1$ for $X \to -\infty$. The RK4 method for one forward step ΔX of fixed size in physical space, that is $X_{i+1} = X_i + \Delta X$ for the i^{th} step, is given for $U_{i+1} = U(X_{i+1})$ and $\mathcal{T}_{i+1} = \mathcal{T}(X_{i+1})$ as follows:

$$U_{i+1} = U_i + \frac{1}{6}\left(k_{1,f} + 2k_{2,f} + 2k_{3,f} + k_{4,f}\right), \tag{4.15}$$

$$\mathcal{T}_{i+1} = \mathcal{T}_i + \frac{1}{6}\left(k_{1,g} + 2k_{2,g} + 2k_{3,g} + k_{4,g}\right). \tag{4.16}$$

The variables $k_{i,f}$ and $k_{i,g}$, with $i = 1, 2, 3, 4$, are given by the expressions:

$$k_{1,f} = f\big(X_i, U_i, \mathcal{T}_i\big)\Delta X, \tag{4.17}$$

$$k_{1,g} = g\big(X_i, U_i, \mathcal{T}_i\big)\Delta X, \tag{4.18}$$

$$k_{2,f} = f\big(X_i + \Delta X/2, U_i + k_{1,f}/2, \mathcal{T}_i + k_{1,g}/2\big)\Delta X, \tag{4.19}$$

$$k_{2,g} = g\big(X_i + \Delta X/2, U_i + k_{1,f}/2, \mathcal{T}_i + k_{1,g}/2\big)\Delta X, \tag{4.20}$$

$$k_{3,f} = f\big(X_i + \Delta X/2, U_i + k_{2,f}/2, \mathcal{T}_i + k_{2,g}/2\big)\Delta X, \tag{4.21}$$

$$k_{3,g} = g\big(X_i + \Delta X/2, U_i + k_{2,f}/2, \mathcal{T}_i + k_{2,g}/2\big)\Delta X, \tag{4.22}$$

$$k_{4,f} = f\big(X_i, U_i + k_{3,f}, \mathcal{T}_i + k_{3,g}\big)\Delta X, \tag{4.23}$$

$$k_{4,g} = g\big(X_i, U_i + k_{3,f}, \mathcal{T}_i + k_{3,g}\big)\Delta X, \tag{4.24}$$

as outlined in the book on numerical methods by Faires and Burden [84].

A shooting technique is combined with the space marching outlined above to obtain numerical solutions for the shock-front transitions satisfying the boundary conditions at $X \to \pm\infty$. This method is illustrated in Fig. 4.1. The transition solutions for U and $\mathcal{T}$ with X are obtained by first integrating the two coupled ODEs of Eqs. (4.12) and (4.13) using the RK4 method downstream into region (2), starting from the shock-front transition center $U_\mathrm{o} = U(X_\mathrm{o} = 0)$ with the initial guess $\mathcal{T}_\mathrm{o}$. A value of $\mathcal{T}_\mathrm{o}$ that is too low yields the solution (a) in Fig. 4.1 that diverges towards $U \to +\infty$ for $X \to -\infty$. Conversely, a value of $\mathcal{T}_\mathrm{o}$ that is too high yields the solution (b) in Fig. 4.1 that diverges towards $U \to -\infty$ for $X \to -\infty$. The converged solution (c) in Fig. 4.1 is obtained when the convergence criterion $|U_{i+1} - U_i| < \epsilon$ is satisfied in region (2), where ϵ is a

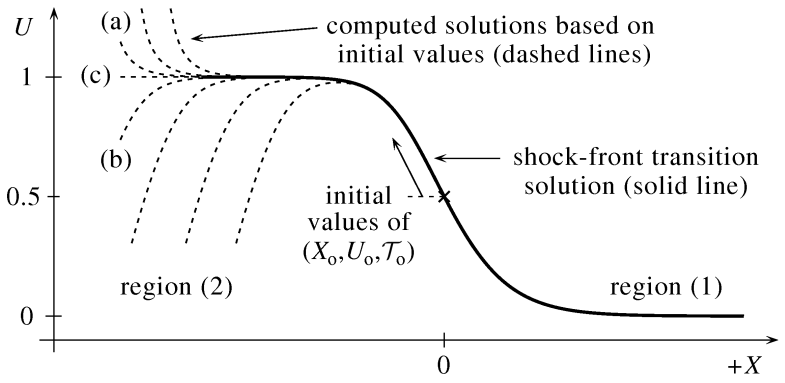

Figure 4.1: Numerical shooting method for the solution of shock-front transitions.

small convergence tolerance typically in the range of $\epsilon \approx 10^{-7}$ for the computations presented in this chapter. The upstream integration of the coupled ODEs of Eqs. (4.12) and (4.13) for the solution of U and $\mathcal{T}$ with X into region (1) ahead of the shock front follows once the solution for U with X in the downstream region (2) is deemed converged. A similar shooting technique for shock-front transitions has recently been employed by Elizarova and co-researchers [85].

The shock-front transition profiles for the variables D, P and S with X are computed following the solution of U and $\mathcal{T}$ with X, using the corresponding relations and expressions presented within Eqs. (4.7), (4.8) and (4.11) for each of these non-dimensional variables. The dimensional forms of the primitive solution variables ρ, u, p, T, s and x through the shock-front transition may then deduced from Eq. (4.7) by re-arranging the respective equations for D, U, P, $\mathcal{T}$, S and X. This requires an evaluation of the conventional Rankine-Hugoniot equations for p_2/p_1, ρ_2/ρ_1, T_2/T_1 and $\Delta u_i/a_1$ using Eqs. (3.4) through (3.7) to get the flow properties in region (2) downstream of the shock front, given the initial flow condition in region (1) upstream of the shock front as well as a measure of the shock-wave strength or shock Mach number M_i.

The ODE solutions for the transition of flow properties through an argon shock wave with $p_2/p_1 = 4.0$ (or $M_i \approx 1.84$) are illustrated in Fig. 4.2 using both physical- and state-plane representations. These computational results are shown using the non-dimensional flow variables of $\mathcal{T}, P, D, U$ and S, as they each transition smoothly from an upstream value of 0 towards a downstream value of 1.

Through the shock-front transition, D varies monotonically from 0 to 1, as does U from 0 to 1. The entire transition profiles of D and U tend to the same shape when $\rho_2/\rho_1 \to 1$ as $M_i \to 1$, i.e. for the case of very weak shock waves approaching the sonic limit. Otherwise, $D \approx \rho_1 U/\rho_2$ when $U \approx 0$ at the beginning of the shock-front transition profile, $D \approx U$ when $U \approx 1$ at the end, and the central regions differ.

The behaviour of P increases monotonically from 0 to 1 while $\mathrm{d}U/\mathrm{d}X$ varies from 0 to a maximum negative value and back to 0 again. As a result, the first and last sections of the

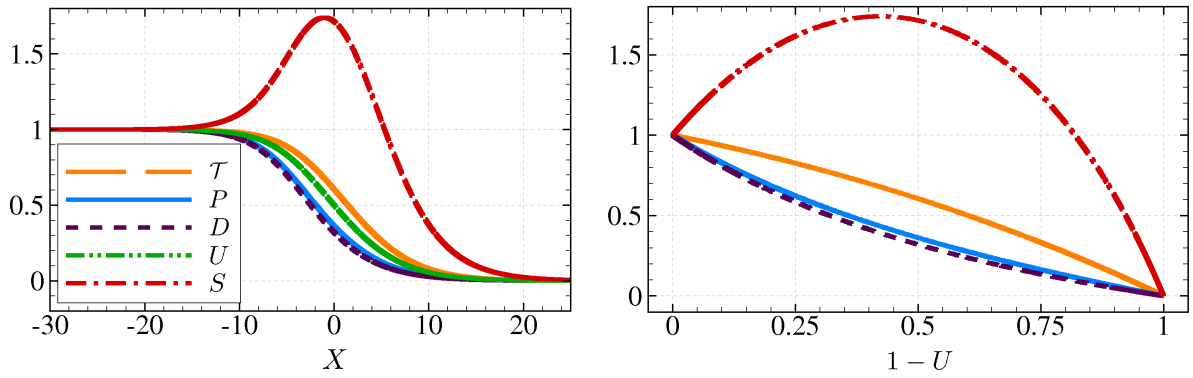

Figure 4.2: A comparison of both physical (left-hand side) and state (right-hand side) planes for a shock wave of strength $p_2/p_1 = 4.0$ (or $M_\mathrm{i} \approx 1.84$) in argon.

transition profiles for P and U are the same shape because $U \to 0$ and $U \to 1$ when $\mathrm{d}U/\mathrm{d}X \approx 0$. Otherwise, the center sections of the P and U shock-front transitions are different.

The transition profile for T increases monotonically from 0 to 1 along with the general variation of D, U and P from 0 to 1. Hence, $\mathrm{d}T/\mathrm{d}X$ behaves similarly to $\mathrm{d}U/\mathrm{d}X$, increasing from 0 to a maximum negative value and then decreasing back to 0 once more. Note that within the homogeneous pre- and post-shock equilibrium states of regions (1) and (2), the derivatives $\mathrm{d}U/\mathrm{d}X$ and $\mathrm{d}T/\mathrm{d}X$ are equal to zero.

The entropy S through the shock front increases from 0 in region (1) to a maximum $S_\mathrm{max} > 1$ just behind the center of the shock-front transition, and then decreases from S_max to a value of 1 in region (2). See the paper by Morduchow and Libby [86] and the book by Liepmann and Roshko [87] for more information on the entropy change across a shock wave.

4.3 Numerical Results and Comparisons with Experiments

Numerical results based on solutions of the governing Navier-Stokes equations, with and without volume viscosity, are presented herein for the transition and thickness of shock waves occurring in argon, molecular nitrogen and atmospheric air. The predicted numerical shock-front transitions are compared to experimental measurements of shock-front structures to illustrate the accuracy of the ODE solution method as well as the validity of the computed results.

Comparisons to experiments are also made in regard to the variation of reciprocal shock wave thickness, $\lambda/\Delta x_\mathrm{s}$, as a function of the shock Mach number, M_i, for the predicted numerical results. For each of the aforementioned gases of interest, the mean free path, λ, is defined from gas-kinetic theory as

$$\lambda = \frac{16\mu_1}{5\rho_1\sqrt{2\pi RT_1}}, \tag{4.25}$$

based on molecular collisions of rigid, impenetrable spheres. The shock wave thickness, Δx_s, has been calculated from the velocity profile according to the standard maximum-slope thickness method of Becker [88], given by the expression

$$\Delta x_s = \frac{|u_2 - u_1|}{|{}^{du}/_{dx}|_{max.}}, \tag{4.26}$$

where $|{}^{du}/_{dx}|_{max.}$ denotes the maximum gradient of velocity with respect to distance within the entirety of the shock front.

4.3.1 Shock Waves in Argon

The numerically predicted ODE shock structures for the variation of density through moderate-strength shock waves are compared in Fig. 4.3 to the experimental measurements of Alsmeyer [64] for shock-front transitions in argon. The results are presented in normalized form, ranging in particular from 0 to 1 in D as a function of the distance, x, divided by the mean free path, λ, and are shown for shock Mach numbers of $M_i = 1.55, 1.76, 2.05, 2.31, 3.38$ and 3.80, respectively. Argon is a monatomic molecule, has no rotational modes and has no volume viscosity. The distributions of density through the shock fronts are similar in shape and length with distance about the center, as can be seen in each of Figs. 4.3(a) through (f). In comparison to the experimental transitions of density obtained by Alsmeyer [64], the numerical ODE results appear to be in good agreement in the upstream region of the shock front where $D \approx 0$ and show slightly worse agreement in the downstream section where $D \approx 1$. This trend is consistent for all Mach numbers presented in Fig. 4.3 for shock waves in argon.

The predicted reciprocal shock thicknesses, $\lambda/\Delta x_s$, in argon, computed from the ODE solutions for shock wave strengths of $1.0 < M_i < 7.0$, are plotted in Fig. 4.4. The numerical results are compared to the previous experimental measurements taken from the paper by Alsmeyer [64]. In general, the reciprocal shock thickness increases as a function of the shock Mach number from weak- to moderate-strength shock waves and then plateaus for stronger shock waves. The numerical computations of shock thickness as obtained in this study over the range of $1.0 < M_i < 7.0$ follow this pattern. The comparison of results indicates that the numerically predicted reciprocal shock thicknesses are in good agreement with the experiments for $1.0 < M_i < 2.0$; however, the ODE solutions begin to slightly underpredict the experimental measurements of shock thickness for $2.0 < M_i < 7.0$. This underprediction is most likely due to the limitations of the Navier-Stokes equations for modelling rapid and sparse collision processes in argon at elevated temperatures, where kinetic theory predictions are perhaps more appropriate to use.

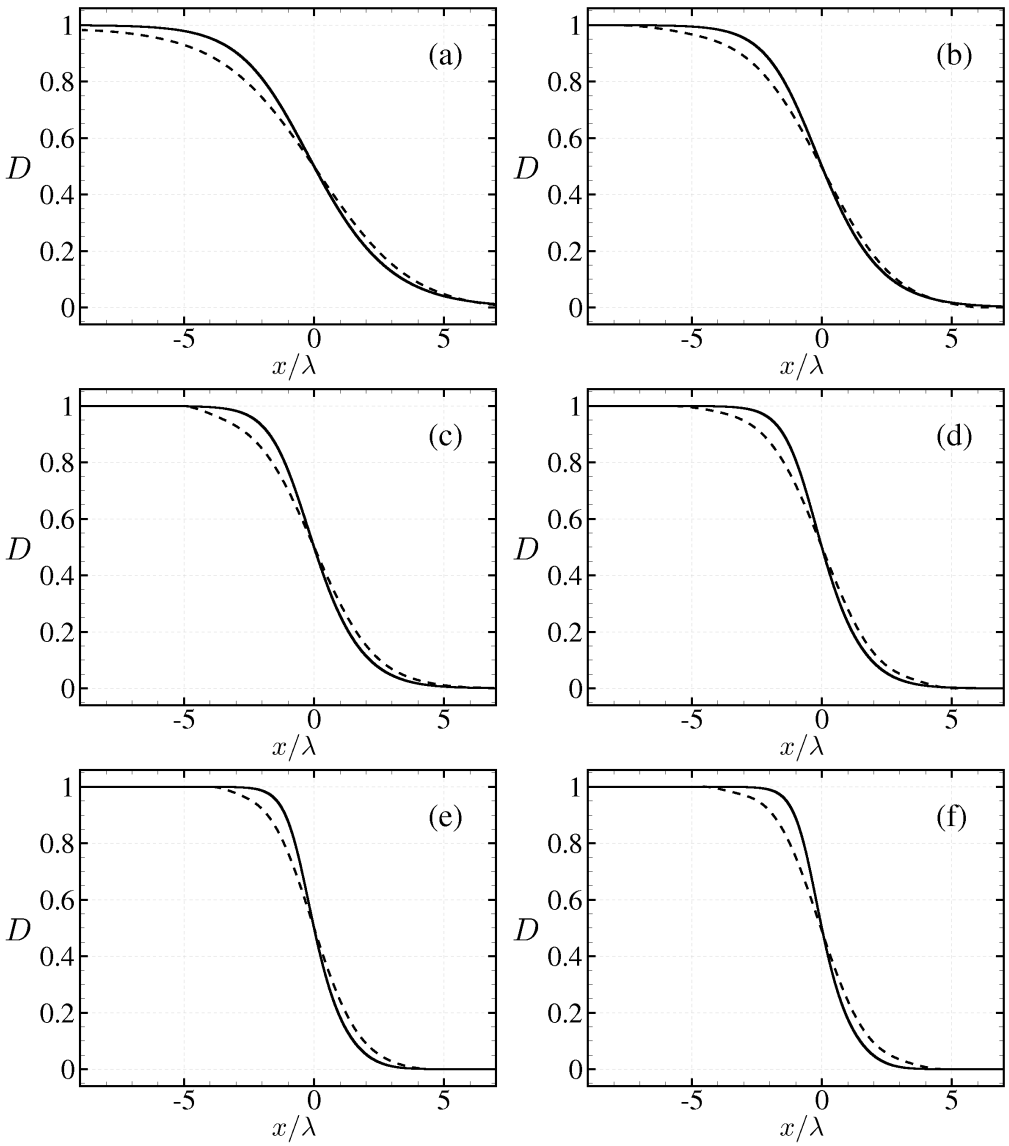

Figure 4.3: Comparisons of numerical ODE solutions (solid lines) against experimental measurements (dashed lines; see the paper by Alsmeyer [64]) for transitions of density through shock fronts in argon with (a) $M_{\mathrm{i}} = 1.55$; (b) $M_{\mathrm{i}} = 1.76$; (c) $M_{\mathrm{i}} = 2.05$; (d) $M_{\mathrm{i}} = 2.31$; (e) $M_{\mathrm{i}} = 3.38$; (f) $M_{\mathrm{i}} = 3.80$.

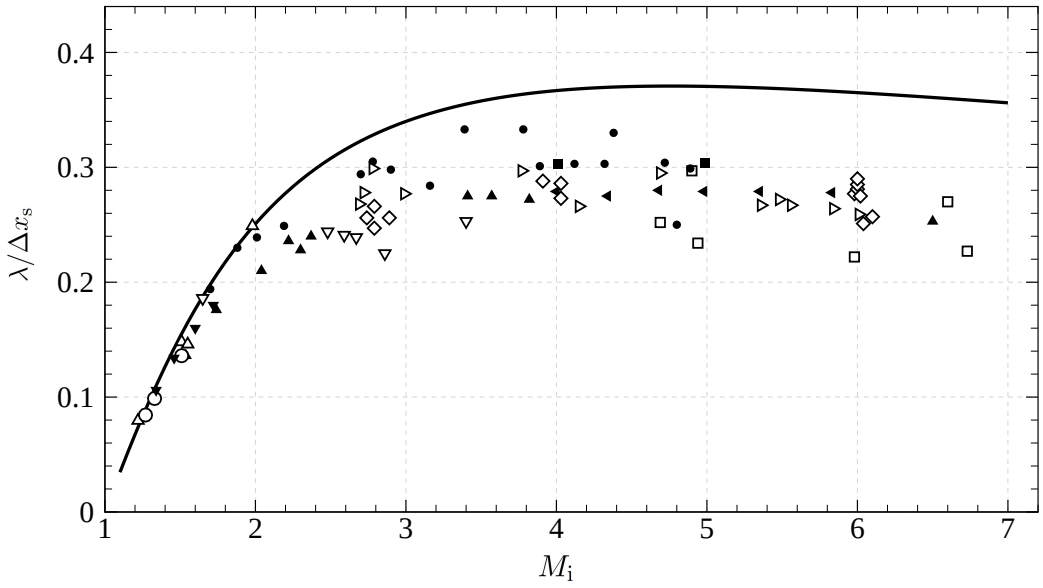

Figure 4.4: Comparisons of numerical ODE solutions (solid line) against experimental markers (see the paper by Alsemeyer [64]) for reciprocal shock wave thicknesses in argon.

4.3.2 Shock Waves in Molecular Nitrogen

The Navier-Stokes predictions of the variation of density as a function of distance, through shocks of varying strength in molecular nitrogen, are presented and compared to experimental shock-front transitions obtained by Alsmeyer [64] in Fig. 4.5. The results are presented for the normalized density D varying from 0 to 1 as a function of $\lambda/\Delta x_s$, shown for shock Mach numbers of $M_i = 1.53, 1.70, 2.00, 2.40, 3.20$ and 3.80, respectively. The ODE results have been obtained using the compressible, fully viscous and heat-conducting Navier-Stokes equations with the additional effects of volume viscosity. The predicted transitions of density are in good agreement with the experimental results, as seen in Figs. 4.5(a) through (f). The density variations differ only a little in the downstream regions where $D \approx 1$ and tend to agree better in the upstream regions where $D \approx 0$.

The numerically predicted reciprocal shock thicknesses in molecular nitrogen, computed from the ODE solution method for shock wave strengths of $1.0 < M_i < 7.0$, are provided in Fig. 4.6. The numerical reciprocal shock thickness increases as a function of shock strength from weak- to moderate-strength shock waves and then plateaus for stronger shocks. Experimental measurements for shock wave thicknesses in molecular nitrogen that are taken from the paper by Alsmeyer [64] are included in Fig. 4.6. The ODE solutions for reciprocal shock thickness have been calculated with and without the added effects of volume viscosity (η_v). The comparison of the ODE solutions for shock thickness to experimental measurements shows excellent agreement between predictions (when $\eta_v \neq 0$) and experiments for the entire range of shock Mach numbers given by $1.0 < M_i < 7.0$. The predicted shock-front transitions are about 64% thicker in

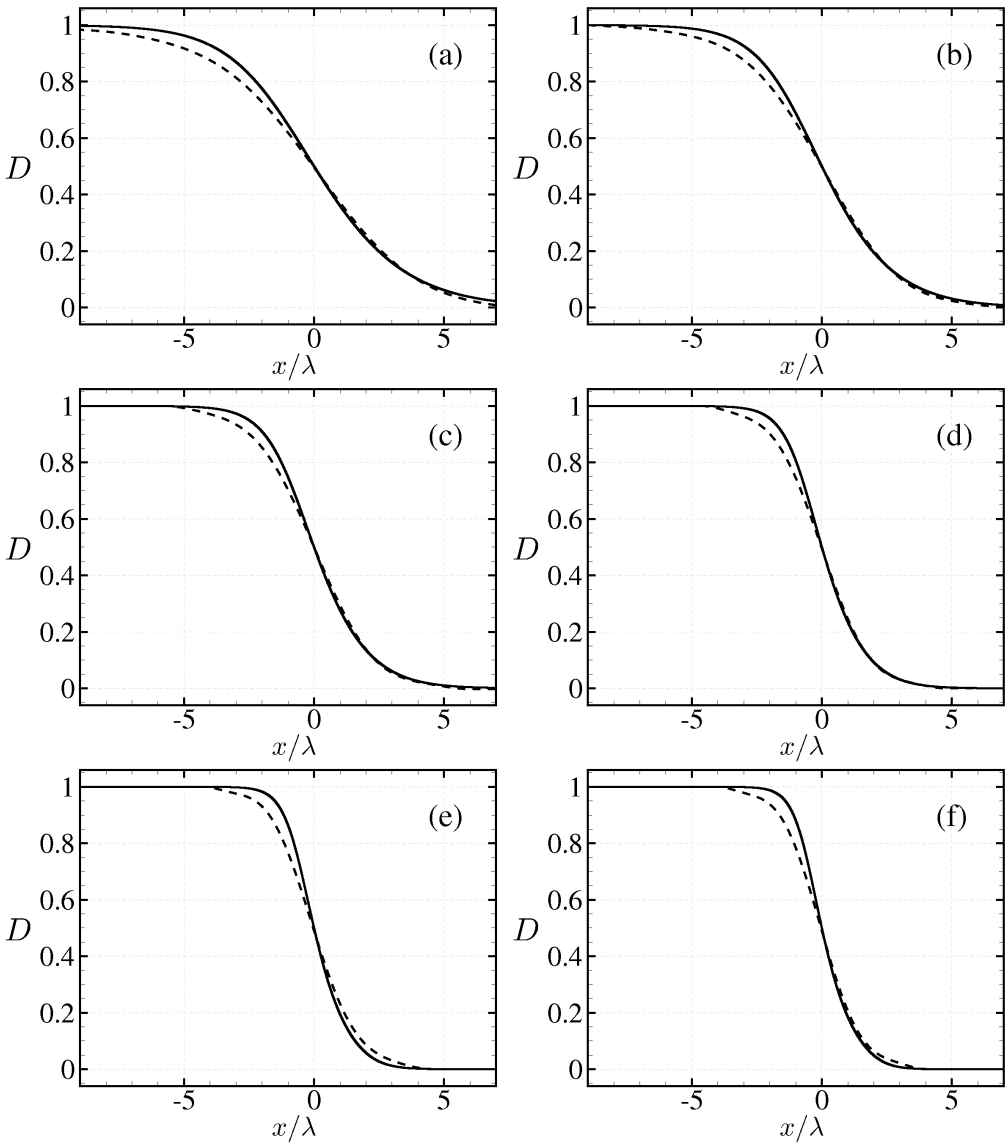

Figure 4.5: Comparisons of numerical ODE solutions with volume viscosity (solid lines) against experimental measurements (dashed lines; see the paper by Alsmeyer [64]) for transitions of density through shock fronts in nitrogen with (a) $M_{\mathrm{i}} = 1.53$; (b) $M_{\mathrm{i}} = 1.70$; (c) $M_{\mathrm{i}} = 2.00$; (d) $M_{\mathrm{i}} = 2.40$; (e) $M_{\mathrm{i}} = 3.20$; (f) $M_{\mathrm{i}} = 3.80$.

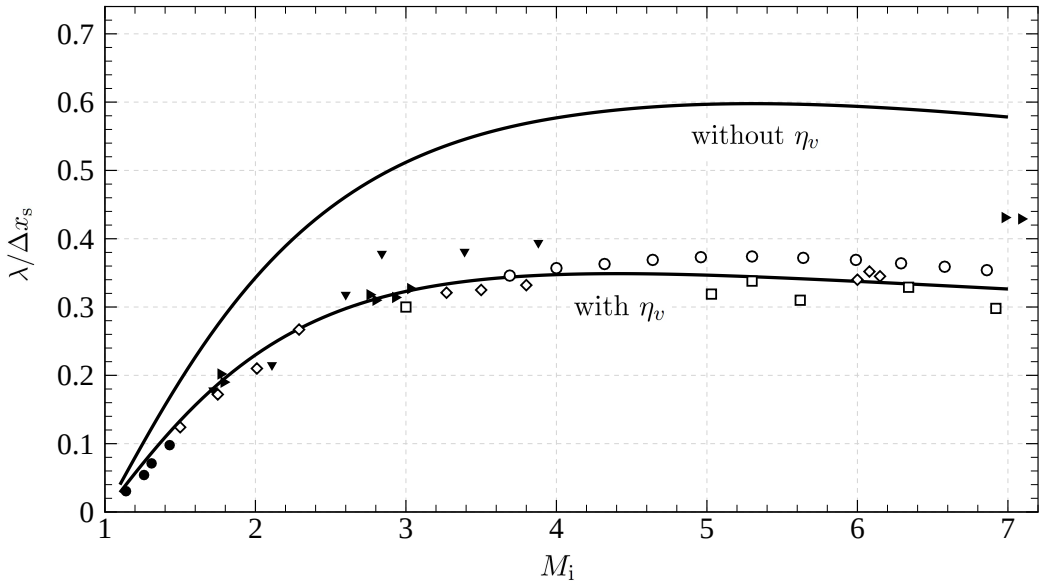

Figure 4.6: Comparisons of numerical ODE solutions (solid lines) against experimental markers (see the paper by Alsemeyer [64]) for reciprocal shock wave thicknesses in nitrogen.

molecular nitrogen with the addition of volume viscosity over the range of $1.0 < M_\mathrm{i} < 7.0$, as shown in Fig. 4.6. The generally strong agreement of the Navier-Stokes computations with past experimental data implies that the continuum fluid-dynamic description of gases provides better and more accurate transition and thickness predictions for shock waves than previously thought or expected (e.g. see the paper by Elizarova and co-researchers [85]), even at relatively high shock Mach numbers.

The smooth but rapid transition of non-dimensional flow properties through a shock front of moderate strength $p_2/p_1 = 4.0$ (or $M_\mathrm{i} \approx 1.89$) in molecular nitrogen, computed using the ODE solution method, is presented in Fig. 4.7. The computations are illustrated in both the physical (left-hand side) and state (right-hand side) planes, without (top half) and with (bottom half) the added effects of volume viscosity. The solutions in the physical plane on the left-hand side of this diagram demonstrate that volume viscosity increases the shock-front dissipation and produces a larger shock thickness (bottom, left-hand diagram of Fig. 4.7). However, volume viscosity does not affect the Rankine-Hugoniot shock jump conditions, so the solution on either side of the shock front is unchanged with or without volume viscosity. The gradients of temperature, pressure, density and flow velocity within the shock front are smaller for thicker shock fronts (i.e. when volume viscous effects are larger). The smaller temperature gradient, in particular, results in a reduced localized heat conduction through the shock front, which consequently gives a lower peak entropy value, as illustrated in the bottom half of Fig. 4.7. The corresponding solutions in the state plane are provided on the right-hand side of Fig. 4.7 and show the variation of non-dimensional flow properties as a function of the non-dimensional flow velocity.

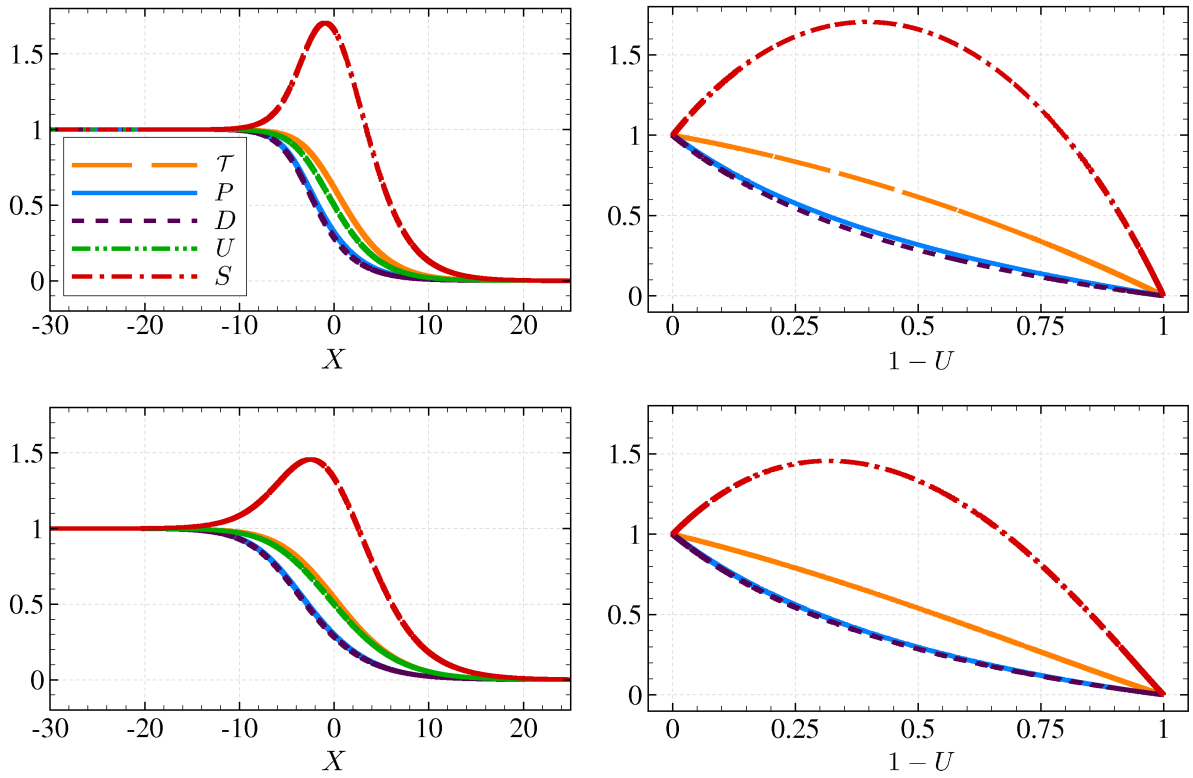

Figure 4.7: A comparison of both physical (left-hand side) and state (right-hand side) planes for a shock wave of strength $p_2/p_1 = 4.0$ (or $M_\mathrm{i} \approx 1.89$) in nitrogen, without η_v (top half) and with η_v (bottom half).

4.3.3 Shock Waves in Atmospheric Air

The computed ODE solutions for the transition of temperature through shock fronts in atmospheric air are illustrated and compared to experimental measurements in Fig. 4.8 for several different shock Mach numbers. This graph presents the ODE results in relation to the experimental markers of Sherman [89]. The transition of the normalized temperature $\mathcal{T}$ varies from 0 to 1 as a function of x/λ, and it is presented for shock strengths of $M_\mathrm{i} = 1.78, 1.85, 1.90, 1.98, 3.70$ and 3.91. The fully viscous, heat-conducting Navier-Stokes equations with volume viscosity have been used to model the transition of flow properties through these shocks. In general, the numerical results agree well with the experimental data for low- to moderate-strength shock waves in Figs. 4.8(a) through (d), and show slightly worse agreement at stronger shock Mach numbers in Figs. 4.8(e) and (f), particularly in the downstream regions of the shock fronts.

The predicted reciprocal shock thickness in atmospheric air has been computed with and without volume viscosity and is presented against some experimental shock thicknesses reported by Sherman [89] in Fig. 4.9. Experimental data for shock wave thicknesses in air is scarce, so the comparisons to experiments are quite limited over the entire range of $1.0 < M_\mathrm{i} < 7.0$. However,

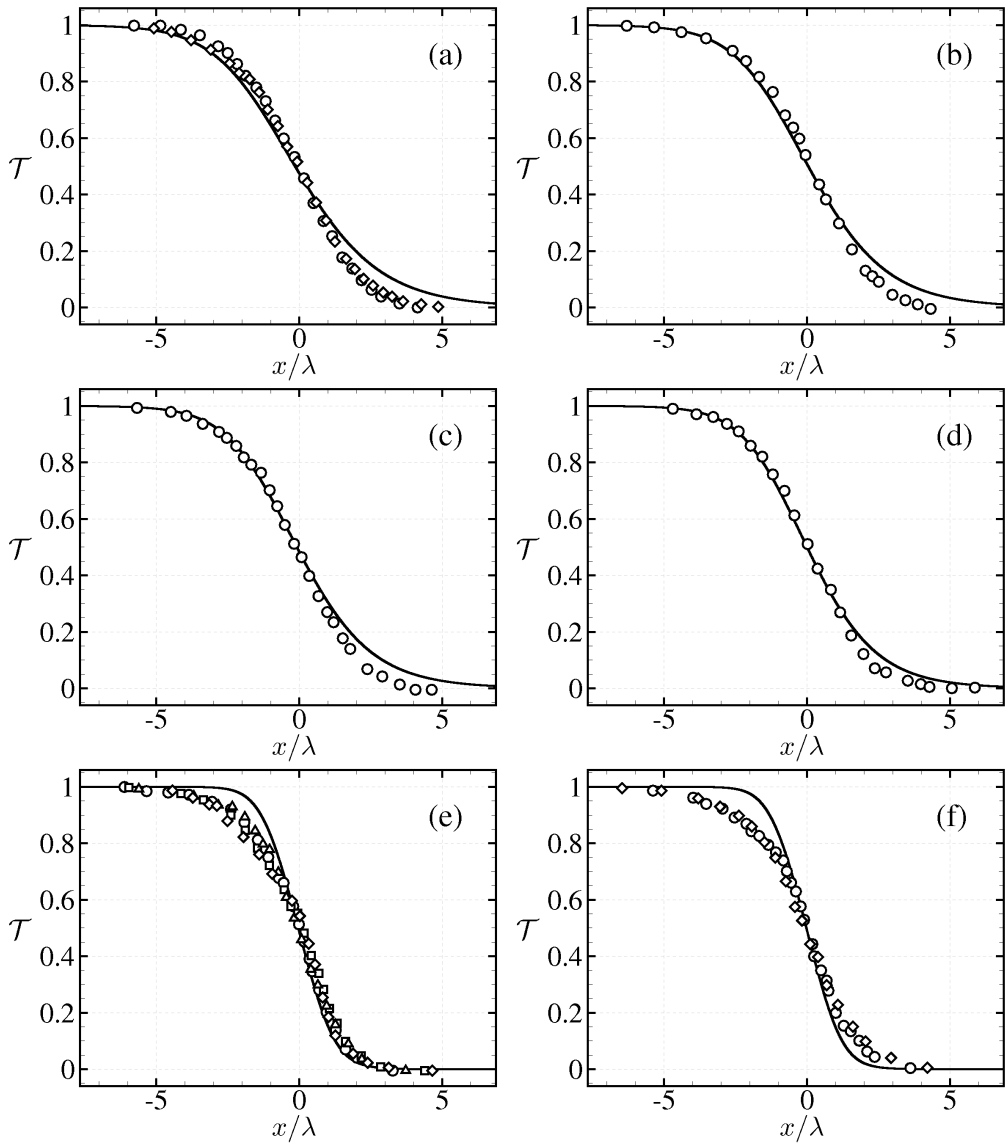

Figure 4.8: Comparisons of numerical ODE solutions with volume viscosity (solid lines) against experimental markers (see the paper by Sherman [89]) for transitions of temperature through shock fronts in atmospheric air with (a) $M_{\mathrm{i}} = 1.78$; (b) $M_{\mathrm{i}} = 1.85$; (c) $M_{\mathrm{i}} = 1.90$; (d) $M_{\mathrm{i}} = 1.98$; (e) $M_{\mathrm{i}} = 3.70$; (f) $M_{\mathrm{i}} = 3.91$.

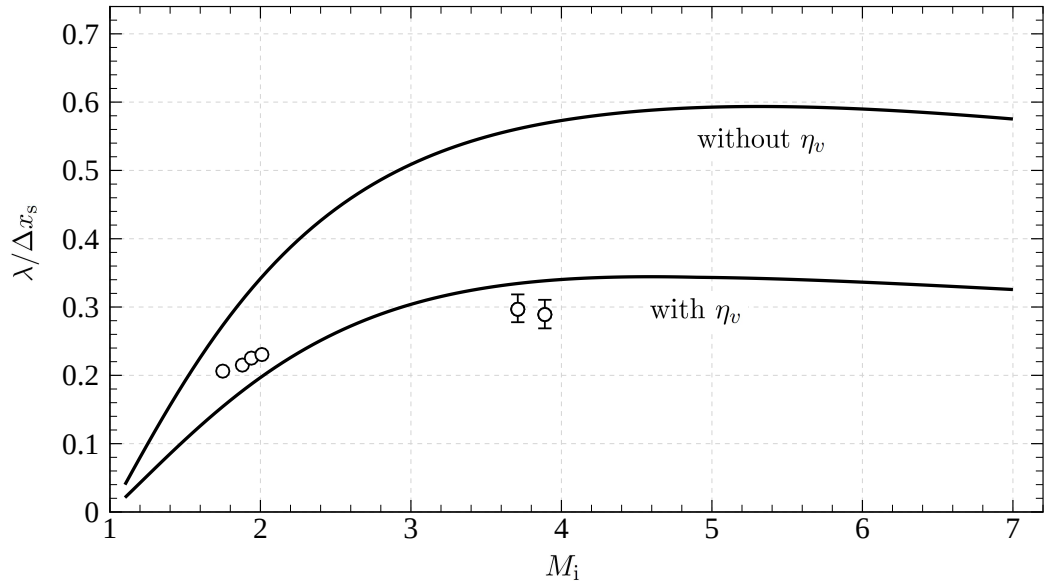

Figure 4.9: Comparisons of numerical ODE solutions (solid lines) against experimental markers (see the paper by Sherman [89]) for reciprocal shock wave thicknesses in atmospheric air.

the predicted shock thicknesses with volume viscosity are typically around 73% thicker over this range of shock Mach numbers than those which do not take into account these added effects of volume viscosity. It can be seen that for low Mach numbers in the range $1.0 < M_i < 2.0$, the ODE solutions seem to slightly underpredict the reciprocal shock thickness when volume viscosity is accounted for in the governing Navier-Stokes equations. For relatively weak- to moderate-strength shocks, the curve for air with volume viscosity appears to indicate marginally thicker shock waves than those obtained in experiment. For stronger shock strengths, the ODE results predict that the reciprocal shock thickness plateaus as a function of Mach number.

A comparison of both physical- and state-plane solutions for the transition of non-dimensional flow properties through a moderate-strength shock wave with $p_2/p_1 = 4.0$ (or $M_i \approx 1.89$) in atmospheric air, with and without volume viscosity, is presented in Fig. 4.10. Similar to the aforementioned results in molecular nitrogen, volume viscosity tends to cause a thickening of the shock front in atmospheric air and, consequently, a reduction in the peak specific entropy value due to the smaller temperature gradient within the shock wave. The corresponding variations of non-dimensional flow properties, plotted as a function of the non-dimensional flow velocity, are also illustrated in Fig. 4.10, for reference.

(This space intentionally left blank.)

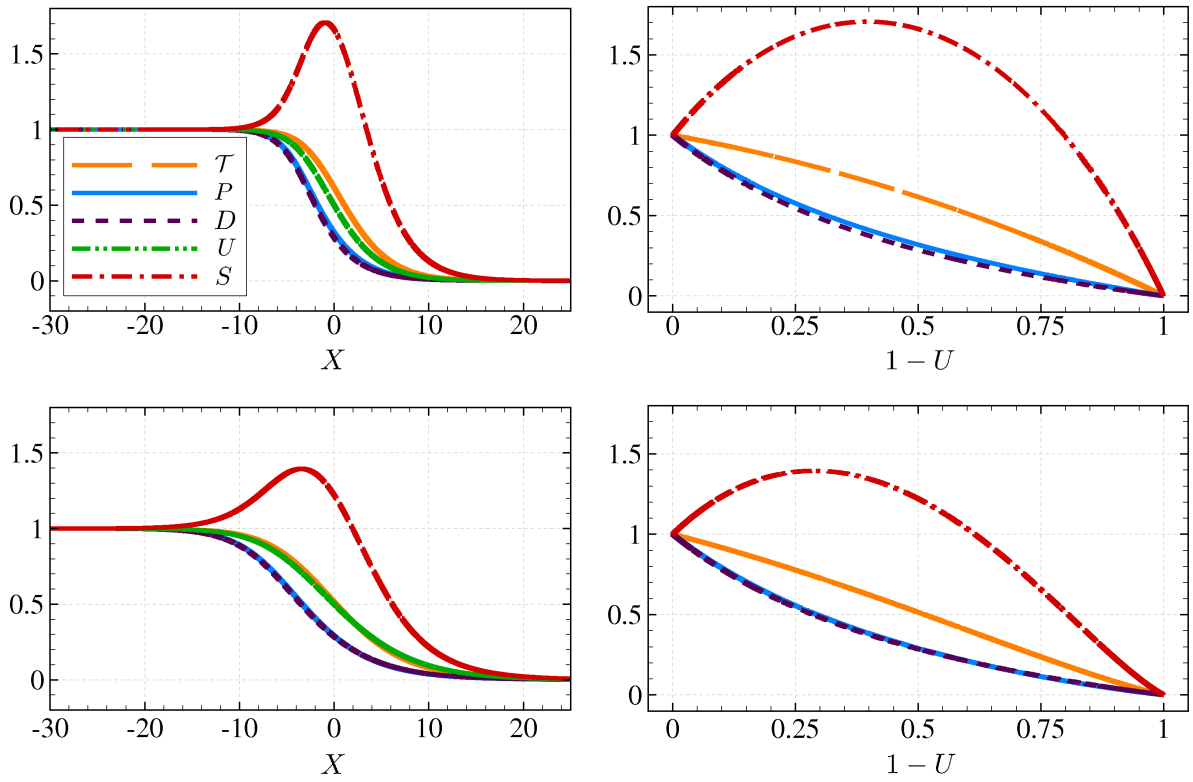

Figure 4.10: A comparison of both physical (left-hand side) and state (right-hand side) planes for a shock wave of strength $p_2/p_1 = 4.0$ (or $M_\mathrm{i} \approx 1.89$) in atmospheric air, without η_v (top half) and with η_v (bottom half).

4.4 Concluding Remarks

For argon, and possibly for other monatomic gases, the Navier-Stokes solutions for shock-front transition and thickness are well predicted for shock Mach numbers of $1.0 < M_\mathrm{i} < 2.0$, but solutions using gas-kinetic theory are likely needed for stronger shock waves of $M_\mathrm{i} > 2.0$. For molecular nitrogen and atmospheric air, and possibly other diatomic and polyatomic gases, the Navier-Stokes solutions are better than previously believed or expected for shock Mach numbers of $1.0 < M_\mathrm{i} < 7.0$, when volume viscosity is included. This finding is partly due to the more accurate modelling of volume viscosity in modern research, which was included in previous studies on shock waves but with a smaller magnitude than in the present work (e.g. see the paper by Talbot and Scala [90]).

Chapter 5

CFD Algorithm

The numerical simulation of two-dimensional, unsteady, oblique shock-wave reflection phenomena has a rather long history going back more than thirty years. Early research focused on the prediction of such flows using Godunov-type finite-volume solution methods [91] for the Euler equations governing inviscid compressible flows on simple uniform Cartesian meshes. This early research includes the studies of Colella and Glaz [92], Woodward and Colella [93] and Glaz and co-researchers [94, 95]. Subsequent work by Colella and Glaz [96] as well as Colella and Henderson [97] considered the application of patch-based, solution-directed adaptive mesh refinement (AMR) techniques on Cartesian meshes with localized mesh refinement in designated regions of the flow field. In subsequent studies, other possibly more general mesh adaptation schemes have been developed and applied by Fursenko, Timofeev, Voinovich and co-researchers [98–102], Sun and Takayama [103] and Henderson and co-researchers [104] for treating compressible, inviscid, unsteady flows with shock waves and their complex interactions.

More recently, the extension of upwind-based finite-volume schemes with AMR to the solution of the Navier-Stokes equations governing unsteady, compressible, viscous flows with shocks has permitted researchers to examine the significance of molecular transport properties on the behaviour of a range of simple and complex compressible flow phenomena. For example, Colella and co-researchers [105, 106], Timofeev, Ofengeim, Voinovich and co-researchers [107–110], as well as Henderson and co-researchers [111, 112] have all considered and/or proposed AMR schemes for the solution of viscous flows associated with unsteady oblique reflections of shock waves. Additionally, Graves and co-researchers [113] have proposed a Cartesian mesh AMR scheme for the solution of the compressible Navier-Stokes equations with an embedded boundary treatment.

In spite of these successes, the capabilities of AMR gridding strategies have to date not permitted the fully resolved numerical solution of viscous, unsteady flow applications contain-

ing shock waves in which the shock is fully resolved for a wide range of Reynolds numbers. Furthermore, the grid independence of simulations, even for inviscid cases, has been difficult to establish. Apart from the numerical investigations of Henderson and co-researchers [30], as well as Ivanov and co-researchers [114,115], who each used very fine, uniform computational meshes to obtain fully resolved, unsteady and steady computations, respectively, there is a scarcity of published numerical studies with fully resolved internal shock structures. In turn, this has not allowed a full evaluation of the effects of micro-scale molecular transport on oblique reflection processes.

To overcome some of the preceding difficulties, the anisotropic block-based AMR finite-volume scheme of Zhang and Groth [116], Williamschen and Groth [117] and Freret and Groth [118] is used here to obtain solutions of both inviscid and laminar, two-dimensional, compressible flows governed by the Euler and Navier-Stokes equations, respectively. The finite-volume spatial discretization scheme is coupled with both parallel explicit and fully implicit time-marching schemes. The latter is based on Newton's method [119–121]. The anisotropic AMR technique mitigates the inherently large computational memory and storage requirements associated with the use of the very fine spatial resolution needed for fully resolved viscous simulations of shocks, whereas the implicit time-marching scheme provides unconditional stability of the algorithm and the freedom to select the physical time step for unsteady shock reflection problems based solely on a consideration of solution accuracy, not stability constraints. Details of the parallel finite-volume AMR scheme are given in this chapter, whereas the benefits, capabilities, and parallel performance of the method are demonstrated in Chapter 6 for unsteady oblique shock reflection problems in which the internal shock structure is fully resolved. The same solution algorithm with explicit time marching is also used thereafter for the computation of the flow-fields pertaining to unsteady shock-wave interactions with rigid wedges in inviscid and polytropic gases based on the Euler equations, to determine the transition boundary separating regular and Mach reflections (as will be discussed in Chapters 7 and 9). Note that the numerical solution method is also described in the recent paper by Hryniewicki, Groth and Gottlieb [122].

5.1 Conservation Equations for Unsteady Gas Flows

5.1.1 Navier-Stokes Equations

The partial differential equations provided by Eqs. (2.1) through (2.3) for solving unsteady compressible gas flows can be expressed using matrix-vector notation as

$$\frac{\partial \mathbf{U}}{\partial t} + \vec{\nabla} \cdot \vec{\mathbf{F}} = 0, \tag{5.1}$$

which, for a two-dimensional Cartesian coordinate system (x, y), can be written as

$$\frac{\partial \mathbf{U}}{\partial t} + \frac{\partial \mathbf{F}}{\partial x} + \frac{\partial \mathbf{G}}{\partial y} = \frac{\partial \mathbf{F_v}}{\partial x} + \frac{\partial \mathbf{G_v}}{\partial y}, \tag{5.2}$$

where $\vec{\mathbf{F}} = (\mathbf{F} - \mathbf{F_v}, \mathbf{G} - \mathbf{G_v})$ is the total solution flux dyad. In Eq. (5.2), the vector of conserved solution variables, $\mathbf{U}$, the inviscid flux vectors, $\mathbf{F}$ and $\mathbf{G}$, and the viscous flux vectors, $\mathbf{F_v}$ and $\mathbf{G_v}$, are given by

$$\mathbf{U} = \begin{bmatrix} \rho \\ \rho u \\ \rho v \\ \rho e \end{bmatrix}, \qquad \mathbf{F} = \begin{bmatrix} \rho u \\ \rho u^2 + p \\ \rho uv \\ \rho u \left(e + \frac{p}{\rho} \right) \end{bmatrix}, \qquad \mathbf{G} = \begin{bmatrix} \rho v \\ \rho uv \\ \rho v^2 + p \\ \rho v \left(e + \frac{p}{\rho} \right) \end{bmatrix}, \tag{5.3}$$

$$\mathbf{F_v} = \begin{bmatrix} 0 \\ \tau_{xx} \\ \tau_{xy} \\ -q_x + u\tau_{xx} + v\tau_{xy} \end{bmatrix}, \qquad \mathbf{G_v} = \begin{bmatrix} 0 \\ \tau_{xy} \\ \tau_{yy} \\ -q_y + u\tau_{xy} + v\tau_{yy} \end{bmatrix}, \tag{5.4}$$

respectively, and t is the physical time. In Eq. (5.4), the normal and tangential elements of the viscous stress tensor, τ_{xx}, τ_{yy} and τ_{xy}, are given as

$$\tau_{xx} = \eta \left(\frac{4}{3} \frac{\partial u}{\partial x} - \frac{2}{3} \frac{\partial v}{\partial y} \right) + \eta_v \left(\frac{\partial u}{\partial x} + \frac{\partial v}{\partial y} \right), \tag{5.5}$$

$$\tau_{yy} = \eta \left(\frac{4}{3} \frac{\partial v}{\partial y} - \frac{2}{3} \frac{\partial u}{\partial x} \right) + \eta_v \left(\frac{\partial u}{\partial x} + \frac{\partial v}{\partial y} \right), \tag{5.6}$$

$$\tau_{xy} = \eta \left(\frac{\partial u}{\partial y} + \frac{\partial v}{\partial x} \right) = \tau_{yx}. \tag{5.7}$$

Also in Eq. (5.4), the x- and y-components of the heat flux vector, q_x and q_y, are given as

$$q_x = -\kappa \frac{\partial T}{\partial x}, \tag{5.8}$$

$$q_y = -\kappa \frac{\partial T}{\partial y}. \tag{5.9}$$

5.1.2 Euler Equations

For the inviscid flow fields which are of principal concern here, the viscous flux vectors $\mathbf{F_v}$ and $\mathbf{G_v}$ in Eq. (5.2) are omitted as the terms η, η_v and κ in Eqs. (5.5) through (5.9) all equal to zero. For a two-dimensional Cartesian coordinate system (x, y), the resultant partial differential equations are given as

$$\frac{\partial \mathbf{U}}{\partial t} + \frac{\partial \mathbf{F}}{\partial x} + \frac{\partial \mathbf{G}}{\partial y} = 0 \tag{5.10}$$

in matrix-vector form, where t is the physical time. In Eq. (5.10), the vector of conserved solution variables, $\mathbf{U}$, and the inviscid flux vectors, $\mathbf{F}$ and $\mathbf{G}$, are given by Eq. (5.3), and now $\vec{\mathbf{F}} = (\mathbf{F}, \mathbf{G})$ is the total solution flux dyad.

5.2 Finite-Volume Method

The finite-volume method represents and evaluates a set of partial differential equations as a system of algebraic equations, and the flow properties are calculated at discrete places on a meshed geometry. See the book of LeVeque [123]. In two spatial dimensions, the finite-volume method reduces to a finite-area method. The preceding differential form of the governing equations given by Eq. (5.2) for both the inviscid and viscous flow cases is recast into an integral form that is convenient for the application of a high-resolution, cell-centred, finite-volume spatial discretization procedure utilized herein. Equation (5.2) is multiplied by $\mathrm{d}x\mathrm{d}y$ and two integrations are included. The first term $\int_y \int_x (\partial \mathbf{U}/\partial t)\,\mathrm{d}x\mathrm{d}y$ reduces to the integral $\int_A (\partial \mathbf{U}/\partial t)\,\mathrm{d}A$ over an arbitrary area A. The last term $\int_y \int_x (\vec{\nabla}\cdot\vec{\mathbf{F}})\,\mathrm{d}x\mathrm{d}y$ is converted into a single integral for a closed path around the area A by using the divergence or Green's theorem. Equation (5.1) then becomes

$$\frac{\mathrm{d}}{\mathrm{d}t}\int_A \mathbf{U}\,\mathrm{d}A + \oint_\Gamma \vec{\mathbf{F}}\cdot\vec{n}\,\mathrm{d}\Gamma = 0, \tag{5.11}$$

in which Γ denotes the closed path and $\vec{n}$ is the outward unit vector that is normal to the control surface of interest.

Let the arbitrary shaped area in this equation be replaced by a cell of finite area from an arbitrary computational mesh of quadrilateral shaped cells. A schematic illustrating one such cell with the side lengths Δl_k and unit outward normal vectors $\vec{n}_k = n_{x,k}\hat{\imath} + n_{y,k}\hat{\jmath}$, with $k = 1, 2, \ldots, 4$ and where $\hat{\imath}$ and $\hat{\jmath}$ are the x- and y-coordinate direction unit vectors, is shown in Fig. 5.1. For this quadrilateral cell (i, j), using the mid-point rule (for second-order accuracy) for the integration, Eq. (5.11) then reduces to the semi-discrete algebraic form given by

$$\frac{\mathrm{d}\bar{\mathbf{U}}_{i,j}}{\mathrm{d}t} = -\frac{1}{A_{i,j}}\sum_{k=1}^{4}\left(\vec{\mathbf{F}}\cdot\vec{n}\,\Delta l\right)_{i,j,k} = \mathbf{R}_{i,j}(\mathbf{U}), \tag{5.12}$$

via Gaussian quadrature integration, in which

$$\bar{\mathbf{U}}_{i,j} = \frac{1}{A}\int_A \mathbf{U}_{i,j}\mathrm{d}A \tag{5.13}$$

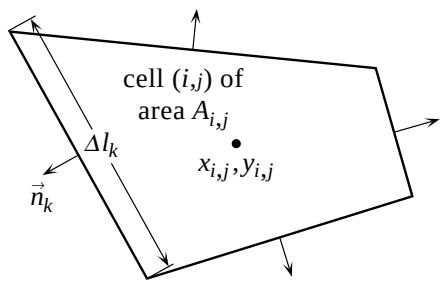

Figure 5.1: Quadrilateral cell for the finite-volume method.

is the cell-averaged value of the conserved solution vector and $\mathbf{R}$ is the physical-time residual vector. The construction of the spatial variation of the conserved solution vector $\mathbf{U}$ within each cell as well as the evaluation of the fluxes $\vec{\mathbf{F}}$ at the cell interfaces, to yield a conservative scheme for the integration of Eq. (5.12) in time, is presented in the following subsections. For solution methods pertaining to two-dimensional cells that include a curved boundary, see the work by Ivan and Groth [124]. Finite-volume methods have an important attribute of preserving the conservation properties of the underlying PDEs discretely for each computational cell and thereby the entire domain, because the flux crossing a boundary into one cell is identical to that leaving the abutting cell via the same boundary, and these fluxes are directly related to the time rate of change of the vector of conserved solution variables $\mathbf{U}$ within each cell.

5.2.1 Slope-Limited, Piecewise-Linear, Least-Squares Reconstruction

The calculation of the inviscid and viscous components of the numerical flux passing through each computational cell requires knowledge of both the solution values as well as their derivatives along the edges of each of these cells. While a first-order accurate, piecewise-constant, cell-averaged solution given by $\bar{\mathbf{U}}_{i,j}$ in Eq. (5.13) can be utilized to provide a very rudimentary estimate of the spatial variation of the solution within a particular cell (i, j), such an approximation is typically not favored for practical application as it tends to yield excessive dissipation via artificial viscosity and may ultimately lead to a loss in the global accuracy of the numerical solution. Alternatively, the progressively more accurate second- and higher-order type of spatial reconstruction often leads to insufficient amounts of dissipation and consequently results in solutions that contain non-monotonic, oscillatory behaviour within discontinuous regions of the flow field. As a result, to ensure solution monotonicity near discontinuities while maintaining higher-order accuracy in smooth regions of the flow field, higher-resolution spatial discretization techniques are often implemented in conjunction with slope limiters that are used to restrict the spatial variations of the solution within each cell to physically realizable and meaningful values. The framework for this class of methods has been developed extensively by researchers such as Boris and Book [125], van Leer [126] and Harten [127], and is described briefly herein.

In the present work, a second-order, slope-limited, piecewise-linear, least-squares solution reconstruction technique is employed to provide a mathematical description of the spatial variation of the solution within each computational cell. Spatial reconstruction in (x, y) for the conserved solution variables $\mathbf{U}$ is then given by

$$\mathbf{U}_{i,j}(x, y) = \bar{\mathbf{U}}_{i,j} + \Phi_{i,j}\left[\left.\frac{\partial \mathbf{U}}{\partial x}\right|_{i,j}(x - x_{i,j}) + \left.\frac{\partial \mathbf{U}}{\partial y}\right|_{i,j}(y - y_{i,j})\right], \tag{5.14}$$

in which the solution is represented as a linear function that is dependent on the two solution derivatives, where location $(x_{i,j}, y_{i,j})$ is the centroid of an arbitrary cell (i, j) in the computational domain. In Eq. (5.14), Φ is the slope limiter and $\partial\mathbf{U}/\partial x$ and $\partial\mathbf{U}/\partial y$ are the gradients of

the conserved solution vector in the x- and y-coordinate directions, respectively. The evaluation of each of these three terms will be discussed in the following paragraphs. Standard midpoint rule quadrature is used to evaluate the solution fluxes through each of the $k = 1, 2, \ldots, 4$ quadrature points along the cell boundary. The reconstruction enables the calculation of $\mathbf{U}_{i,j}^{(k)}$ at the four centers of the quadrilateral edges. These four edge values $\mathbf{U}_{i,j}^{(k)}$ and the corresponding edge values $\mathbf{U}_{i\pm1,j\pm1}^{(k)}$ of the neighbouring, adjacent cells can either agree or differ discontinuously, providing the basis for computing the numerical fluxes across each cell boundary.

Slope limiting is applied during the reconstruction phase to ensure oscillation-free, monotonic solution behaviour near regions of strong gradients and sharp discontinuities within the flow field. In this research, the non-linear slope limiter developed by Venkatakrishnan [128] is employed to provide values in the range of $0 \leq \Phi_{i,j} \leq 1$ for Eq. (5.14). It is given by $\Phi_{i,j} = \min_k \left(\Phi_{i,j}^{(k)}\right)$, in which

$$\Phi_{i,j}^{(k)} = \begin{cases} \min\left(1.0, \frac{\mathbf{U}_{i,j}^{\max} - \bar{\mathbf{U}}_{i,j}}{\mathbf{U}_{i,j}^{(k)} - \bar{\mathbf{U}}_{i,j}}\right) & \text{for} \quad \left(\mathbf{U}_{i,j}^{(k)} - \bar{\mathbf{U}}_{i,j}\right) > 0 \\ \min\left(1.0, \frac{\mathbf{U}_{i,j}^{\min} - \bar{\mathbf{U}}_{i,j}}{\mathbf{U}_{i,j}^{(k)} - \bar{\mathbf{U}}_{i,j}}\right) & \text{for} \quad \left(\mathbf{U}_{i,j}^{(k)} - \bar{\mathbf{U}}_{i,j}\right) < 0 \\ 1.0 & \text{otherwise} \end{cases}, \tag{5.15}$$

wherein $\mathbf{U}_{i,j}^{\max} = \max\left(\bar{\mathbf{U}}_{i,j}, \bar{\mathbf{U}}_{i\pm1,j\pm1}\right)$ and $\mathbf{U}_{i,j}^{\min} = \min\left(\bar{\mathbf{U}}_{i,j}, \bar{\mathbf{U}}_{i\pm1,j\pm1}\right)$, where $\bar{\mathbf{U}}_{i\pm1,j\pm1}$ are the neighbouring, adjacent, cell-averaged conserved solution vectors that are used in the second-order reconstruction of $\mathbf{U}_{i,j}$, and $\mathbf{U}_{i,j}^{(k)}$ is the unlimited, second-order accurate, piecewise-linear, reconstructed solution (with $\Phi_{i,j}^{(k)} = 1$) at the respective quadrature point k along the boundary of cell (i, j). The spatial reconstruction of Eqs. (5.14) and (5.15) recovers the unlimited, second-order accurate, piecewise-linear solution when $\Phi_{i,j} = 1$ in smooth regions of the flow field and degrades to the fully limited, first-order accurate, piecewise-constant, cell-average solution when $\Phi_{i,j} = 0$, wherever discontinuities exist.

The spatial gradients of the conserved solution vector, $\partial\mathbf{U}/\partial x$ and $\partial\mathbf{U}/\partial y$, used in the second-order reconstruction via Eq. (5.14) are determined by applying a least-squares approach [129]. The least-squares problem can by solved to approximate the solution gradients of a given cell (i, j) by considering its N_c neighbouring cells, with $N_c = 8$ in two dimensions, and minimizing the error, $\mathcal{E}$, that is defined by

$$\mathcal{E}^2 = \sum_{n=1}^{N_c} \mathcal{E}_n^2 = \sum_{n=1}^{N_c} \left[\Delta\bar{\mathbf{U}}_n - \left(\left.\frac{\partial\mathbf{U}}{\partial x}\right|_{i,j}(x_n - x_{i,j}) + \left.\frac{\partial\mathbf{U}}{\partial y}\right|_{i,j}(y_n - y_{i,j})\right)\right]^2, \tag{5.16}$$

where $\Delta\bar{\mathbf{U}}_n = \bar{\mathbf{U}}_n - \bar{\mathbf{U}}_{i,j}$ for $\bar{\mathbf{U}}_n$ taken as the cell-averaged value of the conserved solution vector of a neighbouring cell n. The resulting system of equations arising from the differentiation of Eq. (5.16) and subsequent minimization of the error $\mathcal{E}$ is expressed in matrix form as

$$\begin{bmatrix} \overline{(\Delta x)_{i,j}^2} & \overline{(\Delta x \Delta y)_{i,j}} \\ \overline{(\Delta x \Delta y)_{i,j}} & \overline{(\Delta y)_{i,j}^2} \end{bmatrix} \begin{bmatrix} \left.\frac{\partial\bar{\mathbf{U}}}{\partial x}\right|_{i,j} \\ \left.\frac{\partial\bar{\mathbf{U}}}{\partial y}\right|_{i,j} \end{bmatrix} = \begin{bmatrix} \overline{(\Delta\mathbf{U}\Delta x)_{i,j}} \\ \overline{(\Delta\mathbf{U}\Delta y)_{i,j}} \end{bmatrix}, \tag{5.17}$$

where

$$\overline{(\Delta x)^2_{i,j}} = \frac{1}{N_c}\sum_{n=1}^{N_c}(x_n - x_{i,j})^2\,, \tag{5.18}$$

$$\overline{(\Delta x \Delta y)_{i,j}} = \frac{1}{N_c}\sum_{n=1}^{N_c}(x_n - x_{i,j})(y_n - y_{i,j})\,, \tag{5.19}$$

$$\overline{(\Delta y)^2_{i,j}} = \frac{1}{N_c}\sum_{n=1}^{N_c}(y_n - y_{i,j})^2\,, \tag{5.20}$$

$$\overline{(\Delta \mathbf{U} \Delta x)_{i,j}} = \frac{1}{N_c}\sum_{n=1}^{N_c}\Delta\bar{\mathbf{U}}_n(x_n - x_{i,j})\,, \tag{5.21}$$

$$\overline{(\Delta \mathbf{U} \Delta y)_{i,j}} = \frac{1}{N_c}\sum_{n=1}^{N_c}\Delta\bar{\mathbf{U}}_n(y_n - y_{i,j})\,. \tag{5.22}$$

The solution of the system of equations given by Eq. (5.17) can be obtained by using Cramer's rule to yield the solution derivatives

$$\left.\frac{\partial \mathbf{U}}{\partial x}\right|_{i,j} = \frac{\overline{(\Delta \mathbf{U}\Delta x)_{i,j}}\;\overline{(\Delta y)^2_{i,j}} - \overline{(\Delta x \Delta y)_{i,j}}\;\overline{(\Delta \mathbf{U}\Delta y)_{i,j}}}{\overline{(\Delta x)^2_{i,j}}\;\overline{(\Delta y)^2_{i,j}} - \left[\overline{(\Delta x \Delta y)_{i,j}}\right]^2}, \tag{5.23}$$

$$\left.\frac{\partial \mathbf{U}}{\partial y}\right|_{i,j} = \frac{\overline{(\Delta \mathbf{U}\Delta y)_{i,j}}\;\overline{(\Delta x)^2_{i,j}} - \overline{(\Delta x \Delta y)_{i,j}}\;\overline{(\Delta \mathbf{U}\Delta x)_{i,j}}}{\overline{(\Delta x)^2_{i,j}}\;\overline{(\Delta y)^2_{i,j}} - \left[\overline{(\Delta x \Delta y)_{i,j}}\right]^2}, \tag{5.24}$$

thereby facilitating the second-order accurate, piecewise-linear solution reconstruction technique utilized in this research.

5.2.2 Inviscid (Hyperbolic) Flux Evaluation

The inviscid or hyperbolic components $\mathbf{F}$ and $\mathbf{G}$ of the flux $\vec{\mathbf{F}}$ at each cell interface represent the net rate of solution flux of the conserved solution quantities between neighbouring computational cells in the x- and y-coordinate directions, respectively. For any two adjacent cells, each with a given solution state $\mathbf{U}$, there may exist a discontinuity in the solution state amongst the left- and right-hand sides of the intercellular boundary, i.e. between $\mathbf{U}_\mathrm{L}$ and $\mathbf{U}_\mathrm{R}$, separating these two adjoining cells. For example, in a two-dimensional computational domain composed of quadrilateral cells, the left and right solution states could be $\mathbf{U}_\mathrm{L} = \bar{\mathbf{U}}_{i,j}$ and $\mathbf{U}_\mathrm{R} = \bar{\mathbf{U}}_{i+1,j}$ for neighbouring cells (i,j) and $(i+1,j)$ in the x-coordinate direction, following solution reconstruction. The evaluation of the inviscid component of the flux at a particular Gauss quadrature point along the cellular interface $\left(i+\frac{1}{2},j\right)$ is hence

$$\vec{\mathbf{F}}_{i+1/2,j}\cdot\vec{n}_{i+1/2,j} = \hat{\mathbf{F}}\left(\mathbf{U}_\mathrm{L}, \mathbf{U}_\mathrm{R}, \vec{n}_{i+1/2,j}\right), \tag{5.25}$$

where $\hat{\mathbf{F}}$ is the inviscid component of the intercellular numerical flux in the x-coordinate direction that results from the solution to the Riemann problem. Along the boundaries of cell (i,j)

that are given as remaining combinations of $\left(i \pm \frac{1}{2}, j \pm \frac{1}{2}\right)$, analogous formulations apply in the x- and y-coordinate directions.

For a polytropic gas, the Riemann problem may either be solved exactly, as described in the paper by Gottlieb and Groth [130], or alternatively using approximate methods, such as those developed by Roe [131]; Harten, Lax and van Leer [132]; Einfeldt [133]; Toro, Spruce and Speares [134]; Liou [135] and Linde [136], amongst others. In this research, the inviscid component of the numerical flux at the cell interfaces is evaluated using the approximate Riemann solver of Harten, Lax and van Leer [132] with contributions by Einfeldt [133]. For a simplified, one-dimensional computational domain that is aligned with the x-coordinate direction and whose discontinuous, two-state initial data is prescribed by

$$\mathbf{U}(x, t=0) = \begin{cases} \mathbf{U}_{\mathrm{L}} & \text{for} \quad x < 0 \\ \mathbf{U}_{\mathrm{R}} & \text{for} \quad x \geq 0 \end{cases}, \tag{5.26}$$

the self-similar solution $\mathbf{U}$ in the physical plane for all time $t > 0$ is taken to have the form

$$\mathbf{U}\left(\tfrac{x}{t} = 0\right) = \begin{cases} \mathbf{U}_{\mathrm{L}} & \text{for} \quad \frac{x}{t} \leq \lambda^{-} \\ \mathbf{U}_{\star} & \text{for} \quad \lambda^{-} < \frac{x}{t} < \lambda^{+} \\ \mathbf{U}_{\mathrm{R}} & \text{for} \quad \frac{x}{t} \geq \lambda^{+} \end{cases}, \tag{5.27}$$

where the corresponding inviscid component $\hat{\mathbf{F}}$ of the intercellular numerical flux is given by

$$\hat{\mathbf{F}}\left(\mathbf{U}_{\mathrm{L}}, \mathbf{U}_{\mathrm{R}}, \tfrac{x}{t} = 0\right) = \begin{cases} \mathbf{F}_{\mathrm{L}} & \text{for} \quad \frac{x}{t} \leq \lambda^{-} \\ \mathbf{F}_{\star} & \text{for} \quad \lambda^{-} < \frac{x}{t} < \lambda^{+} \\ \mathbf{F}_{\mathrm{R}} & \text{for} \quad \frac{x}{t} \geq \lambda^{+} \end{cases}, \tag{5.28}$$

in which $\mathbf{F}_{\mathrm{L}} = \mathbf{F}\left(\mathbf{U}_{\mathrm{L}}\right)$ and $\mathbf{F}_{\mathrm{R}} = \mathbf{F}\left(\mathbf{U}_{\mathrm{R}}\right)$. In Eq. (5.27), the intermediate solution state $\mathbf{U}_{\star}$ is given by

$$\mathbf{U}_{\star} = \frac{\lambda^{+}\mathbf{U}_{\mathrm{R}} - \lambda^{-}\mathbf{U}_{\mathrm{L}}}{\lambda^{+} - \lambda^{-}} - \frac{\mathbf{F}_{\mathrm{R}} - \mathbf{F}_{\mathrm{L}}}{\lambda^{+} - \lambda^{-}}, \tag{5.29}$$

while, in Eq. (5.28), the corresponding intermediary flux $\mathbf{F}_{\star}$ is determined using

$$\mathbf{F}_{\star} = \frac{\lambda^{+}\mathbf{F}_{\mathrm{L}} - \lambda^{-}\mathbf{F}_{\mathrm{R}}}{\lambda^{+} - \lambda^{-}} + \frac{\lambda^{+}\lambda^{-}}{\lambda^{+} - \lambda^{-}}\left(\mathbf{U}_{\mathrm{R}} - \mathbf{U}_{\mathrm{L}}\right). \tag{5.30}$$

The selection criteria residing within Eqs. (5.27) and (5.28) for choosing the appropriate conserved solution state and corresponding inviscid component of the numerical flux are based upon the magnitudes of the rightward- and leftward-moving characteristic signal speeds, denoted by λ^{+} and λ^{-}, respectively. In Eqs. (5.27) through (5.30), these finite acoustic modes are

$$\lambda^{+} = \max\left(\lambda_{\mathrm{R}}^{\max}, \hat{\lambda}^{\max}\right) = \max\left(u_{\mathrm{R}} + a_{\mathrm{R}}, \hat{u} + \hat{a}\right), \tag{5.31}$$

$$\lambda^{-} = \min\left(\lambda_{\mathrm{L}}^{\min}, \hat{\lambda}^{\min}\right) = \min\left(u_{\mathrm{L}} - a_{\mathrm{L}}, \hat{u} - \hat{a}\right), \tag{5.32}$$

wherein the flow variables indicated by overhats denote Roe-averaged quantities. Within this context, for an arbitrary solution variable denoted by ω, the corresponding Roe-averaged quantity $\hat{\omega}$ is calculated according to a mass-weighting of the left and right states as

$$\hat{\omega} = \frac{\omega_{\mathrm{L}}\sqrt{\rho_{\mathrm{L}}} + \omega_{\mathrm{R}}\sqrt{\rho_{\mathrm{R}}}}{\sqrt{\rho_{\mathrm{L}}} + \sqrt{\rho_{\mathrm{R}}}} \,. \tag{5.33}$$

The exceptions to this rule include the Roe-averaged density, which is calculated via $\hat{\rho} = \sqrt{\rho_{\mathrm{L}}\rho_{\mathrm{R}}}$, and the Roe-averaged sound speed, which is computed according to $\hat{a} = \sqrt{\gamma\hat{p}/\hat{\rho}}$. With knowledge of the correct characteristic wave speeds with which information in the computational domain propagates, the evaluation of the inviscid component of the numerical flux can be readily calculated by means of the aforementioned approximate Riemann solver, with straightforward extension to two spatial dimensions for the applications presented herein.

5.2.3 Viscous (Elliptic) Flux Evaluation

The viscous or elliptic components $\mathbf{F_v}$ and $\mathbf{G_v}$ of the flux $\vec{\mathbf{F}}$ at each cell interface represent the net rate of diffusion of the conserved solution quantities between neighbouring cells in the x- and y-coordinate directions, respectively. However, unlike the inviscid counterpart, the viscous component of the numerical flux depends not only on the solution state $\mathbf{U}$ that exists on the left- and right-hand sides of a given cell boundary of interest, but also depends on the solution gradients $\vec{\nabla}\mathbf{U}$ that arise along either side of the cell interface. The evaluation of the viscous component of the flux at a particular Gauss quadrature point along the cellular interface $\left(i+\frac{1}{2}, j\right)$ between neighbouring cells (i, j) and $(i+1, j)$ in the x-coordinate direction is hence

$$\vec{\mathbf{F}}_{i+1/2,j} \cdot \vec{n}_{i+1/2,j} = \hat{\mathbf{F}}_{\mathbf{v}}\left(\mathbf{U}_{\mathrm{M}}, \vec{\nabla}\mathbf{U}_{\mathrm{M}}\right), \tag{5.34}$$

where $\hat{\mathbf{F}}_{\mathbf{v}}$ is the viscous component of the intercellular numerical flux in the x-coordinate direction and $\mathbf{U}_{\mathrm{M}} = \left(\mathbf{U}_{\mathrm{L}} + \mathbf{U}_{\mathrm{R}}\right)/2$ and $\vec{\nabla}\mathbf{U}_{\mathrm{M}} = \left(\vec{\nabla}\mathbf{U}_{\mathrm{L}} + \vec{\nabla}\mathbf{U}_{\mathrm{R}}\right)/2$ are two arithmetic means for the reconstructed solution state and its corresponding gradients, respectively. Numerical quadrature is performed in an analogous manner over the remaining cell faces of cell (i, j), that are given as combinations of $\left(i \pm \frac{1}{2}, j \pm \frac{1}{2}\right)$, to yield the desired viscous fluxes through each cell boundary. To avoid instabilities associated with even/odd decoupling and disjoint solution states amongst adjacent computational cells, a central scheme using the diamond-path reconstruction technique of Coirier and Powell [137] is applied.

5.2.4 Explicit Time Marching via Second-Order Runge-Kutta Method

Following the discretization of the spatial derivatives, a second-order, predictor-corrector time-marching method is utilized to effectively integrate the semi-discrete form given by Eq. (5.12) in time and thereby obtain temporally accurate solutions to most of the unsteady flow problems

studied in this research (both inviscid and viscous). For the explicit, second-order accurate Runge-Kutta (RK2) method, the advancement of the solution state $\mathbf{U}$ from an initial time level n to that of a subsequent time level $(n+1)$ is performed through a temporary, intermediate stage given by time level $(n+\frac{1}{2})$. In predictor-corrector form, this temporal evolution of $\mathbf{U}$ from $\mathbf{U}^{(n)}$ to $\mathbf{U}^{(n+1)}$ is written for quadrilateral cell (i,j) as

$$\mathbf{U}_{i,j}^{(n+1/2)} = \mathbf{U}_{i,j}^{(n)} - \frac{\Delta t}{A_{i,j}} \sum_{k=1}^{4} \left(\vec{\mathbf{F}} \cdot \vec{n}\, \Delta l \right)_{i,j,k}^{(n)}, \tag{5.35}$$

$$\mathbf{U}_{i,j}^{(n+1)} = \mathbf{U}_{i,j}^{(n)} - \frac{1}{2} \frac{\Delta t}{A_{i,j}} \sum_{k=1}^{4} \left(\vec{\mathbf{F}} \cdot \vec{n}\, \Delta l \right)_{i,j,k}^{(n+1/2)}. \tag{5.36}$$

In Eqs. (5.35) and (5.36), the inviscid components $\hat{\mathbf{F}}$ and $\hat{\mathbf{G}}$ of the intercellular numerical flux arise from the method described in Section 5.2.2, whereas the viscous components $\hat{\mathbf{F}}_{\mathbf{v}}$ and $\hat{\mathbf{G}}_{\mathbf{v}}$ of the intercellular numerical flux arise from the method described in Section 5.2.3. The physical time step Δt in Eqs. (5.35) and (5.36) for advancing viscous flow-field solutions in time throughout all cells simultaneously is set by considering both the inviscid Courant-Friedrichs-Lewy (CFL) stability condition as well as the viscous von Neumann stability criterion:

$$\Delta t = n_t \cdot \min \left[\frac{\Delta l}{(|\vec{u}| + a)_{\max}}, \frac{\rho \Delta l^2}{\eta} \right], \tag{5.37}$$

computed in each coordinate direction (see the book by Lomax, Pulliam and Zingg [138]). For solutions to the Euler equations, the latter stability criterion is omitted. In Eq. (5.37), the constant $n_t = 0.60$ in this study, relating to the stability contour of the RK2 time-marching method, the velocity magnitude $|\vec{u}| = \sqrt{u^2 + v^2}$, the sound speed $a = \sqrt{\gamma p/\rho}$ and minimum and maximum values are obtained from a global search through all cells within the computational domain. This method considers a continuous, time-dependent path towards completion and is terminated once the physical time measure at time level n reaches the desired solution time.

5.2.5 Implicit Time Marching and Newton's Method

A fully implicit Newton-Krylov-Schwarz (NKS) iterative solution method, as developed by Groth and Northrup [119–121], is also considered herein to reliably and efficiently integrate the semi-discrete form of the system of the conservation equations given by Eq. (5.12). This implicit method is particularly well-suited for obtaining highly resolved numerical solutions for cases in which the stability limits of an explicit time-marching method would likely result in severe limitations on the maximum allowable physical time step, as dictated by the smallest cells in the mesh. While the explicit time marching scheme described above was found to be sufficient in most cases, when used in combination with an anisotropic adaptive mesh refinement gridding technique, the implicit iterative scheme has been shown to provide significant computational savings for the calculation of steady shock and fully resolved oblique shock reflection problems (see the paper by Hryniewicki, Groth and Gottlieb [122] for details).

Solution of the Steady-State Problem via Newton's Method

Steady-state solutions of Eq. (5.12) satisfy

$$\mathbf{R}(\mathbf{U}) = \frac{\mathrm{d}\mathbf{U}}{\mathrm{d}t} = 0, \tag{5.38}$$

the solution of which requires the solution of a large, coupled, non-linear system of algebraic equations. Newton's method is used here to determine the solution of Eq. (5.38). Starting with an initial estimate, $\mathbf{U}^{(0)}$, successively improved estimates of the solution at each iteration level, m, of Newton's method can be obtained by solving the linear system

$$\left(\frac{\partial \mathbf{R}}{\partial \mathbf{U}}\right)^{(m)} \Delta\mathbf{U}^{(m)} = \mathbf{J}^{(m)}\Delta\mathbf{U}^{(m)} = -\mathbf{R}(\mathbf{U}^{(m)}) \tag{5.39}$$

where $\mathbf{J} = \partial\mathbf{R}/\partial\mathbf{U}$ is the Jacobian of the residual vector with respect to the conserved solution vector. Improved approximations of the solution are then given by

$$\mathbf{U}^{(m+1)} = \mathbf{U}^{(m)} + \Delta\mathbf{U}^{(m)}, \tag{5.40}$$

and the iterative procedure is repeated until a desired reduction in an appropriate norm of the solution residual vector is achieved, that is, until $||\mathbf{R}(\mathbf{U}^{(m)})||_2 < \epsilon||\mathbf{R}(\mathbf{U}^{(0)})||_2$, where ϵ is some small convergence tolerance typically in the range of $\epsilon \approx 10^{-7}-10^{-5}$ for the steady-state computations presented herein.

Each iteration level in Newton's method requires the solution of a large, sparse, and non-symmetric system of linear equations given by Eq. (5.39). This system is of the general form $\mathbf{Jx} = \mathbf{b}$, where $\mathbf{x}$ and $\mathbf{b}$ designate the solution and residual vectors, respectively. To solve for such non-symmetric linear systems, the present algorithm employs a class of Krylov subspace iterative methods known as generalized minimum residual (GMRES) methods [139] with an additive Schwarz global preconditioner. The application of the GMRES method within Newton's method results in an overall solution algorithm that consists of a nested iterative procedure: inner-loop iterations to determine a solution of the linear system at each Newton step using the GMRES method and outer-loop iterations to solve the non-linear problem using Newton's method. For improved performance, an inexact Newton method is adopted wherein the GMRES method is only partially converged at each iteration level of Newton's method, i.e. the inner-loop iterations are deemed complete when $||\mathbf{R}^{(m)} + \mathbf{J}^{(m)}\Delta\mathbf{U}^{(m)}||_2 \leq \zeta||\mathbf{R}^{(m)}||_2$, where ζ is some small convergence tolerance (typically, $\zeta \approx 0.01-0.5$ herein).

Dual-Time-Stepping-Like Approach for Time-Accurate Computations

For the high-resolution solution of time-dependent or unsteady problems, such as those encountered in the study of viscous oblique shock reflections with fully resolved internal shock

structures, the aforementioned implicit NKS method can be extended by adopting a dual-time-stepping-like procedure [121, 140]. In the implicit dual-time-stepping method, a pseudo time, τ, and pseudo time derivative of $\mathbf{U}$ are introduced, resulting in a modified semi-discrete form of the governing equations given by

$$\frac{\mathrm{d}\mathbf{U}}{\mathrm{d}\tau} + \mathbf{R}^*(\mathbf{U}) = 0, \tag{5.41}$$

where the vector $\mathbf{R}^*(\mathbf{U})$ is the dual-time residual given by

$$\mathbf{R}^*(\mathbf{U}) = \frac{\mathrm{d}\mathbf{U}}{\mathrm{d}t} + \mathbf{R}(\mathbf{U}). \tag{5.42}$$

Steady state solutions in pseudo time of Eq. (5.41) are sought by applying an unconditionally stable implicit second-order backward differencing formula (BDF2) to the temporal discretization of the physical time derivative, yielding

$$\mathbf{R}^*(\mathbf{U}^{(n+1)}) = \frac{3\mathbf{U}^{(n+1)} - 4\mathbf{U}^{(n)} + \mathbf{U}^{(n-1)}}{2\Delta t} + \mathbf{R}(\mathbf{U}^{(n+1)}) = 0. \tag{5.43}$$

Although numerous time-marching schemes are compatible for use in a dual-time stepping approach, the BDF2 exhibits favorable stability properties [140] and has been used quite successfully to facilitate computations for a variety of practical flow applications, such as those studied by Northrup and Groth [120, 121], Isono and Zingg [141], as well as Tabesh and Zingg [142].

For the unsteady case, solution of the modified non-linear system of algebraic equations given by Eq. (5.43) is again obtained via Newton's method and requires the solution of the following linear system of equations at each Newton step:

$$\left[\left(\frac{3}{2\Delta t}\right)\mathbf{I} + \left(\frac{\partial \mathbf{R}}{\partial \mathbf{U}}\right)^{(n+1,m)}\right]\Delta\mathbf{U}^{(n+1,m)} = \mathbf{J}^*\Delta\mathbf{U}^{(n+1,m)} = -\mathbf{R}^*(\mathbf{U}^{(n+1,m)}), \tag{5.44}$$

Here, $\Delta\mathbf{U}^{(n+1,m)}$ is the m^{th} Newton estimate for the solution change at physical time level n. Successively improved estimates for the solution in physical time are given by

$$\mathbf{U}^{(n+1,m)} = \mathbf{U}^{(n)} + \Delta\mathbf{U}^{(n+1,m)}. \tag{5.45}$$

In Eq. (5.44), $\mathbf{I}$ denotes the identity matrix and $\mathbf{J}^* = \partial\mathbf{R}^*/\partial\mathbf{U}$ is the Jacobian of the modified residual vector. The physical time step, Δt, is determined via Eq. (5.37), as per the explicit case. In the dual-time-stepping approach, the iterative procedure is repeated until $||\mathbf{R}^*(\mathbf{U}^{(n+1,m)})||_2 < \epsilon||\mathbf{R}^*(\mathbf{U}^{(n)})||_2$, where a value of $\epsilon \approx 10^{-3}$–10^{-2} was found sufficient for the high-resolution, time-accurate computations presented herein.

5.3 Anisotropic Block-Based Adaptive Mesh Refinement

The spatial discretization of the partial differential equations is implemented on a computational grid that subdivides the physical domain into a finite representation of geometric cells. To

achieve the desired level of solution accuracy for a given numerical scheme, a minimum spatial resolution is required to capture pertinent features of the flow field with sufficient detail and precision. While a uniformly dense grid tessellation is a simple strategy to meet this demand, it is inefficient computationally and inherently over-resolves localized regions of homogeneity within a complex flow field.

Block-based AMR methods have been developed previously using both Cartesian and body-fitted, multi-block meshes for fluid flows involving a wide variety of complicated physical and chemical phenomena, as well as complex flow geometries, by Berger and co-researchers [143–145], De Zeeuw and Powell [146], Powell, Roe and Quirk [147], Quirk and Hanebutte [148], as well as Groth and co-researchers [149–154], amongst others. Despite the success of this previous research, one major limitation of these isotropic AMR gridding strategies has been the accurate and efficient treatment of multi-scale anisotropic physics. Recently, Zhang and Groth [116] proposed a treatment that addresses this important challenge by considering a parallel anisotropic block-based AMR method for solutions of a model linear advection-diffusion equation as well as the fully non-linear Euler equations governing two-dimensional, compressible, inviscid, gaseous flows. This work was shortly thereafter extended to applications in three-dimensions by Williamschen and Groth [117] and Freret and Groth [118].

Solution of the coupled non-linear ODEs given by Eq. (5.12) yields area-averaged solution quantities defined within quadrilateral computational cells. In the multi-block AMR scheme, these cells are embedded in structured, body-fitted grid blocks and a flexible block-based hierarchical binary tree data structure is used to facilitate automatic and local solution-directed mesh adaptation of the individual grid blocks. The refinement procedure can be performed independently in each of the ξ and ζ local computational coordinate directions for the body-fitted grid block or domain of interest when dealing with strong anisotropic flow features. In regions requiring increased mesh resolution, a single parent block can be partitioned into two children blocks, with each new child block having the same number of cells as its parent block. The resolution in the coordinate direction of refinement is thereby doubled, while remaining unchanged in the other direction. Conversely, coarsening takes place by combining two children blocks into one parent block. This process is elucidated in Fig. 5.2, where the advantages of anisotropic AMR become apparent, in comparison to a traditional isotropic AMR approach, for dealing with flows exhibiting large solution gradients in one direction but not in the other. To ensure a smooth variation in the overall solution, refinement ratios are limited to 2:1 between adjacent grid blocks and the minimum resolution of the computational domain is limited to that of the initial, i.e. coarsest, mesh.

At regular intervals during the computation, the coarsening and/or refinement of blocks within the flow field is directed using multiple physics-based refinement criteria. User-defined percentage thresholds are specified to refine blocks with criteria above the refinement threshold and to coarsen blocks with criteria below the coarsening threshold. This technique is

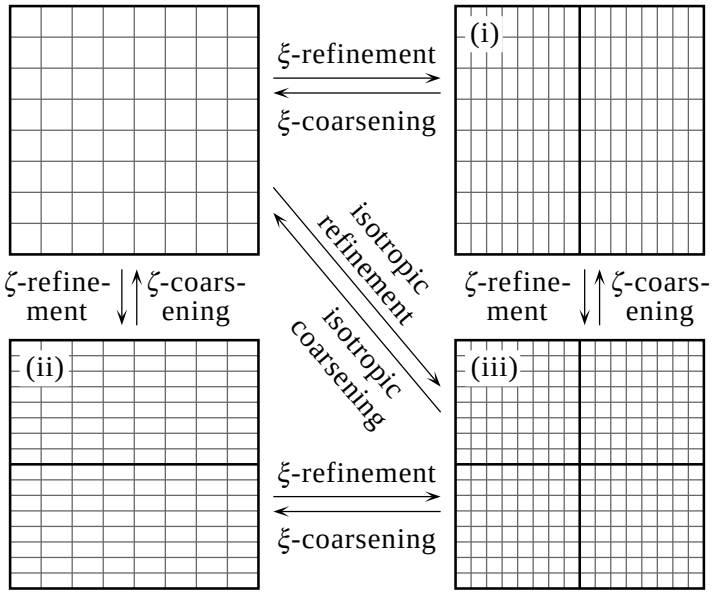

Figure 5.2: Refinement and coarsening of an 8×8 cell block during (i) anisotropic AMR in the ξ-direction, (ii) anisotropic AMR in the ζ-direction and (iii) isotropic AMR.

implemented to treat flows with disparate spatial and temporal scales and to properly detect important flow features such as shock fronts, triple-shock confluence and reflection points, contact surfaces, as well as both thermal and viscous boundary and shear layers, whilst limiting the number of necessary computational cells required to accurately resolve these complex flow configurations. For any given solution variable of interest, u, the direction-dependent refinement criteria for anisotropic AMR are based on the measures

$$\varepsilon_\xi = \vec{\nabla} u \cdot \Delta\tilde{\mathbf{X}}/|u| \qquad \text{and} \qquad \varepsilon_\zeta = \vec{\nabla} u \cdot \Delta\tilde{\mathbf{Y}}/|u|, \tag{5.46}$$

where $\Delta\tilde{\mathbf{X}}$ and $\Delta\tilde{\mathbf{Y}}$ are the vector differences between the mid-points of the cell faces in each of the logical coordinate directions. These indicators provide a representative measure of the total solution change across individual cells in each coordinate direction and regulate mesh adaptation in regions containing strong anisotropic characteristics of the flow. In this research, the direction-dependent refinement for anisotropic AMR is performed once every six time steps and is specified using both the gradient of density as well as the gradient of flow velocity.

The benefits and capabilities of dynamic mesh adaptation via anisotropic AMR with n_r levels of refinement is demonstrated in Fig. 5.3. The initial mesh at time zero consists of only two grid blocks depicted in Fig. 5.3(a), and each grid block consists of a set of 8-by-8 cells that are not displayed. The shock discontinuity is shown as a dashed line in the first block. Before the flow-field computations begin, anisotropic AMR is implemented to refine the grid blocks around the shock discontinuity, and these results are shown in Fig. 5.3(b). During the computations the shock-on-wedge flow field evolves with time, and so does the mesh, tracking and helping to accurately define all complicated features of the flow field. Grid blocks are illustrated at early

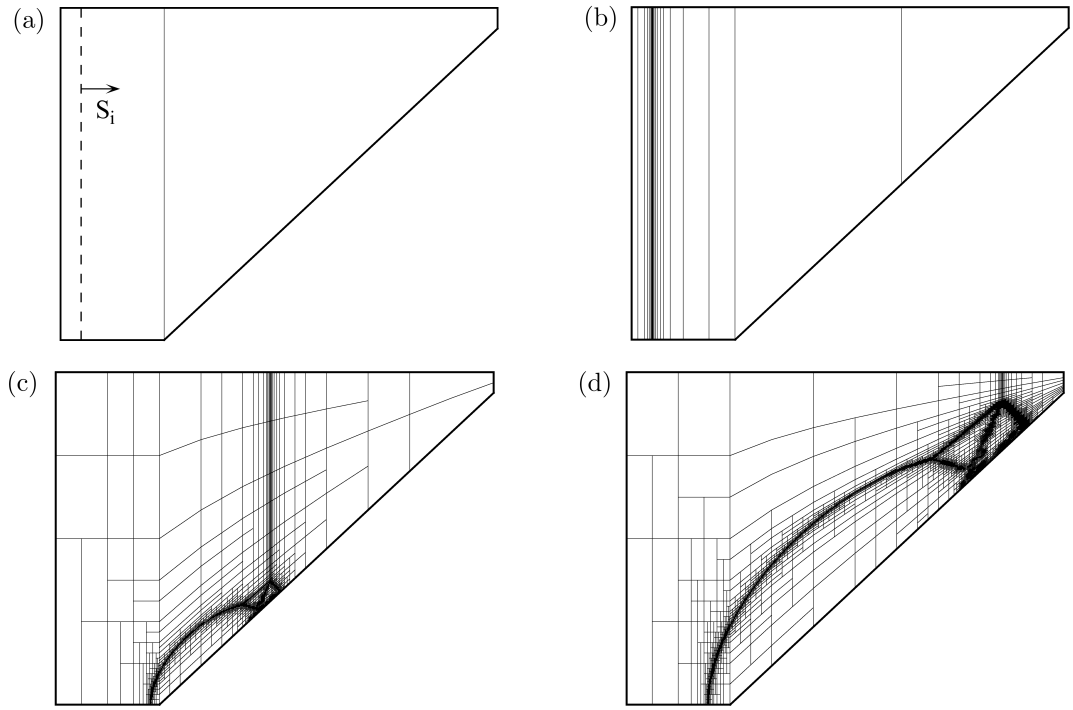

Figure 5.3: Grid blocks at various stages of a DMR simulation in air ($M_i = 4.0$, $\theta_w = 43.0°$, $n_r = 10$): (a) solution initialization, (b) initial anisotropic AMR application, (c) early interaction of incident shock with a wedge, and (d) late interaction.

and late times in Figs. 5.3(c) and 5.3(d), respectively. These four mesh snapshots correspond to the DMR flow-field configuration computed and shown earlier in Fig. 1.1(d).

A square grid block with equal side lengths Δl and 8-by-8 interior cells features initial cell side lengths of $2^{-3}\Delta l$. For n_r levels of refinement, the smallest cell side length is reduced to $2^{-n_r-3}\Delta l$. For $n_r = 10$, this corresponds to the smallest cell side length of $1.22\times10^{-4}\Delta l$ and a refinement factor 2^{n_r} given by 1024. The number of refinement levels is specified at the beginning of each CFD flow-field simulation, and n_r varies from 10 to 13 in this study for unsteady shock-wave interactions with rigid wedges in inviscid and polytropic gases to generate mesh-independent flow-field simulations with a high spatial resolution. At this specified level of refinement, upwards of 2×10^4 grid blocks (or approximately 1.28×10^6 computational cells) exist within the computed flow fields upon completion of the CFD flow-field simulations.

5.4 Parallel Implementation

The CFD solution technique used herein lends itself naturally to parallelization via block-based domain decomposition, implemented with the C++ programming language as well as the Message Passing Interface (MPI) library. The self-similar solution blocks are distributed

amongst awaiting available processors within a multi-processor architecture, with more than one block permitted on each processor core. For homogeneous multi-processor architectures, the self-similar solution blocks are distributed and treated equally amongst the processors; for heterogeneous systems, a weighted distribution of the blocks is adopted to allocate more blocks to faster processors and fewer blocks to slower ones. A Morton ordering algorithm is used to place neighbouring grid blocks on the same processor in an effort to mitigate interprocessor communication and ensure efficient load balancing throughout the system [155]. In this research, the simulations were performed on a large-scale, high-performance IBM System x iDataPlex dx360 M2 computational cluster, built using 3780 nodes in total with two quad-core 2.53 GHz Intel Xeon E5540 Nehalem x86-64 processors and 16 GB of main memory per node. A highly scalable and efficient algorithm results.

5.5 Computational Domain, Boundary and Initial Conditions

The computational domain, boundaries, dimensions, and initial conditions ahead of the incident shock wave in region (1), are documented in Fig. 5.4. The flow properties behind the incident shock in region (2) are obtained by using the Rankine-Hugoniot jump conditions given by Eqs. (3.4) through (3.7). The wedge length of 1.2 m was selected so the incident shock could interact and move along the wedge a distance of 1.0 m for all computed flow-field simulations with incident shock Mach numbers M_{i} ranging from 1.0 to 4.0. The 1.0 m height and horizontal pre-wedge distances ensured that the reflected wave would not reach the upper and left boundaries during all CFD flow-field simulations.

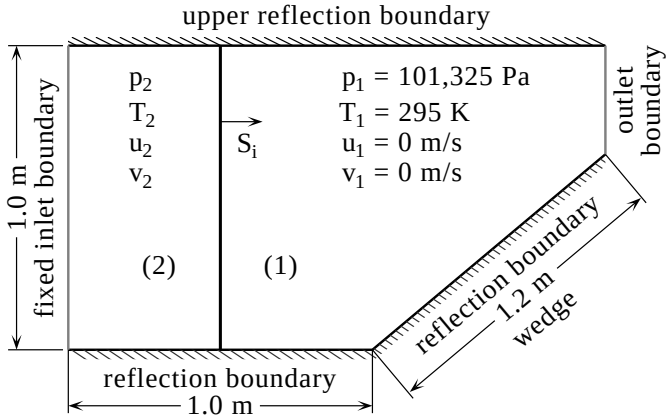

Figure 5.4: Initial and boundary conditions for the numerical simulation of unsteady shock-wave reflections from a wedge.

Chapter 6

Algorithm Verification and Validation

Prior to carrying out the oblique shock-wave reflection simulations presented in Chapters 7 and 9 for the determination of the numerical transition boundary separating regular and Mach reflections, an investigation was performed to first verify and validate some aspects of solutions of the parallel, anisotropic, block-based AMR, finite-volume scheme. The validity of the numerical solutions was assessed for several flow problems involving shocks. The solutions and mesh resolution requirements for the prediction of steady one-dimensional planar shock structure in a viscous gas was first investigated. Specifically, resolution requirements for mesh-independent predictions of steady shock structure obtained using the CFD solution method were explored via comparison to one-dimensional ODE solutions (see Chapter 4). Additionally, a direct comparison of anisotropic and isotropic block-based AMR strategies was made for oblique shock-wave reflections with under-resolved internal shock structures, in an effort to forecast the anticipated computational savings of the anisotropic AMR approach when applied to a fully resolved case. The predictive capabilities of the numerical solution method were also assessed for a range of oblique shock-wave reflection problems considered in other previous studies. In particular, the present numerical predictions were compared to the experimental results of Henderson and Gray [156] for the diffraction of strong incident shock waves over rigid concave corners. Lastly, to demonstrate the efficacy of the CFD algorithm, a fully resolved simulation of a single-Mach reflection configuration was considered. The latter provides evidence of the validity of the numerical framework in the prediction of unsteady oblique shock-wave reflection processes of interest in this research.

6.1 Mesh Resolution Study for Shock-Front Structure

In order to establish the resolution requirements of the numerical solution method for the prediction of fully resolved shock waves, a mesh resolution study was conducted in which the parallel, implicit, finite-volume scheme with anisotropic AMR was applied to the prediction of one-dimensional stationary shock structure where the working gas was molecular nitrogen (N_2). The predictions of the finite-volume scheme were compared to several ODE results for shock-front transitions (see Chapter 4). Such comparisons provide a useful validation of the high-resolution CFD solution method in terms of its ability to compute accurate and highly resolved internal structures of shock fronts.

Stationary solutions for a shock wave in molecular nitrogen with a shock Mach number of $M_{\rm i} = 1.95$ were considered. A simple rectangular domain made up of two adjacent square blocks with 0.1 m side lengths was used in which the initial mesh was composed of 10×10 cell blocks. The shock jump conditions were imposed as initial data and supersonic inflow boundary conditions and subsonic outflow boundary conditions were enforced at the upstream and downstream boundaries, respectively, so as ensure that the shock remains centered indefinitely within the computational domain. The implicit NKS method described in Subsection 5.2.5 for steady flows was used to quickly and efficiently converge the solution of this problem to steady-state. Smoothing of the solution on the coarse initial mesh was achieved by performing 10 steps of an explicit multi-stage time-marching scheme with optimal smoothing, at which point a steady-state solution was computed directly on the same mesh by using the NKS method with limiter-freezing enabled to assist in solution convergence. Once the solution on the initial grid was fully converged to steady-state, the process was repeated following the application of a single level of anisotropic AMR. This process was then successively repeated until additional levels of mesh refinement ceased to affect the variation of flow properties through the shock front. The refinement and coarsening thresholds for the anisotropic mesh adaptation were set to values of 0.125 and 0.075, respectively, encouraging refinement of the grid with each additional level of refinement in regions with strong gradients in density, velocity and specific entropy.

The predicted steady-state solutions for the stationary shock, illustrating the asymptotic convergence of the predicted profiles for the specific entropy as well as density through the shock wave for 16 through 23 levels of anisotropic AMR are compared in Fig. 6.1. The corresponding convergence histories for the computations on each successively refined mesh are presented in Fig. 6.2, where it can be seen that the residual is reduced by at least 5 orders of magnitude in an average of approximately 25 GMRES iterations per Newton step with 6 to 9 Newton iterations on each grid. It is evident from the results of the mesh resolution study presented in Fig. 6.1 that a total of 23 levels of anisotropic AMR are required to accurately capture and fully resolve the transition of flow properties through the shock front, although it appears as though as few as 20 levels would suffice and provide sufficient accuracy for many applications.

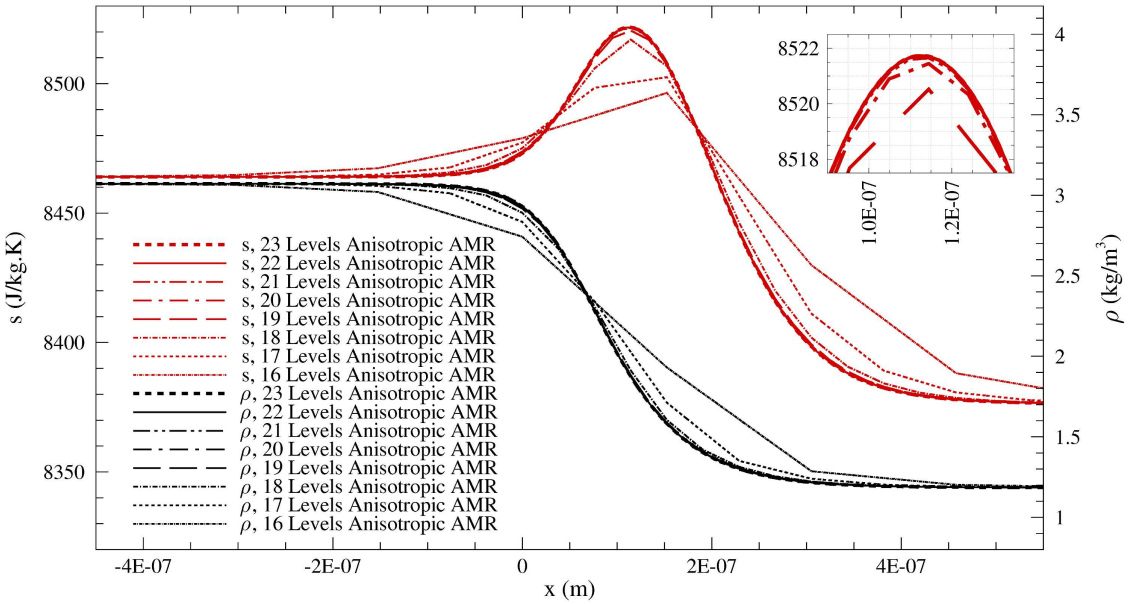

Figure 6.1: Mesh resolution study illustrating the smooth but rapid transition of specific entropy and density profiles through a one-dimensional, planar shock wave of strength $M_i = 1.95$ in molecular nitrogen. The inset diagram highlights the convergence of specific entropy profiles at their maximum peak value within the shock front.

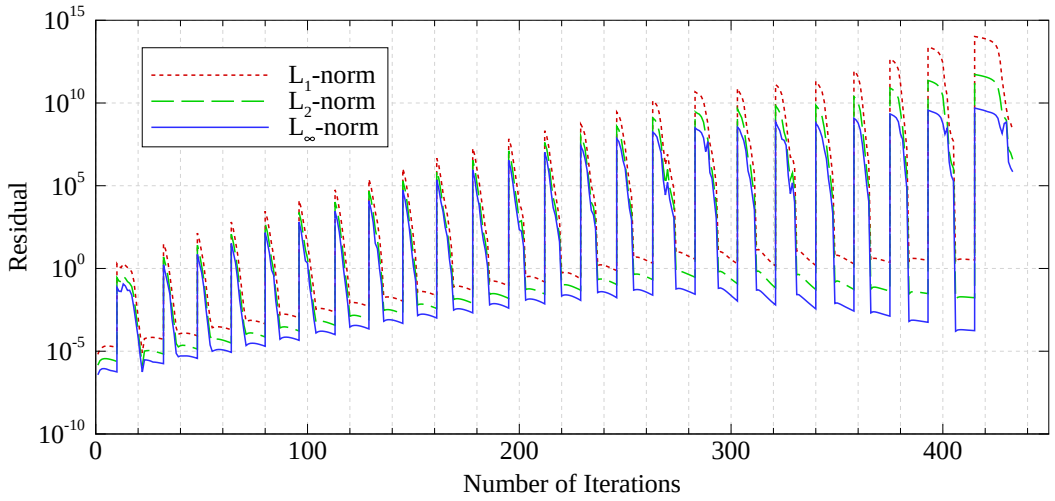

Figure 6.2: Steady-state convergence history with anisotropic AMR, corresponding to the preceding results of the mesh resolution study presented in Fig. 6.1, for a one-dimensional, planar shock wave of strength $M_i = 1.95$ in molecular nitrogen.

Note that in the case of 23 levels of refinement, the finest cells in the mesh are more than 8×10^6 (or 2^{23}) times smaller than the coarsest cells present in the computational domain. As detailed in the inset of Fig. 6.1, the predicted peak in the specific entropy profiles through the shock front nearly coincide for the solutions with 22 and 23 levels of anisotropic AMR, signifying a mesh-independent solution has been achieved.

The predicted shock-wave thickness obtained using the parallel, implicit, finite-volume scheme with anisotropic AMR was found to be accurate to within 0.07% of the results obtained from standard ODE solutions [85, 157], when 23 levels of anisotropic AMR were used. In this study, the shock thickness was calculated from the velocity profile according to the method presented by Taylor and Maccoll [158]. It is believed that this minor discrepancy in the computed thickness is largely attributed to small differences in the physical modelling adopted in the present finite-volume and ODE solutions. The good agreement between the ODE solutions and finite-volume predictions provide a strong indication of the mesh densities required for accurately predicting shock structure. A detailed listing that compares the accuracy of the predicted shock thickness results obtained using the anisotropic AMR mesh with 16 through 23 levels of refinement is presented in table 6.1. In particular, the convergence of shock properties, including the maximum peak specific entropy value, $s_{\max}$, as well as the shock thickness, Δx, are given as a function of the number of levels of refinement. It is evident from the results of the table that, in order to ensure recovery of fully resolved, mesh-independent, shock transitions in nitrogen under standard atmospheric conditions, the minimum cell sizes, $\Delta l_{\min}$, must be about 10^{-9} m, or 1 nm. Depending on the strength of the shock wave, this translates to requiring approximately 100 to 200 cells to reside within the shock transition structure.

Table 6.1: Overview of the numerical results of the mesh resolution study for a one-dimensional, planar shock wave of strength $M_{\mathrm{i}} = 1.95$ in molecular nitrogen.

AMR levels	$\Delta l_{\min}$ (nm)	$s_{\max}$ ($^{\mathrm{J}}/_{\mathrm{kg\cdot K}}$)	Δx (nm)	$\left\lvert 1 - \frac{\Delta x}{\Delta x_{\mathrm{ODE}}} \right\rvert \cdot 100\%$
23	1.25	8521.74	211.3916	0.0609
22	2.50	8521.73	211.4462	0.0868
21	4.80	8521.66	211.5776	0.1490
20	9.40	8521.45	212.3932	0.5350
19	18.75	8520.52	215.2458	1.8853
18	38.50	8517.04	225.1612	6.5787
17	74.50	8502.50	271.0596	28.3044
16	151.75	8496.41	353.0420	67.1103

6.2 Anisotropic versus Isotropic AMR for Shock Reflections

The performance benefits of the anisotropic block-based AMR procedure were characterized herein by assessing the total reductions in mesh size provided by using the anisotropic approach, as opposed to the usual isotropic method, for an unsteady oblique shock-wave reflection problem. The particular case examined corresponds to the single-Mach reflection flow in nitrogen

examined previously by Henderson and Gray [156] with an incident shock Mach number of $M_{\mathrm{i}} = 1.732$ and a wedge angle of $\theta_{\mathrm{w}} = 36.90^{\circ}$. The simulations have been carried out using a both AMR strategies (isotropic and anisotropic) with adapted meshes having refinement levels ranging from 7 to 10. A fixed physical time step of $\Delta t = 1.25 \times 10^{-7}$ s was used. The AMR procedure was applied once every 7 physical time steps and criteria based on the gradient of density with refinement and coarsening thresholds of 0.125 and 0.075, respectively, were used throughout the mesh refinement process.

The predicted distributions of the density for the single-Mach reflection flow obtained using both isotropic and anisotropic AMR methods with refinement levels ranging from 7 to 10 are depicted in Fig. 6.3. Each of predicted results are shown at a solution time of $t = 9.34 \times 10^{-5}$ s after the incident shock wave has passed the corner of the wedge and the oblique shock-wave reflection process has ensued. The corresponding Reynolds number $\mathrm{Re}_z = \rho_1 a_1 z/\eta_1$, based on the distance z that the incident shock wave propagates up the wedge surface, is 1.670×10^6 for these computations. The grid blocks for the refined isotropic and anisotropic AMR meshes are overlayed onto distributions of the density field and the plots reveal the regions of the domain where large density gradients exist and, as a result, the mesh concentrations are highest. The latter correspond to regions near the incident and reflected shocks, Mach stem, viscous shear layers, and thermal boundary layers, as expected. The total number of computational cells, N_{cells}, as well as the refinement efficiency, η, are listed in each case. Here, the refinement efficiency for both isotropic and anisotropic AMR is defined as $\eta = 1 - N_{\mathrm{cells}}/N_{\mathrm{uniform}}$, where N_{uniform} denotes the total number of computational cells that would exist on a uniform, isotropic mesh whose maximum refinement level equals the highest level of refinement in any computational coordinate direction on the current mesh.

It is evident from Fig. 6.3 that the application of the anisotropic AMR scheme for the single-Mach reflection pattern of interest provides reductions in the mesh size of upwards of 78% when using up to 10 levels of refinement, when compared to the isotropic AMR method, while still achieving the same overall solution accuracy. Assuming that the computational memory and storage requirements scale linearly with the mesh size, this translates to a factor of nearly 5 in computational savings. It is estimated that similar or perhaps even slightly higher levels of computational savings could be expected approaching the simulation of fully resolved, mesh-independent oblique shock-wave reflections, wherein flow features such as the shock structure as well as the combined viscous and thermal boundary layer lend themselves quite naturally to resolution via an anisotropic AMR approach. The results indicate that anisotropic AMR is markedly more effective than its isotropic counterpart when dealing with flows having strong anisotropic features.

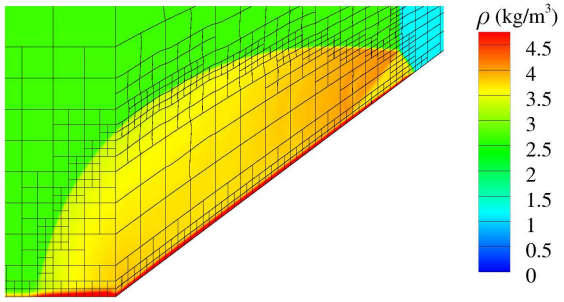

(a) 7 levels of isotropic AMR with $N_{\text{cells}} = 105200$ and $\eta = 0.87158$.

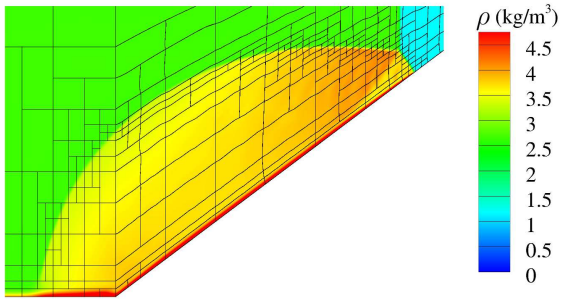

(b) 7 levels of anisotropic AMR with $N_{\text{cells}} = 47100$ and $\eta = 0.94251$.

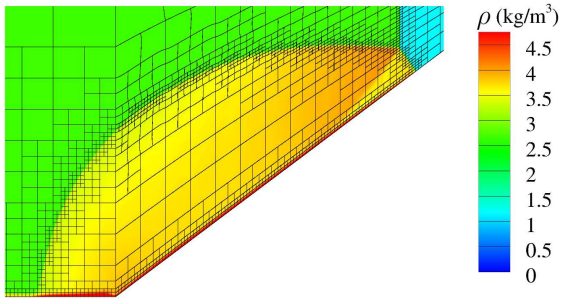

(c) 8 levels of isotropic AMR with $N_{\text{cells}} = 218000$ and $\eta = 0.93347$.

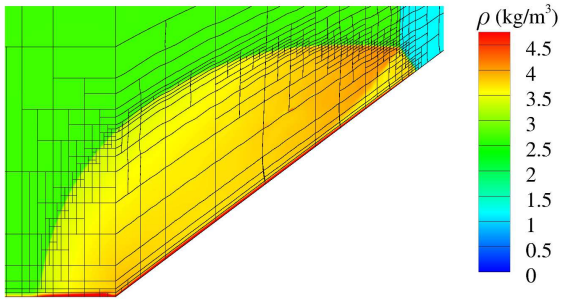

(d) 8 levels of anisotropic AMR with $N_{\text{cells}} = 92000$ and $\eta = 0.97192$.

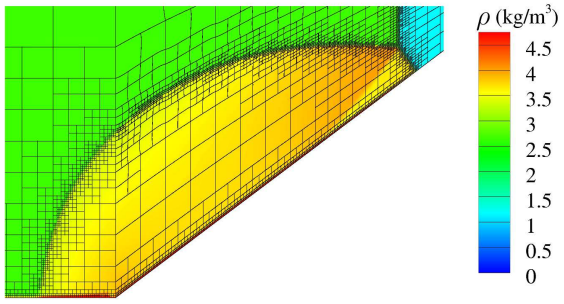

(e) 9 levels of isotropic AMR with $N_{\text{cells}} = 476300$ and $\eta = 0.96366$.

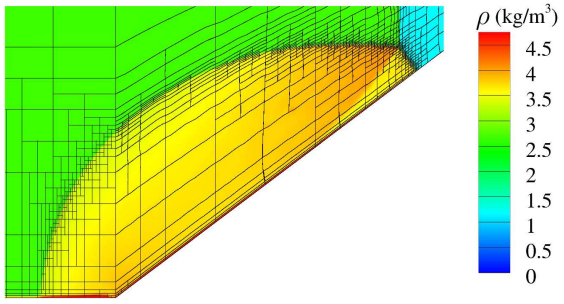

(f) 9 levels of anisotropic AMR with $N_{\text{cells}} = 138400$ and $\eta = 0.98944$.

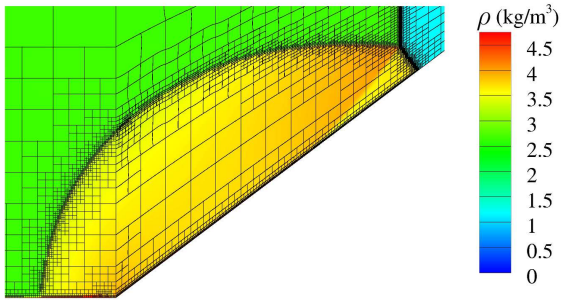

(g) 10 levels of isotropic AMR with $N_{\text{cells}} = 854600$ and $\eta = 0.98370$.

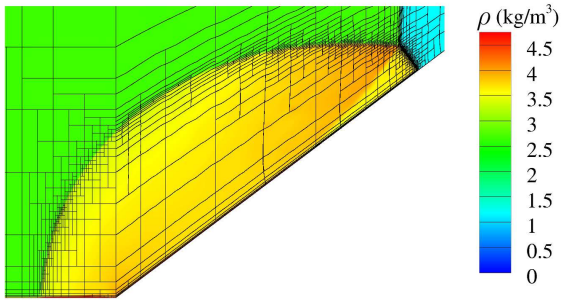

(h) 10 levels of anisotropic AMR with $N_{\text{cells}} = 189600$ and $\eta = 0.99638$.

Figure 6.3: Comparison of isotropic and anisotropic AMR methods for simulating an unsteady single-Mach reflection problem ($M_{\text{i}} = 1.732$ and $\theta_{\text{w}} = 36.90°$) in molecular nitrogen at $t = 9.34 \times 10^{-5}$ s after the initial interaction of the incident shock wave with the wedge corner.

6.3 Comparisons with Experiments on Shock Reflections

The predictive capabilities of the parallel, implicit, finite-volume scheme with AMR have also been assessed herein by comparing numerical predictions to published experimental measurements for several unsteady oblique shock-wave reflection flows. The previous experimental results of Henderson and Gray [156] were again considered pertaining to the diffraction of shocks over rigid concave corners in nitrogen. In addition to the single-Mach reflection case outlined in Section 6.2, a relatively simple regular reflection pattern with $M_\mathrm{i} = 1.721$ and $\theta_\mathrm{w} = 52.36°$, as well as a more complex double-Mach reflection configuration with $M_\mathrm{i} = 2.391$ and $\theta_\mathrm{w} = 46.17°$, were all investigated. Numerical predictions for each one of these three flows was performed

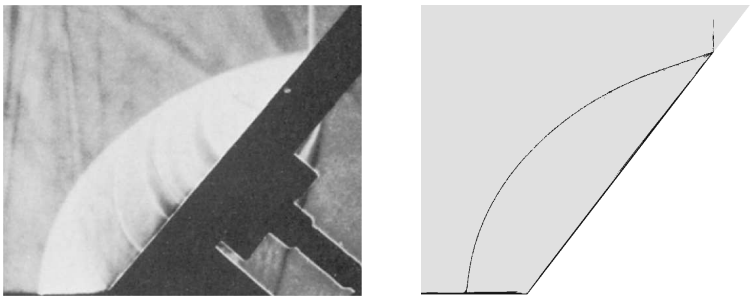

(a) Regular reflection pattern with $M_\mathrm{i} = 1.721$ and $\theta_\mathrm{w} = 52.36°$.

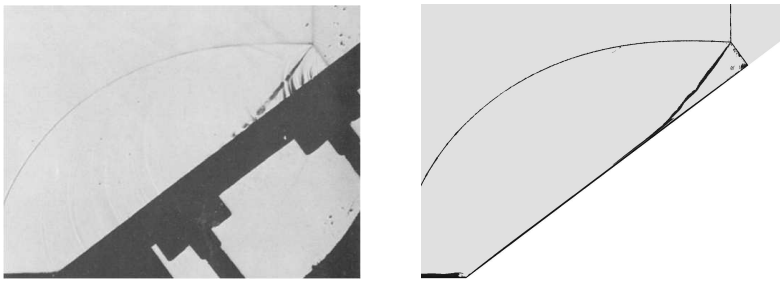

(b) Single-Mach reflection pattern with $M_\mathrm{i} = 1.732$ and $\theta_\mathrm{w} = 36.90°$.

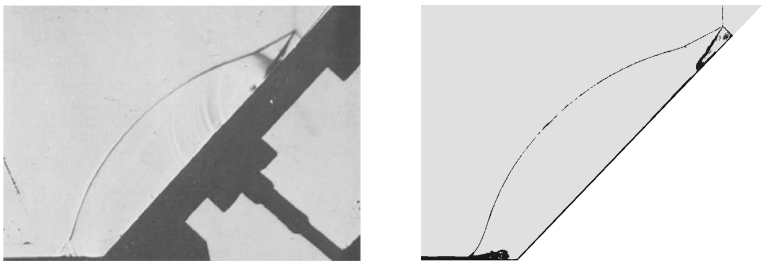

(c) Double-Mach reflection pattern with $M_\mathrm{i} = 2.391$ and $\theta_\mathrm{w} = 46.17°$.

Figure 6.4: Numerical schlieren images (right) replicating the oblique shock-wave reflection configurations studied in the experiments of Henderson and Gray [156] (left) for the diffraction of shock waves in molecular nitrogen over rigid concave corners. Experimental photographs reprinted from Henderson and Gray [156].

using 10 levels of anisotropic AMR based on the gradient of density, with refinement and coarsening thresholds set to 0.10 and 0.05, respectively. A CFL number of 0.2 was imposed for each case and anisotropic AMR was applied once every 10 physical time steps.

The simulated or numerical schlieren images based on the predicted contours of the density gradient for each of the three oblique shock-wave reflection cases are illustrated in Fig. 6.4 and compared to the actual experimental schlieren images. The regular, single-Mach, and double-Mach reflection computations are shown at physical solution times of $t = 5.13 \times 10^{-5}$ s, 6.67×10^{-5} s and 4.19×10^{-5} s after the incident shock wave has passed the wedge corner, respectively. These values correspond to the propagation of the incident shock wave a distance of $z = 0.05$ m up the surface of the inclined wedge. The Reynolds number $\mathrm{Re}_z = \rho_1 a_1 z/\eta_1$, based on this distance z, is 1.181×10^6 for these simulations. It is evident that the predicted solutions of the shock-wave reflection process are very similar to those of the experiments in each case. Flow features such as boundary layers and slipstreams, as well as locations of planar incident, curved reflected, and resultant Mach-stem shock waves are reproduced with accuracy. Moreover, the qualitative agreement between the numerical results and previous experimental images provides evidence of the validity of the CFD algorithm for predicting unsteady, oblique shock-wave reflections in gaseous media.

6.4 Simulation of Fully Resolved Oblique Shock Reflection

As a final demonstration of the capabilities of the parallel, implicit, anisotropic AMR finite-volume scheme for predicting the physics of unsteady oblique shock-wave reflection processes, a fully resolved simulation of the single-Mach reflection configuration studied previously is briefly considered. The process of choosing an appropriate physical time step for use in the implicit BDF2 approach is first described and then the results of the numerical simulation with fully resolved shock-front transition profiles are presented and discussed. See the paper by Hryniewicki, Groth and Gottlieb [122] for more details pertaining to the simulation of fully resolved oblique shock reflections.

6.4.1 Physical Time Step Selection

For the time-accurate computation of unsteady compressible flows, implicit time-marching schemes such as the BDF2 can provide the opportunity to achieve much larger physical time steps than those permissible with the capabilities of an explicit time-marching method. However, the use of increasingly larger physical time steps tends to progressively degrade the overall accuracy of a numerical solution. As a result, it is important to first ensure that reasonably accurate numerical results can still be attained when sufficiently large physical time steps are used within the solution method.

In order to examine the effects of time step selection on solution accuracy, an unsteady shock transition problem is studied, consisting of a one-dimensional planar shock wave with a strength of $M_\mathrm{i} = 1.732$ propagating in the positive x-direction through a nitrogen-filled shock tube with straight walls ($\theta_\mathrm{w} = 0°$). Numerical simulations were carried out using a variety of fixed physical time steps with the BDF2 scheme described in Subsection 5.2.5 and the solutions for the propagating shock were determined for a total solution time of 4.0×10^{-9} s. Based on the mesh resolution study of Section 6.1, 20 levels of anisotropic AMR are employed. This was deemed to be sufficient to capture the full transition of flow properties through the shock wave. The results obtained using the BDF2 time-marching method were compared to a reference solution that was obtained using a similarly dense mesh and the explicit, fourth-order Runge-Kutta (RK4) time-marching method with a small time step. The reference solution was assumed to contain negligible error as it is calculated with a very small fixed physical time step.

The predicted temporal variations in the density at a selected point of interest produced by the passage of the shock wave as obtained using the implicit BDF2 scheme with various fixed physical time steps are compared to the predicted reference solution obtained using the explicit RK4 time-marching method with a very small time step in Fig. 6.5. While it is evident that the BDF2 scheme allows use of large physical time steps, it is observed from the results shown in the figure that care must be exercised in selecting the time step. It should not be overly large so as to corrupt the numerical accuracy of the predicted solution. From Fig. 6.5, it appears that using a physical time step of $\Delta t = 5 \times 10^{-11}$ s provides the BDF2 scheme with a reasonably large time step with a tolerable loss in accuracy, in comparison to the reference RK4 solution, when 20 levels of anisotropic AMR are used. For this case, the more restrictive von Neumann or diffusive stability limit generally dominates and dictates the time step selection for explicit time-marching schemes. The viscous von Neumann number for this value of the physical time

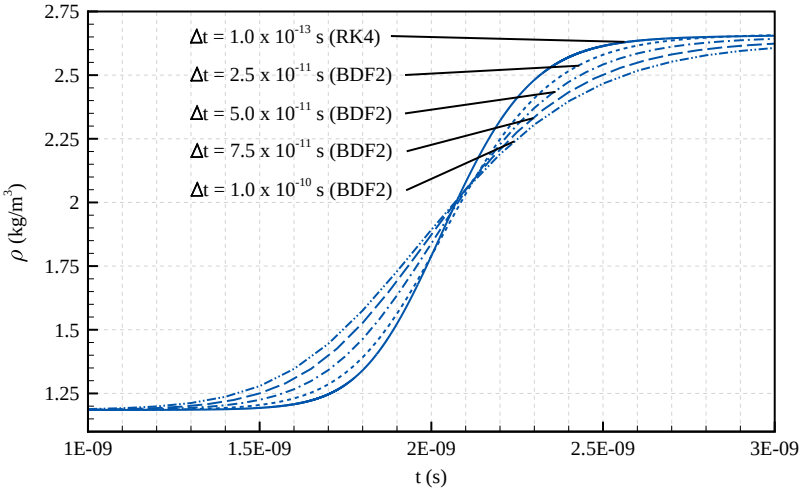

Figure 6.5: Temporal variation of density due to the passage of a shock wave of strength $M_\mathrm{i} = 1.732$ in nitrogen gas, captured using various fixed physical time steps for the fully implicit BDF2 approach.

step is in the range from 7 to 8 for all cells in the computational domain. Conversely, it should be noted that the inviscid CFL number is not exceedingly large for this value of the physical time step and falls in the range from 2 to 3 for all cells in the computational domain.

6.4.2 Computation of a Fully Resolved Single-Mach Reflection

Numerical predictions of the unsteady single-Mach reflection pattern in nitrogen gas with $M_\mathrm{i} = 1.732$ and $\theta_\mathrm{w} = 36.90^\circ$ were obtained using the anisotropic AMR technique alongside the fully implicit BDF2 time-marching method. The simulation was first initiated on a coarse mesh using 2 adjacent 10×10 cell blocks and then started on an ensuing refined mesh following 20 levels of initial anisotropic AMR. Unsteady AMR was carried out once every 7 physical time steps, wherein refinement and coarsening was governed by thresholds of 0.125 and 0.075, respectively. This led to the refinement of the mesh with each additional level of anisotropic AMR in regions where strong density, velocity and entropy gradients existed within the flow field. The fixed physical time step used in the time-marching of the solution was $\Delta t = 5 \times 10^{-11}$ s, as per the findings presented in Subsection 6.4.1.

The numerical results of the fully resolved simulation are illustrated in Fig. 6.6 at a solution time of $t = 5.14 \times 10^{-7}$ s after the initial reflection of the incident shock wave from the wedge surface. At this time, a total of 39,106 10×10 cell blocks with 3,910,600 computational cells are present in the simulation with 20 levels of anisotropic AMR, yielding a refinement efficiency of 0.99999993. The Reynolds number $\mathrm{Re}_z = \rho_1 a_1 z/\eta_1$, based on the distance z that the incident shock wave propagates up the wedge surface, is 8.868×10^3 for this simulation. The internal structures of the incident, reflected and Mach-stem shock waves are well resolved. Furthermore, as with the under-resolved solution presented earlier, the predicted fully resolved solution obtained using the parallel implicit anisotropic block-based AMR scheme agrees well the experimental images of Henderson and Gray [156].

The application of the anisotropic AMR scheme was found to provide a reduction of 78% in mesh size when compared to the isotropic AMR case, while achieving the same solution accuracy. Additionally, a further 42% in computational savings was attained by exploiting the ability of the implicit BDF2 scheme to take a larger time step than that permissible with the conditionally stable explicit RK2 time-marching method without significantly compromising accuracy (see the paper by Hryniewicki, Groth and Gottlieb [122] for details). It then follows that the overall speedup provided by the combination of the anisotropic AMR and parallel fully implicit BDF2 time-marching methods for this fully resolved case is estimated to be a factor of more than 10^9, when using 256 cores and assuming a 50% parallel efficiency due to latency and interprocessor communication, compared to a serial computation performed using the explicit RK2 scheme on a uniform mesh with a resolution equal to that of the finest mesh blocks.

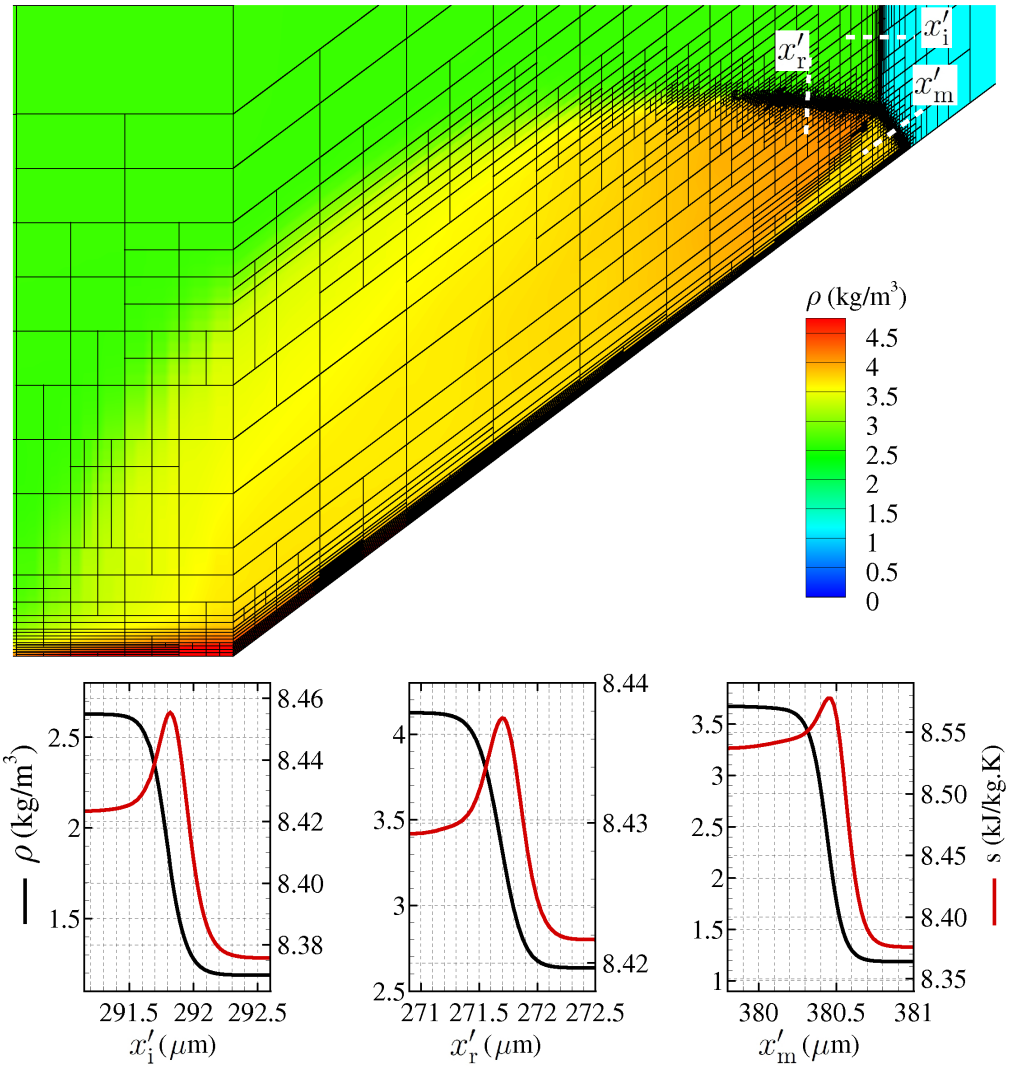

Figure 6.6: Predicted density contours with overlaid 10×10 cell blocks of an unsteady single-Mach reflection problem ($M_{\mathrm{i}} = 1.732$ and $\theta_{\mathrm{w}} = 36.90°$) in molecular nitrogen at $t = 5.14 \times 10^{-7}$ s after the incident shock wave strikes the corner of the wedge. The internal structures of the incident, reflected and Mach-stem shock waves are fully resolved; the inset diagrams illustrate the smooth but rapid transitions of specific entropy and density measured along the dashed distances x'_{i}, x'_{r} and x'_{m}, aligned in the directions normal to each of these respective shock waves.

Chapter 7

Methodology for the Determination of the Numerical Transition Boundary Between RR and MR

The transition boundary between regular reflection (RR) and Mach reflection (MR), determined analytically by von Neumann [5] based on the extreme-angle criterion, given by Eqs. (3.19) to (3.26) and shown in Fig. 1.2, is examined by performing detailed numerical or CFD flow-field simulations of planar shock reflections from an inclined wedge. The methodology for determining the numerical transition boundary precisely from CFD flow-field simulations requires the following: (i) RR and MR (SMR, TMR and DMR) flow fields concentrated about a point on a previous analytical transition boundary are computed accurately, and (ii) the wedge angle θ_{w} and incident shock Mach number M_{i} for a point on the resulting numerical transition boundary are then computed accurately based on the disappearance of the Mach stem from the MR pattern and the first occurrence of the RR configuration. The first requirement is well met by using the CFD algorithm described in Chapters 5 and 6. For the second requirement, a methodology of post-processing the CFD flow fields is developed and described herein to permit the determination of numerous coordinate points $(M_{\mathrm{i}}, \theta_{\mathrm{w}})$ along the numerical transition boundary with an accuracy that is much superior than that achievable by human inspection and interpretation of CFD flow-field images (and also by human interpretation of experimental flow-field photographs).

7.1 Selected $(M_{\mathrm{i}}, \theta_{\mathrm{w}})$-Coordinates for CFD Simulations

Von Neumann's [5] transition boundary between RR and MR (SMR, TMR and DMR), based on the extreme-angle criterion, is used as a starting point for the determination of the numerical transition boundary based on CFD flow-field simulations. Twenty coordinate points along this transition boundary were selected, as given in tables 7.1(a) and 7.1(b) for argon and atmospheric air, respectively. These points along the transition boundary are also plotted and numbered in Figs. 7.1(a) and 7.1(b) as the sine of the wedge angle θ_{w} versus the incident shock Mach number M_{i}. At each reference point $(M_{\mathrm{i}}^{\star}, \sin(\theta_{\mathrm{w}}^{\star}))$ on the extreme-angle boundary, a set of coordinate points $(M_{\mathrm{i}}, \sin(\theta_{\mathrm{w}}))$ normal to and crossing the extreme-angle boundary are specified for the CFD flow-field simulations. These points marked with '$\times$' signs are normal to and cross the extreme-angle boundary, as shown in points 6 and 15 in Figs. 7.1(a) and 7.1(b). These points, which are used to define the CFD simulations, are determined by using an (α, β)-coordinate

Table 7.1: Reference points (RP) selected along von Neumann's extreme-angle transition boundary.

(a) Argon.

RP	$M_{\mathrm{i}}^{\star}$	$\theta_{\mathrm{w}}^{\star}$ (°)	$\phi^{\star}$ (°)
1	1.001	5.1010	−1.3040
2	1.006	12.2184	−3.4760
3	1.018	20.1533	−7.2071
4	1.041	28.0871	−14.3370
5	1.089	36.3558	−30.8163
6	1.182	43.4991	−57.6984
7	1.305	47.7127	−74.6128
8	1.435	49.9799	−81.7594
9	1.572	51.3539	−85.1728
10	1.715	52.2405	−86.9823
11	1.855	52.8110	−87.9754
12	2.0	53.2183	−88.5968
13	2.25	53.6680	−89.1901
14	2.5	53.9398	−89.4949
15	2.75	54.1151	−89.6662
16	3.0	54.2340	−89.7690
17	3.25	54.3179	−89.8342
18	3.5	54.3792	−89.8773
19	3.75	54.4252	−89.9068
20	4.0	54.4605	−89.9276

(b) Atmospheric air.

RP	$M_{\mathrm{i}}^{\star}$	$\theta_{\mathrm{w}}^{\star}$ (°)	$\phi^{\star}$ (°)
1	1.001	5.0997	−1.3050
2	1.006	12.2012	−3.4904
3	1.018	20.0766	−7.2854
4	1.041	27.8798	−14.6235
5	1.089	35.8945	−31.7291
6	1.182	42.6428	−59.3245
7	1.305	46.4516	−76.1500
8	1.435	48.3727	−83.0757
9	1.572	49.4404	−86.3081
10	1.715	50.0537	−87.9713
11	1.855	50.3927	−88.8475
12	2.0	50.5908	−89.3669
13	2.25	50.7392	−89.8168
14	2.5	50.7684	−90.0089
15	2.75	50.7463	−90.0907
16	3.0	50.7032	−90.1222
17	3.25	50.6529	−90.1300
18	3.5	50.6021	−90.1267
19	3.75	50.5537	−90.1186
20	4.0	50.5090	−90.1086

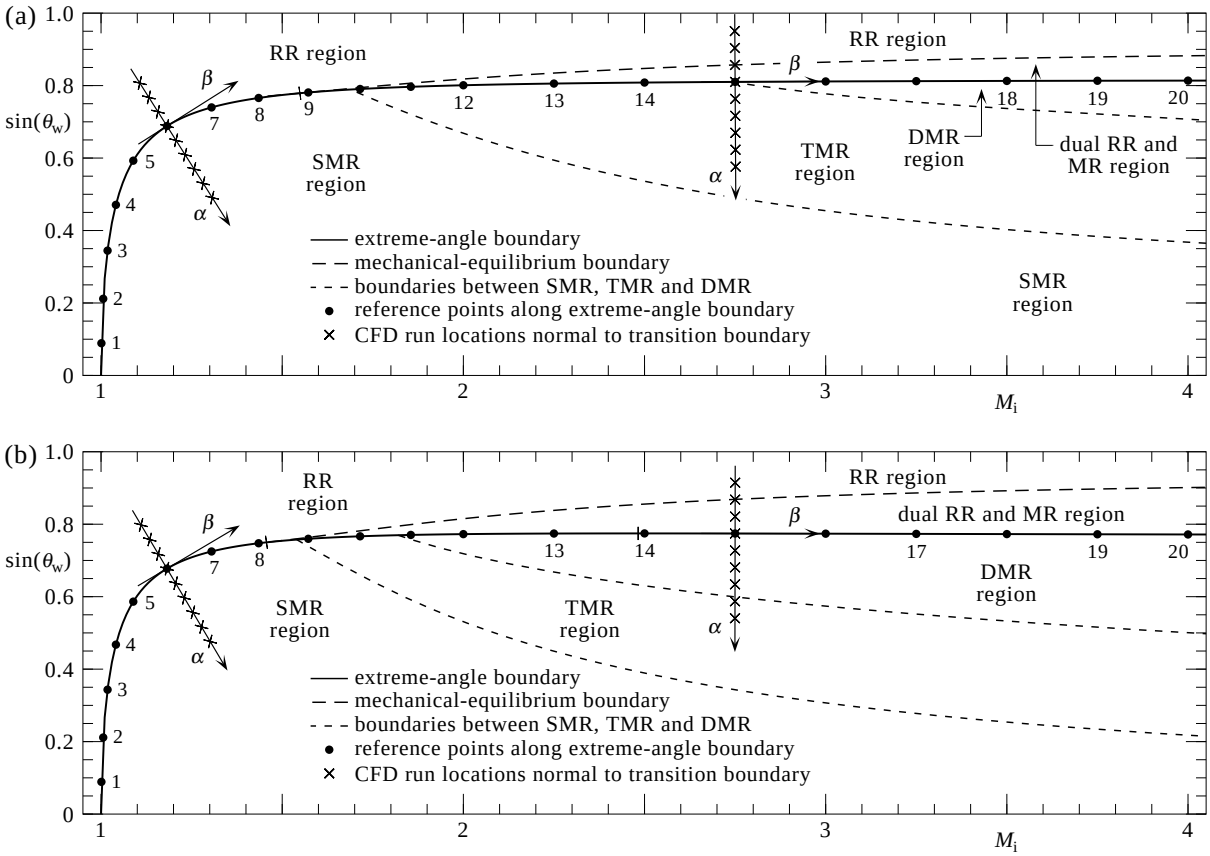

Figure 7.1: Reference points $(M_{\rm i}^\star, \sin(\theta_{\rm w}^\star))$ along von Neumann's extreme-angle boundary between RR and MR in (a) argon and (b) air, and superposed (α-β)-coordinate systems showing the locations of CFD flow-field simulations normal to each respective extreme-angle boundary.

system that is translated from the origin $(M_{\rm i} = 1, \sin(\theta_{\rm w}) = 0)$ to one of the points (e.g. number 6), and then rotated such that the α-abscissa and β-ordinate are respectively perpendicular and parallel to the extreme-angle boundary. The transformation that renders the CFD simulation points is written in terms of the rotation matrix of sines and cosines as

$$\begin{bmatrix} M_{\rm i} - M_{\rm i}^\star \\ \sin(\theta_{\rm w}) - \sin(\theta_{\rm w}^\star) \end{bmatrix} = \begin{bmatrix} \cos(\phi^\star) & -\sin(\phi^\star) \\ \sin(\phi^\star) & \cos(\phi^\star) \end{bmatrix} \begin{bmatrix} \alpha \\ \beta \end{bmatrix}, \tag{7.1}$$

which is summarized for convenience as

$$M_{\rm i} = M_{\rm i}^\star + \alpha\cos(\phi^\star) - \beta\sin(\phi^\star), \tag{7.2}$$

$$\sin(\theta_{\rm w}) = \sin(\theta_{\rm w}^\star) + \alpha\sin(\phi^\star) + \beta\cos(\phi^\star), \tag{7.3}$$

wherein

$$\phi^\star = \tan^{-1}\left(\left.\frac{{\rm d}\sin(\theta_{\rm w})}{{\rm d}M_{\rm i}}\right|_\star\right) - 90^\circ \tag{7.4}$$

is the rotation angle and ${\rm d}\sin(\theta_{\rm w})/{\rm d}M_{\rm i}$ denotes the slope of the extreme-angle boundary at the reference coordinates $M_{\rm i}^\star$ and $\sin(\theta_{\rm w}^\star)$. This derivative was defined previously by Eq. (3.32).

The CFD simulation points are obtained by setting the parameter $\beta = 0$ in the transformation equations given by Eqs. (7.1) to (7.3). The parameter α is then varied such that the CFD simulation points become concentrated in the vicinity of the numerical transition boundary where the Mach stem disappears, which might occur below ($\alpha > 0$), on ($\alpha = 0$), or above ($\alpha < 0$) the extreme-angle transition boundary.

7.2 Mach-Stem Length and Triple-Point Trajectory Angle

A characteristic length of the Mach stem is required for the determination of the numerical or CFD transition boundary, because this length in Mach-reflection configurations diminishes to zero as the flow-field simulations are computed closer and closer to the numerical transition boundary. The characteristic length L' selected for this study is depicted in Fig. 7.2 for the case of a single Mach reflection. This physical length is given by $L' = V_{\mathrm{m}}\delta t - V_{\mathrm{i}}\delta t/\cos(\theta_{\mathrm{w}})$, in which V_{m} denotes the speed of the foot of the Mach stem along the wedge surface, $V_{\mathrm{i}}/\cos(\theta_{\mathrm{w}})$ is the speed of the incident shock along the wedge, and δt denotes the time increment after the incident shock first encounters the wedge apex and a regular- or Mach-reflection pattern begins.

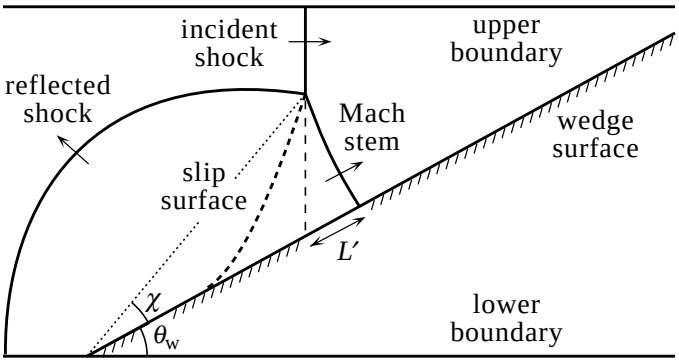

Figure 7.2: Characteristic Mach-stem length L'.

The physical length L' as defined above is inconvenient as it increases continuously from zero with increasing time (δt) for Mach reflections. Hence, the length is normalized by dividing it by $V_{\mathrm{i}}\delta t/\cos(\theta_{\mathrm{w}})$ to overcome this difficulty and one then obtains the normalized length

$$L = \frac{V_{\mathrm{m}}}{V_{\mathrm{i}}}\cos(\theta_{\mathrm{w}}) - 1 = \frac{M_{\mathrm{m}}}{M_{\mathrm{i}}}\cos(\theta_{\mathrm{w}}) - 1, \tag{7.5}$$

which is constant for the case of a self-similar flow field. In the case of a regular-reflection configuration (without a Mach stem), this normalized length L should be zero. The normalized length L is calculated for each CFD flow-field simulation of regular and Mach reflection patterns, as described in the following sections 7.3 to 7.5.

The triple-point trajectory angle χ, defined in Fig. 7.2, is given by

$$\tan(\chi) = \frac{1}{\tan(\theta_{\mathrm{w}})}\left[1 - \frac{V_{\mathrm{i}}}{V_{\mathrm{m}}\cos(\theta_{\mathrm{w}})}\right] = \frac{1}{\tan(\theta_{\mathrm{w}})}\frac{L}{1+L}. \tag{7.6}$$

This important relationship between the Mach-stem length L and the angle χ between the wedge surface and the triple-point trajectory is derived by assuming that the incident shock and Mach stem are straight lines and the Mach stem is perpendicular to the wedge surface.

7.3 Incident Shock Trajectory and Speed

The trajectory and speed of the incident shock are determined by post-processing data obtained from each CFD flow-field simulation, rather than accepting the theoretical shock speed based on the Rankine-Hugoniot equations that were used to initialize the CFD simulation. In the CFD simulations studied here, which are based on solving Euler's equations for inviscid flow, the incident shock front is a rapid transition of flow-field properties typically spread over 3 to 12 cells in this study due to numerical viscosity (note that there is no physical viscosity in these cases). The objective is to determine the distance-time trajectory of the center of the incident shock-front transition and calculate therefrom the shock-front speed as the time derivative of the trajectory distance-time data.

The data collected from each CFD simulation to calculate the incident shock trajectory and speed are briefly described first. During each CFD simulation, all of the cells along the upper boundary, as illustrated in Fig. 7.3, are probed every time step just before AMR is activated (i.e. at every sixth time step), in the order of the cells ahead to behind the incident shock. This probing is done by using a set of specified pressures given by

$$\hat{p}_k = p_1^\star + \frac{k}{K}\left(p_2^\star - p_1^\star\right), \quad k = 1, 2, \ldots, K-1, \tag{7.7}$$

in which $p_1^\star$ and $p_2^\star$ are the theoretical pre- and post-shock pressures, and $K = 20$ is a convenient

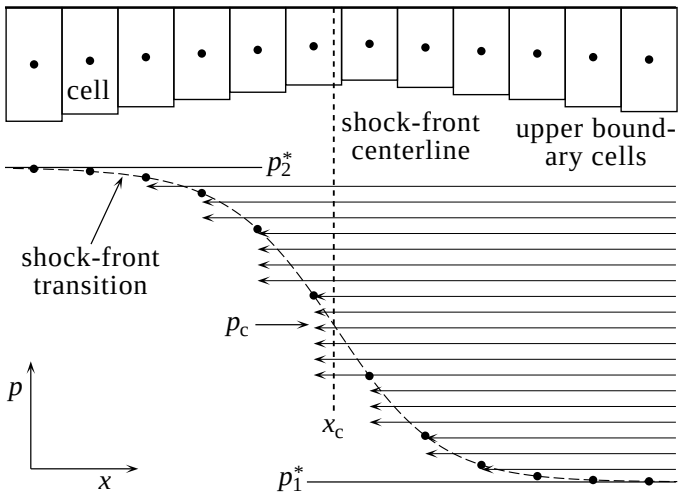

Figure 7.3: Capturing the incident shock-front transition by probing the upper-boundary cells to determine the transition pressure and flow-field locations.

number when the number of discrete incident shock-front data points varies from 3 to 12. On each sweep k, the pressure $\hat{p}_k$ is compared to the cell pressure p_{cell}. If $\hat{p}_k > p_{\text{cell}}$, the sweep continues to the next cell. When $\hat{p}_k < p_{\text{cell}}$, all relevant cell data for defining the incident shock transition are stored for post-processing, and the sweep of probing successive cells for pressure level k is terminated. This probing scheme of successive upper-boundary cells effectively captures the incident shock-front transition as a collection of discrete pressure-distance data at a given time step, as also illustrated in Fig. 7.3. The sweeps for the $\hat{p}_k$ levels can gather repeated data from the same cell. All redundant data are not needed to define the shock-front transition, so they are eliminated from the collected data sets.

The continuous shock-front transition can be constructed by means of a curve fit to the collected data, as shown by the dashed line through the discrete pressure-distance data. Then, the location x_{c} of the center of this transition, where the pressure is given by $p_{\text{c}} = \frac{1}{2}\left(p_1^\star + p_2^\star\right)$, can be obtained, as depicted by the vertical dashed line in Fig. 7.3. Note that $p_2^\star$ is the theoretical Rankine-Hugoniot pressure stemming from the specification of the incident shock Mach number M_{i} used to initiate the computational flow-field simulations.

The shock-front transition is constructed from the interior cell pressures defined by p_i, with $i = 1, 2, \ldots, n$, versus the cell center distances $z_i = x_i - x_{\text{apex}}$ along the upper boundary of the computational domain. The symbol n denotes the total number of discrete cell distances and pressures in the shock transition and x_{apex} is the horizontal distance of the wedge apex on the lower boundary. The center of the shock-front transition propagates through the upper-boundary cells with centers located by the coordinates $(x_{i,j},\, y_{i,j})$, in which the indices i and j denote the arrangement of the cells in the x and y directions. The variations in the vertical cell distances $y_{i,j}$ from the upper wall do not influence the incident shock-front trajectory and speed because the shock-front is assumed normal to the upper boundary, so j and $y_{i,j}$ are omitted from the analysis and equations.

The continuous transition $z = z(p)$ of the incident shock front can be represented as

$$z = \overline{z_i} + \hat{\alpha}\left[\ln\left(p - p_1^\star\right) - \overline{\ln\left(p_i - p_1^\star\right)}\right] + \hat{\beta}\left[\ln\left(p_2^\star - p\right) - \overline{\ln\left(p_2^\star - p_i\right)}\right] + \hat{\gamma}, \tag{7.8}$$

with the property averages defined by

$$\overline{z_i} = \frac{1}{n}\sum_{i=1}^{n} z_i, \tag{7.9}$$

$$\overline{\ln\left(p_i - p_1^\star\right)} = \frac{1}{n}\sum_{i=1}^{n} \ln\left(p_i - p_1^\star\right), \tag{7.10}$$

$$\overline{\ln\left(p_2^\star - p_i\right)} = \frac{1}{n}\sum_{i=1}^{n} \ln\left(p_2^\star - p_i\right). \tag{7.11}$$

The three unknown coefficients in this curve-fit equation, denoted by $\hat{\alpha}$, $\hat{\beta}$ and $\hat{\gamma}$, are determined by means of a standard least-squares fitting method. Note that this logarithmic form of the

curve-fit equation occurs in theoretical shock-front transitions obtained by Rankine [159] for heat conduction only and Taylor [160] and Becker [88] for both heat conduction and dynamic viscosity, although the shock-front structure in the CFD simulations originates from numerical viscosity (i.e. from ensuring non-oscillatory solution behaviour).

The global error is defined as the sum of the square of the local errors and given by

$$E = \sum_{i=1}^{n} \left\{ w_i \hat{\alpha} \left[\ln\left(p_i - p_1^\star\right) - \overline{\ln\left(p_i - p_1^\star\right)} \right] + w_i \hat{\beta} \left[\ln\left(p_2^\star - p_i\right) - \overline{\ln\left(p_2^\star - p_i\right)} \right] + w_i \hat{\gamma} - w_i \left(z_i - \overline{z_i}\right) \right\}^2 \tag{7.12}$$

and the weights w_i used in this study are defined by

$$w_i^2 \;=\; \frac{7}{\max\left(1, 7\left|\frac{z_i - z_o'}{\Delta z_o}\right|\right)}. \tag{7.13}$$

The square of the weights w_i^2 ranges from a maximum value of 7, when $\left(z_i - z_o'\right)/\Delta z_o$ is zero or close to zero, to much small values when $\left(z_i - z_o'\right)/\Delta z_o$ becomes large. Illustrations of z_o', $z_i - z_o'$ and Δz_o are shown in Fig. 7.4.

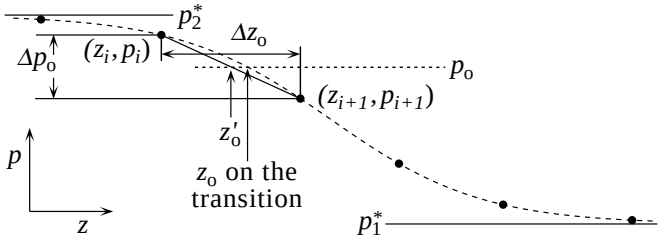

Figure 7.4: Definitions of p_o, Δp_o, z_o', z_o and Δz_o for the incident shock-front transition.

The objective of the curve fit is to construct a continuous shock-front transition from the discrete distance z_i versus pressure p_i data and therefrom determine the location z_o on the transition for some specified pressure p_o (normally the center value). In this process an approximate value of z_o is denoted by z_o', and it is obtained from the intersection of two straight lines; one for the constant pressure p_o and the other that joins the two coordinates pairs (z_i,p_i) and (z_{i+1},p_{i+1}) that bracket the specified value of p_o. Also defined in Fig. 7.4 are the terms $\Delta z_o = z_{i+1} - z_i$ and $\Delta p_o = p_{i+1} - p_i$, such that $z_o' = z_i + \Delta z_o \left(p_o - p_i\right)/\Delta p_o$. When the curve fit has been constructed, the more accurate value of the distance z_o on the shock-front transition is calculated by means of Eq. (7.8) with the pressure $p = p_o$. For the center of the shock-front transition, $z = z_o \to z_\mathrm{c}$, and $p = p_o \to p_\mathrm{c} = \frac{1}{2}\left(p_1^\star + p_2^\star\right)$.

In the standard least-square curve fit the three derivatives $\partial E/\partial\hat{\alpha}$, $\partial E/\partial\hat{\beta}$ and $\partial E/\partial\hat{\gamma}$ of

Eq. (7.12) are determined as

$$\frac{\mathrm{d}E}{\mathrm{d}\hat{\alpha}} = 2\sum_{i=1}^{n}\Big\{w_i\hat{\alpha}\left[\ln\left(p_i - p_1^\star\right) - \overline{\ln\left(p_i - p_1^\star\right)}\right] + w_i\hat{\beta}\left[\ln\left(p_2^\star - p_i\right) - \overline{\ln\left(p_2^\star - p_i\right)}\right] + w_i\hat{\gamma} - w_i\left(z_i - \overline{z_i}\right)\Big\} \cdot w_i\left[\ln\left(p_i - p_1^\star\right) - \overline{\ln\left(p_i - p_1^\star\right)}\right], \tag{7.14}$$

$$\frac{\mathrm{d}E}{\mathrm{d}\hat{\beta}} = 2\sum_{i=1}^{n}\Big\{w_i\hat{\alpha}\left[\ln\left(p_i - p_1^\star\right) - \overline{\ln\left(p_i - p_1^\star\right)}\right] + w_i\hat{\beta}\left[\ln\left(p_2^\star - p_i\right) - \overline{\ln\left(p_2^\star - p_i\right)}\right] + w_i\hat{\gamma} - w_i\left(z_i - \overline{z_i}\right)\Big\} \cdot w_i\left[\ln\left(p_2^\star - p_i\right) - \overline{\ln\left(p_2^\star - p_i\right)}\right], \tag{7.15}$$

$$\frac{\mathrm{d}E}{\mathrm{d}\hat{\gamma}} = 2\sum_{i=1}^{n}\Big\{w_i\hat{\alpha}\left[\ln\left(p_i - p_1^\star\right) - \overline{\ln\left(p_i - p_1^\star\right)}\right] + w_i\hat{\beta}\left[\ln\left(p_2^\star - p_i\right) - \overline{\ln\left(p_2^\star - p_i\right)}\right] + w_i\hat{\gamma} - w_i\left(z_i - \overline{z_i}\right)\Big\} \cdot w_i, \tag{7.16}$$

and subsequently set to zero to yield the matrix equation

$$\begin{bmatrix} a & b & c \\ b & d & e \\ c & e & f \end{bmatrix}\begin{bmatrix} \hat{\alpha} \\ \hat{\beta} \\ \hat{\gamma} \end{bmatrix} = \begin{bmatrix} g \\ h \\ i \end{bmatrix} \tag{7.17}$$

for the solution of $\hat{\alpha}$, $\hat{\beta}$ and $\hat{\gamma}$. The elements of the square matrix and right-hand vector are given by

$$a = \overline{w_i^2\left[\ln\left(p_i - p_1^\star\right) - \overline{\ln\left(p_i - p_1^\star\right)}\right]^2}, \tag{7.18}$$

$$b = \overline{w_i^2\left[\ln\left(p_i - p_1^\star\right) - \overline{\ln\left(p_i - p_1^\star\right)}\right]\left[\ln\left(p_2^\star - p_i\right) - \overline{\ln\left(p_2^\star - p_i\right)}\right]}, \tag{7.19}$$

$$c = \overline{w_i^2\left[\ln\left(p_i - p_1^\star\right) - \overline{\ln\left(p_i - p_1^\star\right)}\right]}, \tag{7.20}$$

$$d = \overline{w_i^2\left[\ln\left(p_2^\star - p_i\right) - \overline{\ln\left(p_2^\star - p_i\right)}\right]^2}, \tag{7.21}$$

$$e = \overline{w_i^2\left[\ln\left(p_2^\star - p_i\right) - \overline{\ln\left(p_2^\star - p_i\right)}\right]}, \tag{7.22}$$

$$f = \overline{w_i^2}, \tag{7.23}$$

$$g = \overline{w_i^2\left(z_i - \overline{z_i}\right)\left[\ln\left(p_i - p_1^\star\right) - \overline{\ln\left(p_i - p_1^\star\right)}\right]}, \tag{7.24}$$

$$h = \overline{w_i^2\left(z_i - \overline{z_i}\right)\left[\ln\left(p_2^\star - p_i\right) - \overline{\ln\left(p_2^\star - p_i\right)}\right]}, \tag{7.25}$$

$$i = \overline{w_i^2\left(z_i - \overline{z_i}\right)}, \tag{7.26}$$

and these are averages like those defined earlier by Eqs. (7.9) to (7.11). The solution of Eq. (7.17)

follows as

$$\hat{\gamma} = \frac{(ad-b^2)i+(bc-ae)h+(be-cd)g}{(ad-b^2)f+(bc-ae)e+(be-cd)c}, \tag{7.27}$$

$$\hat{\beta} = \frac{ah-bg}{ad-b^2}+\frac{bc-ae}{ad-b^2}\hat{\gamma}, \tag{7.28}$$

$$\hat{\alpha} = \frac{dg-bh}{ad-b^2}+\frac{be-cd}{ad-b^2}\hat{\gamma}, \tag{7.29}$$

for the curve-fit coefficients. Note that when the curve fit is done without using weights (i.e. $w_i^2 = 1$), then $c = 0$, $e = 0$, $f = 1$ and $i = 0$ from Eqs. (7.20), (7.22), (7.23) and (7.26), such that the coefficient $\hat{\gamma}$ is then equal to zero. This occurs because of the specific curve-fit construction given by Eq. (7.8).

The resulting continuous shock-front transitions of the incident shock by the preceding curve fits to CFD flow-field data are illustrated in Fig. 7.5(a) for reference points RP–1, 5 and 19 with $\alpha = 0.0017$, -0.0023 and -0.011 in argon and in Fig. 7.5(b) for reference points RP–4, 8 and 16 with $\alpha = 0.005$, 0.005 and 0.0 in air (all normal to the extreme-angle transition boundary). Shown also are the interpolated shock-front transition centers from using $p = p_c = \frac{1}{2}(p_1^\star + p_2^\star)$ to obtain $z = z_c$ by using Eq. (7.8). These results were chosen from CFD runs with different shock Mach numbers to illustrate the shock-front constructions for the cases when the number of discrete distance-pressure data were 9, 3 and 6 for reference points RP–1, 5 and 19 in argon and 11, 6 and 4 for reference points RP–4, 8 and 16 in air, respectively. These illustrations

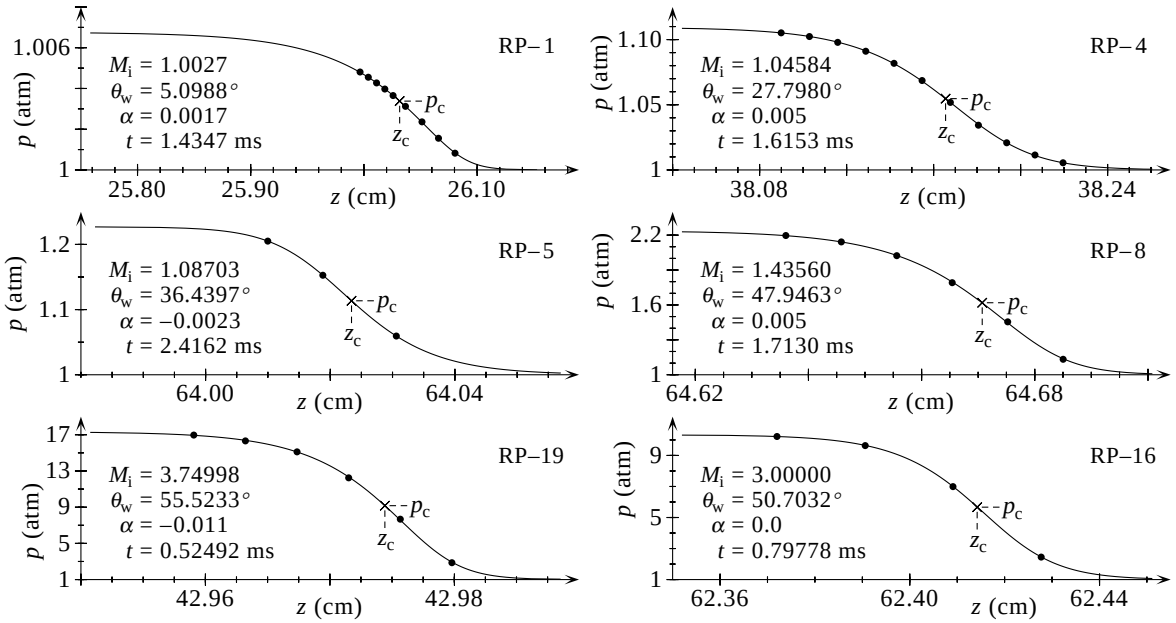

(a) In argon when the AMR level $n_r = 12$.

(b) In air when the AMR level $n_r = 10$.

Figure 7.5: Continuous transitions of the incident shock front constructed by curve fits using discrete CFD flow-field data.

are typical of all curve fits for the incident-shock front. It is quite apparent that the curve-fit expression given by Eq. (7.8) is successful in capturing the incident shock-front transitions associated with the numerical solutions to the Euler equations.

The trajectory of the incident shock front along the upper boundary during a CFD run occurs from its start before the wedge apex and ends when the shock progresses along the upper boundary by the distance (1 m)$\cos(\theta_{\rm w})$ and along the wedge surface by 1 m. The trajectory consists of numerous $z_{\rm c}$ values determined at every sixth time step during the CFD run. Such results are illustrated in Fig. 7.6(a) for reference points RP–2, 8 and 17 with $\alpha = 0.0018$, -0.0046 and -0.0167 in argon and in Fig. 7.6(b) for reference points RP–3, 10 and 18 with $\alpha = 0.005$, -0.023 and 0.0 in air, respectively. Each shock-front trajectory is plotted as a chain of numerous small dots, each dot corresponding to the time t at which the shock-front curve-fit equation gave the transition center value $z_{\rm c}$.

The shock-front trajectories that are presented in Fig. 7.6 for the incident shock are typical of those obtained in this study for all of the reference points and different values of α. The shock-front trajectories look extremely linear. However, the actual advancement of the center of the incident shock in the CFD simulations is always forward but somewhat nonuniform or jerky with distance. This jerkiness in movement is very small and it decreases when the CFD time steps (Δt) are reduced. Hence, trajectory jerkiness is less severe when using more levels of AMR in the CFD simulations, and also when flow-field simulations contain complex flow structures with larger flow velocities and sound speeds, because the time steps are thereby reduced.

The curve fit to the incident shock-front trajectory data ($z_i = z_{{\rm c},i}, t_i$) is given by the second-order polynomial

$$z = \overline{z_i} + \hat{a}\left(t - \overline{t_i}\right) + \hat{b}\left(t^2 - \overline{t_i^2}\right), \tag{7.30}$$

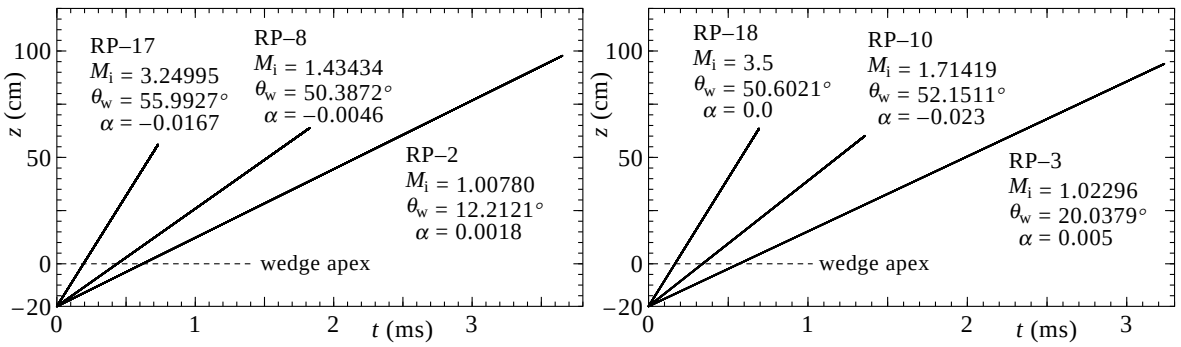

(a) In argon as a chain of 8946, 8376 and 8688 dots for RP–2, 8 and 17, respectively, when the AMR level $n_r = 12$.

(b) In air as a chain of 4699, 4131 and 4702 dots for RP–3, 10 and 18, respectively, when the AMR level $n_r = 11$.

Figure 7.6: Incident shock-front trajectories.

along with relevant intermediate equations and the curve-fit coefficients $\hat{b}$ and $\hat{a}$ given by

$$\hat{b} = \frac{ae - bd}{ac - b^2}, \tag{7.31}$$

$$\hat{a} = \frac{d - b\hat{b}}{a}, \tag{7.32}$$

where

$$a = \overline{\left(t_i - \overline{t_i}\right)^2} = \overline{t_i^2} - \overline{t_i}^2, \tag{7.33}$$

$$b = \overline{\left(t_i - \overline{t_i}\right)\left(t_i^2 - \overline{t_i^2}\right)} = \overline{t_i^3} - \overline{t_i}\,\overline{t_i^2}, \tag{7.34}$$

$$c = \overline{\left(t_i^2 - \overline{t_i^2}\right)^2} = \overline{t_i^4} - \overline{t_i^2}^2, \tag{7.35}$$

$$d = \overline{\left(z_i - \overline{z_i}\right)\left(t_i - \overline{t_i}\right)} = \overline{z_i t_i} - \overline{z_i}\,\overline{t_i}, \tag{7.36}$$

$$e = \overline{\left(z_i - \overline{z_i}\right)\left(t_i^2 - \overline{t_i^2}\right)} = \overline{z_i t_i^2} - \overline{z_i}\,\overline{t_i^2}. \tag{7.37}$$

The first-order solution is obtained by setting $\hat{b} = 0$ in Eqs. (7.30) to (7.32). The data used for the incident shock-front curve fits are always confined to the region of z from 10 cm to the end of the computer run when the incident shock reaches the final distance of about $z_e = (1\text{ m})\cos(\theta_\text{w})$ along the top boundary, or a corresponding distance along the wedge of 1 m. The curve fits are more accurate when the distance-time data corresponds to the incident shock reflecting from the wedge surface, because the time steps are then smaller than when the incident shock has not yet reached the wedge apex.

The goodness of the curve fit is tied closely to the standard deviation of the data from the fitted curve, which is calculated as

$$\sigma_z = \left[\frac{1}{m}\sum_{i=1}^{m}\left\{z(t_i) - z_i\right\}^2\right]^{1/2}, \tag{7.38}$$

for which m is the number of (z_i, t_i) data pairs. For the incident shock in this study, the standard deviations were approximately 18, 9 and 4 microns for AMR levels $n_\text{r} = 10$, 11 and 12, respectively, which correspond to about 1/8 of the size of the smallest computational cell edges within the flow field.

The incident shock-front velocity follows from the derivative of Eq. (7.30) and is given by

$$V_\text{i} = \hat{a} + 2\hat{b}t_e, \tag{7.39}$$

in which t_e is the time at the end of the computer run corresponding to the final distance z_e. For the trajectory data illustrated in Fig. 7.6(a) for RP–2, 8 and 17 in argon, the processing of the CFD simulations via Eq. (7.39) yielded incident shock-front velocities of 322.3984, 458.8673 and 1039.7366 m/s. These computed values are in excellent agreement with the corresponding theoretical values from the Rankine-Hugoniot equations that were utilized to initiate the computer

runs, differing by 0.0019, 0.0016 and 0.0042%, respectively. For the trajectory data illustrated in Fig. 7.6(b) for RP–3, 10 and 18 in air, the post-processing of the CFD simulations via Eq. (7.39) yielded incident shock-front velocities of 352.151, 590.216 and 1205.028 m/s. These computed values differ from the corresponding theoretical values by 0.02, 0.008 and 0.005%, respectively. Although the incident shock trajectories in the CFD simulations are extremely linear and a straight-line fit could have been used to fit the data instead of the second-order polynomial, the second term $2\hat{b}t_e \ll \hat{a}$ in Eq. (7.39), such that the incident shock velocity V_i is dictated primarily by the value of $\hat{a}$ from Eq. (7.32).

7.4 Mach-Stem Trajectory and Speed

In order to categorize the shock-reflection behaviour, the objective is to determine the distance-time trajectory of the center of the Mach-stem shock front along the wedge and calculate therefrom the Mach-stem speed from the time derivative of this trajectory. Although the process is similar to that for the incident shock front in the previous section, there are some significant differences to explain and difficulties to overcome.

During the collection of CFD simulation data that is used to perform the Mach-stem trajectory calculations, all of the cells along the wedge surface, in the order of the cells ahead to behind the Mach stem, are probed for each time step just before AMR is activated (i.e. every

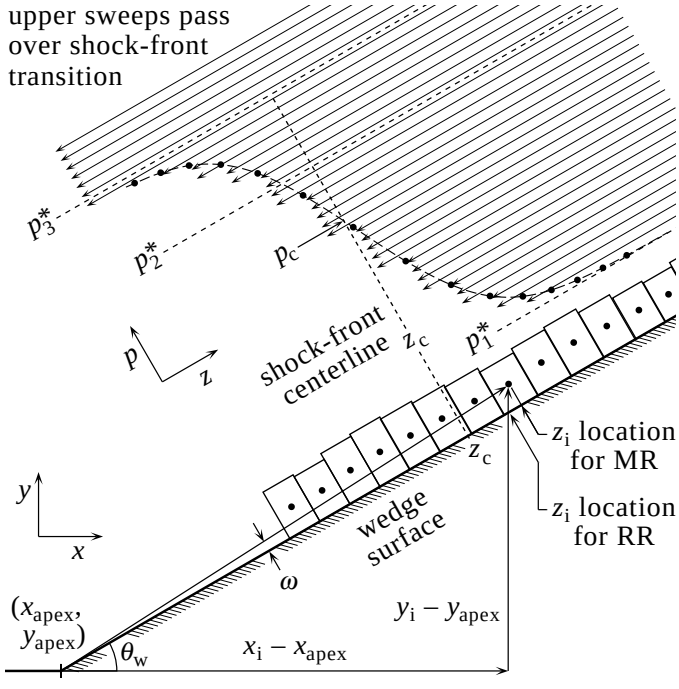

Figure 7.7: Capturing the Mach-stem shock-front transition by probing the cells along the wedge to determine the transition pressures and flow-field locations.

sixth time level), as illustrated in Fig. 7.7. This probing procedure is done with the set of specified pressures

$$p_k = p_1^\star + \frac{k}{K}\left(p_2^\star - p_1^\star\right), \quad k = 1, 2, \ldots, 3K, \tag{7.40}$$

in which $p_1^\star$ and $p_2^\star$ are the pre- and post-shock pressures of the incident shock front, and $K = 20$ is a convenient number as used previously in Eq. (7.7). The pressure difference between pressure levels (i.e. $p_{k+1} - p_k$) remains the same as that used for the incident shock front, but the pressure range has been increased substantially from $K - 1$ to $3K$, because the Mach-stem shock (when it occurs) is not only stronger than the incident shock but its post-shock pressure $p_3^\star$ is also unknown. These additional upper sweeps are required to ensure that the entire shock-front transition is captured at each time level of interest, as depicted in Fig. 7.7.

The data collected from the cell centers consist primarily of the cell pressures $p_{i,j}$ and locations ($x_{i,j}$,$y_{i,j}$). These data are converted into the pressures p_i (j is ignored) and the distances z_i, along the lower boundary before the wedge apex and then along the inclined wedge surface, by means of

$$z_i = \begin{cases} x_i - x_{\text{apex}} & \text{before wedge apex,} \\ \frac{x_i - x_{\text{apex}}}{\cos(\theta_{\text{w}})} & \text{RR at wedge surface,} \\ h\cos(\omega) & \text{MR at wedge surface,} \end{cases} \tag{7.41}$$

with relevant information shown in Fig. 7.7. Note that

$$h = \sqrt{\left(x_i - x_{\text{apex}}\right)^2 + \left(y_i - y_{\text{apex}}\right)^2}, \tag{7.42}$$

$$h\cos(\omega) = \left(x_i - x_{\text{apex}}\right)\cos(\theta_{\text{w}}) + \left(y_i - y_{\text{apex}}\right)\sin(\theta_{\text{w}}), \tag{7.43}$$

so that the calculations of the hypotenuse h, small angle ω and $h\cos(\omega)$ are not required, because $h\cos(\omega)$ in Eq. (7.41) is replaced by the results of Eq. (7.43). The first calculation of z_i covers the case of the incident shock front moving along the lower boundary, and this is equivalent to that used for the incident shock front moving along the upper boundary. The second calculation of z_i is for the case of regular reflection (without a Mach stem) when the incident shock front contacts and moves along the wedge surface, and the distance extrapolation to the wedge surface is vertically downward or parallel to the incident shock front. The third calculation of z_i covers the last case of Mach reflection when the Mach stem contacts the wedge surface and the extrapolation is parallel to the foot of the Mach stem, which is assumed normal to the wedge surface.

Each set of data for the incident or Mach-stem shock front at the wedge surface is numbered $i = 1, 2, \ldots, n''$, and it contains repeated data (i.e. same shock-front pressures and locations). These redundant data are not needed to define the shock front, so they are removed, and the number of data n'' is thereby reduced to n'. This data set still contains additional data collected from the flow-field behind the shock front, stemming from the upper sweeps that pass

the shock-front transition (see Fig. 7.7). This extraneous data is also removed from the data set by doing the calculations

$$r = \frac{z_i - z_{i+1}}{\overline{\Delta z}}, \tag{7.44}$$

where

$$\overline{\Delta z} = \frac{z_1 - z_i}{i - 1}, \tag{7.45}$$

from $i = 3, 4, \ldots, n' - 1$. If the ratio r of the current cell-center separation by the average separation is less than 1.1 for $3 \leq i \leq n' - 1$, then all of the data is kept and $n = n'$. However, if $r > 1.1$ for a particular value of i, then the calculations stop and $n = i$. This truncates all of the extraneous data behind the shock front, because n' is reduced to n. The data set (z_i,p_i), $i = 1, 2, \ldots, n$ now contains data only for the shock-front transition at the wedge surface. Note that this previous procedure is effective in capturing the shock-front transition data, because the AMR in the CFD algorithm concentrates cells of small widths within and near shock fronts.

The continuous shock-front transition $z = z(p)$ for the incident-shock or Mach-stem data is then obtained by using the curve-fit equation

$$z = \overline{z_i} + \hat{\alpha}\left[\ln\left(p - p_1^\star\right) - \overline{\ln\left(p_i - p_1^\star\right)}\right] + \hat{\beta}\left[\ln\left(p_3^\star - p\right) - \overline{\ln\left(p_3^\star - p_i\right)}\right] + \hat{\gamma}, \tag{7.46}$$

with the post-shock pressure $p_3^\star$ replacing $p_2^\star$ in Eqs. (7.8) to (7.11). This post-shock pressure $p_3^\star$ and the curve fit to the shock-front data is determined in the following manner and illustrated in Fig. 7.8. A value of $p_3^\star$ is guessed to be slightly greater than p_n from the shock-front data set. The curve-fit coefficients $\hat{\alpha}$, $\hat{\beta}$ and $\hat{\gamma}$ in Eq. (7.46) are determined by using Eqs. (7.17) to (7.26) with $p_3^\star$ replacing $p_2^\star$. The corresponding global error E is then calculated by using Eq. (7.12), once again with $p_3^\star$ replacing $p_2^\star$, and the derivative

$$\begin{aligned}\frac{\mathrm{d}E}{\mathrm{d}p_3^\star} = 2\sum_{i=1}^{n}\Bigg\{ & w_i\hat{\alpha}\left[\ln\left(p_i - p_1^\star\right) - \overline{\ln\left(p_i - p_1^\star\right)}\right] + w_i\hat{\beta}\left[\ln\left(p_3^\star - p_i\right) - \overline{\ln\left(p_3^\star - p_i\right)}\right] \\ & + w_i\hat{\gamma} - w_i\left(z_i - \overline{z_i}\right)\Bigg\} \cdot w_i\hat{\beta}\left[\left(p_3^\star - p_i\right)^{-1} - \overline{\left(p_3^\star - p_i\right)^{-1}}\right]\end{aligned} \tag{7.47}$$

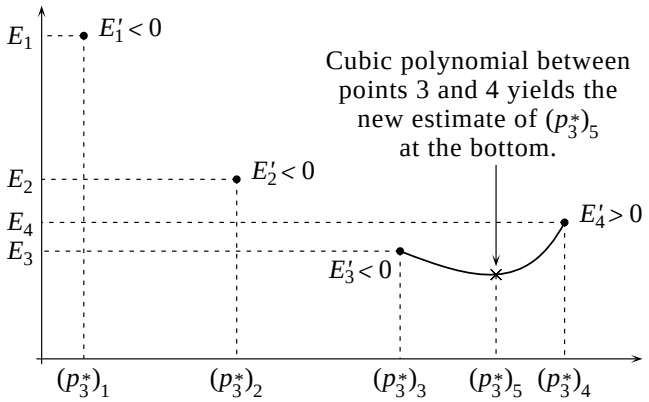

Figure 7.8: Determining the post-shock pressure $p_3^\star$ and curve fit of the Mach-stem shock front by minimizing the global error.

is calculated. This derivative should be negative if the value of $p_3^\star$ is sufficiently close to that of p_n. The value of $p_3^\star$ is then increased and the procedure is repeated until the derivative changes to a positive value. When this occurs the minimum in the global error E has been bracketed between the last two choices of $p_3^\star$, as illustrated in Fig. 7.8. A cubic polynomial is then constructed between the two data points with known slopes that bracket the global-error minimum to determine the new estimate of $p_3^\star$, which is obtained by setting the derivative of the cubic polynomial to zero. The global error E can also be calculated for this new estimate of $p_3^\star$. The process is iterative by applying the cubic polynomial between points that bracket the minimum more closely, yielding a final accurate result for $p_3^\star$. When this iteration is finished, the curve fit of the shock front is also completed, and the value of the shock-front center z_c is obtained by using $p = p_\mathrm{c} = \frac{1}{2}\,(p_1^\star + p_3^\star)$ in Eq. (7.46).

The resulting continuous shock-front transitions of the Mach stem by the preceding curve fits to CFD flow-field data are illustrated in Fig. 7.9(a) for reference points RP–6, 11 and 14 with $\alpha = 0.0$, -0.0032 and -0.007 in argon and in Fig. 7.9(b) for reference points RP–3, 9 and 17 with $\alpha = 0.015$, 0.004 and -0.0138 in air (all normal to the extreme-angle transition boundary). Shown also are the interpolated shock-front transition centers from using $p = p_\mathrm{c} = \frac{1}{2}\,(p_1^\star + p_3^\star)$ to obtain $z = z_\mathrm{c}$ in Eq (7.46). These shock-front constructions are for three cases with discrete distance-pressure shock transition data of 10, 5 and 7 for reference points RP–6, 11 and 14 in argon and 10, 6 and 4 for reference points RP–3, 9 and 17 in air, respectively. These constructions are typical of all curve fits for the Mach stem occurring in this study. It is readily

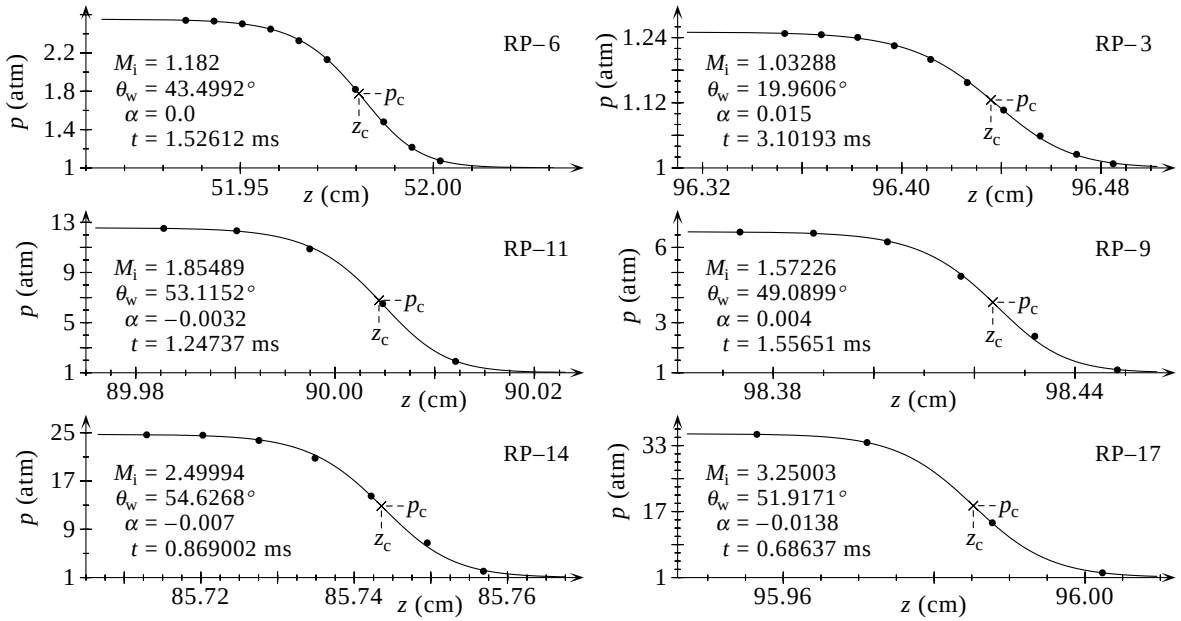

(a) In argon when the AMR level $n_\mathrm{r} = 12$.

(b) In air when the AMR level $n_\mathrm{r} = 11$.

Figure 7.9: Continuous transitions of the Mach-stem shock front constructed by curve fits using discrete CFD flow-field data.

apparent that the curve fit given by Eq. (7.46) successfully captures the Mach-stem shock-front transitions associated with the numerical solutions to the Euler equations.

The trajectory of the center of the shock front of the Mach stem along the wedge surface during a CFD run, from its start at the wedge apex and ending when it progresses along the wedge surface by about 1 m, is obtained from numerous z_c values determined at every sixth time level during the CFD run. Such results are illustrated in Fig. 7.10(a) for reference points RP–3, 7 and 20 with $\alpha = 0.009$, 0.0125 and -0.01 in argon and in Fig. 7.10(b) for reference points RP–3, 8 and 19 with $\alpha = 0.005$, 0.004 and 0.0 in air, respectively. Each shock-front trajectory is plotted as a chain of numerous small dots, each dot corresponding to the time t at which the curve fit gave the center value z_c. The Mach-stem trajectories are slightly kinked at the wedge apex ($z = 0$ cm), because the shock speed along the lower boundary before the wedge apex essentially equals that of the incident shock, but later along the wedge surface the Mach-stem shock is stronger than the incident shock and its speed is larger.

The shock-front trajectories that are presented in Fig. 7.10 for the Mach stem are typical of those obtained in this study for all of the reference points and different values of α. The two portions of each shock-front trajectory are almost linear, and the actual advancement of the center of the Mach-stem transition in the CFD simulations is always forward but jerky with distance, very similar to that for the motion of the incident shock along the upper boundary. The speed of the Mach stem along the wedge surface is determined by fitting a second-degree polynomial to the distance-time data, as given earlier by Eq. (7.30) for the incident shock wave. The distance-time data used for this curve fit spans the distances along the wedge from 50 cm to the end of the CFD run at 100 cm, or slightly larger because the Mach stem is ahead of the incident shock front. The time derivative of the curve fit then yields the Mach-stem speed $V_m = \hat{a} + 2\hat{b}t_e$ at the end of the shock-front trajectory.

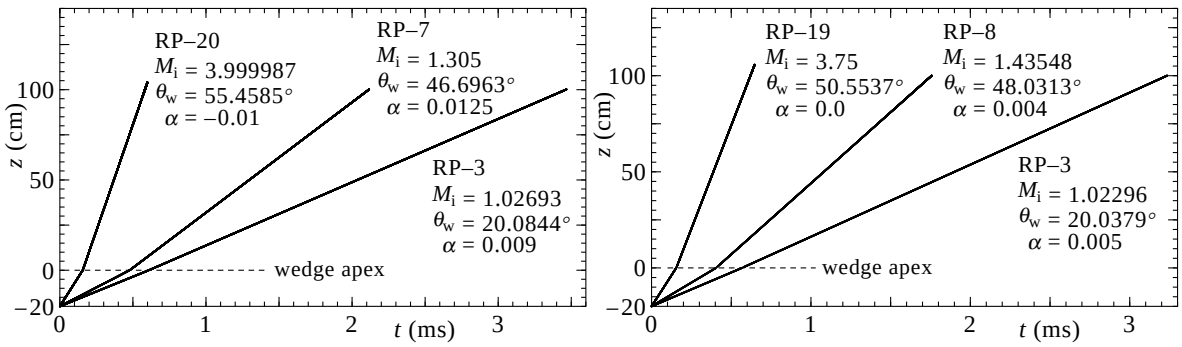

(a) In argon as a chain of 9537, 8509 and 9228 dots for RP–3, 7 and 20, respectively, when the AMR level $n_r = 12$.

(b) In air as a chain of 4689, 3972 and 4464 dots for RP–3, 8 and 19, respectively, when the AMR level $n_r = 11$.

Figure 7.10: Mach-stem shock-front trajectories.

The goodness of the polynomial fit is tied closely to the standard deviation of the data from the second-order curve fit, and the standard deviations given by

$$\sigma_z = \left[\frac{1}{m} \sum_{i=1}^{m} \{z(t_i) - z_i\}^2 \right]^{1/2} \tag{7.48}$$

can vary markedly for the case of the Mach stem, in contrast to those reported earlier for the incident shock. For regular reflection from the wedge surface the standard deviations are typically 2 to 4 times as high as those for the incident shock. For Mach reflections with large Mach stems that emerge and stabilize rapidly as the wedge apex is encountered and passed, the standard deviations are 2 to 20 times higher than those for the incident shock. However, for Mach reflections close to the numerically determined transition boundary, the emergence of an extremely small Mach stem and its stabilization with distance along the wedge is somewhat erratic, and the standard deviations are much larger as a result. In such cases the Mach stem can either emerge suddenly and then decelerate or it can emerge slowly and then accelerate to a final speed. The distance-time trajectories of such Mach stems are somewhat curved and the use of a second-order polynomial curve fit to these trajectories yields smaller standard deviations of the data from the fitted curves in comparison to those computed from a first-order polynomial curve fit.

7.5 Numerical Transition Boundary Between RR and MR from CFD Near-Field Data

The methodology and related post-processing tools developed and described in the previous sections of this chapter are now combined to determine the numerical transition boundary between regular and Mach reflections by processing the CFD flow-field data for the 20 reference points defined earlier in tables 7.1(a) and 7.1(b) for argon and atmospheric air, respectively, and shown previously in Figs. 7.1(a) and 7.1(b) as well.

Plots of the Mach-stem length L versus the parameter α (normal to von Neumann's extreme-angle boundary) are shown in Fig. 7.11 for reference points RP–3, 7, 11, 15 and 18 in argon as well as air. Each plot originates from the post-processing of numerous closely spaced CFD flow fields around the numerical transition boundary (i.e. near-field data), such that the transition value α_c can be obtained accurately when the Mach-stem length L from Mach reflection patterns diminishes to zero and the Mach reflection configurations first switch into that of a regular reflection.

The method of obtaining the numerical transition boundary from such L versus α plots is explained. Two sets of post-processed data are determined for each plot shown in Fig. 7.11. The first data set originates from calculations for which all shock reflection patterns from the wedge

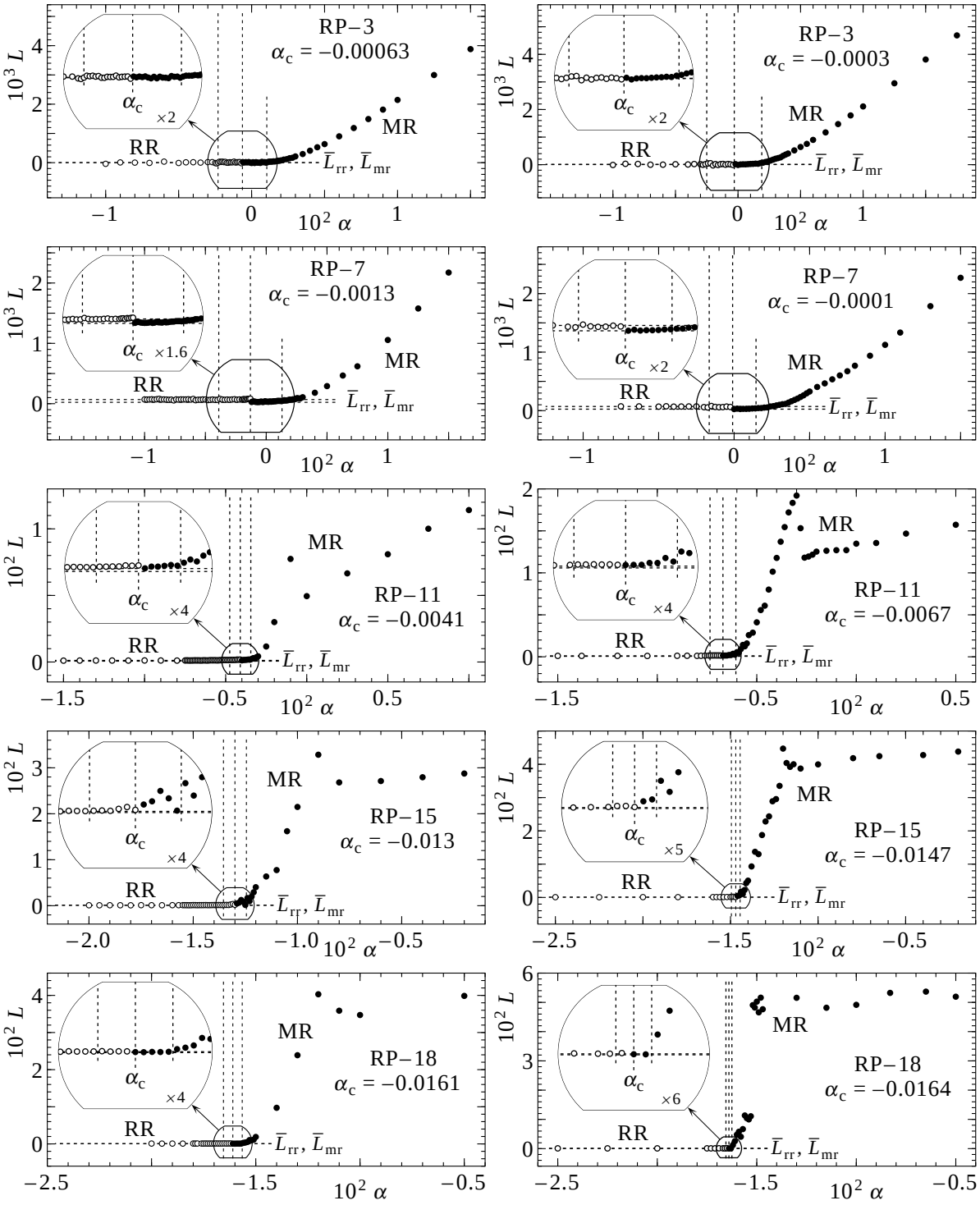

Figure 7.11: Mach-stem length L versus the parameter α in argon (left-hand side) and air (right-hand side) for RP–3, 7, 11, 15 and 18, when the AMR level $n_r = 12$.

surface are assumed to be regular reflection, and the data for z_i in the post-processing phase is mapped downward onto the wedge surface, parallel to the incident shock wave, as illustrated earlier in Fig. 7.7. Some of these data are shown on the left side of the plots in Fig. 7.11 as the white-filled circles, and they are labelled RR for regular reflection. The second data set originates from calculations for which all shock reflection patterns from the wedge surface are assumed to be Mach reflection, and the data for z_i in the post-processing phase is mapped onto the wedge surface, normal to the surface and parallel to the Mach stem (if it exists or it does not), as also illustrated earlier in Fig. 7.7. Some of these data are shown on the right side of the plots in Fig. 7.11 as the black-filled circles or black dots, and they are labelled MR for Mach reflection. The average value of the left-most data for the RR white-filled circles in each plot is calculated, denoted by $\overline{L}_{\rm rr}$, and shown as a horizontal dashed line in each plot given in Fig. 7.11. The average value of the left-most data for the MR black dots (not shown on the left side of each plot) is also calculated, denoted by $\overline{L}_{\rm mr}$, and shown as another horizontal dashed line. Both averages are nearly zero because they correspond to regular-reflection patterns, the average $\overline{L}_{\rm mr}$ is always lower than $\overline{L}_{\rm rr}$, and the differences between the two are noticeable only for incident shock Mach numbers $M_{\rm i}$ between 1.1 to 1.7 and wedge angles from 40 to 50°.

The data for the case of regular reflection (white-filled circles) are more sensitive to the emergence of the Mach stem than the data for the case of Mach reflection (black dots). For the case of the mapping of z_i downward onto the wedge surface (parallel to the incident shock), a disturbance must have a speed slightly greater than the incident shock speed $V_{\rm i}$ to emerge as a partial or full Mach stem. For the other case of the mapping of z_i normal to the wedge surface (parallel to the Mach stem), a disturbance must have a speed slightly greater than $V_{\rm i}/\cos(\theta_{\rm w})$ to emerge as a partial or full Mach stem.

As α increases in the plots shown in Fig. 7.11, the regular-reflection data therefore indicates the early or premature arrival of the onset of Mach reflection, whereas the Mach reflection data indicates the late or delayed arrival of the onset of Mach reflection. Hence, the first indication in the regular-reflection data of a disturbance or Mach stem is flagged, and shown by the leftmost vertical dashed line among the white-filled circles in the plots in Fig. 7.11. Furthermore, the delayed indication in the Mach-reflection data of a strong change to a Mach stem is correspondingly flagged, and shown by the rightmost vertical dashed line among the black dots.

These two flag placements are based on changes in the data by about 2 or more standard deviations from the average values of $\overline{L}_{\rm rr}$ and $\overline{L}_{\rm mr}$. The numerical transition-boundary value of α, denoted by $\alpha_{\rm c}$, is simply taken as the center value or average of the early and late indications of the emergence of a Mach stem. Furthermore, once the center value $\alpha_{\rm c}$ has been determined, only the regular-reflection data (white-filled circles) are plotted on the left-hand side of this center value, and only the Mach-reflection data (black dots) are plotted on the right-hand side, as illustrated in all of the plots in Fig. 7.11.

The plots of L versus α for incident shock Mach numbers $M_{\rm i}$ ranging from 1.0 to 1.5, before the dual region of regular and Mach reflection shown in Fig. 7.1, exhibit fairly gradually and smoothly changing values of L from large values in the Mach reflection region to zero (or nearly zero) as the numerical transition boundary is approached. See such changes in Fig. 7.11 for reference points RP–3 and 7. This also means that the change in the size of the Mach stem from Mach to regular reflection is also fairly smooth and gradual, occurring over a wide range of α values and diminishing slowly to zero as the transition boundary is approached.

For the case of higher incident shock Mach numbers from 1.5 to 4.0 (and upward), in the dual region of regular and Mach reflection, the reduction in the size of the Mach stem from Mach to regular reflection is much more rapid and even discontinuous, occurring over a narrow range of α values. See such changes in Fig. 7.11 for reference points RP–11, 15 and 18. Such nearly discontinuous Mach-stem changes from Mach to regular reflection at the transition boundary, from a sizable Mach stem to no Mach stem, were noticed and explained in the early experimental results and theoretical research by Bleakney and Taub [8] and Kawamura and Saito [10].

The L versus α results presented in this research for the stronger incident shocks are smoothed somewhat through the numerical transition boundary from the numerical computations that ensure solution monotonicity near discontinuities. Note that the width of this smearing is reduced when the accuracy of the CFD simulations is improved by increasing the number of AMR levels. The 12 refinement levels for AMR used in this research were carefully selected by assessment testing to ensure that the numerical transition boundary was accurately defined and essentially independent of the mesh densities used in the CFD simulations. See Subsection 7.6 for further discussion of CFD flow-field convergence and solution accuracy.

The entire set of post-processed data for the twenty reference points on von Neumann's extreme-angle transition boundary are included for completeness in Appendix A for argon and in Appendix B for atmospheric air.

Contoured flow-fields images from CFD simulations for Mach reflection changing to regular reflection are presented in Figs. 7.12 and 7.13 for reference points RP–6 and 18 in argon and in Figs. 7.14 and 7.15 for reference points RP–5 and 16 in air. Each collection of four images is arranged normal to von Neumann's extreme-angle transition boundary and features in sequence two Mach-reflection patterns with diminishing Mach-stem lengths, then the pattern at the numerical transition boundary when the Mach stem just disappears, and finally one regular-reflection pattern just beyond this transition boundary. These images are focused on the shock-reflection patterns close to the wedge surface, and the lengths of 5 mm and 5 cm that are included in these figures provide a reference length scale.

The SMR patterns presented in Figs. 7.12(a) and 7.12(b) for RP–6 argon and in Figs. 7.14(a) and 7.14(b) for RP–5 in air occur rather far from the numerical transition-boundary values of $\alpha_{\rm c} = -0.0011$ and 0.0001 that are shown in Figs. 7.12(c) and 7.14(c), respectively. In these

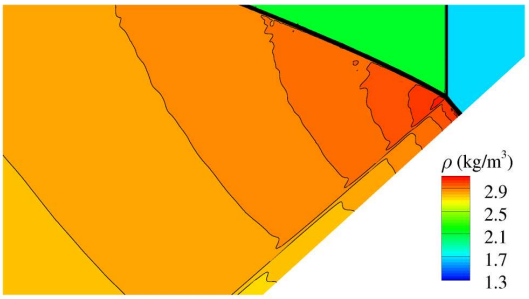

(a) SMR: $\alpha = 0.0175$, $L = 0.001665$, $M_\mathrm{i} = 1.19135$, $\theta_\mathrm{w} = 42.3418°$; $V_\mathrm{i} = 381.13$ m/s, $V_\mathrm{m} = 516.50$ m/s.

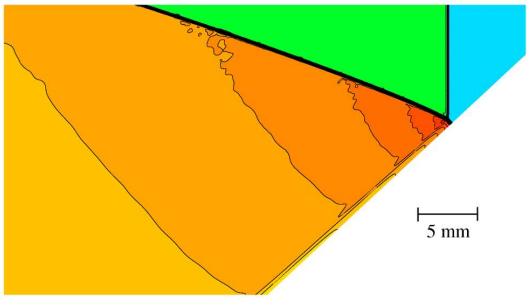

(b) SMR: $\alpha = 0.009$, $L = 0.000457$, $M_\mathrm{i} = 1.18681$, $\theta_\mathrm{w} = 42.9012°$; $V_\mathrm{i} = 379.67$ m/s, $V_\mathrm{m} = 518.54$ m/s.

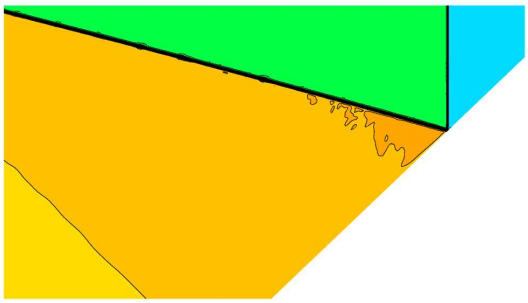

(c) Transition: $\alpha = -0.0011$; $L \approx 0$; $M_\mathrm{i} = 1.18141$, $\theta_\mathrm{w} = 43.5726°$; $V_\mathrm{i} = 377.95$ m/s, $V_\mathrm{m} = 521.70$ m/s.

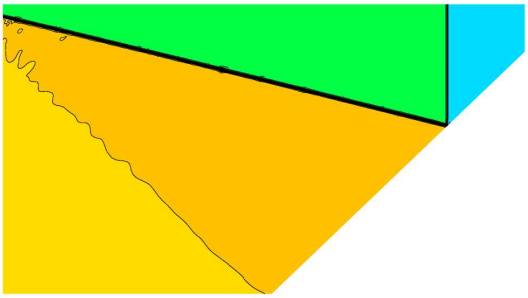

(d) RR: $\alpha = -0.0036$, $L \approx 0$; $M_\mathrm{i} = 1.18008$, $\theta_\mathrm{w} = 43.7400°$; $V_\mathrm{i} = 377.52$ m/s, $V_\mathrm{m} = 522.57$ m/s.

Figure 7.12: Transition from MR to RR for RP–6 in argon ($M_\mathrm{i}^\star = 1.182$, $\theta_\mathrm{w}^\star = 43.4991°$, $n_\mathrm{r} = 12$).

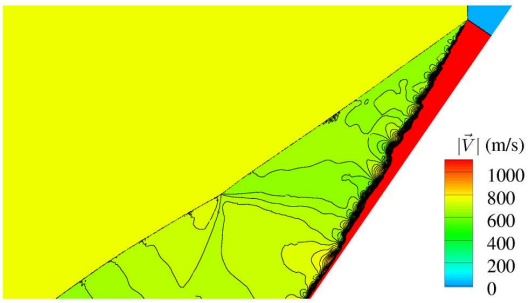

(a) DMR: $\alpha = -0.01$, $L = 0.034718$; $M_\mathrm{i} = 3.49998$, $\theta_\mathrm{w} = 55.3751°$; $V_\mathrm{i} = 1119.72$ m/s, $V_\mathrm{m} = 2039.06$ m/s.

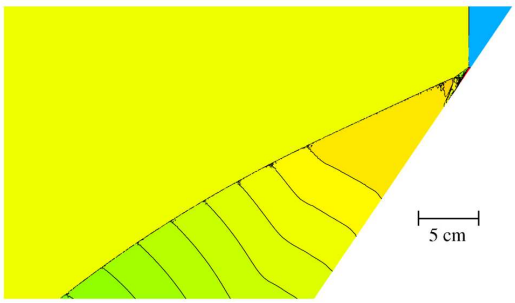

(b) DMR: $\alpha = -0.014$, $L = 0.009722$; $M_\mathrm{i} = 3.49997$, $\theta_\mathrm{w} = 55.7805°$; $V_\mathrm{i} = 1119.72$ m/s, $V_\mathrm{m} = 2010.45$ m/s.

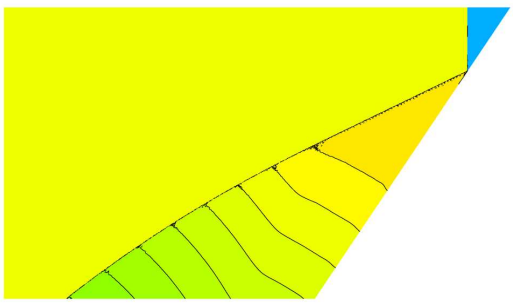

(c) Transition: $\alpha = -0.0161$, $L \approx 0$; $M_\mathrm{i} = 3.49997$, $\theta_\mathrm{w} = 55.9950°$; $V_\mathrm{i} = 1119.72$ m/s, $V_\mathrm{m} = 2002.43$ m/s.

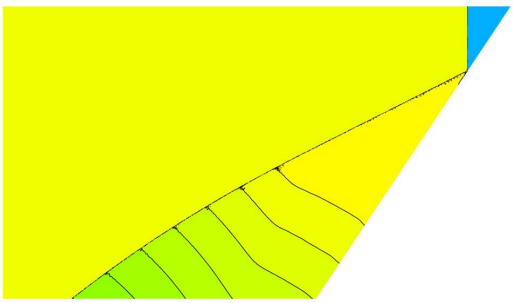

(d) RR: $\alpha = -0.0185$, $L \approx 0$; $M_\mathrm{i} = 3.49996$, $\theta_\mathrm{w} = 56.2417°$; $V_\mathrm{i} = 1119.72$ m/s, $V_\mathrm{m} = 2015.17$ m/s.

Figure 7.13: Transition from MR to RR for RP–18 in argon ($M_\mathrm{i}^\star = 3.5$, $\theta_\mathrm{w}^\star = 54.3792°$, $n_\mathrm{r} = 12$).

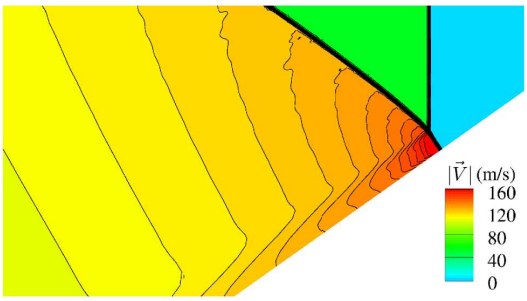

(a) SMR: $\alpha = 0.015$, $L = 0.001238$; $M_\mathrm{i} = 1.10176$, $\theta_\mathrm{w} = 35.3386°$; $V_\mathrm{i} = 379.29$ m/s, $V_\mathrm{m} = 465.53$ m/s.

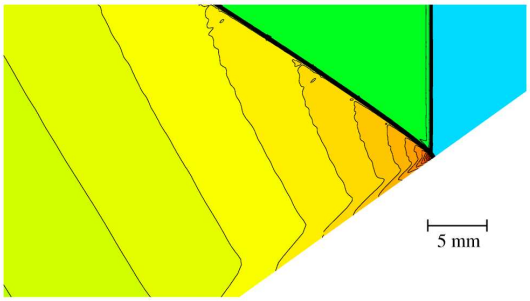

(b) SMR: $\alpha = 0.0075$, $L = 0.000306$; $M_\mathrm{i} = 1.09538$, $\theta_\mathrm{w} = 35.6161°$; $V_\mathrm{i} = 377.09$ m/s, $V_\mathrm{m} = 464.00$ m/s.

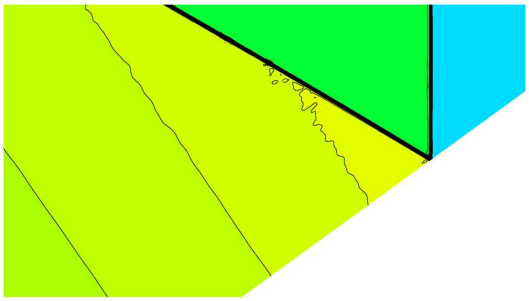

(c) Transition: $\alpha = 0.0001$; $L \approx 0$; $M_\mathrm{i} = 1.08909$, $\theta_\mathrm{w} = 35.8908°$; $V_\mathrm{i} = 374.92$ m/s, $V_\mathrm{m} = 462.82$ m/s.

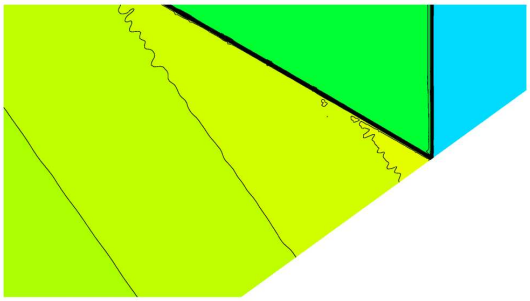

(d) RR: $\alpha = -0.0005$, $L \approx 0$; $M_\mathrm{i} = 1.08857$, $\theta_\mathrm{w} = 35.9131°$; $V_\mathrm{i} = 374.75$ m/s, $V_\mathrm{m} = 462.73$ m/s.

Figure 7.14: Transition from MR to RR for RP–5 in air ($M_\mathrm{i}^\star = 1.089$, $\theta_\mathrm{w}^\star = 35.8945°$, $n_\mathrm{r} = 12$).

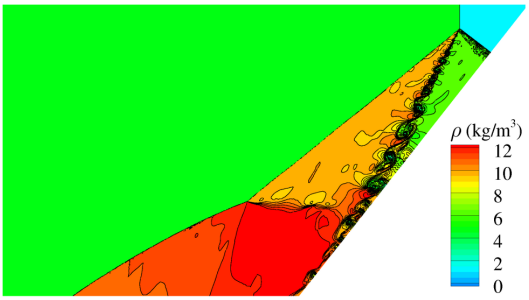

(a) DMR: $\alpha = -0.0126$, $L = 0.045962$; $M_\mathrm{i} = 3.00000$, $\theta_\mathrm{w} = 51.8573°$; $V_\mathrm{i} = 1032.87$ m/s, $V_\mathrm{m} = 1749.20$ m/s.

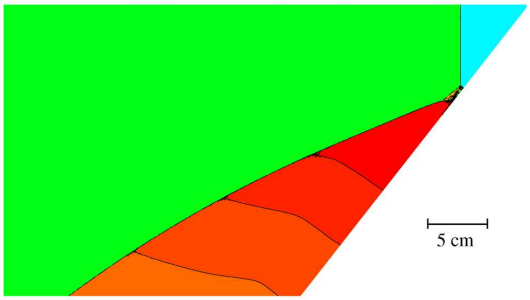

(b) DMR: $\alpha = -0.0138$, $L = 0.020689$; $M_\mathrm{i} = 3.00003$, $\theta_\mathrm{w} = 51.9688°$; $V_\mathrm{i} = 1032.87$ m/s, $V_\mathrm{m} = 1711.18$ m/s.

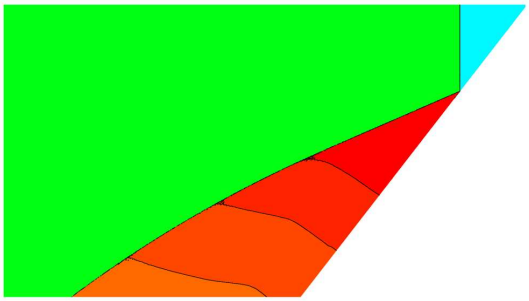

(c) Transition: $\alpha = -0.0154$, $L \approx 0$; $M_\mathrm{i} = 3.00003$, $\theta_\mathrm{w} = 52.1178°$; $V_\mathrm{i} = 1032.87$ m/s, $V_\mathrm{m} = 1682.41$ m/s.

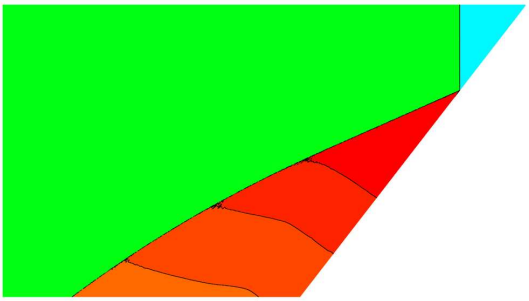

(d) RR: $\alpha = -0.0165$, $L \approx 0$; $M_\mathrm{i} = 3.00004$, $\theta_\mathrm{w} = 52.2206°$; $V_\mathrm{i} = 1032.87$ m/s, $V_\mathrm{m} = 1686.17$ m/s.

Figure 7.15: Transition from MR to RR for RP–16 in air ($M_\mathrm{i}^\star = 3.0$, $\theta_\mathrm{w}^\star = 50.7032°$, $n_\mathrm{r} = 12$).

computed flow-field images, the Mach stems and slip streams are otherwise too small to be easily observed by the human eye, i.e. for α values that are sufficiently close to the numerical transition boundary. The opposite is true for the DMR patterns presented in Figs. 7.13(a) and 7.13(b) for RP–18 in argon and in Figs. 7.15(a) and 7.15(b) for RP–16 in air. In these computed flow-field images (close to the numerical transition-boundary values of $\alpha_c = -0.0161$ and -0.0154 that are shown in Figs. 7.13(c) and 7.15(c), respectively), the Mach stems and slip streams are much more pronounced, because these results occur in the dual region where either Mach or regular reflection can occur.

The triple point trajectory angles χ, corresponding to the Mach-reflection patterns in argon shown in Figs. 7.12(a) and 7.13(a) with the largest Mach stems, are given by 0.105° and 1.33°, respectively. The triple-point angles for the Mach-reflection patterns in argon shown in Figs. 7.12(b) and 7.13(b), with slightly smaller Mach stems (i.e. closer to the numerical transition boundary), are given by 0.0282° and 0.375°, respectively. The related set of triple-point angles χ for Mach-reflection patterns in air are given by 0.100°, 1.98°, 0.0245° and 0.908°, corresponding to the CFD flow-fields illustrated in Figs. 7.14(a), 7.15(a), 7.14(b) and 7.15(b), respectively. All of these angles were calculated by using Eq. (7.6) and the information on L and θ_w provided in the captions. These calculated values of the triple-point trajectory angles χ are more precise than those that can be measured directly from CFD flow-field images, such as those in Figs. 7.12 through 7.15.

The numerical transition-boundary points from post-processing all of the CFD flow-field data for the twenty reference points on von Neumann's extreme-angle transition boundary are summarized in table 7.2 for argon and air. The values of the transition value α_c from data like those shown in Fig. 7.11, and the corresponding incident shock Mach number M_i and wedge angle θ_w calculated by using Eqs. (7.2) and (7.3), appear in columns 4 to 6 for each gas.

(This space intentionally left blank.)

Table 7.2: Numerical transition boundary between regular and Mach reflections for a wedge without a boundary layer.

(a) Argon.

RP	reference points		numerical transition points		
	$M_{\mathrm{i}}^{\star}$	$\theta_{\mathrm{w}}^{\star}$ (°)	α_{c}	M_{i}	θ_{w} (°)
1	1.001	5.1010	0.00022	1.00122	5.1007
2	1.006	12.2184	−0.00060	1.00540	12.2206
3	1.018	20.1533	−0.00063	1.01738	20.1581
4	1.041	28.0871	−0.00020	1.04081	28.0903
5	1.089	36.3558	−0.00050	1.08857	36.3741
6	1.182	43.4992	−0.00110	1.18141	43.5726
7	1.305	47.7127	−0.00130	1.30466	47.8195
8	1.435	49.9799	−0.00080	1.43489	50.0505
9	1.572	51.3539	−0.00080	1.57193	51.4271
10	1.715	52.2405	−0.00270	1.71486	52.4935
11	1.855	52.8110	−0.00410	1.85486	53.2012
12	2.0	53.2183	−0.00670	1.99984	53.8641
13	2.25	53.6680	−0.00945	2.24987	54.5920
14	2.5	53.9398	−0.01160	2.49990	55.0847
15	2.75	54.1151	−0.01300	2.74992	55.4060
16	3.0	54.2340	−0.01460	2.99994	55.6911
17	3.25	54.3179	−0.01510	3.24996	55.8291
18	3.5	54.3792	−0.01610	3.49997	55.9950
19	3.75	54.4252	−0.01625	3.74997	56.0583
20	4.0	54.4606	−0.01640	3.99998	56.1106

Table 7.2 (continued): Numerical transition boundary between regular and Mach reflections for a wedge without a boundary layer.

(b) Atmospheric air.

RP	reference points		numerical transition points		
	$M_{\mathrm{i}}^{\star}$	$\theta_{\mathrm{w}}^{\star}$ (°)	α_{c}	M_{i}	θ_{w} (°)
1	1.001	5.0997	0.0003	1.00130	5.0993
2	1.006	12.2012	−0.0001	1.00590	12.2016
3	1.018	20.0766	−0.0003	1.01770	20.0789
4	1.041	27.8798	−0.0008	1.04023	27.8929
5	1.089	35.8945	−0.0002	1.08883	35.9020
6	1.182	42.6428	−0.0001	1.18195	42.6495
7	1.305	46.4516	−0.0001	1.30498	46.4596
8	1.435	48.3727	−0.0001	1.43499	48.3812
9	1.572	49.4404	−0.0019	1.57188	49.6077
10	1.715	50.0537	−0.0040	1.71486	50.4117
11	1.855	50.3927	−0.0067	1.85487	50.9986
12	2.0	50.5908	−0.0091	1.99990	51.4194
13	2.25	50.7392	−0.0121	2.24996	51.8478
14	2.5	50.7684	−0.0137	2.50000	52.0265
15	2.75	50.7463	−0.0147	2.75002	52.0970
16	3.0	50.7032	−0.0156	3.00003	52.1365
17	3.25	50.6529	−0.0160	3.25004	52.1220
18	3.5	50.6021	−0.0164	3.50004	52.1068
19	3.75	50.5537	−0.0167	3.75003	52.0847
20	4.0	50.5090	−0.0170	4.00003	52.0665

7.6 Study of Mesh Refinement on Solution Accuracy

An investigation was performed to determine the effects of mesh refinement on the accuracy of the CFD flow-field solutions and the subsequent post-processing determination of the new numerical transition boundary between regular and Mach reflections. The assessment was performed to evaluate the resolution requirements in argon and atmospheric air for the twenty selected reference points (table 7.1) to yield the set of twenty transition points for the transition value α_c, related incident shock Mach number M_i and related wedge angle θ_w reported in table 7.2 for each gas. This study was done to demonstrate that the mesh was sufficiently refined at twelve levels of anisotropic adaptive mesh refinement (AMR) such that the final results for the new numerical transition boundary were converged (i.e. grid independent) and considered accurate.

Four plots of the normalized Mach-stem length L versus the parameter α for AMR levels $n_r = 10$, 11, 12 and 13 are presented for reference points RP–5 and 16 in Fig. 7.16 for argon and in Fig. 7.17 for atmospheric air. The results for RP–5 for each gas are typical of all reference points for incident shock Mach numbers in the range $1.0 < M_i < 1.6$, for which the new numerical transition boundary agrees well with the closely spaced sonic and extreme-angle boundaries of von Neumann [5]. The results for RP–16 for each gas are typical of all reference points for incident shock Mach numbers in the range $1.6 < M_i < 4.0$, for which the new numerical transition boundary trends above the closely spaced sonic and extreme-angle boundaries into the dual region of regular and Mach reflections.

As the mesh is refined from AMR levels $n_r = 10$ to 13 for reference points RP–5 and 16 in Fig. 7.16 for argon and in Fig. 7.17 for atmospheric air, (i) the two averages $\overline{L}_{rr}$ and $\overline{L}_{mr}$ become more equal and converge toward the true value of zero, (ii) the variations in the data for regular reflection (white-filled circles) diminishes substantially (especially for RP–1 to 8), (iii) the variations in the data for Mach reflection (black dots) diminishes marginally, (iv) the bottom transition region between regular and Mach reflections becomes narrower (RP–5) and sharper (RP–16), and (v) the early and late indicators of the emergence of a Mach stem, denoted by the two outer vertical dashed lines, contract for increasing mesh refinement levels of AMR. However, the average of these early and late indications, given by the center dashed line labelled α_c, shifts slightly leftward (away from the sonic and extreme-angle boundaries), less and less as the value of α_c converges to a nearly constant value. Note that the accuracy of the post-processed L versus α results is generally better for stronger incident shocks ($M_i > 1.6$) within the dual region of regular and Mach reflections than it is for weaker incident shocks ($1.0 < M_i < 1.6$) before the dual region. For example, compare the transition profiles of RP–16 with those of RP–5 for a given AMR level in Figs. 7.16 and 7.17.

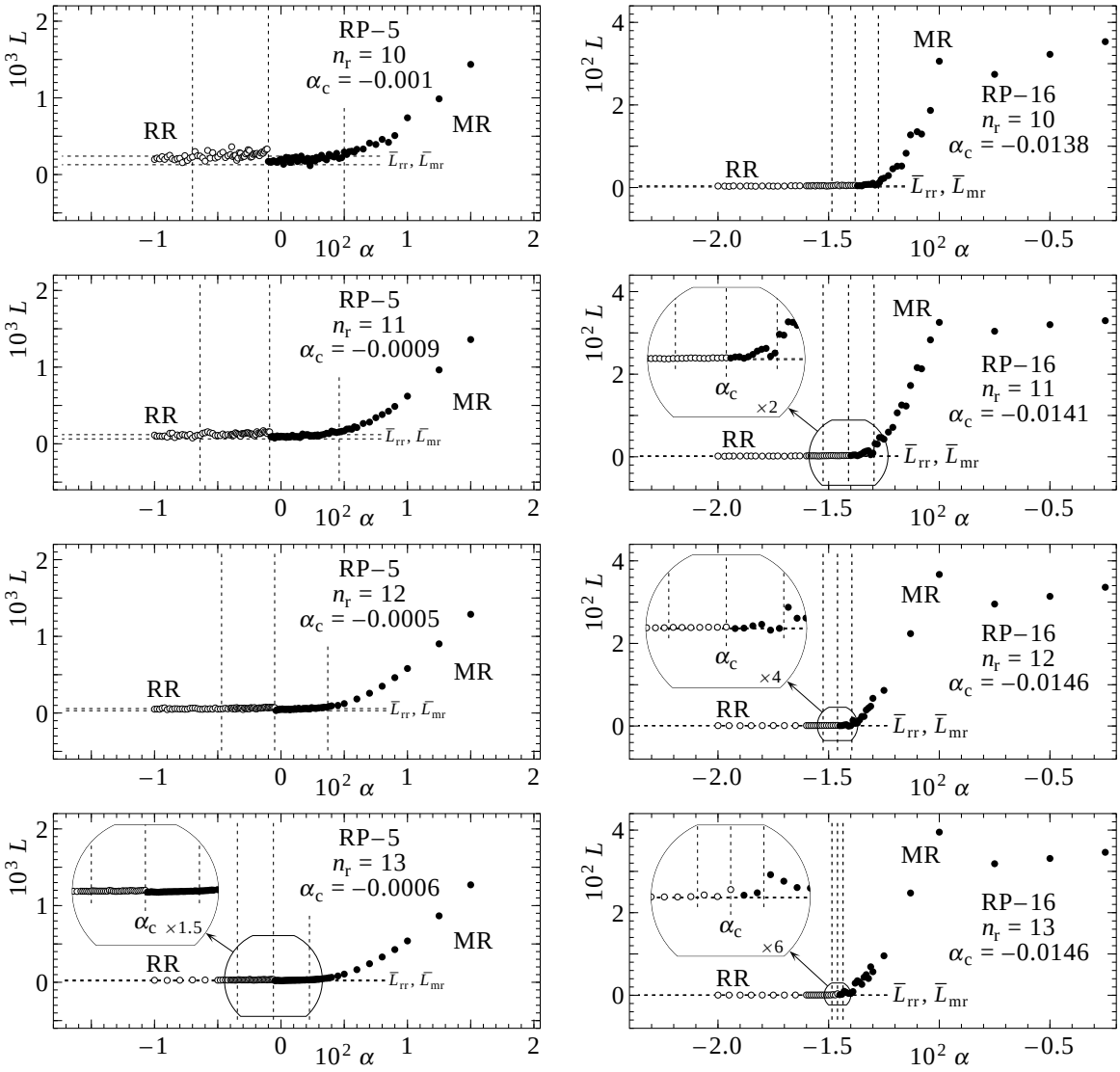

Figure 7.16: Mach-stem length L versus parameter α for RP–5 (left-hand side) and RP–16 (right-hand side) in argon, when the AMR level $n_r = 10$, 11, 12 and 13.

The small changes in the transition values of α_c for RP–5 and 16 with increasing AMR levels $n_r = 10$ to 13, as shown in Fig. 7.16 for argon and in Fig. 7.17 for atmospheric air, are not significant in changing the numerically determined transition-boundary points (M_i, θ_w) presented in table 7.2. If the early and late vertical dashed-line indicators of the emergence of the Mach stem in the plots of L versus α are considered as error bars on the transition value of α_c, then the results presented in table 7.2 for M_i and θ_w computed using twelve levels of AMR are accurate in the worst cases to within ±0.33% and ±0.47%, respectively, in argon and ±0.22% and ±0.27%, respectively, in atmospheric air, for all twenty reference points selected along von Neumann's extreme-angle transition boundary. The resulting error bars on symbols used to plot the incident shock Mach number M_i versus the wedge angle θ_w for the numerically

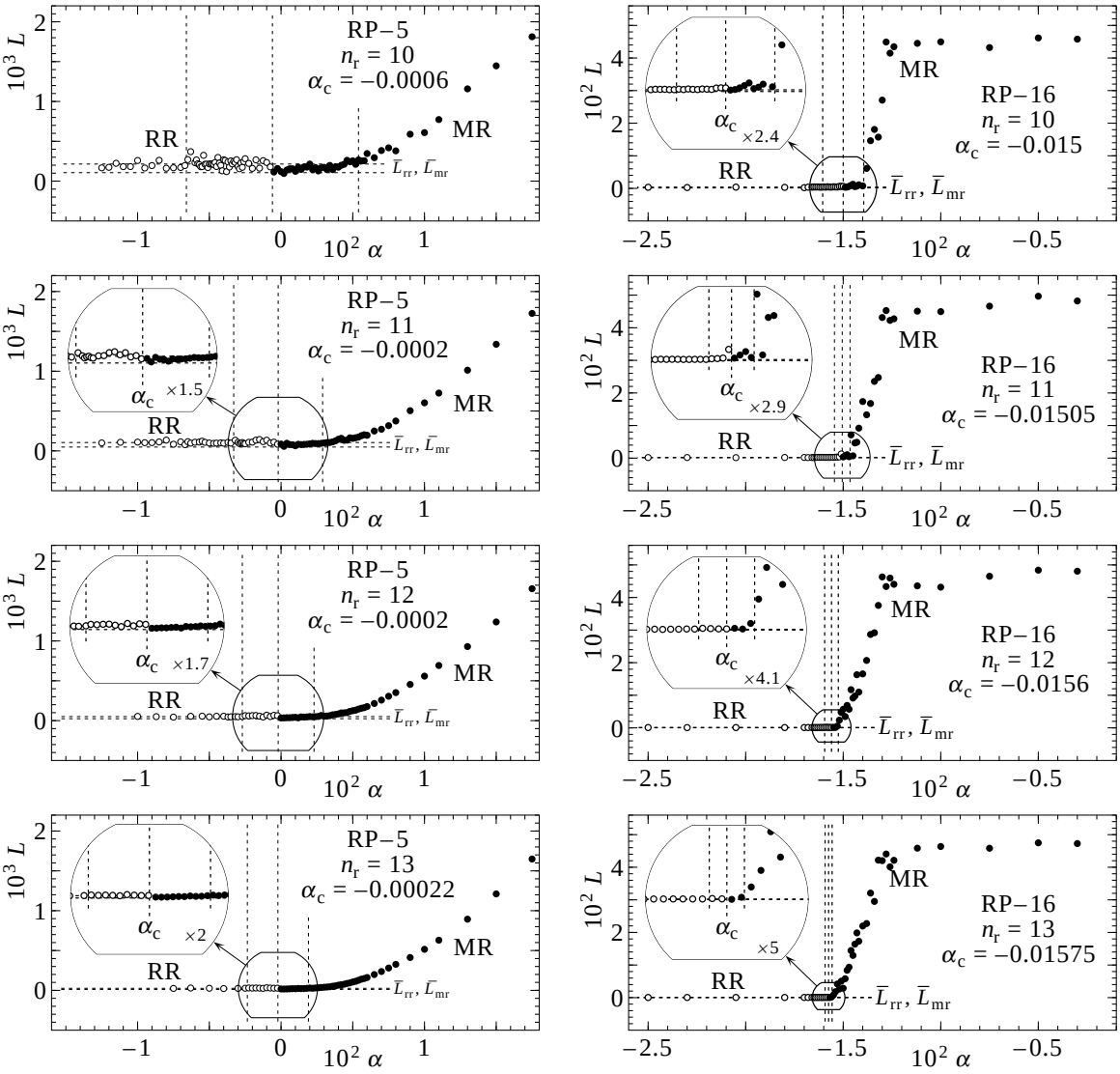

Figure 7.17: Mach-stem length L versus parameter α for RP–5 (left-hand side) and RP–16 (right-hand side) in air, when the AMR level $n_r = 10$, 11, 12 and 13.

determined transition points (like data shown in Fig. 1.2) are not noticeable, because they would each be covered by the white-filled circles or black-dot markers used to plot these points.

The use of twelve levels of AMR is considered sufficient to accurately determine the new transition boundary separating regular and Mach reflections in this research. This conclusion is based on the present mesh refinement study on CFD solution accuracy, in conjunction with the preceding results presented in sections 7.3 and 7.4 that illustrate the high accuracy of the post-processing method in the computations of the incident and Mach shock speeds V_i and V_m, respectively. At the mesh resolution of twelve levels of AMR, the predicted CFD flow-field solutions and post-processed transition-boundary points are considered as essentially independent of the mesh densities used for the CFD simulations.

7.7 Alternate Numerical Transition Boundary Between RR and MR from CFD Far-Field Data

The plots of the characteristic Mach-stem length L versus the parameter α (normal to the extreme-angle transition boundary), similar to those presented previously in Fig. 7.11(a) for argon, are replotted herein in terms of the triple-point angle χ versus α. The angle χ is defined in Fig. 7.2. The change from using the Mach-stem length L to the triple-point angle χ is done by means of Eq. (7.6). Four plots of the alternate representations of the data for determining the transition boundary between regular and Mach reflection are presented in Fig. 7.18 for reference points RP–13, 15, 18 and 20, which correspond to the reference incident shock Mach numbers $M_{\mathrm{i}}^{\star}$ on the extreme-angle boundary of 2.25, 2.75, 3.5 and 4.0, respectively. These results for χ versus α correspond to incident shock Mach numbers within the range $1.5 < M_{\mathrm{i}} < 4.0$ for the dual region of regular and Mach reflection in argon, shown previously in Fig. 7.1(a).

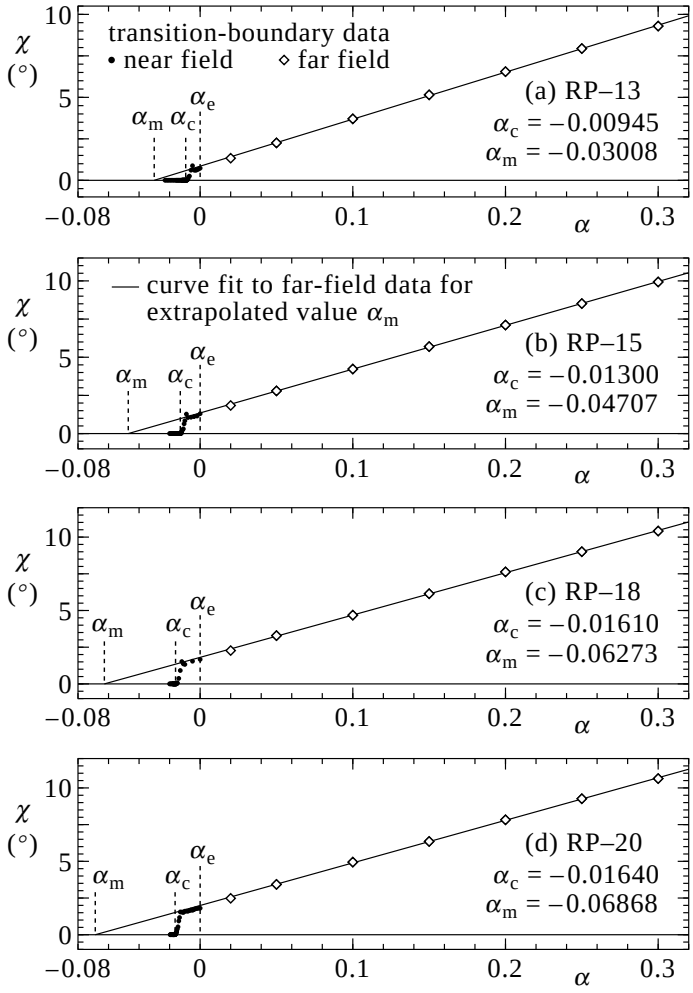

Figure 7.18: Three possible transition boundaries between RR and MR in argon given by the locations α_{e}, α_{c} and α_{m}.

The post-processed data for χ versus α from CFD flow-field simulations of regular and Mach reflections are subdivided into two groups in Fig. 7.18. The closely packed near-field data, included as the collection of black dots, was used previously in Section 7.5 to determine the new numerical transition boundary between regular and Mach reflection (without a boundary layer on the wedge surface), yielding the values of α_c given in table 7.2. The location of α_c occurs when the characteristic length L and the triple-point angle χ both diminish to zero for the transition from Mach to regular reflection. The location of α_c among these closely packed near-field data is depicted by a vertical dashed line labelled α_c in each plot in Fig. 7.18.

The location of the transition boundary between regular and Mach reflection from von Neumann [5], based on his extreme-angle or detachment criterion, is also shown in each plot as a vertical dashed line labelled α_e. This location occurs at the point $\alpha = 0$, which stems from our definition of α that starts on and runs perpendicular to the extreme-angle boundary. Based on the data shown in Fig. 7.18 for the dual region of regular and Mach reflection, von Neumann's transition boundary is not valid for inviscid flows (no boundary layer). The CFD flow-field simulations do not feature L and χ equal to zero in the dual region for the sonic and extreme-angle criteria.

A second group of post-processed data for χ versus α is shown as a set of white-filled diamonds in Fig. 7.18. This group is called far-field data, partly because they do not surround the new transition boundary location α_c between regular and Mach reflection, and partly because they do not surround the transition boundary location α_e stemming from von Neumann's extreme-angle criterion. Instead, these far-field data lie farther away and on the right-hand side of both α_c and α_e. The straight line in each plot in Fig. 7.18 is based on a least-squares curve fit to the far-field data only. The extrapolation of this straight line of χ versus α to a zero value for χ yields the value of α_m. This value of α_m versus the incident shock Mach number M_i provides a hypothetical transition boundary between regular and Mach reflection for the dual region ($M_i > 1.55$).

The numerical transition-boundary points from post-processing the CFD flow-field data for reference points RP–9 to 20 to obtain the extrapolated values of α_m are collected in table 7.3 (column 4). The corresponding incident shock Mach number M_i and wedge angle θ_w, calculated by means of Eqs. (7.2) and (7.3), are listed in columns 5 and 6.

An interpretation and discussion of the two possible transition boundaries between regular and Mach reflection given in terms of the near-field data for α_c and the far-field data for α_m versus the incident shock Mach number are provided in Chapter 9.

Table 7.3: Alternate numerical transition boundary between RR and MR in argon using extrapolated far-field data.

RP	reference points		extrapolated transition points		
	$M_{\mathrm{i}}^{\star}$	$\theta_{\mathrm{w}}^{\star}$ (°)	α_{m}	M_{i}	θ_{w} (°)
9	1.572	51.3539	0.003480	1.57229	51.03689
10	1.715	52.2405	−0.004456	1.71477	52.65886
11	1.855	52.8110	−0.011772	1.85458	53.94097
12	2.0	53.2183	−0.019298	1.99953	55.10628
13	2.25	53.6680	−0.030077	2.24958	56.68586
14	2.5	53.9398	−0.039184	2.49966	57.94961
15	2.75	54.1151	−0.047072	2.74973	59.01114
16	3.0	54.2340	−0.052726	2.99979	59.78421
17	3.25	54.3179	−0.057870	3.24983	60.47441
18	3.5	54.3792	−0.062732	3.49987	61.11857
19	3.75	54.4252	−0.063878	3.74990	61.31053
20	4.0	54.4606	−0.068683	3.99991	61.93304

Chapter 8

Experimental Transition Boundary Between RR and MR Without A Boundary Layer

Experimental data are collected herein to verify the numerical transition boundary between regular and Mach reflection from a wedge, for the specific case when no shear or boundary layer exists on the inclined reflecting surface. Only seven such experimental results have been published for shock-wave reflections in air.

Smith [21] in 1959 was the first researcher to propagate a shock wave at an almost constant speed V_i or shock number M_i along a rectangular shock-tube channel and then reflect this planar shock from an angled channel end. His experimental setup is illustrated in Fig. 8.1(a) for the case of Mach reflection. The two reflected shocks from the two angled channel ends interact by reflecting from each other along the channel center plane. Flow visualization tools including parallel fringe interferometry as well as shadowgraph and schlieren photography were used to quantify shock strengths and measure corresponding wave angles. The reflected shock angle with the channel centerline is shown in the figure as θ_i, and the wedge angle is given by $\theta_\mathrm{w} = 90^\circ - \theta_\mathrm{i}$. Because the shock reflecting surface behind the two reflecting shocks is gaseous and moving behind the shocks, no boundary or shear layer is produced at the reflecting surface. As a consequence, regular and Mach reflection processes are essentially inviscid, without the shear effects of viscosity and heat transfer by conduction at an otherwise rigid material surface. To determine the transition boundary between regular and Mach reflection, the channel-end angle θ_e must be changed gradually from one shock-tube experimental to the next (for the same incident shock strength), so that the Mach stem diminishes to zero and regular reflection just begins.

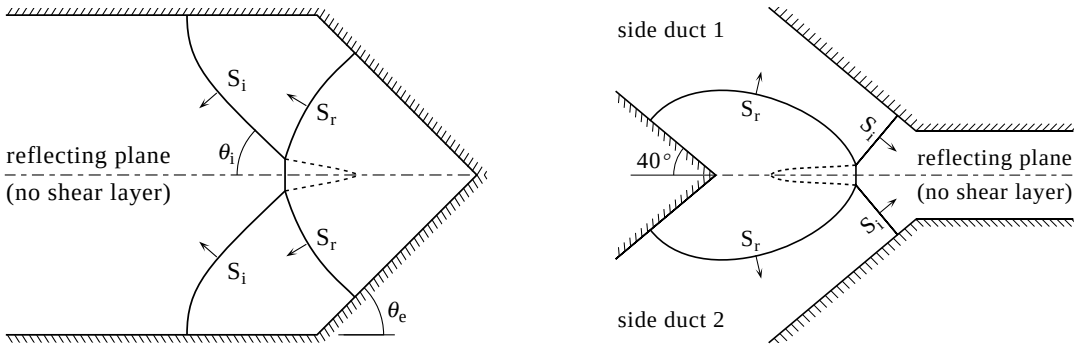

(a) Mach reflection in a shock tube with a wedge-shaped or angled reflecting duct end.

(b) Mach reflection in a bifurcated shock tube where the upper and lower ducts rejoin.

Figure 8.1: Experimental techniques used to generate oblique shock-wave reflections from reflecting planes without a combined viscous and thermal boundary layer.

Henderson and Lozzi [16, 22] adopted the shock-tube technique of Smith [21] for some of their work in 1975 and 1979. The reflection patterns arising from their experimental setup were hence also assumed to be independent of wall boundary layer effects. A schlieren optical system was employed to measure the shock-wave angles and infer properties regarding the composition of the recorded flow fields. Experimental results to be used later in this research, in terms of the incident shock Mach number M_{i} and wedge angle θ_{w}, were extracted from various diagrams and figures in the papers of Smith [21] and Henderson and Lozzi [16, 22]. These final results are presented in table 8.1.

Barbosa and Skews [23] in 2002 criticized the technique of Smith [21] with an angled shock-tube end as being too small in size and lacking interpretation accuracy. Instead, they built a large shock tube with a channel that first bifurcates into two equal-sized diverging ducts, which slowly bend back together, and finally rejoin, as illustrated in Fig 8.1(b). A splitter mechanism located downstream of a double-diaphragm driver was employed to facilitate this process by splitting an incident shock front into two synchronized plane waves. These two equal-strength shocks then travel down separate channels and emerge from the two respective duct ends to come together and reflect from each other along a perfect, inviscid, symmetric reflection boundary. Maintaining a constant gas temperature in the upper and lower ducts before experiments was difficult.

The final shock reflection process for the case of a wedge angle of 40° from Barbosa and Skews [23] is depicted in Fig. 8.1(b), for the case of Mach reflection. The shock reflecting surface is gaseous and moving behind the reflecting shocks, as in Smith's apparatus, such that no shear or boundary layer is produced. Hence, the shock reflection process is essentially inviscid. The strength of the incident shock waves is systematically varied to make the Mach-stem length approach zero to determine the transition between regular and Mach reflection. Holographic interferometry and shadowgraph flow visualization were used for experimental

measurement. Further bifurcated shock-tube experiments using 20° and 48° wedge angles with inviscid, gaseous reflecting surfaces were performed in 2011 by Herron and Skews [24]. The experimental results for the incident shock Mach numbers M_i and wedge angles θ_w used in these studies are taken directly from the papers by Barbosa and Skews [23] as well as Herron and Skews [24]. These final results are also included in table 8.1.

Table 8.1: Experimental data for the transition between RR and MR for reflecting planes without a combined viscous and thermal boundary layer in atmospheric air.

M_i	θ_w (°)	year	reference
1.039	27.5	1959	Smith [21]
1.88	51.0	1975	Henderson and Lozzi [16]
1.08	33.5	1979	Henderson and Lozzi [22]
1.13	38.8		
1.144	40.0	2002	Barbosa and Skews [23]
1.0223	20.0	2011	Herron and Skews [24]
1.3724	48.0		

Chapter 9

Results and Discussion

The regions and transition boundaries between regular and Mach reflections (i.e. RR, SMR, TMR and DMR) in argon and air are presented in Figs. 9.1(a) and 9.1(b), respectively, in plots of the wedge angle θ_{w} versus the incident shock Mach number M_{i}. The new numerical transition boundary between regular and Mach reflections, which was determined by post-processing closely spaced CFD near-field flow simulation data (inviscid), for the case of shock-reflections from an inclined wedge without a boundary layer on the wedge surface, is defined by the string of twenty white-filled circles in these figures. This is done for all twenty reference points selected along von Neumann's extreme-angle transition boundary in Section 7.1, and the data was taken directly from earlier results collected in tables 7.2(a) and 7.2(b).

For low incident shock Mach numbers M_{i} ranging from 1.0 to 1.6 the numerical transition boundary is in excellent agreement with the analytical results of von Neumann [5] for the sonic and extreme-angle transition boundaries, which are very close together. However, for higher Mach numbers from 1.6 to 4.0, the numerical transition boundary trends higher than the sonic and extreme-angle boundaries by as much as 1.6°. This trend at larger incident shock Mach numbers is noticeable, increases continuously without fluctuations, and is significantly higher than von Neumann's sonic and extreme-angle boundaries. This upward shift of the numerical transition boundary above the closely spaced sonic and extreme-angle boundaries occurs only in the dual region where either regular or Mach reflection can occur. The upward trend of this numerical transition boundary (inviscid, no boundary layer) in the dual region is somewhat unanticipated, because it was expected that the numerical transition boundary would be in close agreement with the closely spaced sonic and extreme-angle transition boundaries of von Neumann [5].

Transition-boundary results for regular to Mach reflections from shock-tube experiments with inclined surfaces that are gaseous and moving without a shear or boundary layer behind

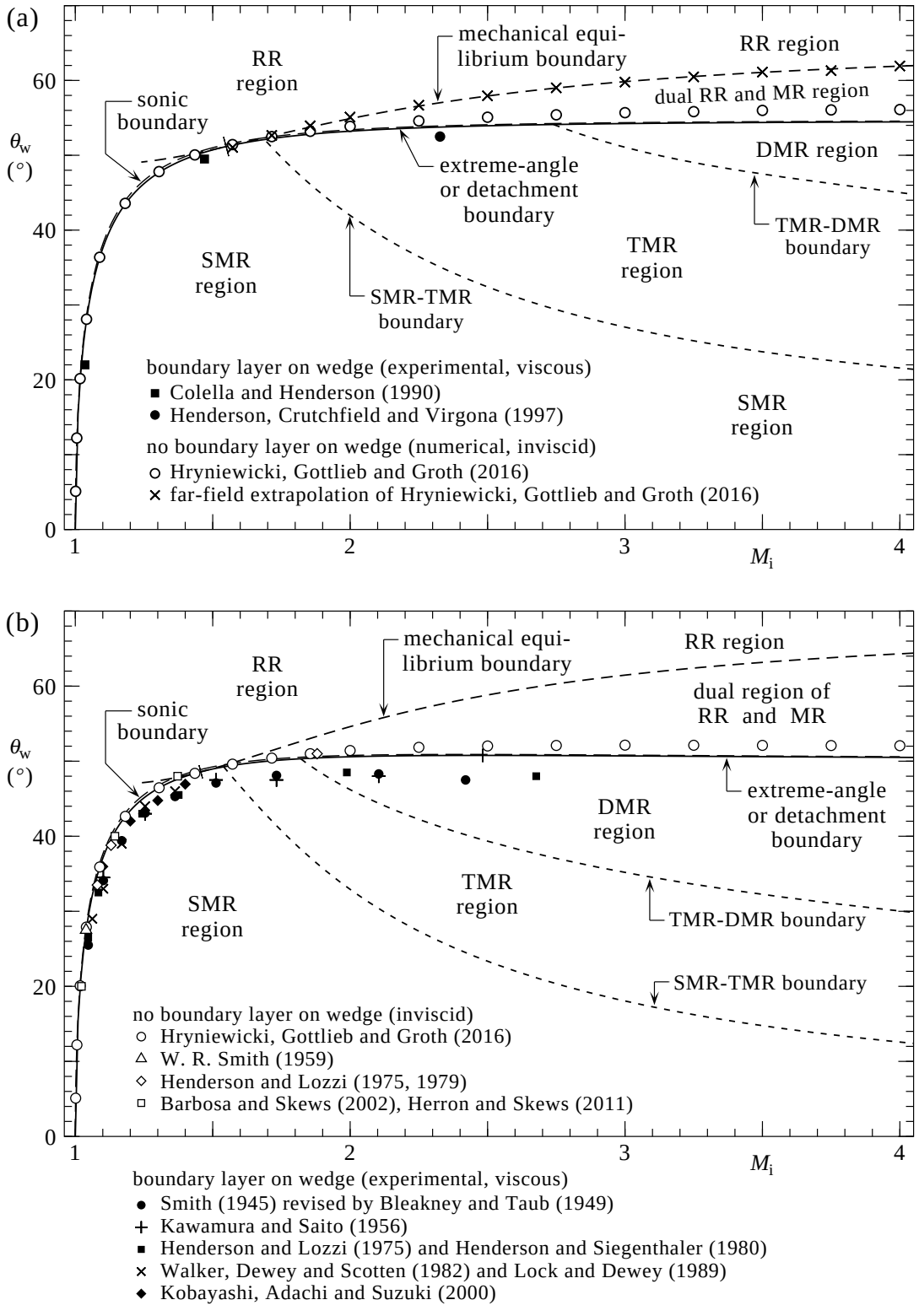

Figure 9.1: Regular to Mach reflection transition boundaries in (a) argon and (b) atmospheric air. The numerical transition boundary determined in this research for each gas is defined by the string of twenty white-filled circles in each diagram.

the shocks, as described in Chapter 8 and given in table 8.1, are included in Fig. 9.1(b) for the case of air. Most of these experimental results are for low incident shock Mach numbers M_{i} below 1.4. These results are in good agreement with von Neumann's analytical sonic and extreme-angle transition boundaries, and also in good agreement with the results for the new numerical transition boundary. The numerical transition boundary, in the range $1.0 < M_{\mathrm{i}} < 1.6$, is not sufficient to accurately provide a definitive conclusion as to whether it agrees better with either the sonic or extreme-angle boundary, primarily because the sonic and extreme-angle boundaries are so close together. However, the new numerical transition boundary typically lies between the closely spaced sonic and extreme-angle boundaries within this lower range of incident shock Mach numbers.

The upward trend of this numerical transition boundary (inviscid) is somewhat unanticipated, because the transition-boundary results from past shock-tube experiments in air shown in Fig. 9.1(b), for the case of inclined wedges on which there is a combined viscous and thermal boundary layer, clearly trend below the sonic and extreme-angle transition boundaries. This persistence of RR into the MR regions in air occurs for all experimental cases with a combined viscous and thermal boundary layer for incident shock Mach numbers ranging from 1.05 to 2.68 in Fig. 9.1(b). These sparse data would imply that for the case of a combined viscous and thermal boundary layer on the wedge surface, the transition boundary lies below von Neumann's sonic and extreme-angle boundaries. This implication is much evident for the case of moving shock reflections in air, because the experimental data are plentiful and yield a recognizable experimental transition boundary.

The shift of up to three degrees in Figs. 9.1(a) and 9.1(b) between the new numerical-transition boundary without a boundary layer (inviscid) and the experiments with a boundary layer (viscous) illustrates the importance of the viscous effects associated with the combined viscous and thermal boundary layer on the wedge surface. Regular reflections with a boundary layer on the wedge persist downward into the Mach-reflection region, across the dual region and both the new numerical transition boundary and sonic and extreme-angle transition boundaries. Alternatively, Mach reflections without a boundary layer on the wedge persist upward from the Mach reflection region into the dual region of regular and Mach reflection, terminating at the new numerical transition boundary. The CFD images of simulated flow-fields without a boundary layer on the wedge obtained in this research are always regular-reflection patterns for the region between our new numerical transition boundary and von Neumann's mechanical-equilibrium transition boundary.

The physical mechanism and reasons for the upward shift in the new numerical transition boundary, in the range $1.6 < M_{\mathrm{i}} < 4.0$, above von Neumann's closely spaced sonic and extreme-angle boundaries, within the dual region of regular and Mach reflections, is not yet fully understood. The shift does not stem from flow perturbations, numerical disturbances or modelling errors in the CFD flow-field simulations. The string of twenty white-filled circles for

the new numerical transition boundary originates from a large number of carefully conducted two-dimensional CFD flow-field simulations. The transition-boundary points as a string of data are neither erratic nor jerky in behaviour; instead, they occur in a uniform and systematic manner, as shown in Figs. 9.1(a) and 9.1(b). The new numerical-transition boundary is generated by high-resolution CFD flow-field simulations, which account fully for the shock-reflection process from the inclined wedge. The effects of the corner disturbance or signal are included in these computations, as are those of the curved reflected shock when the corner disturbance overtakes the incident shock in RR and the triple point in MR. Consequently, it should not necessarily be expected that the new numerical transition boundary will agree well with the closely spaced sonic and extreme-angle boundaries for larger incident shock Mach numbers. Von Neumann's transition boundaries based on sonic and detachment criteria stem from fairly simple analytical considerations in which the incident, reflected and Mach-stem shocks, and the slip stream, are all assumed planar and straight. Moreover, von Neumann's analytical formulations ignore the corner disturbance for the extreme-angle boundary, only taking its arrival into account for the sonic transition boundary.

One shock-tube result from Henderson and Lozzi [16] for $M_\mathrm{i} = 1.88$ in air lies inside the dual region of regular or Mach reflection, definitively above von Neumann's analytical sonic and extreme-angle boundaries, as shown in Fig. 9.1(b). This result, however, is in good agreement with the new numerical transition boundary. Unfortunately, experimental shock-tube results like those of Smith [21], Henderson and Lozzi [16, 22], Barbosa and Skews [23], and Herron and Skews [24] are not available at higher incident shock Mach numbers for argon and atmospheric air to provide a more conclusive confirmation that the numerical transition boundary for inviscid gas flows is a better transition boundary than those of von Neumann for the sonic and extreme-angle boundaries.

The new numerical transition boundary between regular and Mach reflection clearly does not agree with the mechanical-equilibrium boundary of von Neumann [5] for the present case of unsteady or pseudo-steady flows for moving shock waves interacting with an inclined wedge. See Fig. 9.1. However, for the case of steady supersonic flows over wedges, the transition boundaries between regular and Mach reflection are well known to be von Neumann's mechanical-equilibrium and sonic or extreme-angle boundaries that encompass the dual region. Hysteresis effects involving the changing back and forth between regular and Mach reflection patterns by slow cyclic changes in the wedge angle are known to occur; see the book by Ben-Dor [14] and the paper by Ivanov, Gimelshein and Beylich [161]. Such hysteresis effects do not occur for planar moving shocks interacting with wedges of fixed angle. See the paper by Hornung [28] for more information about the differences between shock-wave reflections from wedges in pseudo-steady flows (i.e. with moving shock waves) and those in steady supersonic flows.

As a recap, the occurrences of regular and/or Mach reflection in various ranges of the wedge angle θ_w, for inviscid flows without a boundary layer and viscous flows with a boundary layer,

Table 9.1: Regular and Mach reflection when $1.0 < M_{\mathrm{i}} < 1.6$.

θ_{w} range	inviscid flow without a boundary layer	viscous flow with a boundary layer
$\theta_{\mathrm{w}} > \theta_{\mathrm{sb}} \approx \theta_{\mathrm{nb}} \approx \theta_{\mathrm{eab}} \approx \theta_{\mathrm{exp}}^{\mathrm{if}}$	RR	
$\theta_{\mathrm{w}} < \theta_{\mathrm{sb}} \approx \theta_{\mathrm{nb}} \approx \theta_{\mathrm{eab}} \approx \theta_{\mathrm{exp}}^{\mathrm{if}}$	MR†	
$90^{\circ} > \theta_{\mathrm{w}} > \theta_{\mathrm{sb}}$		RR
$\theta_{\mathrm{sb}} > \theta_{\mathrm{w}} > \theta_{\mathrm{nb}}$		RR
$\theta_{\mathrm{nb}} > \theta_{\mathrm{w}} > \theta_{\mathrm{eab}}$		RR
$\theta_{\mathrm{eab}} > \theta_{\mathrm{w}} > \theta_{\mathrm{exp}}^{\mathrm{vf}}$		RR
$\theta_{\mathrm{exp}}^{\mathrm{vf}} > \theta_{\mathrm{w}} > 0^{\circ}$		MR†

†MR is either vNR or SMR.

Table 9.2: Regular and Mach reflection for $M_{\mathrm{i}} > 1.6$ (dual region of RR and MR).

θ_{w} range	inviscid flow without a boundary layer	viscous flow with a boundary layer
$90^{\circ} > \theta_{\mathrm{w}} > \theta_{\mathrm{meb}}$	RR	RR
$\theta_{\mathrm{meb}} > \theta_{\mathrm{w}} > \theta_{\mathrm{nb}} \approx \theta_{\mathrm{exp}}^{\mathrm{if}}$	RR	RR
$\theta_{\mathrm{exp}}^{\mathrm{if}} \approx \theta_{\mathrm{nb}} > \theta_{\mathrm{w}} > \theta_{\mathrm{sb}}$	MR†	RR
$\theta_{\mathrm{sb}} > \theta_{\mathrm{w}} > \theta_{\mathrm{eab}}$	MR†	RR
$\theta_{\mathrm{eab}} > \theta_{\mathrm{w}} > \theta_{\mathrm{exp}}^{\mathrm{vf}}$	MR†	RR
$\theta_{\mathrm{exp}}^{\mathrm{vf}} > \theta_{\mathrm{w}} > 0^{\circ}$	MR†	MR†

†MR is either TMR or DMR.

are summarized in tables 9.1 and 9.2. These tables pertain to incident shock Mach numbers in the ranges $1.0 < M_{\mathrm{i}} < 1.6$ before the dual region of RR and MR, and $M_{\mathrm{i}} > 1.6$ for the dual region, respectively. In these tables, the new symbols θ_{sb}, θ_{eab}, θ_{meb} and θ_{nb} denote the respective wedge angles for the sonic, extreme-angle, mechanical-equilibrium and new numerical transition boundaries. Also, $\theta_{\mathrm{exp}}^{\mathrm{if}}$ and $\theta_{\mathrm{exp}}^{\mathrm{vf}}$ denote the transition boundaries from the string of experimental results without and with a boundary layer on the wedge surface, respectively, corresponding to inviscid and viscous flows. The tabulated regions of RR and MR stem from previous and current studies.

An alternate numerical transition boundary between RR and MR for the case of argon is introduced to elaborate on the foregoing discussion. Data was generated in Section 7.7 and collected in table 7.3 from the extrapolation of far-field MR data for χ versus α to obtain the value of α_{m} when $\chi = 0$ (see Fig. 7.18). The corresponding results of M_{i} and θ_{w} for the twelve α_{m} values in table 7.3 are each plotted as an '$\times$' in Fig. 9.1(a) for argon. These data fall on, or are very close to, the mechanical-equilibrium boundary of von Neumann throughout the dual RR and MR region. Based on this close agreement, one could mistakenly believe

that the mechanical-equilibrium boundary is the transition boundary between RR and MR for moving shock reflections (pseudo-steady shock reflections), if the new numerical boundary was not known. Note that the results in Fig. 7.18 illustrate that the far-field data for χ diminishes linearly with α, whereas the near-field data undergoes a rapid transition to $\chi = 0$ (at the new numerical transition boundary), well before the location of the falsely extrapolated transition boundary at α_{m}.

The method of extrapolating far-field data in the dual region of the form χ versus θ_{w} at a constant incident shock Mach number M_{i} was used in the mid 1940s by Smith [2] to determine the experimental transition boundary between regular and Mach reflection. The resulting error in the prediction of the transition boundary by using far-field data in the extrapolation was later recognized and corrected in 1949 by Bleakney and Taub [8], and it was also explained in 1956 by Kawamura and Saito [10]. The correction was to obtain more closely spaced experimental photographs near the transition boundary to determine the sudden transition that occurs within the dual region of regular and Mach reflections.

Chapter 10

Concluding Remarks

The two analytical sets of equations to determine the transition boundaries for von Neumann's extreme-angle and mechanical-equilibrium criteria have been revised in Chapter 3 into concise forms that are more appropriate for modern usage than past formulations. Relevant details of their contact point and maximum value were also provided for polytropic gases with specific heat ratios of $\gamma = 5/3$ as well as $7/5$. These analyses have been performed because of their relevance and importance to the new results characterizing the numerical transition boundary between regular reflection (RR) and Mach reflection (MR) for the case of moving planar shock waves in argon and atmospheric air for the case of a moving, planar shock wave impinging on a rigid, inclined wedge without a boundary layer.

Numerical solutions of the thickness and transition of flow properties for one-dimensional, planar shock waves in viscous, heat-conducting gases have been computed in Chapter 4 based on solutions of the Navier-Stokes equations, with and without volume viscosity. The results have been presented for several pure species as well as their mixtures, including monatomic argon, molecular nitrogen and atmospheric air. For polyatomic gases, the inclusion of volume viscosity in the governing Navier-Stokes equations leads to good agreement of the predicted numerical results with experimental measurements, for both shock-front transitions as well as shock wave thicknesses, over a wide range of shock Mach numbers. Comparisons of the Navier-Stokes computations reported herein with existing experimental data indicates that the continuum fluid-dynamic description of gases using the Navier-Stokes equations provides better and more accurate results for shock-front transitions and thicknesses than previously thought or expected from kinetic theory, even at relatively high shock Mach numbers.

A parallel, fully implicit, anisotropic block-based AMR finite-volume scheme has been described in Chapter 5 for solving both inviscid and laminar, two-dimensional, compressible, unsteady, gaseous fluid flows governed by the Euler and Navier-Stokes equations, respectively.

Verification and validation of the numerical solution method was performed in Chapter 6 to assess the predictive capabilities of the algorithm for several flow problems involving shocks, demonstrating the benefits, capabilities and parallel performance of the approach. The combination of anisotropic AMR and parallel implicit time-marching techniques adopted in the computational scheme has been shown to readily enable time-accurate numerical simulations of complex multi-shock interaction problems, as represented by unsteady oblique shock reflection processes with fully resolved internal shock structures. Thereafter, the high-resolution CFD solution method with explicit time marching was used extensively in the computation of the Euler equations for flow fields pertaining to unsteady shock-wave interactions with rigid inclined wedges in inviscid and polytropic gases, to facilitate the determination of the numerical transition boundary separating regular and Mach reflections within these flows.

An accurate and systematic methodology for determining the numerical transition boundary between regular and Mach reflections from CFD flow-field simulations without a boundary layer on the wedge surface has been developed and well established in Chapter 7. Important details were provided regarding the procedures for calculating the speeds of the incident shock and Mach stem, calculating the normalized (self-similar) Mach-stem length, and extracting the numerical transition-boundary point from closely packed CFD flow-fields across but normal to von Neumann's extreme-angle boundary. The procedure was applied at the twenty reference points within the plane defined by the wedge angle θ_{w} versus the incident shock Mach number M_{i}, as defined earlier in tables 7.1(a) and 7.1(b) for both argon as well as atmospheric air, respectively. The twenty new numerical transition-boundary points (M_{i},θ_{w}) given in table 7.2(a) and 7.2(b) have been carefully determined for each of these gases with an accuracy superior to that possible by human inspection and interpretation of numerical images from simulated flow fields and experimental photographs from experiments.

The numerical transition boundary separating regular and Mach reflections for shock waves striking wedges in inviscid and non-heat-conducting fluid flows has been documented in Chapter 9, using both argon as well as atmospheric air as the working media. For each individual gas that has been examined in this research, this new numerical transition boundary agrees well with the corresponding analytical extreme-angle and sonic transition boundaries of von Neumann [5] for low shock Mach numbers from 1.0 to 1.6, as might be expected, but this new numerical transition boundary trends unexpectedly upward by as much as 1.6° at larger shock Mach numbers from 1.6 to 4.0. Although this upward trend is small, it is noticeable, consistent, significant and confirmed by one experiment by Henderson and Lozzi [16] in air. For inviscid flow along the wedge surface, with no boundary layer, stronger Mach reflections therefore persist upward from the Mach-reflection region into the dual region of regular and Mach reflections. This is exactly the opposite behaviour of what occurs for the case of observed experimental shock reflections with a combined viscous and thermal boundary layer on the wedge surface, where regular reflections persist downward into the Mach reflection region (see Fig. 1.2). Hence, for shock reflections with a boundary layer on the inclined wedge surface,

the persistence of experimental regular reflection patterns occurs from the regular reflection region, across the entire dual region and the new numerical transition boundary, over the sonic and extreme-angle transition boundaries and down into the Mach-reflection regions of TMR and DMR. The experimental persistence is therefore larger than previously understood, in that it is now considered to progress past the new numerical transition boundary, instead of the lower sonic and extreme-angle transition boundaries. The reason for this upward shift in the new numerical transition boundary is believed to be due to the incorporation of the effects of the corner disturbance as well as those of the curved reflected shock (when the corner disturbance overtakes the incident shock in RR and the triple point in MR) included in these computations, which account fully for the shock-reflection process from the inclined wedge. Von Neumann's transition boundaries are based on simple analytical considerations in which the incident, reflected and Mach-stem shocks, and the slip stream, are all assumed planar and straight. Moreover, von Neumann's analytical formulations ignore the corner disturbance for the extreme-angle boundary and only take its arrival into account for the sonic boundary.

10.1 Original Contributions

The primary contributions made as a result of this research are:

- A new numerical transition boundary between regular and Mach reflections has been determined accurately and analyzed in Chapter 9 for moving shock waves striking wedges without a combined viscous and thermal boundary layer on the wedge surface in argon as well as atmospheric air.
- An effective post-processing methodology has been developed in Chapter 7 for the determination of the transition between regular and Mach reflections from CFD simulation data, providing a technique whose accuracy is far superior to that previously achievable by human inspection and interpretation of flow-field diagrams.
- The parallel anisotropic block-based AMR finite-volume scheme described in Chapter 5 has been utilized in Chapter 6 to obtain the first-known high-spatial-resolution and time-accurate computations for unsteady oblique shock-wave reflection processes with fully resolved internal shock structures.

In addition, several secondary contributions include:

- Analytical solutions for regular reflection and the corresponding solutions for the extreme-angle and mechanical-equilibrium transition criteria of von Neumann [5] have been revisited and revised in Chapter 3 into concise forms that are convenient for modern usage.
- An ODE solution method based on a continuum fluid-dynamic approach using the Navier-Stokes equations has been developed in Chapter 4 and used therein to predict numerical shock-front transitions with and without volume viscosity for several viscous, heat-conducting gases.

10.2 Recommendations for Future Research

The analytical, computational-fluid-dynamic and post-processing techniques that have been developed and described in this dissertation lay the foundation for further studies of shock-wave reflection transition boundaries and their accurate determination from closely spaced computational flow fields. Among the many available avenues for future research, the following are most highly recommended:

- For inviscid and polytropic flow fields, the transition boundary between regular and Mach reflections in carbon dioxide (CO_2) should be determined. This work is a direct extension of the current study, and involves the solution of the Euler equations for shock-wave reflections from a wedge without a combined viscous and thermal boundary layer. The objective would be to gain further insight into the polytropic-gas assumption for the new numerical transition boundary ($\gamma_{CO_2} = 1.29973$ is lower than most other gases).
- The persistence of regular reflection across both the new numerical transition boundary and the sonic and extreme-angle transition boundaries (all of which are inviscid) into the Mach reflection region in air should be investigated. This study involves the solution of the Navier-Stokes equations for shock-wave reflections from an inclined wedge with a combined viscous and thermal boundary layer. The objective would be to develop a better understanding as to why the experimental results in air (with a boundary layer on the wedge surface) shown in Fig. 1.2 persist noticeably below the inviscid transition boundaries and to explore the effect of wedge length on this persistence.

It is noted that computational experiments do not suffer from repeatability problems and are more readily modified than experimental shock-tube facilities (e.g. turning the boundary layer off and on, modifying initial flow and boundary conditions, etc.), particularly in large parametric studies such as these, encouraging their use to quantify the numerous regions and boundaries of unsteady shock-wave reflections within gaseous flow fields.

References

[1] E. Mach, *Über den verlauf der funkenwellen in der ebene und im raum.* Sitzungsber. Akad. Wiss. Wien., **77**, 819–839, 1878.

[2] L. G. Smith, *Photographic investigation of the reflection of plane shocks in air.* N. D. R. C. Technical Report No. A-350 and O.S.R.D. Report No. 6271, 1945.

[3] D. R. White, *An experimental survey of the Mach reflection of shock waves.* Dept. Phys. Tech. Report II-10, Princeton University, 1951.

[4] J. von Neumann, *Theory of shock waves.* U.S. Dept. Comm. Off. Tech. Serv. No. PB32719 (Reprinted in: J. von Neumann, *Collected Works*, **6**, 178–202, 1963), 1943.

[5] J. von Neumann, *Oblique reflection of shocks.* U.S. Dept. Comm. Off. Tech. Serv. Report No. PB37079 (Reprinted in: J. von Neumann, *Collected Works*, **6**, 238–299, 1963), 1943.

[6] J. von Neumann, *Refraction, intersection and reflection of shock waves.* U.S. Naval Ord. (NAVORD) Report No. 203–45 (Reprinted in: J. von Neumann, *Collected Works*, **6**, 300–308, 1963), 1945.

[7] R. Courant and K. O. Friedrichs, *Hypersonic flow and shock waves.* Wiley Interscience, 1948.

[8] W. Bleakney and A. H. Taub, *Interaction of shock waves.* Reviews of Modern Physics, **21**(4), 584–605, 1949.

[9] H. Cabannes, *Lois de la réflexion des ondes de choc dans les écoulements plans non stationnaires.* O.N.E.R.A., **80**, 1955.

[10] R. Kawamura and H. Saito, *Reflection of shock waves – 1. pseudostationary case.* J. Phys. Soc. Jpn., **11**(5), 584–592, 1956.

[11] G. Ben-Dor and I. I. Glass, *Domains and boundaries of nonstationary oblique shock-wave reflexions I: diatomic gas.* Journal of Fluid Mechanics, **92**, 459–496, 1979.

[12] G. Ben-Dor and I. I. Glass, *Domains and boundaries of non-stationary oblique shock-wave reflexions II: monatomic gas.* Journal of Fluid Mechanics, **96**, 735–756, 1980.

[13] I. I. Glass and J. P. Sislian, *Nonstationary flows and shock waves.* Claredon Press, 1994.

[14] G. Ben-Dor, *Shock wave reflection phenomena, 2e.* Springer, 2007.

[15] A. N. Semenov, M. K. Berezkina, and I. V. Krassovskaya, *Classification of pseudo-steady shock wave reflection types.* Shock Waves, **22**(4), 307–316, 2012.

[16] L. F. Henderson and A. Lozzi, *Experiments on transition of Mach reflexion.* J. Fluid Mech., **68**, 139–155, 1975.

[17] L. F. Henderson and A. Siegenthaler, *Experiments on the diffraction of weak blast waves: the von Neumann paradox.* Proc. R. Soc. Lond. A, **369**, 537–555, 1980.

[18] D. K. Walker, J. M. Dewey, and L. N. Scotten, *Observation of density discontinuities behind reflected shocks close to the transition from regular to Mach reflection.* Appl. Phys., **53**(3), 1398–1400, 1982.

[19] G. D. Lock and J. M. Dewey, *An experimental investigation of the sonic criterion for transition from regular to Mach reflection of weak shock waves.* Exps. in Fluids , **7**(5), 289–292, 1989.

[20] S. Kobayashi, T. Adachi, and T. Suzuki, *On the unsteady transition phenomenon of weak shock waves.* Theo. Appl. Mech., **49**, 271–278, 2000.

[21] W. R. Smith, *Mutual reflection of two shock waves of arbitrary strengths.* Phys. Fluids, **2**(5), 533–541, 1959.

[22] L. F. Henderson and A. Lozzi, *Further experiments on transition to Mach reflexion.* J. Fluid Mech., **94**, 541–559, 1979.

[23] F. J. Barbosa and B. W. Skews, *Experimental confirmation of the von Neumann theory of shock wave reflection transition.* Journal of Fluid Mechanics, **472**(1), 263–282, 2002.

[24] T. Herron and B. Skews, *On the persistence of regular reflection.* Shock Waves, **21**(6), 573–578, 2011.

[25] D. C. Pack, *The reflexion and diffraction of shock waves.* J. Fluid Mech., **18**, 549–576, 1964.

[26] W. C. Griffith, *Shock waves.* J. Fluid Mech., **106**, 81–101, 1981.

[27] T. V. Bazhenova, L. G. Gvozdeva, and M. A. Nettleton, *Unsteady interactions of shock waves.* Progress in Aerospace Sciences, **21**(4), 249–331, 1984.

[28] H. G. Hornung, *Regular and Mach reflection of shock waves.* Ann. Rev. Fluid Mech., **18**, 33–58, 1986.

[29] G. Ben-Dor, *Steady, pseudo-steady and unsteady shock wave reflections.* Progress in Aerospace Sciences, **25**(4), 329–412, 1988.

[30] L. F. Henderson, K. Takayama, W. Y. Crutchfield, and S. Itabashi, *The persistence of regular reflection during strong shocks diffracting over rigid ramps.* J. Fluid Mech., **431**, 273–296, 2001.

[31] T. Adachi, A. Sakurai, and S. Kobayashi, *Effect of boundary layer on Mach reflection over a wedge surface.* Shock Waves, **11**(4), 271–278, 2002.

[32] C. Hirsch, *Numerical computation of internal and external flows, v1: fundamentals of computational fluid dynamics.* John Wiley and Sons, Inc., 1989.

[33] U.S. Government Printing Office, Washington, D.C., 1976.

[34] S. Y. Park, J. S. Kim, J. B. Lee, M. B. Esler, R. S. Davis, and R. I. Wielgosz, *A redetermination of the argon content of air for buoyancy corrections in mass standard comparisons.* Metrologia, **41**(6), 387–395, 2004.

[35] A. Picard, R. S. Davis, M. Gläser, and K. Fujii, *Revised formula for the density of moist air (CIPM–2007).* Metrologia, **45**(2) 149–155, 2008.

[36] B. J. McBride, M. J. Zehe, and S. Gordon, *NASA Glenn coefficients for calculating thermodynamic properties.* National Aeronautics and Space Administration (NASA) NASA/TP–2002–211556, 2002.

[37] J. A. de Gouw and E. R. Lovejoy, *Reactive uptake of ozone by liquid organic compounds.* Geophysical Research Letters, **25**(6), 931–934, 1998.

[38] S. Gordon and B. J. McBride, *Computer program for calculation of complex chemical equilibrium compositions and applications, part I – analysis.* National Aeronautics and Space Administration (NASA) NASA RP-1311, 1994.

[39] B. J. McBride and S. Gordon, *Computer program for calculation of complex chemical equilibrium compositions and applications, part II – users manual and program description.* National Aeronautics and Space Administration (NASA) NASA RP-1311, 1996.

[40] R. A. Svehla, *Transport coefficients for the NASA Lewis chemical equilibrium program.* National Aeronautics and Space Administration (NASA) NASA-TM-4647, 1995.

[41] L. Monchick and E. A. Mason, *Transport properties of polar gases.* J. Chem. Phys., **33**(5), 1676–1697, 1961.

[42] R. A. Svehla, *Estimated viscosities and thermal conductivities of gases at high temperatures.* National Aeronautics and Space Administration (NASA) NASA-TR-R-132, 1962.

[43] J. O. Hirschfelder, C. F. Curtiss, and R. B. Bird, *Molecular theory of gases and liquids*. New York Wiley, 1954.

[44] Air Liquide, *Gas encyclopedia*. Retrieved from `http://encyclopedia.airliquide.com/Encyclopedia.asp?GasID=137`, 2016.

[45] W. Sutherland, *The viscosity of gases and molecular force*. Philosophical Magazine Series 5, **36**(223), 507–531, 1893.

[46] A. Wassiljewa, *Heat conduction in gas mixtures*. Physikalische Zeitschrift, **5**(22), 737–742, 1904.

[47] C. R. Wilke, *A viscosity equation for gas mixtures*. J. Chem. Phys., **18**(4), 517–519, 1950.

[48] R. S. Brokaw, *Alignment charts for transport properties. Viscosity, thermal conductivity, and diffusion coefficients for nonpolar gases and gas mixtures at low density.* NASA TR-R-81, 1960.

[49] F. Kreith, *Principles of heat transfer, 3e.* Intext Press, 1973.

[50] R. C. Weast, *"Thermodynamic and transport properties of air" and "Viscosity of gases", CRC handbook of chemistry and physics, 5e.* CRC Press, 1974.

[51] J. P. Holman, *Heat transfer, 4e.* McGraw-Hill Book Company, 1976.

[52] R. L. Daugherty and J. B. Franzini, *Fluid mechanics with engineering applications, 7e.* McGraw-Hill Book Company, 1977.

[53] H. Schlichting, *Boundary-layer theory, 7e.* McGraw-Hill, Inc., 1979.

[54] J. Hilsenrath, *Tables of thermal properties of gases*. U.S. Department of Commerce, 1955.

[55] R. G. Vines, *Measurement of thermal conduction of gases at high temperature*. J. Heat Trans., **82C**, 48–52, 1960.

[56] H. Geier and K. Schäfer. Allg. Waermetech., **10**(4), 1966.

[57] N. V. Tsederberg and Z. A. Ivanova. Teploenergetika, **18**(6), 1971.

[58] A. A. Tarzimanov and R. S. Salmanov. Teplofiz. Vys. Temp., **15**, 1977.

[59] Karim and Rosenhead, *The second coefficient of viscosity of liquids and gases*. Rev. Mod. Phys., **24**(2), 108–116, 1952.

[60] G. J. Prangsma, A. H. Alberga, and J. J. M. Beenakker, *Ultrasonic determination of the volume viscosity of N_2, CO, CH_4 and CD_4 between 77 and 300 K.* Physica, **64**(2), 278–288, 1973.

[61] R. E. Graves and B. M. Argrow, *Bulk viscosity: past to present.* J. Thermophys. Heat Trans., **13**(3), 337–342, 1999.

[62] W. G. Vincenti and C. H. Kruger, *Introduction to physical gas dynamics.* New York Wiley, 1965.

[63] W. C. Griffith, D. Brickl, and V. Blackman, *Structure of shock waves in polyatomic gases.* Phys. Rev., **102**(5), 1209–1216, 1956.

[64] H. Alsmeyer, *Density profiles in argon and nitrogen shock waves measured by the absorption of an electron beam.* Journal of Fluid Mechanics, **74**(3), 497–513, 1976.

[65] A. Ern and V. Giovangigli, *Multicomponent transport algorithms.* Lecture Notes in Physics Monographs, **24**, Springer-Verlag, 1994.

[66] A. Ern and V. Giovangigli, *Volume viscosity of dilute polyatomic gas mixtures.* Eur. J. Mech. B/Fluids, **14**(5), 653–663, 1995.

[67] C. A. Brau and R. M. Jonkman, *Classical theory of rotational relaxation in diatomic gases.* Journal of Chemical Physics, **52**(2), 477–484, 1970.

[68] M. S. Cramer, *Numerical estimates for the bulk viscosity of ideal gases.* Phys. Fluids, **24**, 066102-1–006102-23, 2012.

[69] B. Widom, *Rotational relaxation of rough spheres.* J. Chem. Phys., **32**(3), 913–923, 1960.

[70] J. W. Williams, C. H. Schwingel, and C. H. Winning, *The polarity of the nitrogen tetroxide and nitrogen dioxide molecules.* J. Am. Chem. Soc., **58**(2), 197–203, 1936.

[71] G.Herzberg, *Molecular spectra and molecular structure. III. Electronic spectra and electronic structure of polyatomic molecules.* New York Van Nostrand, 1966.

[72] J. A. Lordi and R. E. Mates, *Rotational relaxation in nonpolar diatomic gases.* Phys. Fluids, **13**(2), 291–308, 1970.

[73] S. Chapman and T. G. Cowling, *The mathematical theory of non-uniform gases, 3e.* Cambridge Press, 1970.

[74] J. O. Hirschfelder, R. B. Bird, and E. L. Spotz, *The transport properties for non-polar gases.* J. Chem. Phys., **16**(10), 968–981, 1948.

[75] L. F. Henderson, *Regions and boundaries of diffracting shock wave systems.* Z. Angew. Math. Mech., **67**(2), 73–86, 1987.

[76] P. A. Thompson, *Compresible-fluid dynamics.* Rensselaer Polytechnic Institute Press, 1988.

[77] F. D. Murnaghan, *The compressibility of media under extreme pressures.* Proc. Natl. Acad. Sci. U.S.A., **30**(9), 244–247, 1944.

[78] J.-P. Poirier, *Introduction to the Earth's interior, 2e.* Cambridge University Press, 2000.

[79] H. Polachek and R. J. Seeger, *Shock wave interactions, Section E, Fundamental of gas dynamics (ed. H. W. Emmons).* Princeton University Press, 482–522, 1958.

[80] G. Ben-Dor, O. Igra, and T. Elperin, *Handbook of shock waves, v2: shock wave interactions and propagation.* Academic Press, 2000.

[81] H. G. Hornung, H. Oertel, and R. J. Sandeman, *Transition to Mach reflexion of shock waves in steady and pseudosteady flow with and without relaxation.* J. Fluid Mech., **90**(3), 541–560, 1979.

[82] H. Grad, *The profile of a steady plane shock wave.* Comm. Pure App. Math., **5**(3), 257–300, 1952.

[83] H. M. Mott-Smith, *The solution of the Boltzmann equation for a shock wave.* Phys. Rev., **82**(6), 885–892, 1951.

[84] J. D. Faires and R. L. Burden, *Numerical methods, 3e.* Brooks Cole, 2003.

[85] T. G. Elizarova, A. A. Khokhlov, and S. Montero, *Numerical simulation of shock wave structure in nitrogen.* Phys. Fluids, **19**(6), 068102-1–068102-4, 2007.

[86] M. Morduchow and P. A. Libby, *On a complete solution of the one-dimensional equations of a viscous, heat conduction compressible gas.* J. Aero. Sci., **16**(11), 674–684, 1949.

[87] H. W. Liepmann and A. Roshko, *Elements of gasdynamics.* New York Wiley, 1965.

[88] R. Becker, *Stoßwelle und detonation.* Zeitschrift für Physik, **8**(1), 321–362, 1922.

[89] F. S. Sherman, *A low-density wind-tunnel study of shock-wave structure and relaxation phenomena in gases.* NACA TN-3298, 1955.

[90] L. Talbot and S. M. Scala, *Shock wave structure in a relaxing diatomic gas.* Proc. 2nd Int. Symp. Rare. Gas Dyn., Berkeley, California, United States of America, 1961.

[91] S. K. Godunov, *Finite-difference method for numerical computations of discontinuous solutions of the equations of fluid dynamics.* Mat. Sb., **47**, 271–306, 1959.

[92] P. Colella and H. M. Glaz, *Numerical modelling of inviscid shocked flows of real gases.* Proceedings of the 8th International Conference on Numerical Methods in Fluid Dynamics, Aachen, Germany, June 28 – July 2, 1982.

[93] P. R. Woodward and P. Colella, *The numerical simulation of two-dimensional fluid flow with strong shocks.* J. Comp. Phys., **54**(1), 115–173, 1984.

[94] H. M. Glaz, P. Colella, I. I. Glass, and R. L. Deschambault, *A numerical study of oblique shock-wave reflections with experimental comparisons.* Proc. R. Soc. Lond. A, **398**, 117–140, 1985.

[95] H. M. Glaz, P. Colella, J. P. Collins, and R. E. Ferguson, *Nonequilibrium effects in oblique shock-wave reflection.* American Institute of Aeronautics and Astronautics (AIAA) J., **26**(6), 698–705, 1988.

[96] P. Colella and H. M. Glaz, *Numerical calculation of complex shock reflections in gases.* Proceedings of the 9$^{\text{th}}$ International Conference on Numerical Methods in Fluid Dynamics, Saclay, France, June 25–29, 1984.

[97] P. Colella and L. F. Henderson, *The von Neumann paradox for the diffraction of weak shock waves.* J. Fluid Mech., **213**, 71–94, 1990.

[98] A. A. Fursenko, D. M. Sharov, E. V. Timofeev, and P. A. Voinovich, *Numerical simulation of shock wave interactions with channel bends and gas nonuniformities.* Comp. Fluids, **21**(3), 377–396, 1992.

[99] A. A. Fursenko, D. M. Sharov, E. V. Timofeev, and P. A. Voinovich, *High-resolution schemes and unstructured grids in transient shocked flow simulation.* Proceedings of the 13$^{\text{th}}$ International Conference on Numerical Methods in Fluid Dynamics, Rome, Italy, July 6–10, 1992.

[100] A. A. Fursenko, D. M. Sharov, E. V. Timofeev, and P. A. Voinovich, *An efficient unstructured Euler solver for transient shocked flows.* Proceedings of the 19$^{\text{th}}$ International Symposium on Shock Waves, Marseille, France, July 26–30, 1993.

[101] M. Beryozkina, D. Ofengeim, M. Syshchikova, E. V. Timofeev, A. A. Fursenko, and P. A. Voinovich, *A combined adaptive structured/unstructured technique for essentially unsteady shock-obstacle interactions at high Reynolds numbers.* Proceedings of the 5$^{\text{th}}$ International Conference on Hyperbolic Problems – Theory, Numerics, Applications, Stony Brook, New York, United States of America, June 13–17, 1994.

[102] P. A. Voinovich, T. Saito, A. A. Fursenko, A. Galyukov, and E. V. Timofeev, *Efficient 2D and 3D locally adaptive unstructured Euler solvers for unsteady shocked gas flows.* Proceedings of the 20$^{\text{th}}$ International Symposium on Shock Waves, Pasadena, California, United States of America, July 23–28, 1995.

[103] M. Sun and K. Takayama, *Conservative smoothing on an adaptive quadrilateral grid.* J. Comp. Phys., **150**(1), 143–180, 1999.

[104] L. F. Henderson, E. I. Vasilev, G. Ben-Dor, and T. Elperin, *The wall-jetting effect in Mach reflection: theoretical consideration and numerical investigation.* J. Fluid Mech., **479**, 259–286, 2003.

[105] E. Steinthorsson, D. Modiano, and P. Colella, *Computations of unsteady viscous compressible flows using adaptive mesh refinement in curvilinear body-fitted grid systems.* National Aeronautics and Space Administration (NASA) NASA TM-106704, 1994.

[106] E. Steinthorsson, D. Modiano, W. Y. Crutchfield, J. B. Bell, and P. Colella, *An adaptive semi-implicit scheme for simulations of unsteady viscous compressible flows.* American Institute of Aeronautics and Astronautics (AIAA) Paper 95-1727, 1995.

[107] D. Ofengeim, E. V. Timofeev, A. A. Fursenko, and P. A. Voinovich, *A hybrid adaptive structured/unstructured technique for essentially unsteady viscous/inviscid interactions.* Proceedings of the 1st Asian Computational Fluid Dynamics Conference, Hong Kong, China, January 16–19, 1995.

[108] D. Ofengeim, E. V. Timofeev, and P. A. Voinovich, *A locally adaptive structured/unstructured Navier-Stokes solver for essentially unsteady shock-obstacle interactions at high Reynolds numbers.* Proceedings of the 20th International Symposium on Shock Waves, Pasadena, California, United States of America, July 23–28, 1995.

[109] E. V. Timofeev, K. Takayama, P. A. Voinovich, A. Galyukov, D. Ofengeim, and T. Saito, *2-D/3-D unstructured grid generators, adaptive Euler/Navier-Stokes solvers and their application to unsteady shocked gas flow analysis.* Proceedings of the 15th International Conference on Numerical Methods in Fluid Dynamics, Monterey, California, United States of America, June 24–28, 1996.

[110] D. Drikakis, D. Ofengeim, E. V. Timofeev, and P. A. Voinovich, *Computation of non-stationary shock-wave/cylinder interaction using adaptive-grid methods.* J. Fluids Struct., **11**(6), 665–692, 1997.

[111] L. F. Henderson, W. Y. Crutchfield, and R. J. Virgona, *The effects of thermal conductivity and viscosity of argon on shock waves diffracting over rigid ramps.* J. Fluid Mech., **331**, 1–36, 1997.

[112] E. I. Vasilev, G. Ben-Dor, T. Elperin, and L. F. Henderson, *The wall-jetting effect in Mach reflection: Navier-Stokes simulations.* J. Fluid Mech., **511**, 363–379, 2004.

[113] D. T. Graves, P. Colella, D. Modiano, J. Johnson, B. Sjogreen, and X. Gao, *A Cartesian grid embedded boundary method for the compressible Navier-Stokes equations.* Comm. Appl. Math. and Comp. Sci., **8**(1), 99–122, 2013.

[114] D. K. Khotyanovsky, Y. A. Bondar, A. N. Kudryavtsev, G. V. Shoev, and M. S. Ivanov, *Viscous effects in steady reflection of strong shock waves.* American Institute of Aeronautics and Astronautics (AIAA) J., **47**(5), 1263–1269, 2009.

[115] M. S. Ivanov, Y. A. Bondar, D. V. Khotyanovsky, A. N. Kudryavtsev, and G. V. Shoev, *Viscosity effects on weak irregular reflection of shock waves in steady flow.* Prog. Aero. Sci., **46**(2–3), 89–105, 2010.

[116] J. Z. Zhang and C. P. T. Groth, *Parallel high-order anisotropic block-based adaptive mesh refinement finite-volume scheme*. American Institute of Aeronautics and Astronautics (AIAA) Paper 2011-3695, 2011.

[117] M. J. Williamschen and C. P. T. Groth, *Parallel anisotropic block-based adaptive mesh algorithm for three-dimensional flows*. American Institute of Aeronautics and Astronautics (AIAA) Paper 2013-2442, 2013.

[118] L. Freret and C. P. T. Groth, *Anisotropic non-uniform block-based adaptive mesh refinement for three-dimensional inviscid and viscous flows*. American Institute of Aeronautics and Astronautics (AIAA) Paper 2015-2613, 2015.

[119] C. P. T. Groth and S. A. Northrup, *Parallel implicit adaptive mesh refinement scheme for body-fitted multi-block mesh*. American Institute of Aeronautics and Astronautics (AIAA) Paper 2005-5333, 2005.

[120] S. A. Northrup and C. P. T. Groth, *Prediction of unsteady laminar flames using a parallel implicit adaptive mesh refinement algorithm*. Proceedings of the 6^{th} U.S. National Combustion Meeting, Ann Arbor, Michigan, United States of America, 2009.

[121] S. A. Northrup and C. P. T. Groth, *Parallel implicit adaptive mesh refinement scheme for unsteady fully-compressible reactive flows*. American Institute of Aeronautics and Astronautics (AIAA) Paper 2013-2433, 2013.

[122] M. K. Hryniewicki, C. P. T. Groth, and J. J. Gottlieb, *Parallel implicit anisotropic block-based adaptive mesh refinement finite-volume scheme for the study of fully resolved oblique shock wave reflections*. Shock Waves, **25**(4), 371–386, 2015.

[123] R. Leveque, *Finite volume methods for hyperbolic problems*. Cambridge University Press, 2002.

[124] L. Ivan and C. P. T. Groth, *High-order solution-adaptive central essentially non-oscillatory (CENO) method for viscous flows*. J. Comput. Phys., **257**(A), 860–862, 2014.

[125] J. P. Boris and D. L. Book, *Flux-corrected transport I: SHASTA, a fluid transport algorithm that works*. Journal of Computational Physics, **11**, 38–69, 1973.

[126] B. van Leer, *Towards the ultimate conservative difference scheme. II. Monotonicity and conservation combined in a second-order scheme*. Journal of Computational Physics, **14**(4), 361–370, 1974.

[127] A. Harten, *High resolution schemes for hyperbolic conservation laws*. Journal of Computational Physics, **49**(3), 357–393, 1983.

[128] V. Venkatakrishnan, *On the accuracy of limiters and convergence to steady state solutions*. American Institute of Aeronautics and Astronautics (AIAA) Paper 93-0880, 1993.

[129] T. J. Barth, *Recent developments in high order k-exact reconstruction on unstructured meshes.* American Institute of Aeronautics and Astronautics (AIAA) Paper 93-0668, 1993.

[130] J. J. Gottlieb and C. P. T. Groth, *Assessment of Riemann solvers for unsteady one-dimensional inviscid flows of perfect gases.* Journal of Computational Physics, **78**(2), 437–458, 1988.

[131] P. L. Roe, *Approximate Riemann solvers, parameter vectors, and difference schemes.* Journal of Computational Physics, **43**(2), 357–372, 1981.

[132] A. Harten, P. D. Lax, and B. V. Leer, *On upstream differencing and Godunov-type schemes for hyperbolic conservation laws.* SIAM Rev., **25**(1), 35–61, 1983.

[133] B. Einfeldt, *On Godunov-type methods for gas dynamics.* SIAM J. Numer. Anal., **25**(2), 294–318, 1988.

[134] E. F. Toro, M. Spruce, and W. Speares, *Restoration of the contact surface in the HLL-Riemann solver.* Shock Waves, **4**(1), 25–34, 1994.

[135] M.-S. Liou, *A sequel to AUSM: AUSM+.* Journal of Computational Physics, **129**(2), 364–382, 1996.

[136] T. Linde, *A practical, general-purpose, two-state HLL Riemann solver for hyperbolic conservation laws.* International Journal for Numerical Methods in Fluids, **40**, 391–402, 2002.

[137] W. J. Coirier and K. G. Powell, *Solution-adaptive Cartesian cell approach for viscous and inviscid flows.* American Institute of Aeronautics and Astronautics (AIAA) J., **34**(5), 938–945, 1996.

[138] H. Lomax, T. H. Pulliam, and D. W. Zingg, *Fundamentals of computational fluid dynamics.* Springer-Verlag, 2001.

[139] Y. Saad and M. H. Schultz, *GMRES: a generalized minimum residual algorithm for solving nonsymmetric linear systems.* SIAM J. Sci. Stat. Comp., **7**(3), 856–869, 1986.

[140] A. Jameson, *Time dependent calculations using multigrid, with applications to unsteady flows past airfoils and wings.* American Institute of Aeronautics and Astronautics (AIAA) Paper 91-1596, 1991.

[141] S. Isono and D. W. Zingg, *A Runge-Kutta-Newton-Krylov algorithm for fourth-order implicit time marching applied to unsteady flows.* American Institute of Aeronautics and Astronautics (AIAA) Paper 2004-0433, 2004.

[142] M. Tabesh and D. W. Zingg, *Higher-order implicit time-marching methods using a Newton-Krylov algorithm.* American Institute of Aeronautics and Astronautics (AIAA) Paper 2009-164, 2009.

[143] M. J. Berger and J. Oliger, *Adaptive mesh refinement for hyperbolic partial differential equations.* Journal of Computational Physics, **53**(3), 484–512, 1984.

[144] M. J. Berger and P. Colella, *Local adaptive mesh refinement for shock hydrodynamics.* Journal of Computational Physics, **82**(1), 68–84, 1989.

[145] M. J. Berger and J. S. Saltzman, *AMR on the CM-2.* Applied Numerical Mathematics, **14**(1–3), 239–253, 1994.

[146] D. L. D. Zeeuw and K. Powell, *An adaptively refined Cartesian mesh solver for the Euler equations.* J. Comp. Phys., **104**(1), 56–68, 1993.

[147] K. G. Powell, P. R. Roe, and J. Quirk, *Adaptive-mesh algorithms for computational fluid dynamics.* Alg. Trends Comp. Fluid Dyn., Springer New York, 303–337, 1993.

[148] J. J. Quirk and U. R. Hanebutte, *A parallel adaptive mesh refinement algorithm.* National Aeronautics and Space Administration (NASA) NASA CR-191530, 1993.

[149] C. P. T. Groth, D. L. D. Zeeuw, K. G. Powell, T. I. Gombosi, and Q. F. Stout, *A parallel solution-adaptive scheme for ideal magnetohydrodynamics.* American Institute of Aeronautics and Astronautics (AIAA) Paper 99-3273, 1999.

[150] S. A. Northrup and C. P. T. Groth, *Solution of laminar diffusion flames using a parallel adaptive mesh refinement algorithm.* American Institute of Aeronautics and Astronautics (AIAA) Paper 2005-0547, 2005.

[151] J. S. Sachdev, C. P. T. Groth, and J. J. Gottlieb, *A parallel solution-adaptive scheme for multi-phase core flows in solid propellant rocket motors.* Int. J. Comp. Fluid Dyn., **19**(2), 159–177, 2005.

[152] J. S. Sachdev, C. P. T. Groth, and J. J. Gottlieb, *Parallel AMR scheme for turbulent multi-phase rocket motor core flows.* American Institute of Aeronautics and Astronautics (AIAA) Paper 2005-5334, 2005.

[153] X. Gao and C. P. T. Groth, *A parallel adaptive mesh refinement algorithm for predicting turbulent non-premixed combusting flows.* Int. J. Comp. Fluid Dyn., **20**(5), 349–357, 2006.

[154] X. Gao and C. P. T. Groth, *Parallel adaptive mesh refinement scheme for turbulent non-premixed combusting flow prediction.* American Institute of Aeronautics and Astronautics (AIAA) Paper 2006-1448, 2006.

[155] M. J. Aftomis, , M. J. Berger, and S. M. Murman, *Application of space-filling curves to Cartesian methods for CFD.* American Institute of Aeronautics and Astronautics (AIAA) Paper 2004-1232, 2004.

[156] L. F. Henderson and P. M. Gray, *Experiments on the diffraction of strong blast waves.* Proc. R. Soc. Lond. A, **377**(1771), 363–378, 1981.

[157] M. K. Hryniewicki, J. J. Gottlieb, and C. P. T. Groth, *Shock transition solutions of Navier-Stokes equations with volume viscosity for nitrogen and air.* Proceedings of the 29$^{\text{th}}$ International Symposium on Shock Waves, Madison, Wisconsin, United States of America, July 14–19, 2013.

[158] G. I. Taylor and J. W. Maccoll, *Division H – the mechanics of compressible fluids.* In Durand, W. F.: Aerodynamic theory – a general review of progress vol. III, 209–250. Peter Smith, 1976.

[159] W. J. M. Rankine, *On the thermodynamic theory of waves of finite longitudinal disturbance.* Phil. Trans. R. Soc. Lond., **160**, 277–288, 1870.

[160] G. I. Taylor, *The conditions necessary for discontinuous motion in gases.* Proc. R. Soc. Lond. A, **84**(571), 371–377, 1910.

[161] M. S. Ivanov, S. F. Gimelshein, and A. E. Beylich, *Hysteresis effect in stationary reflection of shock waves.* Phys. Fluids, **7**(4), 685–667, 1995.

Appendix A

Collection of Post-Processed Data for Numerical Transition Between RR and MR in Argon

A collection of numerical results for the transition from regular to Mach reflections for incident shock waves striking wedges without a combined viscous and thermal boundary layer in argon is presented herein. The flow-field data has been obtained by means of the CFD solution method that is described in Chapter 5 and applied to the unsteady, two-dimensional form of the Euler equations, useful for modelling laminar, compressible, gaseous fluid flows such as the oblique shock-wave reflections of interest here. The analysis for determining the shock speeds and characteristic Mach stem length L for a given data set as a function of the parameter α is then performed via the accompanying post-processing technique outlined in Chapter 7. The resultant L versus α plots for each of the 20 preselected $(M_{\mathrm{i}}^{\star}, \theta_{\mathrm{w}}^{\star})$ reference point pairings presented in table 7.2(a) and illustrated in Fig. 9.1(a) for argon are presented in Figs. A.1 through A.20, respectively. A listing of the early and late indications of the emergence of a Mach stem surrounding the numerical transition boundary between regular and Mach reflections in argon for a wedge without a boundary layer is tabulated in table A.1.

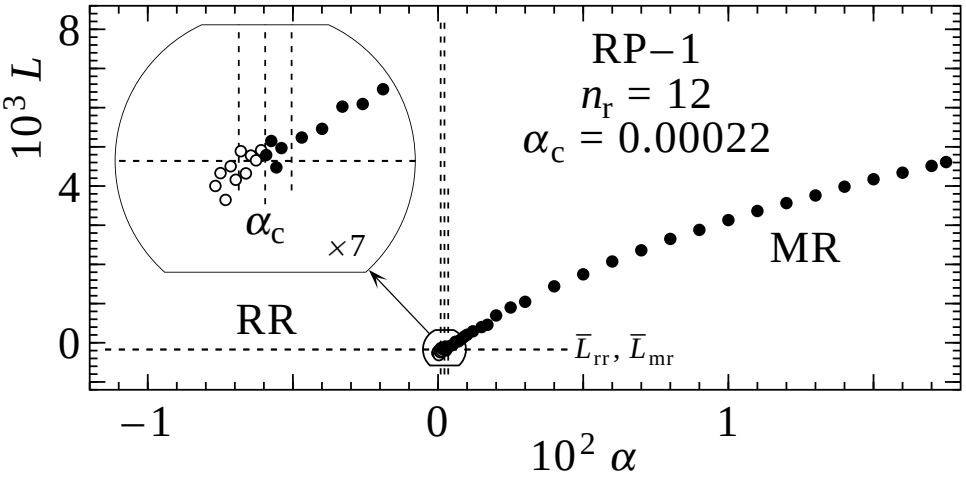

Figure A.1: L versus α plot and numerical transition point for reference point 1 ($M_i^\star = 1.001$ and $\theta_w^\star = 5.1010°$) in inviscid and polytropic argon.

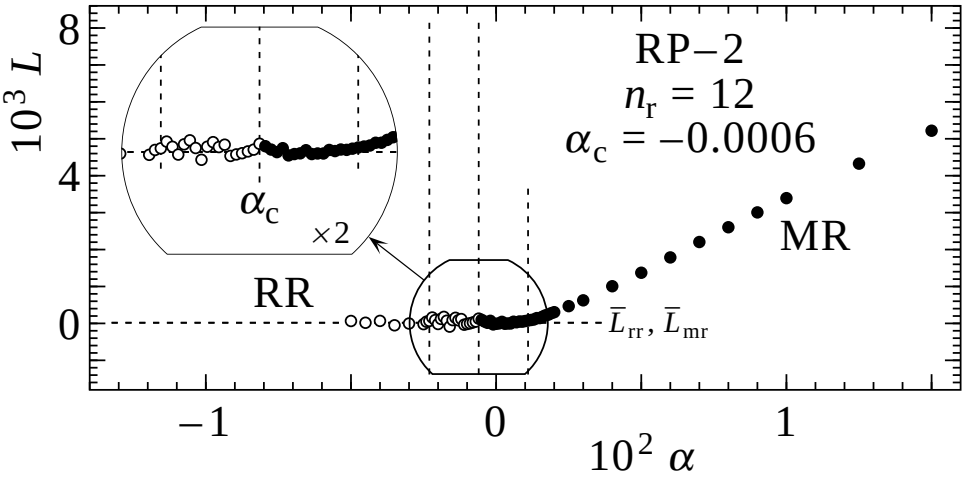

Figure A.2: L versus α plot and numerical transition point for reference point 2 ($M_i^\star = 1.006$ and $\theta_w^\star = 12.2184°$) in inviscid and polytropic argon.

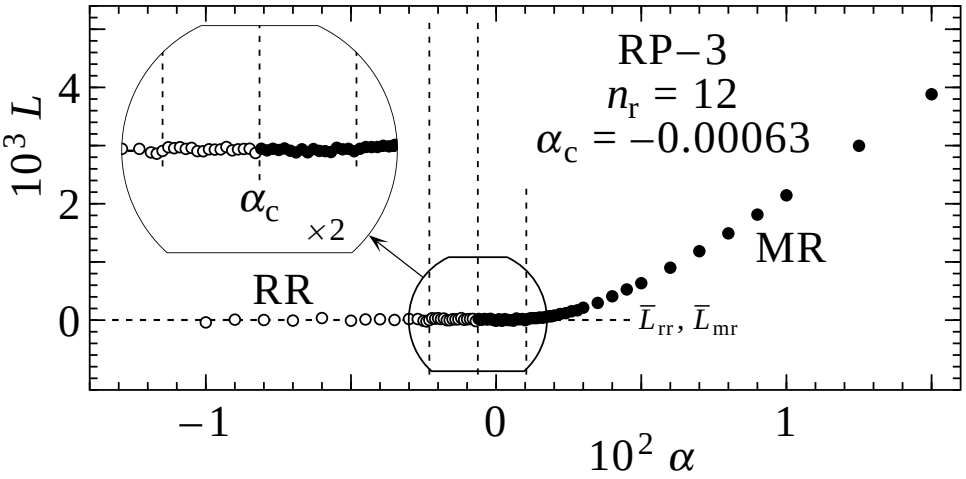

Figure A.3: L versus α plot and numerical transition point for reference point 3 ($M_i^\star = 1.018$ and $\theta_w^\star = 20.1533°$) in inviscid and polytropic argon.

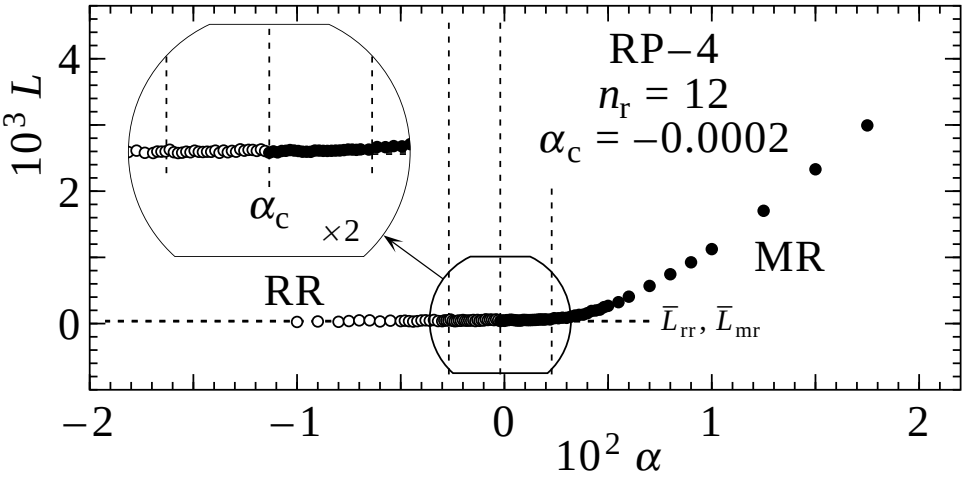

Figure A.4: L versus α plot and numerical transition point for reference point 4 ($M_i^\star = 1.041$ and $\theta_w^\star = 28.0871°$) in inviscid and polytropic argon.

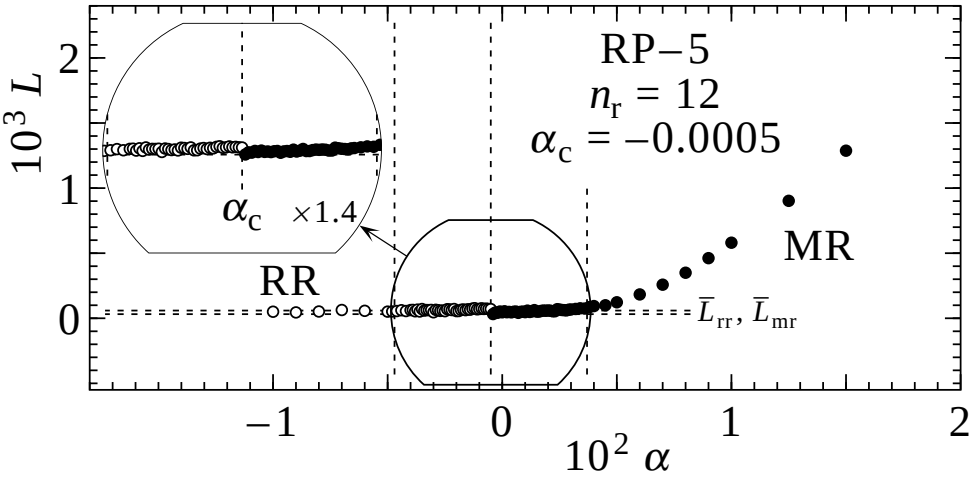

Figure A.5: L versus α plot and numerical transition point for reference point 5 ($M_i^\star = 1.089$ and $\theta_w^\star = 36.3558°$) in inviscid and polytropic argon.

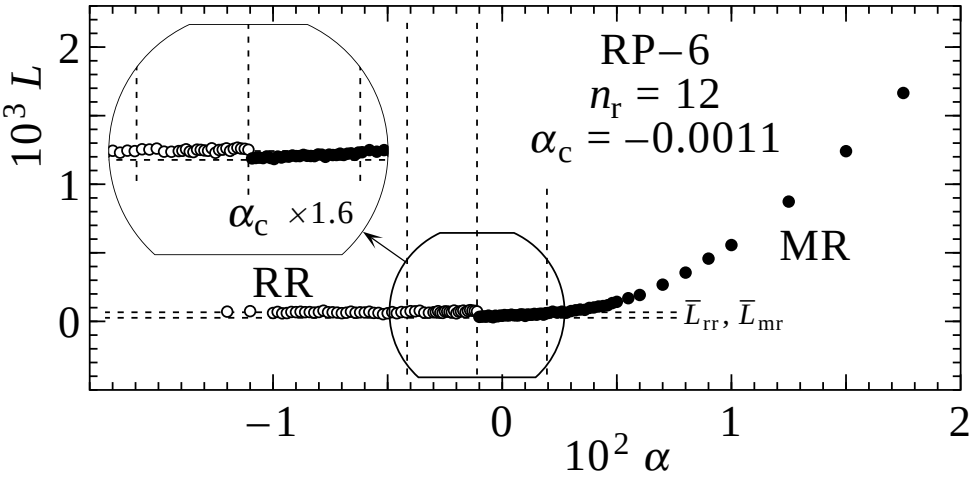

Figure A.6: L versus α plot and numerical transition point for reference point 6 ($M_i^\star = 1.182$ and $\theta_w^\star = 43.4992°$) in inviscid and polytropic argon.

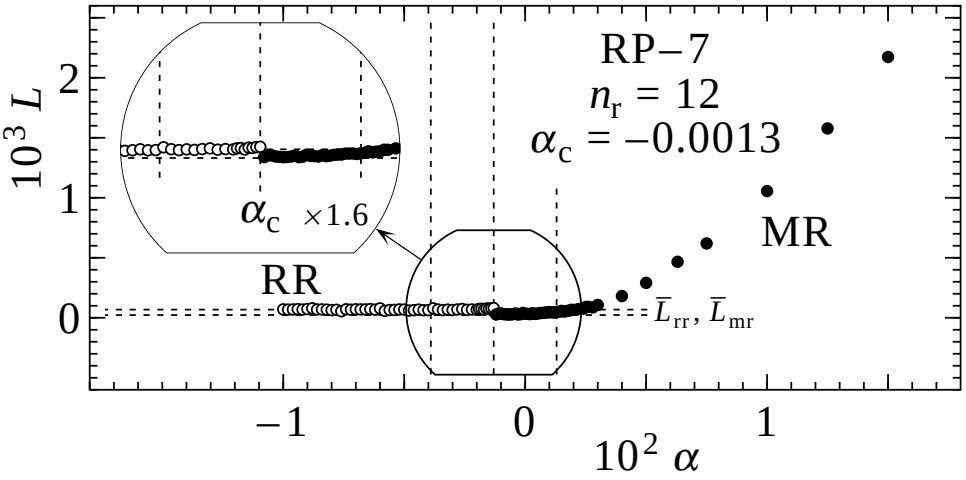

Figure A.7: L versus α plot and numerical transition point for reference point 7 ($M_i^\star = 1.305$ and $\theta_w^\star = 47.7127°$) in inviscid and polytropic argon.

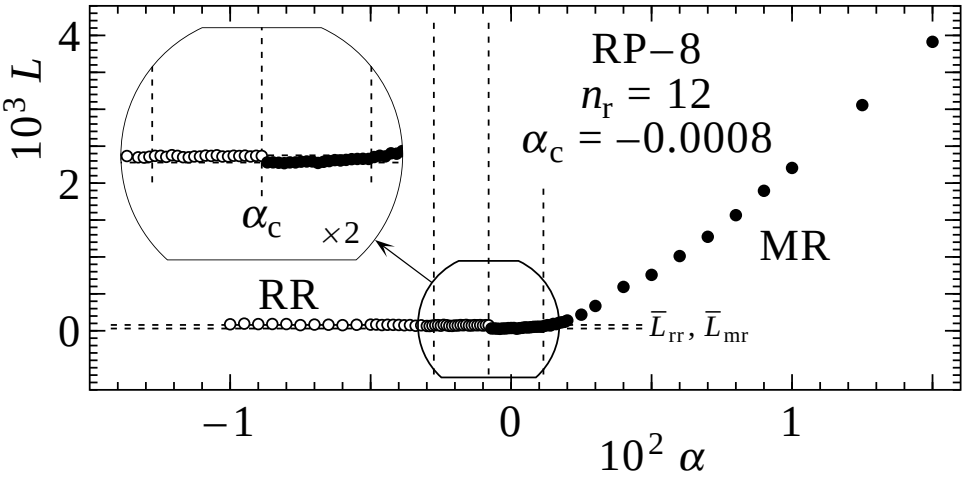

Figure A.8: L versus α plot and numerical transition point for reference point 8 ($M_i^\star = 1.435$ and $\theta_w^\star = 49.9799°$) in inviscid and polytropic argon.

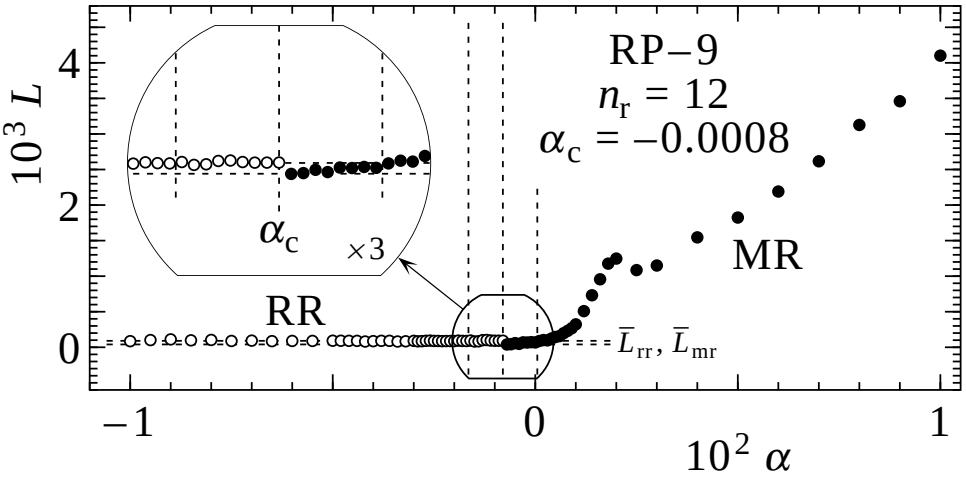

Figure A.9: L versus α plot and numerical transition point for reference point 9 ($M_i^\star = 1.572$ and $\theta_w^\star = 51.3539°$) in inviscid and polytropic argon.

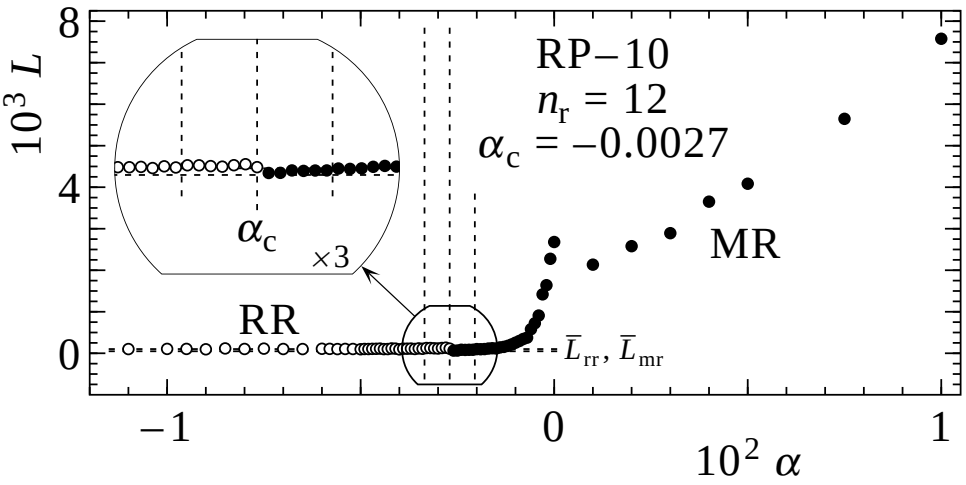

Figure A.10: L versus α plot and numerical transition point for reference point 10 ($M_i^\star = 1.715$ and $\theta_w^\star = 52.2405°$) in inviscid and polytropic argon.

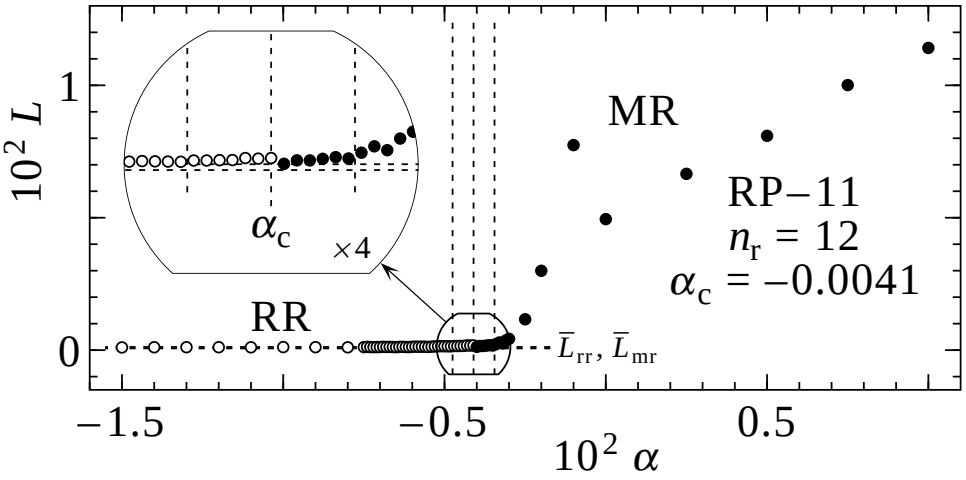

Figure A.11: L versus α plot and numerical transition point for reference point 11 ($M_i^\star = 1.855$ and $\theta_w^\star = 52.8110°$) in inviscid and polytropic argon.

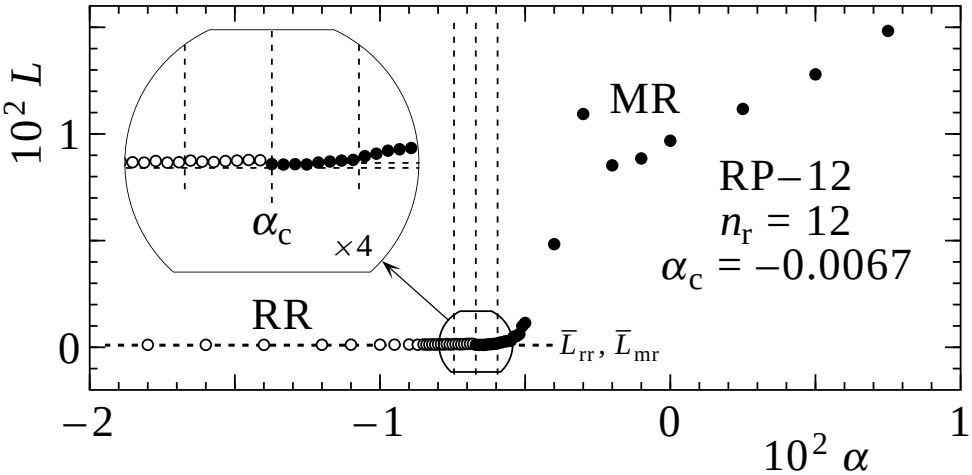

Figure A.12: L versus α plot and numerical transition point for reference point 12 ($M_i^\star = 2.0$ and $\theta_w^\star = 53.2183°$) in inviscid and polytropic argon.

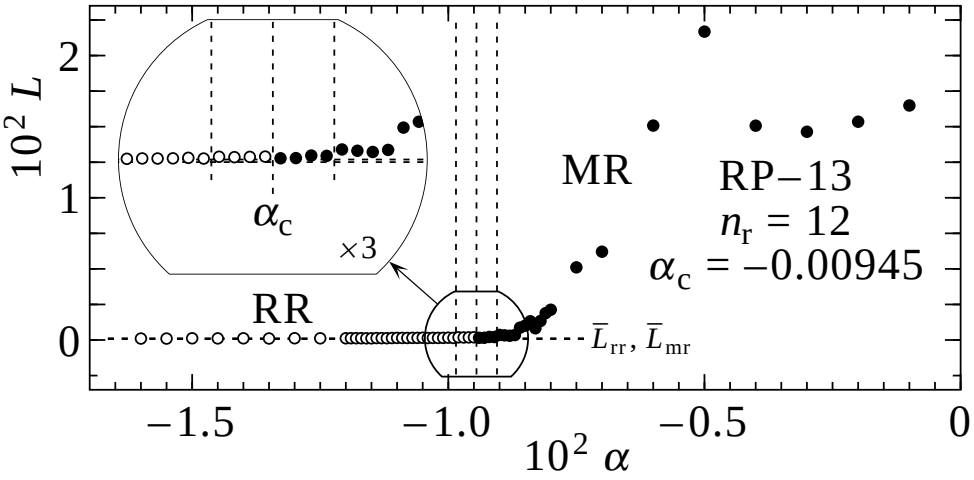

Figure A.13: L versus α plot and numerical transition point for reference point 13 ($M_i^\star = 2.25$ and $\theta_w^\star = 53.6680°$) in inviscid and polytropic argon.

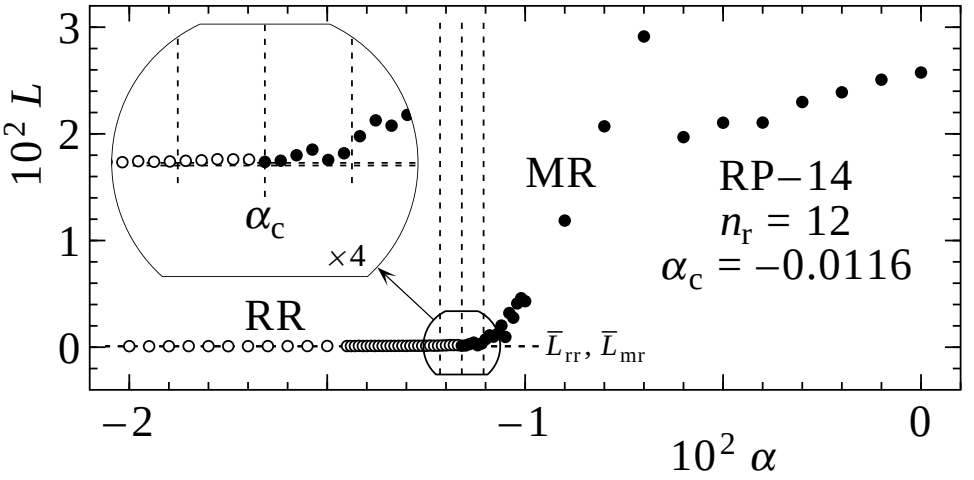

Figure A.14: L versus α plot and numerical transition point for reference point 14 ($M_i^\star = 2.5$ and $\theta_w^\star = 53.9398°$) in inviscid and polytropic argon.

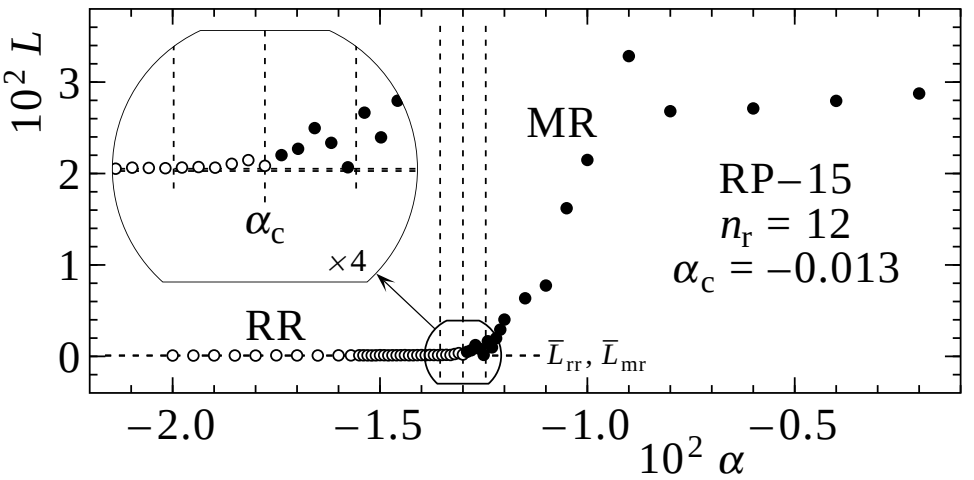

Figure A.15: L versus α plot and numerical transition point for reference point 15 ($M_i^\star = 2.75$ and $\theta_w^\star = 54.1151°$) in inviscid and polytropic argon.

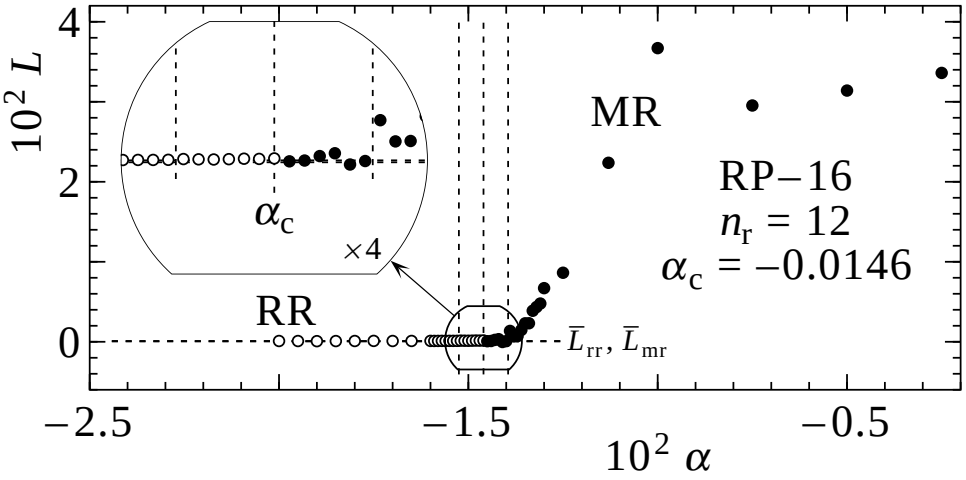

Figure A.16: L versus α plot and numerical transition point for reference point 16 ($M_i^\star = 3.0$ and $\theta_w^\star = 54.2340°$) in inviscid and polytropic argon.

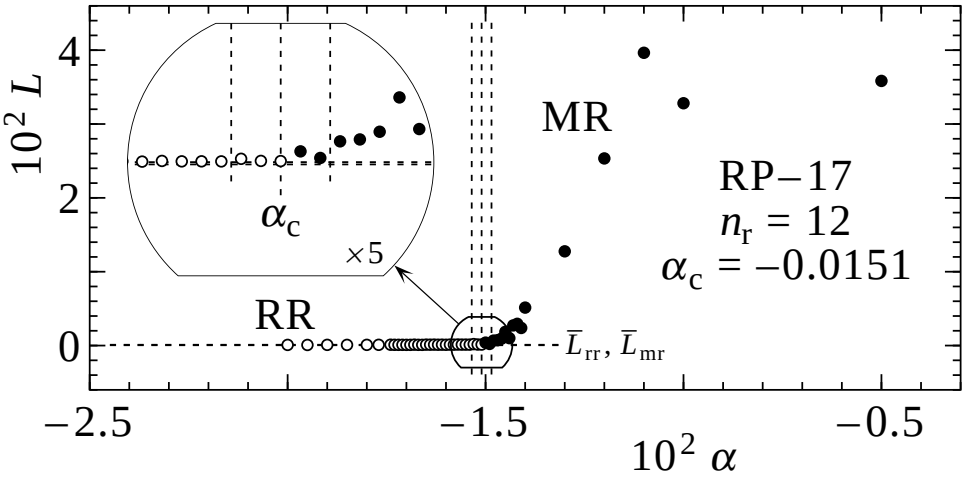

Figure A.17: L versus α plot and numerical transition point for reference point 17 ($M_i^\star = 3.25$ and $\theta_w^\star = 54.3179°$) in inviscid and polytropic argon.

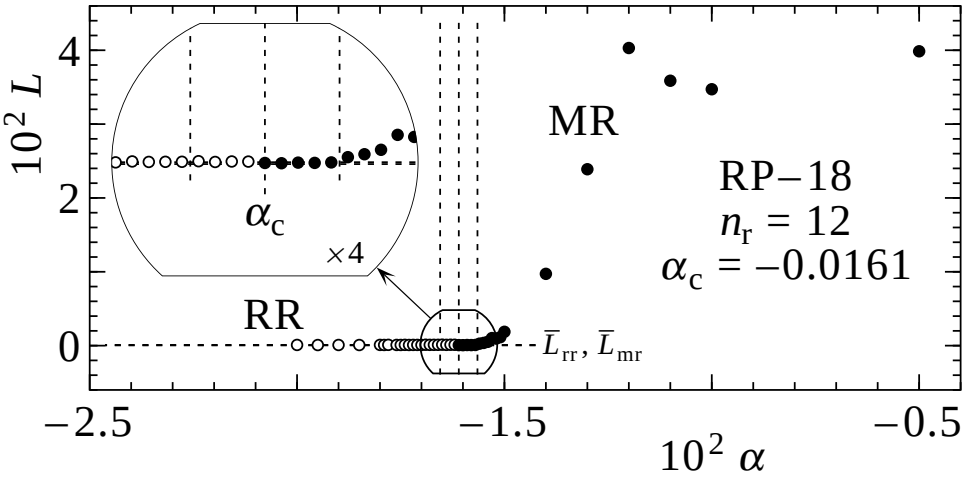

Figure A.18: L versus α plot and numerical transition point for reference point 18 ($M_i^\star = 3.5$ and $\theta_w^\star = 54.3792°$) in inviscid and polytropic argon.

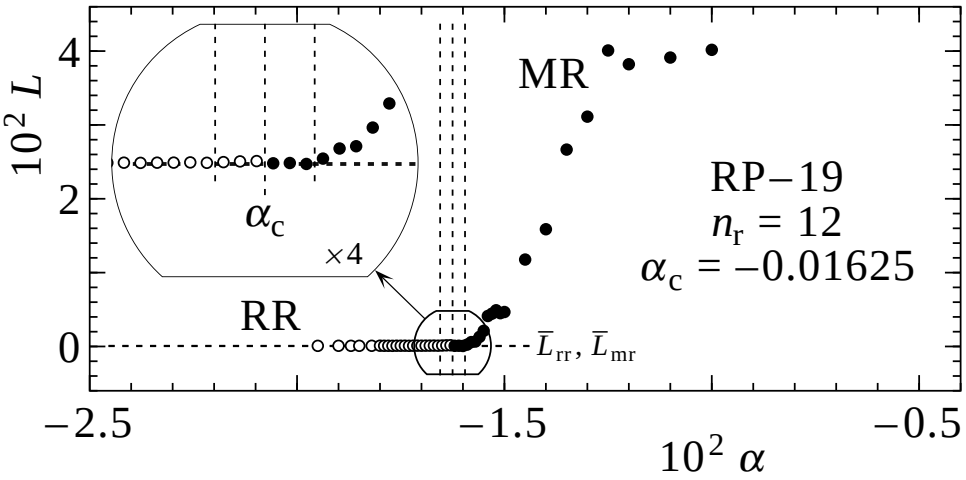

Figure A.19: L versus α plot and numerical transition point for reference point 19 ($M_i^\star = 3.75$ and $\theta_w^\star = 54.4252°$) in inviscid and polytropic argon.

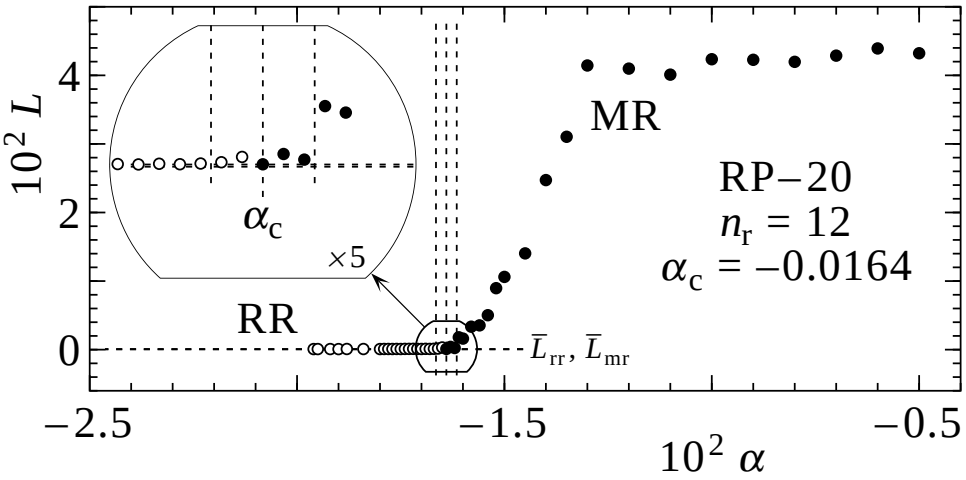

Figure A.20: L versus α plot and numerical transition point for reference point 20 ($M_i^\star = 4.0$ and $\theta_w^\star = 54.4606°$) in inviscid and polytropic argon.

Table A.1: Early and late indications of the emergence of a Mach stem surrounding the numerical transition boundary between regular and Mach reflections in argon for a wedge without a boundary layer.

RP	early indication			transition			late indication			$\frac{\lvert\text{late}-\text{early}\rvert}{2}$	
	α_{early}	M_{i}	$\theta_{\text{w}}(^\circ)$	α_{c}	M_{i}	$\theta_{\text{w}}(^\circ)$	α_{late}	M_{i}	$\theta_{\text{w}}(^\circ)$	$\pm\Delta M_{\text{i}}$	$\pm\Delta\theta_{\text{w}}(^\circ)$
1	0.00009	1.00109	5.1009	0.00022	1.00122	5.1007	0.00035	1.00135	5.1005	0.00013	0.0002
2	−0.00230	1.00370	12.2266	−0.00060	1.00540	12.2206	0.00110	1.00710	12.2145	0.00170	0.0060
3	−0.00230	1.01572	20.1709	−0.00063	1.01737	20.1581	0.00104	1.01903	20.1453	0.00166	0.0128
4	−0.00268	1.03840	28.1302	−0.00020	1.04081	28.0903	0.00228	1.04321	28.0504	0.00240	0.0399
5	−0.00470	1.08496	36.5273	−0.00050	1.08857	36.3741	0.00370	1.09218	36.2211	0.00361	0.1531
6	−0.00415	1.17978	43.7769	−0.00110	1.18141	43.5726	0.00195	1.18304	43.3691	0.00163	0.2039
7	−0.00390	1.30397	48.0339	−0.00130	1.30466	47.8195	0.00130	1.30534	47.6060	0.00069	0.2139
8	−0.00275	1.43461	50.2230	−0.00080	1.43489	50.0505	0.00115	1.43516	49.8786	0.00028	0.1722
9	−0.00165	1.57186	51.5050	−0.00080	1.57193	51.4271	0.00005	1.57200	51.3494	0.00007	0.0778
10	−0.00335	1.71482	52.5547	−0.00270	1.71486	52.4935	−0.00205	1.71489	52.4325	0.00003	0.0611
11	−0.00475	1.85483	53.2634	−0.00410	1.85486	53.2012	−0.00345	1.85488	53.1391	0.00002	0.0621
12	−0.00745	1.99982	53.9370	−0.00670	1.99984	53.8641	−0.00595	1.99985	53.7913	0.00002	0.0728
13	−0.00985	2.24986	54.6316	−0.00945	2.24987	54.5920	−0.00905	2.24987	54.5525	0.00001	0.0396
14	−0.01215	2.49989	55.1398	−0.01160	2.49990	55.0847	−0.01105	2.49990	55.0297	0.00000	0.0551
15	−0.01355	2.74992	55.4616	−0.01300	2.74992	55.4060	−0.01245	2.74993	55.3506	0.00000	0.0555
16	−0.01525	2.99994	55.7572	−0.01460	2.99994	55.6911	−0.01395	2.99994	55.6251	0.00000	0.0661
17	−0.01535	3.24996	55.8546	−0.01510	3.24996	55.8291	−0.01485	3.24996	55.8036	0.00000	0.0255
18	−0.01655	3.49996	56.0412	−0.01610	3.49997	55.9950	−0.01565	3.49997	55.9490	0.00000	0.0461
19	−0.01655	3.74997	56.0891	−0.01625	3.74997	56.0583	−0.01595	3.74997	56.0276	0.00000	0.0308
20	−0.01665	3.99998	56.1363	−0.01640	3.99998	56.1106	−0.01615	3.99998	56.0849	0.00000	0.0257

Appendix B

Collection of Post-Processed Data for Numerical Transition Between RR and MR in Atmospheric Air

A collection of numerical results for the transition from regular to Mach reflections for incident shock waves striking wedges without a combined viscous and thermal boundary layer in atmospheric air is presented herein. The flow-field data has been obtained by means of the CFD solution method that is described in Chapter 5 and applied to the unsteady, two-dimensional form of the Euler equations, useful for modelling laminar, compressible, gaseous fluid flows such as the oblique shock-wave reflections of interest here. The analysis for determining the shock speeds and characteristic Mach stem length L for a given data set as a function of the parameter α is then performed via the accompanying post-processing technique outlined in Chapter 7. The resultant L versus α plots for each of the 20 preselected $(M_{\mathrm{i}}^{\star}, \theta_{\mathrm{w}}^{\star})$ reference point pairings presented in table 7.2(b) and illustrated in Fig. 9.1(b) for atmospheric air are presented in Figs. B.1 through B.20, respectively. A listing of the early and late indications of the emergence of a Mach stem surrounding the numerical transition boundary between regular and Mach reflections in atmospheric air for a wedge without a boundary layer is tabulated in table B.1.

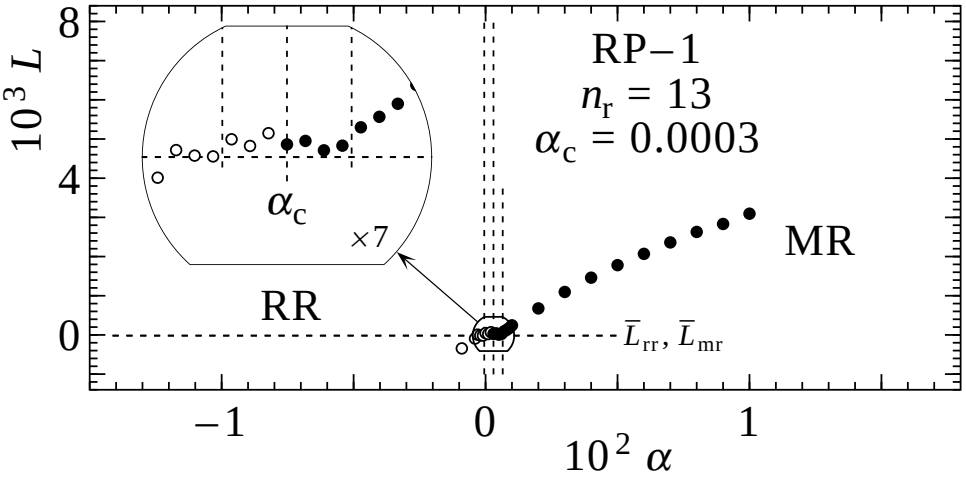

Figure B.1: L versus α plot and numerical transition point for reference point 1 ($M_i^\star = 1.001$ and $\theta_w^\star = 5.0997°$) in inviscid and polytropic air.

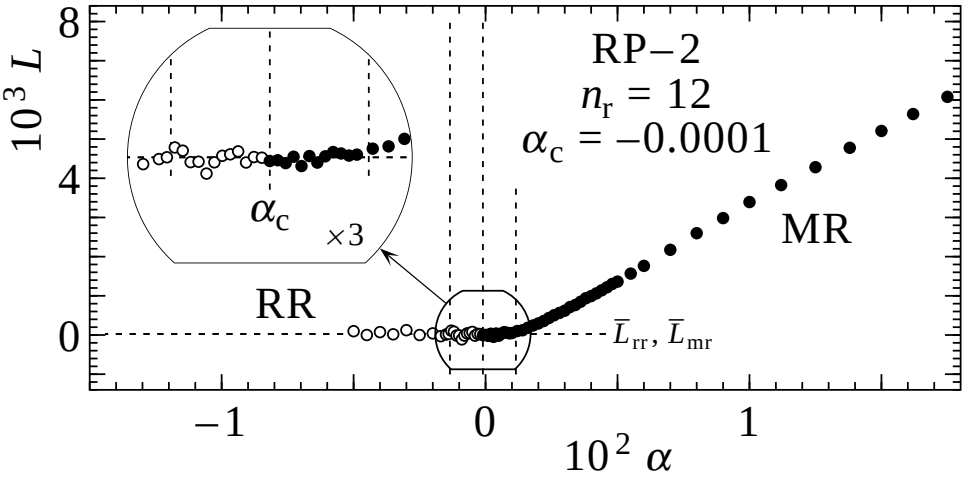

Figure B.2: L versus α plot and numerical transition point for reference point 2 ($M_i^\star = 1.006$ and $\theta_w^\star = 12.2012°$) in inviscid and polytropic air.

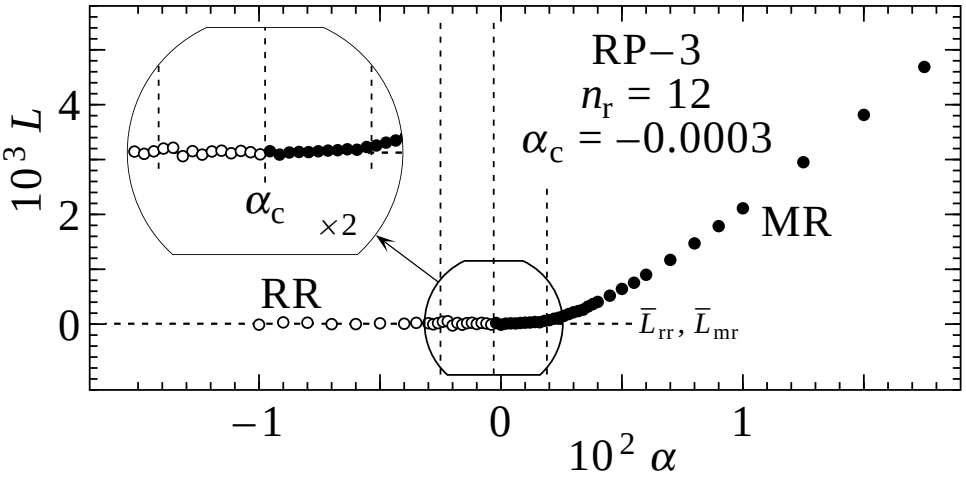

Figure B.3: L versus α plot and numerical transition point for reference point 3 ($M_i^\star = 1.018$ and $\theta_w^\star = 20.0766°$) in inviscid and polytropic air.

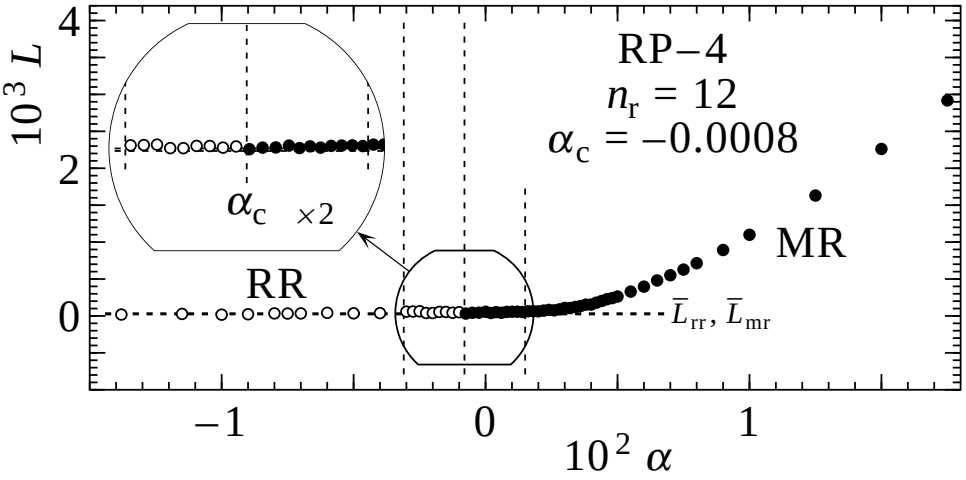

Figure B.4: L versus α plot and numerical transition point for reference point 4 ($M_i^\star = 1.041$ and $\theta_w^\star = 27.8798°$) in inviscid and polytropic air.

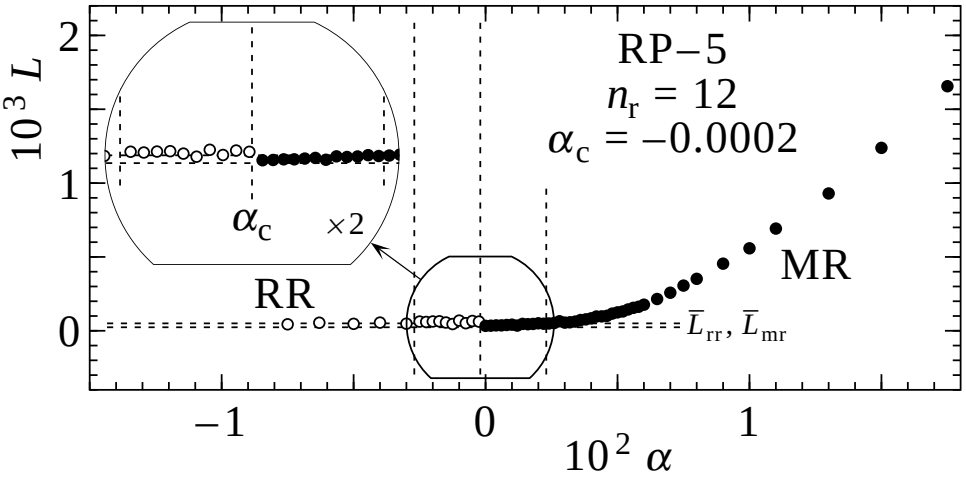

Figure B.5: L versus α plot and numerical transition point for reference point 5 ($M_i^\star = 1.089$ and $\theta_w^\star = 35.8945°$) in inviscid and polytropic air.

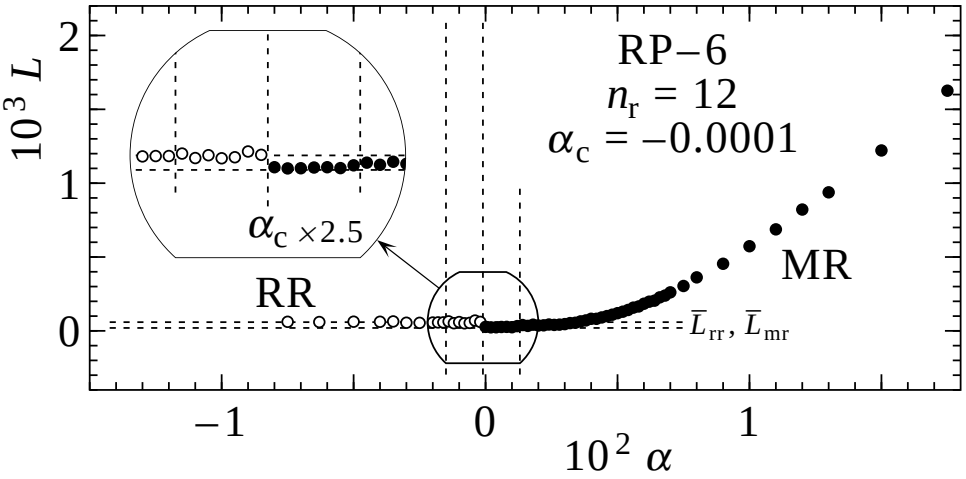

Figure B.6: L versus α plot and numerical transition point for reference point 6 ($M_i^\star = 1.182$ and $\theta_w^\star = 42.6428°$) in inviscid and polytropic air.

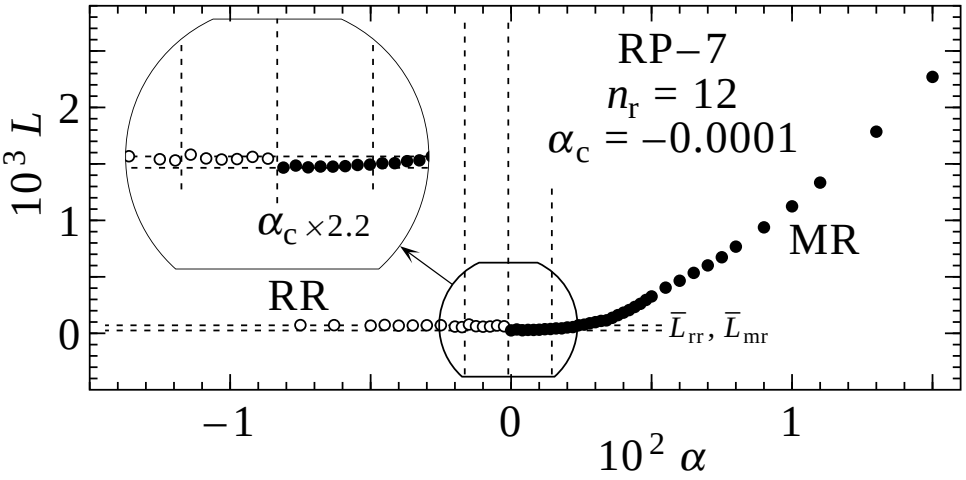

Figure B.7: L versus α plot and numerical transition point for reference point 7 ($M_i^\star = 1.305$ and $\theta_w^\star = 46.4516°$) in inviscid and polytropic air.

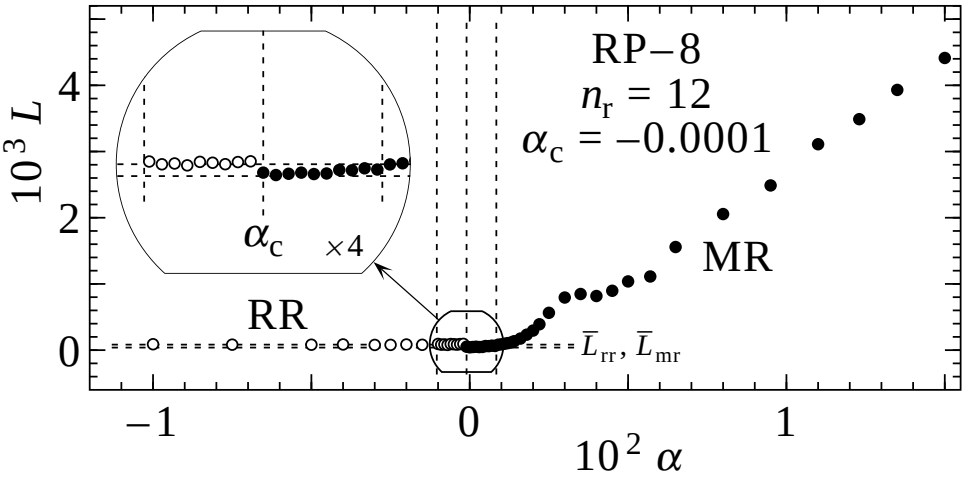

Figure B.8: L versus α plot and numerical transition point for reference point 8 ($M_i^\star = 1.435$ and $\theta_w^\star = 48.3727°$) in inviscid and polytropic air.

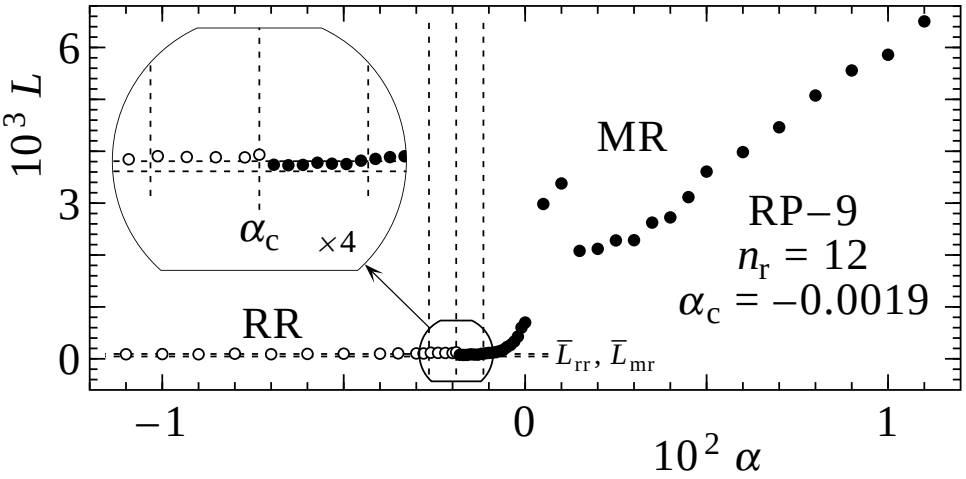

Figure B.9: L versus α plot and numerical transition point for reference point 9 ($M_i^\star = 1.572$ and $\theta_w^\star = 49.4404°$) in inviscid and polytropic air.

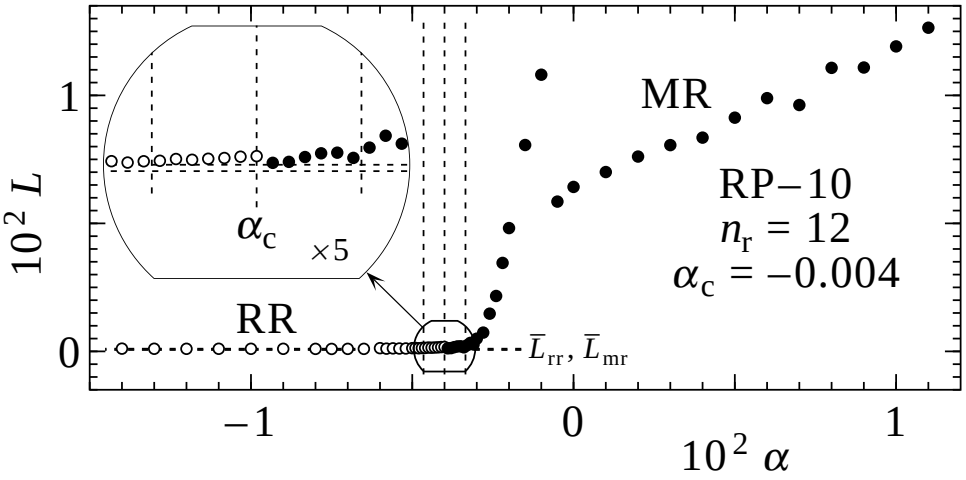

Figure B.10: L versus α plot and numerical transition point for reference point 10 ($M_i^\star = 1.715$ and $\theta_w^\star = 50.0537°$) in inviscid and polytropic air.

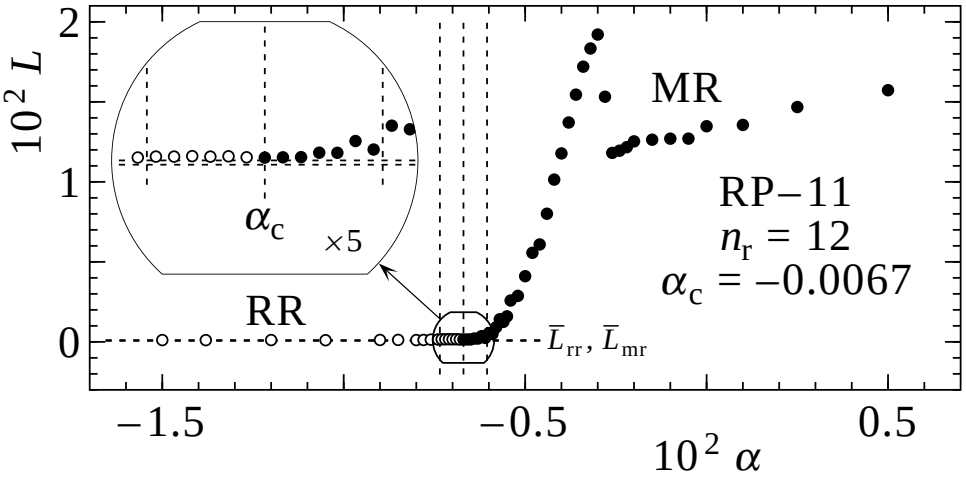

Figure B.11: L versus α plot and numerical transition point for reference point 11 ($M_i^\star = 1.855$ and $\theta_w^\star = 50.3927°$) in inviscid and polytropic air.

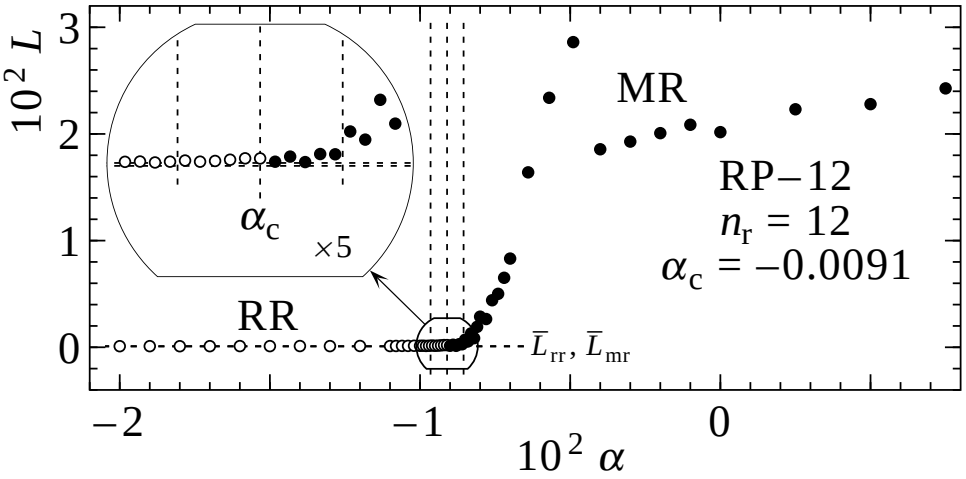

Figure B.12: L versus α plot and numerical transition point for reference point 12 ($M_i^\star = 2.0$ and $\theta_w^\star = 50.5908°$) in inviscid and polytropic air.

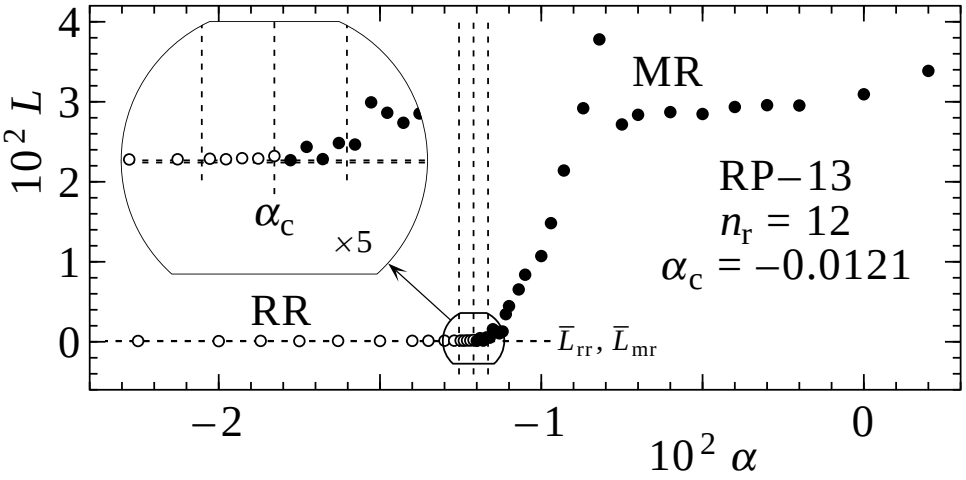

Figure B.13: L versus α plot and numerical transition point for reference point 13 ($M_i^\star = 2.25$ and $\theta_w^\star = 50.7392°$) in inviscid and polytropic air.

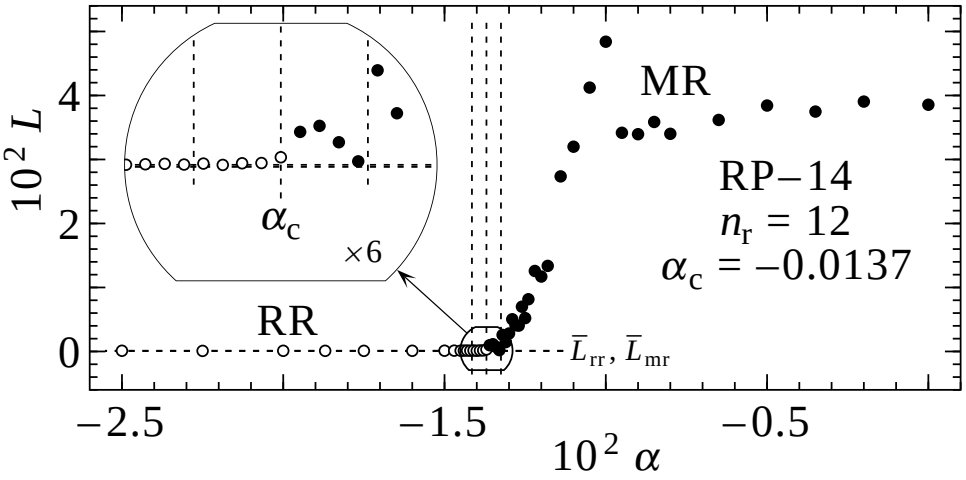

Figure B.14: L versus α plot and numerical transition point for reference point 14 ($M_i^\star = 2.5$ and $\theta_w^\star = 50.7684°$) in inviscid and polytropic air.

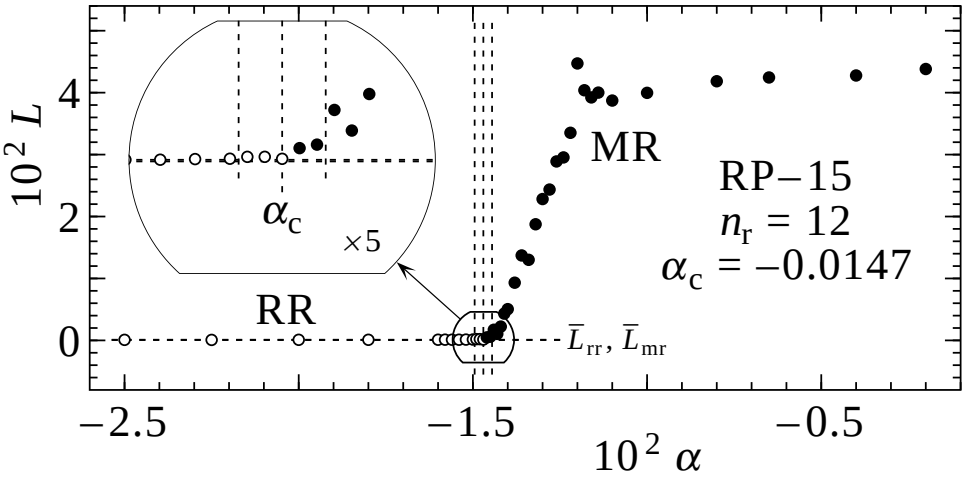

Figure B.15: L versus α plot and numerical transition point for reference point 15 ($M_i^\star = 2.75$ and $\theta_w^\star = 50.7463°$) in inviscid and polytropic air.

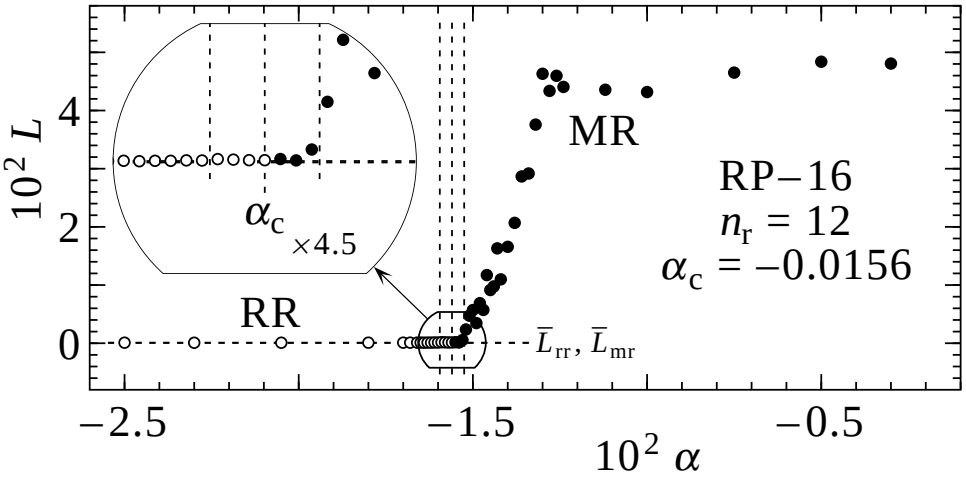

Figure B.16: L versus α plot and numerical transition point for reference point 16 ($M_i^\star = 3.0$ and $\theta_w^\star = 50.7032°$) in inviscid and polytropic air.

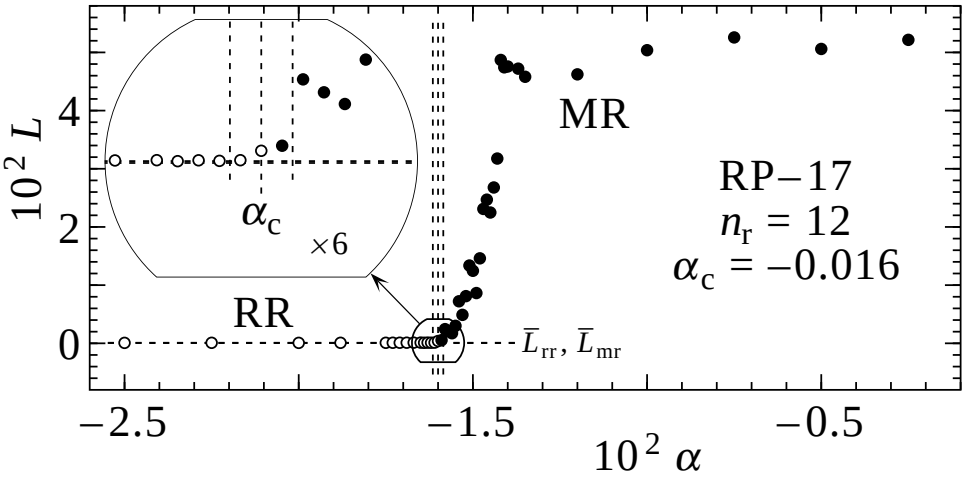

Figure B.17: L versus α plot and numerical transition point for reference point 17 ($M_i^\star = 3.25$ and $\theta_w^\star = 50.6529°$) in inviscid and polytropic air.

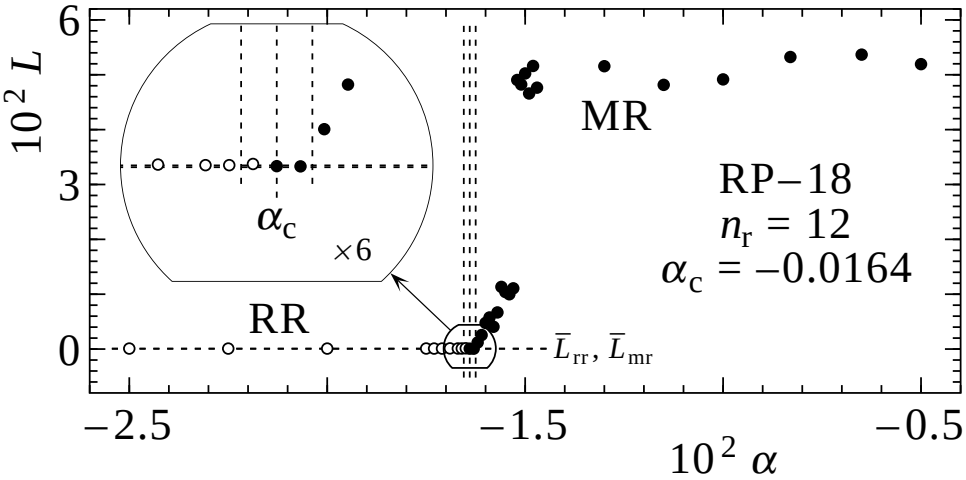

Figure B.18: L versus α plot and numerical transition point for reference point 18 ($M_i^\star = 3.5$ and $\theta_w^\star = 50.6021°$) in inviscid and polytropic air.

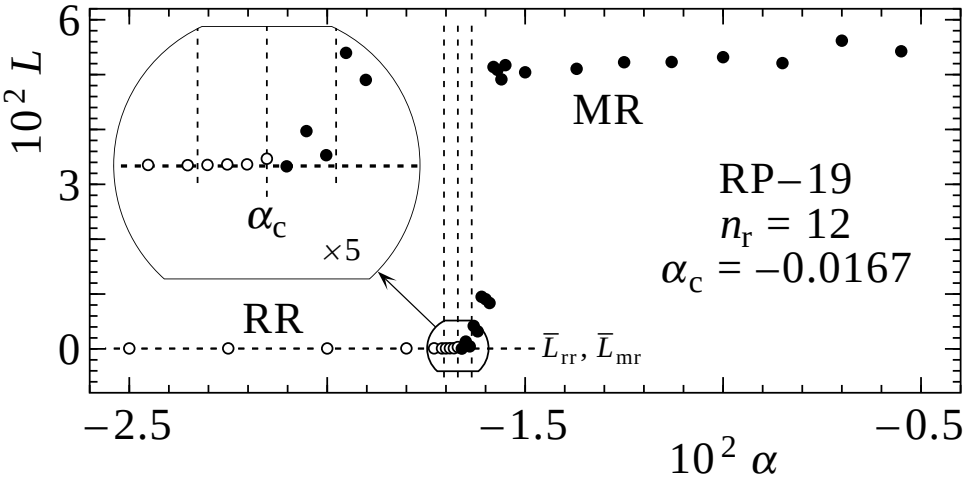

Figure B.19: L versus α plot and numerical transition point for reference point 19 ($M_i^\star = 3.75$ and $\theta_w^\star = 50.5537°$) in inviscid and polytropic air.

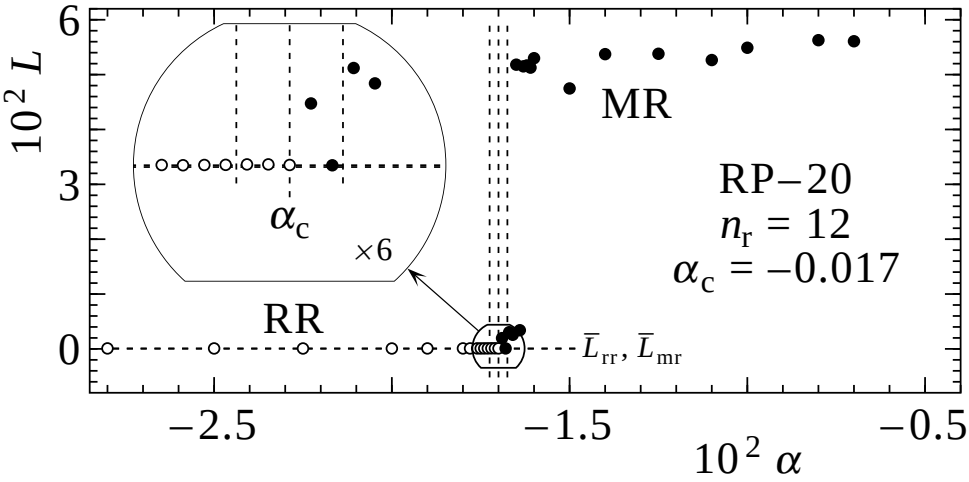

Figure B.20: L versus α plot and numerical transition point for reference point 20 ($M_i^\star = 4.0$ and $\theta_w^\star = 50.5090°$) in inviscid and polytropic air.

Table B.1: Early and late indications of the emergence of a Mach stem surrounding the numerical transition boundary between regular and Mach reflections in atmospheric air for a wedge without a boundary layer.

RP	early indication			transition			late indication			$\frac{\lvert\text{late}-\text{early}\rvert}{2}$	
	α_{early}	M_{i}	$\theta_{\text{w}}(^\circ)$	α_{c}	M_{i}	$\theta_{\text{w}}(^\circ)$	α_{late}	M_{i}	$\theta_{\text{w}}(^\circ)$	$\pm\Delta M_{\text{i}}$	$\pm\Delta\theta_{\text{w}}(^\circ)$
1	−0.00005	1.00095	5.0998	0.0003	1.00130	5.0993	0.00065	1.00165	5.0989	0.00035	0.0005
2	−0.00135	1.00465	12.2060	−0.0001	1.00590	12.2016	0.00115	1.00715	12.1971	0.00125	0.0045
3	−0.00250	1.01552	20.0959	−0.0003	1.01770	20.0789	0.00190	1.01988	20.0619	0.00218	0.0170
4	−0.00310	1.03800	27.9306	−0.0008	1.04023	27.8929	0.00150	1.04245	27.8553	0.00223	0.0376
5	−0.00270	1.08670	35.9950	−0.0002	1.08883	35.9020	0.00230	1.09096	35.8090	0.00213	0.0930
6	−0.00150	1.18123	42.7434	−0.0001	1.18195	42.6495	0.00130	1.18266	42.5558	0.00071	0.0938
7	−0.00165	1.30461	46.5849	−0.0001	1.30498	46.4596	0.00145	1.30535	46.3346	0.00037	0.1252
8	−0.00104	1.43487	48.4618	−0.0001	1.43499	48.3812	0.00084	1.43510	48.3008	0.00011	0.0805
9	−0.00265	1.57183	49.6739	−0.0019	1.57188	49.6077	−0.00115	1.57193	49.5416	0.00005	0.0662
10	−0.00465	1.71484	50.4702	−0.0040	1.71486	50.4117	−0.00335	1.71488	50.3534	0.00002	0.0584
11	−0.00735	1.85485	51.0578	−0.0067	1.85487	50.9986	−0.00605	1.85488	50.9395	0.00001	0.0592
12	−0.00965	1.99989	51.4699	−0.0091	1.99990	51.4194	−0.00855	1.99991	51.3689	0.00001	0.0505
13	−0.01255	2.24996	51.8896	−0.0121	2.24996	51.8478	−0.01165	2.24996	51.8061	0.00000	0.0417
14	−0.01415	2.50000	52.0684	−0.0137	2.50000	52.0265	−0.01325	2.50000	51.9846	0.00000	0.0419
15	−0.01495	2.75002	52.1203	−0.0147	2.75002	52.0970	−0.01445	2.75002	52.0737	0.00000	0.0233
16	−0.01595	3.00003	52.1692	−0.0156	3.00003	52.1365	−0.01525	3.00003	52.1038	0.00000	0.0327
17	−0.01615	3.25004	52.1360	−0.0160	3.25004	52.1220	−0.01585	3.25004	52.1080	0.00000	0.0140
18	−0.01655	3.50004	52.1208	−0.0164	3.50004	52.1068	−0.01625	3.50004	52.0928	0.00000	0.0140
19	−0.01705	3.75004	52.1174	−0.0167	3.75003	52.0847	−0.01635	3.75003	52.0521	0.00000	0.0326
20	−0.01725	4.00003	52.0898	−0.0170	4.00003	52.0665	−0.01675	4.00003	52.0432	0.00000	0.0233